

SPECTRAL ANALYSIS OF GAMMA RAY BURSTS  
WITH  
THERMAL SIGNATURE DURING THEIR PROMPT PHASE

by  
Aslıhan Muazzez ÜNSAL

Submitted to the Graduate School of Engineering and Natural Sciences  
in partial fulfillment of  
the requirements for the degree of  
Doctor of Philosophy

Sabancı University  
August 2015

SPECTRAL ANALYSIS OF GAMMA RAY BURSTS  
WITH  
THERMAL SIGNATURE DURING THEIR PROMPT PHASE

APPROVED BY:

Prof. Ersin Gögüş .....

(Dissertation Supervisor)

Assoc. Prof. Emrah Kalemci .....

Assoc. Prof. Kürşat Şendur .....

Prof. Kazım Yavuz Ekşi .....

Assoc. Prof. Tolga Güver .....

DATE OF APPROVAL: .....

© Aslıhan Muazzez ÜNSAL 2015

All Rights Reserved

*To my family...*

# TABLE OF CONTENTS

<b>1</b>	<b>Introduction</b>	<b>1</b>
1.1	Gamma Ray Bursts . . . . .	1
1.2	Temporal and Spectral Properties of GRBs . . . . .	5
1.2.1	Prompt Emission Phase – Time Profiles . . . . .	5
1.2.2	Prompt Emission Phase Spectral Properties . . . . .	9
1.2.3	Afterglow Phase . . . . .	13
1.3	Models of Progenitors . . . . .	17
1.4	Physics of GRBs . . . . .	19
1.4.1	Compactness problem . . . . .	19
1.4.2	Internal & External Shock Scenario . . . . .	19
1.4.2.1	Internal Shocks . . . . .	20
1.4.2.2	External Shocks . . . . .	22
1.5	Observational Constraints on Synchrotron Emission . . . . .	25
1.6	Photospheric Emission in GRBs . . . . .	26
1.6.1	Dominant Thermal Emission . . . . .	26
1.6.2	Modified Thermal Emission . . . . .	28
1.6.3	Sub-dominant Thermal Emission . . . . .	32
1.6.4	Inferring Parameters of the Expanding Fireball . . . . .	38
1.7	Motivation of Our Work . . . . .	39
<b>2</b>	<b>Gamma-ray Burst Monitor</b>	<b>41</b>
2.1	Scintillation Detectors . . . . .	41
2.1.1	NaI(Tl) Detectors . . . . .	43
2.1.2	BGO Detectors . . . . .	43
2.2	Detector Response Matrices . . . . .	44
2.3	GBM Data Types . . . . .	49
<b>3</b>	<b>Methodology</b>	<b>51</b>
3.1	Systematic Time Resolved Analysis . . . . .	52
3.1.1	Detectors, Data Type and Time Binning . . . . .	52
3.1.2	Spectral Photon Models . . . . .	54
3.1.3	Castor Statistics . . . . .	55
3.1.4	Primary Candidate Bursts Selection . . . . .	57
3.1.5	Thermal Candidate GRBs Sample . . . . .	57
3.2	Analysis of Thermal Candidate GRBs . . . . .	60
3.2.1	Time Resolved Analysis . . . . .	60

3.2.2	Spectral Simulations . . . . .	61
<b>4</b>	<b>Results</b>	<b>67</b>
4.1	GRB 080817A . . . . .	68
4.1.1	Parameter Evolutions . . . . .	68
4.1.1.1	Flux Evolutions . . . . .	69
4.1.2	Pulse Simulations . . . . .	69
4.2	GRB 081215A . . . . .	79
4.2.1	Parameter Evolutions . . . . .	79
4.2.1.1	Flux Evolutions . . . . .	79
4.2.2	Pulse Simulations . . . . .	80
4.3	GRB 090217 . . . . .	91
4.3.1	Parameter Evolutions . . . . .	91
4.3.1.1	Flux Evolutions . . . . .	91
4.3.2	Pulse Simulations . . . . .	92
4.4	GRB 090323A . . . . .	99
4.4.1	Parameter Evolutions . . . . .	99
4.4.1.1	Flux Evolutions . . . . .	100
4.4.2	Pulse Simulations . . . . .	100
4.5	GRB 100414A . . . . .	111
4.5.1	Parameter Evolutions . . . . .	111
4.5.1.1	Flux Evolutions . . . . .	111
4.5.2	Pulse Simulations . . . . .	112
4.6	GRB 100918A . . . . .	122
4.6.1	Parameter Evolutions . . . . .	122
4.6.1.1	Flux Evolutions . . . . .	123
4.6.2	Pulse Simulations . . . . .	123
4.7	GRB 101123A . . . . .	136
4.7.1	Parameter Evolutions . . . . .	136
4.7.1.1	Flux Evolutions . . . . .	136
4.7.2	Pulse Simulations . . . . .	137
4.8	GRB 110721A . . . . .	153
<b>5</b>	<b>Summary and Discussion</b>	<b>160</b>
5.1	Intrinsic Parameters of Expanding Fireball . . . . .	163
5.2	Remaining Questions . . . . .	167
<b>6</b>	<b>Conclusions</b>	<b>169</b>
6.1	Prospects for Future Work . . . . .	170
	<b>Bibliography</b>	<b>171</b>

## LIST OF TABLES

2.1	GBM data types. Each type of data is produced for each GBM detector. . . . .	50
3.1	Several basic properties of the bursts in thermal candidate GRBs sample. . . . .	59
4.1	Fine time interval fit results for GRB 080817A. Best parameter values with their $1\sigma$ uncertainties. . . . .	72
4.2	Fine time interval fit results for GRB 081215A. Best parameter values with their $1\sigma$ uncertainties. . . . .	83
4.3	Fine time interval fit results for GRB 090217A. Best parameter values with their $1\sigma$ uncertainties. . . . .	94
4.4	Fine time interval fit results for GRB 090323A. Best parameter values with their $1\sigma$ uncertainties. . . . .	103
4.5	Fine time interval fit results for GRB 100414A. Best parameter values with their $1\sigma$ uncertainties. . . . .	114
4.6	Fine time interval fit results for GRB 100918A. Best parameter values with their $1\sigma$ uncertainties. . . . .	125
4.7	Fine time interval fit results for GRB 101123A. Best parameter values with their $1\sigma$ uncertainties. . . . .	140
4.8	Fine time interval fit results for GRB 110721A. Best parameter values with their $1\sigma$ uncertainties. . . . .	156
5.1	Estimated ranges for intrinsic flow parameters for all the bursts in thermal candidate sample. . . . .	166

## LIST OF FIGURES

1.1	The sky distribution of 2704 GRBs detected by BATSE, in Galactic coordinates. The intensity of individual bursts indicated by colors as shown in the bottom scale. Credit:NASA. . . . .	4
1.2	Duration distribution for 1000 bursts detected by Fermi-GBM between 14-07-2008 and 26-09-2012, in the energy range 50 – 300 keV. .	6
1.3	Hardness vs. duration plot for Fermi-GBM bursts. Hardness is defined as the ratio of the flux density in 50 – 300 keV to that in 10 – 50 keV. Taken from von Kienlin et al. (2014). . . . .	7
1.4	Light curves of 12 GRBs observed with BATSE. They are almost unique. Duration varies from milliseconds to minutes. Pulses can be smooth or spiky, well separated or overlapped. Credit: J.T. Bonnell (NASA/GSFC). . . . .	8
1.5	The distribution of low-energy spectral index $\alpha$ for fluence spectra of 943 Fermi-GBM bursts. The gray-filled histogram shows the distribution of the low-energy index of the best model out of four photon models applied, for all spectra. The solid histogram shows the power-law index distribution of the spectra for which the PL model is the best model. Similarly, dashed, dashed-dotted, and dashed-triple dotted histograms represents the low-energy index distributions of COMP, BAND, and SBPL models. Taken from Gruber et al. (2014).	12
1.6	Examples afterglow emission. GRB 050315 has a steep-to-shallow transition, GRB 050502B has a large X-ray flare, and GRB050826 has a gradual decline (points are divided by 100 for clarity). Figure is taken from O’Brien et al. (2006a). . . . .	15

1.7	The phases of X-ray Afterglow observed in GRBs. The phase 0 represents the prompt emission. I is the steep-decay, II is the shallower decay, III is the typical afterglow, IV is the jet break phases. Phase V is denoting the X-ray flare. Taken from Zhang et al. (2006). . . . .	16
1.8	The inner engine releases huge amount of energy $\sim 10^{53}$ erg. Most of this energy is used to produce the relativistic jet and the remaining energy decouples from the flow at photospheric radius. The kinetic energy of the jet is dissipated within internal and external shocks which accelerates the electrons to relativistic speeds and gives rise to observed prompt and afterglow emission via synchrotron radiation . Credit: NASA's Goddard Space Flight Center. . . . .	23
1.9	The expected energy flux spectrum of power law distributed electrons synchrotron radiation in fast (a) and slow cooling (b) regimes. Taken from Sari et al. (1998). . . . .	24
1.10	The temperature evolution of the blackbody component in the spectrum of a BATSE burst GRB 971127. Taken from Ryde (2004). . . . .	30
1.11	The $\nu F_\nu$ spectra of two time intervals, $t = 8.1 - 8.5$ s and $t = 15.9 - 16.4$ s, belonging to first and second half of the prompt emission phase for GRB 090902B. Different symbols are referring to different detectors aboard on Fermi. The broadening in the spectrum is clear. Taken from Ryde et al. (2011). . . . .	31
1.12	The evolution of parameters with and without blackbody function for the prompt emission phase of GRB 120323A. Taken from Guiriec et al. (2013). . . . .	34
1.13	The $\nu F_\nu$ spectrum of two different time intervals, before and after the observed discontinuity. Initially the single hump model (BAND) mimics the blackbody component, where later it mimics the non-thermal component of the hybrid model. Taken from Guiriec et al. (2013). . . . .	35

1.14	The rest frame peak energy $E_{\text{peak}}(1 + z)$ versus observed isotropic luminosity L graph for Fermi GRBs with redshift measurement (Lu et al., 2012) and GRB 110721A. The solid and dashed lines correspond to death lines of two candidate redshift measurements for GRB 110721A. The two stars are representing the initial time interval of GRB110721A, which are well above the limits. Taken from Zhang et al. (2012).	37
2.1	The cross sections for gamma-ray interaction processes in a NaI Crystal. Taken from Kaneko et al. (2006).	45
2.2	The positions and orientations of GBM detectors. Numbers from zero to eleven representing the twelve NaI detectors, and numbers 12 and 13 are showing two BGO detectors. The block on top is the LAT. Taken from Meegan et al. (2009).	46
2.3	The energy resolution of a NaI (squares) and a BGO (triangles) detector as a function of energy. Taken from Bissaldi et al. (2009).	47
2.4	The effective area of NaI and BGO detectors as a function of energy, assuming normal incidence. Taken from Bissaldi et al. (2009).	48
3.1	The spectral shapes of the COMP ( $\alpha = -1.5$ and $E_{\text{peak}} = 300\text{keV}$ ), BAND ( $\alpha = -1.5$ , $E_{\text{peak}} = 300\text{keV}$ , and $\beta = -2.5$ ), and BB ( $kT = 30\text{keV}$ ) models in $\nu F_{\nu}$ representation.	56
3.2	The parameter distributions of single (BAND) and hybrid (BANDBB) models resulting from fitting of synthetic spectra produced with BANDBB hybrid model parameters for GRB 090323A. The red dashed lines indicate the real-fit parameters. The green curves are Gaussian fits to distribution of parameters and the peak values are shown by green solid lines. The blue-long dashed lines are showing the $1\sigma$ error intervals.	64

3.3	The parameter distributions of single (BAND) and hybrid (BANDBB) models resulting from fitting of synthetic spectra produced with single BAND model parameters for GRB 090323A. The red dashed lines indicate the real-fit parameters. The green curves are Gaussian fits to distribution of parameters and the peak values are shown by green solid lines. The blue long-dashed lines are showing the $1\sigma$ error intervals. . . . .	65
3.4	The distribution of CSTAT difference obtained from single (BAND) and hybrid (BANDBB) model fits of synthetic spectra produced with single BAND model parameters for GRB 090323A. The red dashed line indicates the real-fit CSTAT improvement obtained by BANDBB model fit over BAND-only model. . . . .	66
4.1	The light curve of GRB 080817A with 64 ms resolution. The solid vertical lines define the pulse intervals as used in pulse simulations. First and second pulses are indicated as P1 and P2, respectively. . .	71
4.2	The evolution of BAND and COMPBB model parameters for GRB 080817A. The dashed histograms represents the photon fluxes for each time interval (right axis). . . . .	74
4.3	The energy flux evolutions of thermal and non-thermal components of COMPBB model for GRB 080817A. The top and middle panels show the energy flux evolutions of COMP and BB models, respectively. The energy flux ratio of thermal to total is seen in the bottom panel. The fluxes are calculated for the energy range 8 keV to 40 MeV. Errors in flux ratio of thermal to total are ignored. The dashed histograms represents the photon fluxes for each time interval (right axis). . . . .	75
4.4	The $\nu F_\nu$ spectrum of BAND and COMPBB models with photon counts and residuals, for the time interval 7.94 - 12.16 s of GRB 080817A, including time bins 5 and 6. . . . .	76
4.5	The model evolutions for GRB 080817A in $\nu F_\nu$ representation. The solid line represents the COMPBB model where the dashed lines show the COMP and BB components separately. The dotted line is denoting the BAND model. . . . .	77

4.6	The light curve of GRB 081215A with 64 ms resolution. The solid vertical lines define the pulse intervals as used in pulse simulations. First, second, and third pulses are indicated as P1, P2, and P3, respectively. . . . .	82
4.7	The evolution of BAND and COMPBB model parameters for GRB 081215A. The dashed histograms represents the photon fluxes for each time interval (right axis). . . . .	85
4.8	The energy flux evolutions of thermal and non-thermal components of COMPBB model for GRB 081215A. The top and middle panels show the energy flux evolutions of COMP and BB models, respectively. The energy flux ratio of thermal to total is seen in the bottom panel. The fluxes are calculated for the energy range 8 keV to 40 MeV. Errors in flux ratio of thermal to total are ignored. The dashed histograms represents the photon fluxes for each time interval (right axis). . . . .	86
4.9	The $\nu F_\nu$ spectrum of BAND and COMPBB models with photon counts and residuals, for the time interval 1.41 - 1.47 s of GRB 081215A, time bin 3. . . . .	87
4.10	The model evolutions for GRB 081215A in $\nu F_\nu$ representation. The solid line represents the COMPBB model where the dashed lines show the COMP and BB components separately. The dotted line is denoting the BAND model. . . . .	88
4.11	The light curve of GRB 090217 with 64 ms resolution. The solid vertical lines define the single pulse interval as used in pulse simulations and indicated as P1. . . . .	93
4.12	The evolution of BAND and COMPBB model parameters for GRB 090217. The dashed histograms represents the photon fluxes for each time interval (right axis). . . . .	95

4.13	The energy flux evolutions of thermal and non-thermal components of COMPBB model for GRB 090217. The top and middle panels show the energy flux evolutions of COMP and BB models, respectively. The energy flux ratio of thermal to total is seen in the bottom panel. The fluxes are calculated for the energy range 8 keV to 40 MeV. Errors in flux ratio of thermal to total are ignored. The dashed histograms represents the photon fluxes for each time interval (right axis). . . . .	96
4.14	The $\nu F_\nu$ spectrum of BAND and COMPBB models with photon counts and residuals, for the time interval 6.08 - 7.17 s of GRB 090217, time bin 4. . . . .	97
4.15	The model evolutions for GRB 090217 in $\nu F_\nu$ representation. The solid line represents the COMPBB model where the dashed lines show the COMP and BB components separately. The dotted line is denoting the BAND model. . . . .	98
4.16	The light curve of GRB 090323A with 64 ms resolution. The solid vertical lines define the pulse intervals as used in pulse simulations. .	102
4.17	The evolution of BAND and COMPBB model parameters for GRB 090323A. The dashed histograms represents the photon fluxes for each time interval (right axis). . . . .	105
4.18	The energy flux evolutions of thermal and non-thermal components of COMPBB model for GRB 090323A. The top and middle panels show the energy flux evolutions of COMP and BB models, respectively. The energy flux ratio of thermal to total is seen in the bottom panel. The fluxes are calculated for the energy range 8 keV to 40 MeV. Errors in flux ratio of thermal to total are ignored. The dashed histograms represents the photon fluxes for each time interval (right axis). . . . .	106
4.19	The $\nu F_\nu$ spectrum of BAND and COMPBB models with photon counts and residuals, for the time interval 15.10 - 18.37 s of GRB 090323A, time bin 3. . . . .	107

4.20	The model evolutions for GRB 090323A in $\nu F_\nu$ representation. The solid line represents the COMPBB model where the dashed lines show the COMP and BB components separately. The dotted line is denoting the BAND model. . . . .	108
4.21	The light curve of GRB 100414A with 64 ms resolution. The hatched region represents the time interval of the single pulse used for spectral simulations. . . . .	113
4.22	The evolution of BAND and COMPBB model parameters for GRB 100414A. The dashed histograms represents the photon fluxes for each time interval (right axis). . . . .	116
4.23	The energy flux evolutions of thermal and non-thermal components of COMPBB model for GRB 100414A. The top and middle panels show the energy flux evolutions of COMP and BB models, respectively. The energy flux ratio of thermal to total is seen in the bottom panel. The fluxes are calculated for the energy range 8 keV to 40 MeV. Errors in flux ratio of thermal to total are ignored. The dashed histograms represents the photon fluxes for each time interval (right axis). . . . .	117
4.24	The $\nu F_\nu$ spectrum of BAND and BANDBB models with photon counts and residuals, for the time interval 18.30 - 19.46 s of GRB 100414A, time bin 14. . . . .	118
4.25	The model evolutions for GRB 100414A in $\nu F_\nu$ representation. The solid line represents the COMPBB model where the dashed lines show the COMP and BB components separately. The dotted line is denoting the BAND model. . . . .	119
4.26	The light curve of GRB 100918A with 64 ms resolution. Vertical lines define the interval of the single pulse used for spectral simulations, and indicated as P1. . . . .	124
4.27	The evolution of BAND and COMPBB model parameters for GRB 100918A. The dashed histograms represents the photon fluxes for each time interval (right axis). . . . .	129

4.28	The energy flux evolutions of thermal and non-thermal components of COMPBB model for GRB 100918A. The top and middle panels show the energy flux evolutions of COMP and BB models, respectively. The flux ratio of thermal to total is seen in the bottom panel. The fluxes are calculated for the energy range 8 keV to 40 MeV. Errors in flux ratio of thermal to total are ignored. The dashed histograms represents the photon fluxes for each time interval (right axis). . . . .	130
4.29	The $\nu F_\nu$ spectrum of BAND and BANDBB models with photon counts and residuals, for the time interval 57.98 - 59.26 s of GRB 100918A, time bin 18. . . . .	131
4.30	The model evolutions for GRB 100918A in $\nu F_\nu$ representation. The solid line represents the COMPBB model where the dashed lines show the COMP and BB components separately. The dotted line is denoting the BAND model. . . . .	132
4.31	The light curve of GRB 101123A with 64 ms resolution. The vertical lines are showing the time intervals of pulses as used for spectral simulations. First, second and third pulses are indicated as P1, P2, and P3. . . . .	139
4.32	The evolution of BAND and COMPBB model parameters for GRB 101123A. The dashed histograms represents the photon fluxes for each time interval (right axis). . . . .	143
4.33	The evolution of BAND and COMPBB model parameters during the 1st pulse of GRB 101123A. The dashed histograms represents the photon fluxes for each time interval (right axis). . . . .	144
4.34	The energy flux evolutions of thermal and non-thermal components of COMPBB model for GRB 101123A. The top and middle panels show the energy flux evolutions of COMP and BB models, respectively. The flux ratio of thermal to total is seen in the bottom panel. The fluxes are calculated for the energy range 8 keV to 40 MeV. Errors in flux ratio of thermal to total are ignored. The dashed histograms represents the photon fluxes for each time interval (right axis). . . . .	145

4.35	The energy flux evolutions of thermal and non-thermal components of COMPBB model during the 1st pulse of GRB 101123A. The top and middle panels show the energy flux evolutions of COMP and BB models, respectively. The flux ratio of thermal to total is seen in the bottom panel. The fluxes are calculated for the energy range 8 keV to 40 MeV. The dashed histograms represents the photon fluxes for each time interval (right axis). . . . .	146
4.36	The $\nu F_\nu$ spectrum of BAND and BANDBB models with photon counts and residuals, for the time interval 46.53 - 46.78 s of GRB 101123A, time bin 10. . . . .	147
4.37	The model evolutions for GRB 100918A in $\nu F_\nu$ representation. The solid line represents the COMPBB model where the dashed lines show the COMP and BB components separately. The dotted line is denoting the BAND model. . . . .	148
4.38	The light curve of GRB 110721A with 64 ms resolution. The vertical lines are showing the time interval of the pulse used for spectral simulations. . . . .	155
4.39	The evolution of BAND and COMPBB model parameters for GRB 110721A. The reported values are shown with diamonds (Axelsson et al. 2012), and kT of the very last bin has only upper limit. The dashed histograms represents the photon fluxes for each time interval (right axis). . . . .	158
4.40	The energy flux evolutions of thermal and non-thermal components of COMPBB model for GRB 110721A. The top and middle panels show the energy flux evolutions of COMP and BB models, respectively. The flux ratio of thermal to total is seen in the bottom panel. The fluxes are calculated for the energy range 8 keV to 40 MeV. Errors in flux ratio of thermal to total are ignored. The dashed histograms represents the photon fluxes for each time interval (right axis). . . . .	159
5.1	Temperature evolutions in logarithmic scale for all the bursts in our thermal candidate sample. The initial times of the GRB 101123A and test burst GRB 110721A are also shown in the last two plots. . . . .	162

## LIST OF SYMBOLS AND ABBREVIATIONS

$A$	Amplitude
$\alpha$	Low-Energy Spectral Index
$B$	Magnetic Field
$\beta$	High-Energy Spectral Index
$c$	Speed of Light
$\delta t$	Variability Timescale
$E_{\text{peak}}$	Peak Energy of Power Spectrum
$E_{\text{pivot}}$	Pivot Energy
$f$	Photon Flux
$kT$	Temperature of the Blackbody
$L_{\text{iso}}$	Isotropic Luminosity
$\Gamma$	Bulk Lorentz Factor
$M_{\text{Sun}}$	Solar Mass
$\nu F_{\nu}$	Power Density Spectrum
$\gamma$	Electron Lorentz Factor
$R_0$	Radius at Base of the Relativistic Outflow
$R_{\text{ph}}$	Photospheric Radius
$R_{\text{is}}$	Internal Shock Radius
$T_{90}$	Time to Accumulate 90 % of Total Counts
$\sigma$	Magnetization of the Relativistic Outflow at the End of Acceleration Phase
$\theta$	Opening Angle of the Relativistic Jet
$z$	Cosmological redshift

BAND	GRB Model
BB	Blackbody Model
COMP	Comptonized Model
CSTAT	Castor C-Statistics
dof	Degrees of Freedom
DRM	Detector Response Matrix
FWHM	Full-Width at Half Maximum
GBM	Gamma-Ray Burst Monitor
GRB	Gamma-Ray Burst
IS	Internal Shocks
LAT	Large Area Telescope
MR	Magnetic Reconnection
PMT	Photo Multiplier Tube
SNR	Signal-to-Noise Ratio
TTE	Time-Tagged Event

# ABSTRACT

Spectral Analysis of Gamma Ray Bursts  
with  
Thermal Signature During their Prompt Phase

Aslıhan Muazzez ÜNSAL

Physics, Ph.D. Thesis, 2015

Supervisor: Ersin Gögüş

Keywords: *gamma – ray bursts, prompt emission phase, thermal*

Gamma Ray Bursts are the most powerful physical phenomena observed in the Universe. A thermal-like photospheric emission originating from the region where relativistic outflow becomes optically thin to Thomson scattering, is expected in the Fireball Model in the gamma ray regime. Although most of the observed GRB prompt spectra have non-thermal characteristics, thermal components have been uncovered in some GRBs detected with Fermi Instrument. The shape and evolution of the thermal component, however, differs from burst to burst. To better understand how and when such photospheric emission emerges, it is crucial to identify more GRBs with this thermal signature. To this end, we performed a systematic time-resolved spectral analysis of 611 Fermi-GBM bursts which are detected between July-2008 and December-2010, with a hybrid model (thermal and non-thermal components.) We identified 11 GRBs (including four with thermal nature previously reported) with a strong statistical preference towards the hybrid model over a single non-thermal model. Here, we present time-resolved spectral analysis of the remaining 7 GRBs, the evolution of the thermal & non-thermal components within these bursts. We also discuss physical properties of the emission site deduced from the thermal component parameters.

# ÖZET

Termal Bileşenli Gama-Işını Patlamalarının Öncü Işıma Evre Spektral Analizi

Aslıhan Muazzez ÜNSAL

Fizik, Doktora Tezi, 2015

Danışman: Prof. Ersin Göğüş

Anahtar kelimeler: *gamma-ışını patlaması, öncü ışına evresi, termal*

Gama-ışını patlamaları (GRB) evrende gözlemlenen oldukça yüksek enerjili astrofiziksel olaylardır. Ateş-topu modeline göre relativistik hızla yayılan plazmanın optik derinliğinin elektron Thomson çarpışmaları için şeffaf hale geldiği bölgede kara cisim (termal) ışınması beklenmektedir. Çoğu GRB öncü ışına spektrumu bahsedilen termal bileşeni içermemektedir. Ancak, bu termal bileşen Fermi teleskopu ile gözlemlenen bazı patlamaların spektrumunda görülmüştür. Gözlemlenen bu termal bileşenin hemen her patlama için farklı karakteristiğe sahip olduğu görülmüştür. Teorik olarak her patlamada gözlemlenmesi beklenen termal bileşenin hangi durumlarda ve hangi özellikte görüldüğünü daha iyi anlayabilmek için, spektrumunda termal bileşen görülen daha çok patlamayı belirlemek gerekmektedir. Bu bağlamda, Fermi teleskopu ile Temmuz-2008 ve Aralık-2010 tarihleri arasında gözlemlenmiş 611 patlamanın sistematik olarak kısa zaman dilimlerine ayrılmış şekilde spektral analizini yaptık. Bu analizin sonucunda yüksek istatistikle termal bileşen içeren 11 adet patlama belirledik. Bu 11 patlamanın 4 tanesinin termal ışına bileşen özellikleri literatürde yayınlanmıştır. Geriye kalan 7 patlamanın herbiri için, termal ve termal olmayan bileşenlerinin öncü ışına evresi boyunca nasıl evrildiğini belirlemek adına, yüksek zaman çözünürlüğünde spektral analizini yaptık. Ayrıca, belirlenen termal bileşen parametrelerini baz alarak relativistik plazmanın fiziksel yapısını inceledik.

## ACKNOWLEDGEMENTS

I would like to thank my advisors Ersin Göğüş and Yuki Kaneko Göğüş for their guidance and support from the beginning to the end. I would also like to thank Sylvain Guiriec for being available and answering my questions with patience all the time. I acknowledge support from TÜBİTAK through grant 109T755.

I would like to thank my mom, dad, Neslihan and Begünhan for their unconditional love and encouragement. I would like to thank my friends Dilek, Kinyas, Sinem, Süphan, Şirin, Vildan, and all my other friends in Sabancı University for the lovely times spent together which helped me much to overcome hard times. I would also like to thank my life-long friends Ayşenur, Zehra, Emine, Alex, Esin, Ülkücan, Esra, İlknur for their endless support. Lastly, I would like to thank Ersin Bayramkaya for listening to me with incredible patience and for his precious advices.

Aslıhan Muazzez ÜNSAL

August 2015

# Chapter 1

## INTRODUCTION

### 1.1 Gamma Ray Bursts

Gamma Ray Bursts (GRBs) are extremely interesting astrophysical phenomena observed in the universe. They are among the most luminous events with isotropic-equivalent energies  $\sim 10^{51} - 10^{54}$  erg (Frail et al. 2001; Greiner et al. 2009) in thermal and/or magnetic form initially, released typically in a few seconds. They have cosmological origin. For example, one burst, GRB 090423, has the highest cosmological redshift measured so far,  $\sim 8.2$  (Salvaterra et al. 2009; Tanvir et al. 2009), corresponding to a distance of  $\sim 9 \times 10^{10}$  ly. Direct and indirect observational evidences indicate that an ultra relativistic jet is involved in GRB emission process, and the bulk Lorentz factor of the jet can be as high as a thousand. The strongest candidate progenitors of GRBs are binary compact object mergers and/or core collapse of super-massive stars which lead to formation of black holes. It is proposed that GRBs could also be the source of ultra high energetic cosmic rays (UHECR). It has been more than 40 years since the discovery of GRBs. So far, thousands of bursts have been observed with broadband spectrum and fine time resolution by many satellites, where several of them have been devoted to GRB science. We now have a wealth of information on GRBs such as: their spectral characteristics, time profiles, host galaxies, locations on sky, and cosmological redshifts. However, the exact nature of GRB prompt emission is still an open question. Understanding the complete picture of GRBs is very important for many fields of physics and astronomy.

GRBs were theoretically predicted before their observation (Colgate, 1968), as

such bursts could be produced within relativistic shocks formed by supernova explosions. Then, the first GRB was detected by Vela 4a satellite on 2 July 1967 and this observation was reported sometime later with 16 more GRB candidate events (Klebesadel et al., 1973). During those times some GRBs were also observed by solar gamma-ray instruments on IMP-6 and IMP-7 (Cline et al., 1973), where some of them were correlated to Vela detected bursts. Since their discovery GRBs have been observed by many other gamma-ray instruments followed up by multi-wavelength observation, which showed us that a GRB is composed of two emission phases; prompt and afterglow. Prompt emission phase, observed in gamma-ray, lasts  $\sim$  milliseconds to thousands of seconds where afterglow, observed in longer wavelengths, lasts  $\sim$  hours to years, respectively. So, the spectrum of a GRB may span almost all the electromagnetic spectrum. As will be discussed later, GRBs are classified according to their prompt emission phase duration, as short and long bursts with durations  $< 2$  s and  $> 2$  s, respectively.

Among these many instruments that detected GRBs, there have been several ones that made/have been making significant contribution to our general understanding of GRBs; most notably BATSE, BeppoSAX, Swift, and Fermi. The Burst and Transient Source Experiment (BATSE) was launched in April 1991, aboard the Compton Gamma Ray Observatory (CGRO) and operated until June 2000. BATSE observed on average 300 GRBs per year, with broad energy range; 20 keV - 10 MeV, and high time resolution; 2 milliseconds. In these respects, BATSE provided a very comprehensive data set to characterize GRB spectra, time profiles, and sky distribution with good statistics. Another important result that BATSE provided us is that the isotropic sky distribution of GRBs (see Figure 1.1) implied that the sources were located at cosmological distances (Meegan et al., 1992), which was verified by redshift measurements later on.

BeppoSAX was an X-ray satellite, launched in 1996 (Piro et al., 1995). In its nearly 6 years of operation, X-ray afterglow emission were detected for 33 bursts (de Pasquale et al., 2006). The first one was the afterglow of GRB 970228 with an X-ray flux of  $(2.8 \pm 0.4) \times 10^{-12}$  erg sec $^{-1}$  cm $^2$  in the 2-10 keV energy range (Costa et al., 1997). In 1997, the very quick X-ray afterglow detection of GRB 970508 by BeppoSAX/NFI allowed a detailed spectral analysis of optical afterglow observed

with Keck telescope which revealed a redshift of  $z = 0.835$ , being the first redshift measurement for a GRB (Metzger et al., 1997).

Swift was launched in November, 2004. It has three instruments covering different energy ranges (gamma-ray, X-ray, UV/optical) on board, allowing detection of a burst, observing its afterglow, and locating it with arcseconds accuracy, only in a few minutes (Gehrels et al., 2004). Swift has been detecting about 100 bursts per year. Almost all long bursts have X-ray afterglow detection, where short bursts have either faint, or no X-ray afterglow detection. For more than half of the bursts observed by Swift optical afterglow has been detected. The very first afterglow emission from a short burst GRB 050509B was also observed by Swift (Gehrels et al., 2005). Quick follow up observation capabilities of Swift provided a relatively large sample of bursts with afterglow detection and subsequent redshift measurement. The average redshift value is  $\sim 2.4$  and  $\sim 0.5$  for long and short bursts, respectively.

Fermi Gamma-ray Space Telescope was launched in June, 2008 and started operation about a month later. There are two instruments on board, Gamma-ray Burst Monitor (GBM) and Large Area Telescope (LAT), which are sensitive between  $\sim 8$  keV to 40 MeV, and  $\sim 30$  MeV to 300 GeV, respectively. GBM is responsible for detecting and locating bursts, then LAT checks for very high energy emission from the bursts (see chapter 2 for details). In the first 4 years of operation GBM triggered 953 GRBs where only for 43 of them there were associated LAT detection (von Kienlin et al., 2014). Fermi is observing  $\sim 240$  bursts per year with the very broad energy range and high time resolution. As will be discussed hereafter, Fermi has been making significant contribution to our understanding of GRB prompt emission mechanism.

# 2704 BATSE Gamma-Ray Bursts

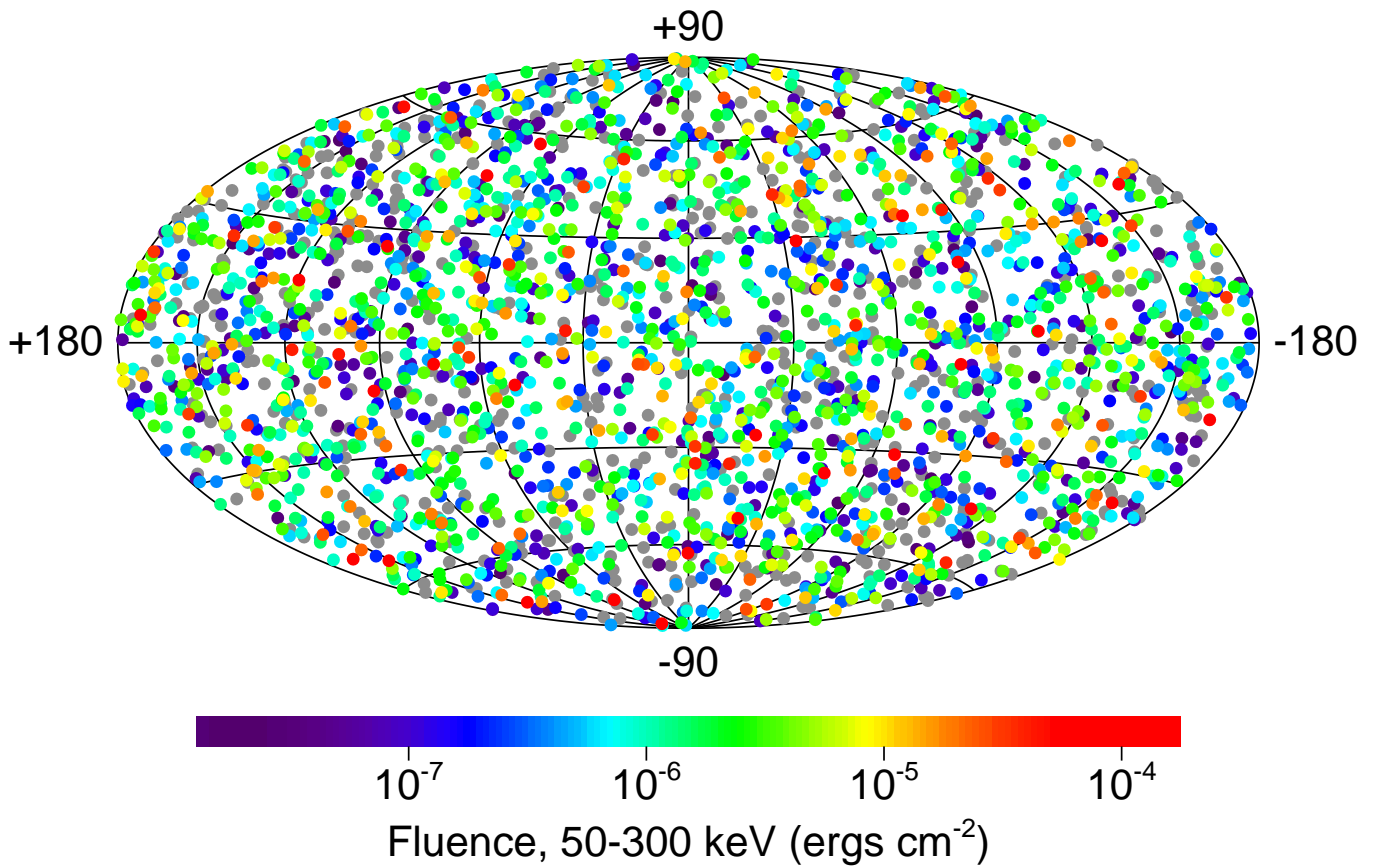


Figure 1.1: The sky distribution of 2704 GRBs detected by BATSE, in Galactic coordinates. The intensity of individual bursts indicated by colors as shown in the bottom scale. Credit:NASA.

## 1.2 Temporal and Spectral Properties of GRBs

In this section I will present the general characteristics of GRB prompt and afterglow emission phases where the emphasis will be to the former one. The statements apply to both short and long bursts if not specified. I discuss the temporal and spectral features of both of the emission phases and their possible implications related to GRB physics.

### 1.2.1 Prompt Emission Phase – Time Profiles

The common definition for the duration of a burst  $T_{90}$  is the time in which 90% of the total counts of the burst is received (Kouveliotou et al., 1993), and this duration can be very different from burst to burst. Figure 1.2 shows the  $T_{90}$  distribution of all GRBs detected by Fermi-GBM up to date. The only classification of GRBs is based on their duration, short and long bursts, with durations below or above 2 seconds, respectively. The detection rate of short bursts is  $\sim 17\%$  for Fermi-GBM bursts (von Kienlin et al., 2014), significantly lower than that of long ones. It was also shown that short GRBs are spectrally harder than the long ones (Kouveliotou et al., 1993). This observation is also verified recently for Fermi-GBM bursts (von Kienlin et al., 2014), as seen in Figure 1.3.

The temporal structures of individual GRBs are almost unique. As seen in Figure 1.4, light curves can be composed of single or multiple, well separated or overlapped pulses. These pulses can be smooth or variable. Variability (defined as the width of the peaks) timescale of  $\sim$  milliseconds has been reported (McBreen et al., 2001). Several temporal characteristics of individual pulses (for long GRBs) are identified as follows; they are generally FRED (fast rise, exponential decay) shape, low energy photons are delayed with respect to high energy ones (Norris et al., 1996), and low energy pulse widths are wider than high energy ones (Fenimore et al., 1995).

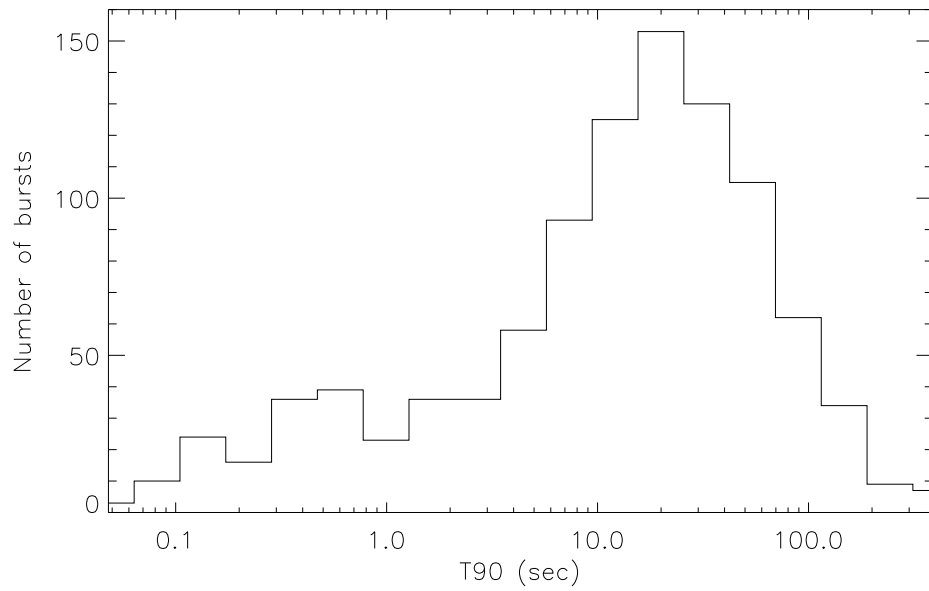


Figure 1.2: Duration distribution for 1000 bursts detected by Fermi-GBM between 14-07-2008 and 26-09-2012, in the energy range 50 – 300 keV.

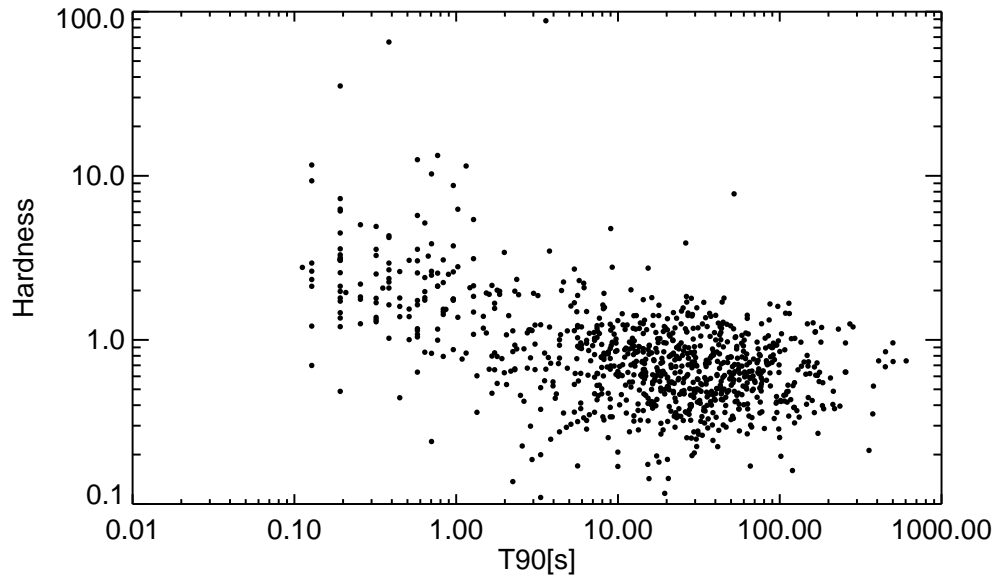


Figure 1.3: Hardness vs. duration plot for Fermi-GBM bursts. Hardness is defined as the ratio of the flux density in 50 – 300 keV to that in 10 – 50 keV. Taken from von Kienlin et al. (2014).

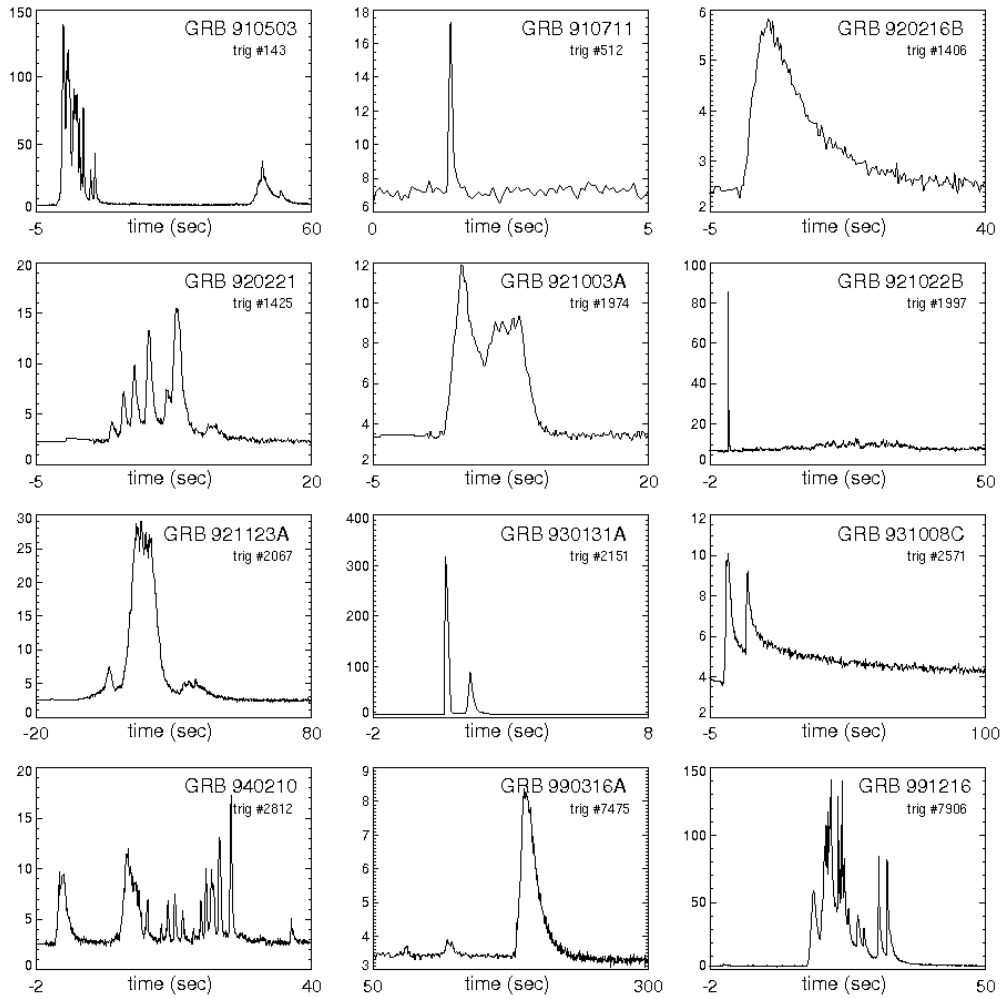


Figure 1.4: Light curves of 12 GRBs observed with BATSE. They are almost unique. Duration varies from milliseconds to minutes. Pulses can be smooth or spiky, well separated or overlapped. Credit: J.T. Bonnell (NASA/GSFC).

### 1.2.2 Prompt Emission Phase Spectral Properties

The GRB gamma-ray prompt emission spectrum is non-thermal and peaks around a few hundred keV in  $\nu F_\nu$  spectrum ( $\nu F_\nu$  is the power density spectrum which shows the total energy flux per energy band). For most of the burst spectra there is a high energy tail, however in some cases this high energy tail is missing, i.e., no emission above  $\sim 300$  keV and these bursts typically have lower luminosities than regular GRBs (Pendleton et al., 1997).

Unlike the diversity in temporal profiles of GRB prompt emission, their non-thermal spectral characteristics have been well described by a relatively simple and empirical, the so called BAND model (Band et al., 1993). This model is composed of two power laws which are smoothly joined at a break energy. The low and high energy power law indices ( $\alpha$  and  $\beta$ , respectively) and the peak energy of the  $\nu F_\nu$  spectrum ( $E_{\text{peak}}$ ) characterize the BAND model (see § 3.1.2 for BAND photon model description and spectral shape in  $\nu F_\nu$  representation). BAND model mostly fits well not only the time integrated spectra (fluence) but also the time resolved spectra (Kaneko et al., 2006).

In a recently published GRB catalog paper; the spectral analysis of 943 GRBs detected by Fermi-GBM in the first four years are presented (Gruber et al., 2014). There, four different photon models are applied: Power-law (PL), Comptonized (COMP), BAND, Smoothly Broken Power-law (SBPL). The distributions of best fit model (the best representative of the spectrum out of the four photon models applied) parameters and good fit model (well-constrained models) parameters are presented. The main fluence spectral properties are as follows;

- As shown in Figure 1.5, the low energy power law index ( $\alpha$ ) distribution has a peak at  $\sim -1.1$ , where 17% of them are violating the  $-2/3$  synchrotron limit (this limit will be discussed in § 1.5).
- The high energy power law index ( $\beta$ ) distribution peaks  $\sim -2.1$ , and has a long tail towards more negative values.
- $E_{\text{peak}}$  values are peaked  $\sim 200$  keV. However, observation of  $E_{\text{peak}}$  values as high as  $\sim 10$  MeV (Axelsson et al., 2012) and as low as  $\sim 10$  keV (Campana et al., 2006) are reported.

These parameter distributions are consistent with previous BATSE GRB catalog results (Kaneko et al., 2006).

Even though the reason is not very clear, it has been observed that there are two common  $E_{\text{peak}}$  evolution patterns in GRB prompt spectra. First trend is the *hard to soft evolution* within a pulse;  $E_{\text{peak}}$  is very high initially then decays independent from the photon intensity. The second one is the *intensity tracking* where  $E_{\text{peak}}$  follows the intensity pattern of the burst (Band 1997; Lu et al. 2012).

As mentioned, the BAND photon function is an empirical model, i.e., it has no physical basis. However the model parameters can be related to physical emission processes. Indeed, most of the time the BAND shape is consistent with the expected spectrum of synchrotron emission from power law distribution of relativistic electrons (Tavani, 1996). This emission mechanism will be discussed in detail in § 1.4.2.1.

Besides the success of this model in fitting most GRB spectra, deviations from BAND model and/or alternative physical models for some burst spectra have been reported (Ryde 2004; Tierney et al. 2013). For example; Tierney et al. (2013) analyzed 45 bright GBM GRBs' both time-integrated and time-resolved spectra. In a systematic way they identified significant deviation from BAND model at low energies in 6 of the bursts, for either the whole duration or some portion of the burst. It is also shown that in these spectra an additional blackbody or a power-law component improved the BAND only fits significantly. In another work, Burgess et al. (2014), a sub-dominant black-body component along with a dominant non-thermal one (BAND) is identified in spectra of 5 bright, single-peaked GBM bursts.

Most of the burst energy is coming as gamma rays and accompanying X-rays, but also photons at other wavelengths, both low and high, can be detected during the prompt phase. In very few cases, prompt optical emission have been observed. First optical emission was observed by ROTSE, simultaneously with BATSE prompt emission from GRB 990123 (Akerlof et al., 1999). Very high energy photons can also be detected either simultaneously with or some time later than prompt emission. For example, EGRET detected photons with energies between hundreds of MeV and tens of GeV coming from seven bursts (Dingus & Catelli, 1998). More recently, LAT aboard Fermi satellite (50 MeV - 100 GeV) has detected 43 bursts with high energy

emission during its first 4 years of operation (von Kienlin et al., 2014). The physical origin of these very high-energy photons is not clear yet. The delays observed in arrival time of these high energy photons may indicate an afterglow origin rather than belonging to prompt phase (Ghisellini et al., 2010). However, another study showed that the high energy emission coming from GRB 090902B during prompt phase can be modelled by a simple power law function which also extends to low energies may indicate a separate spectral component during prompt phase (Abdo et al., 2009).

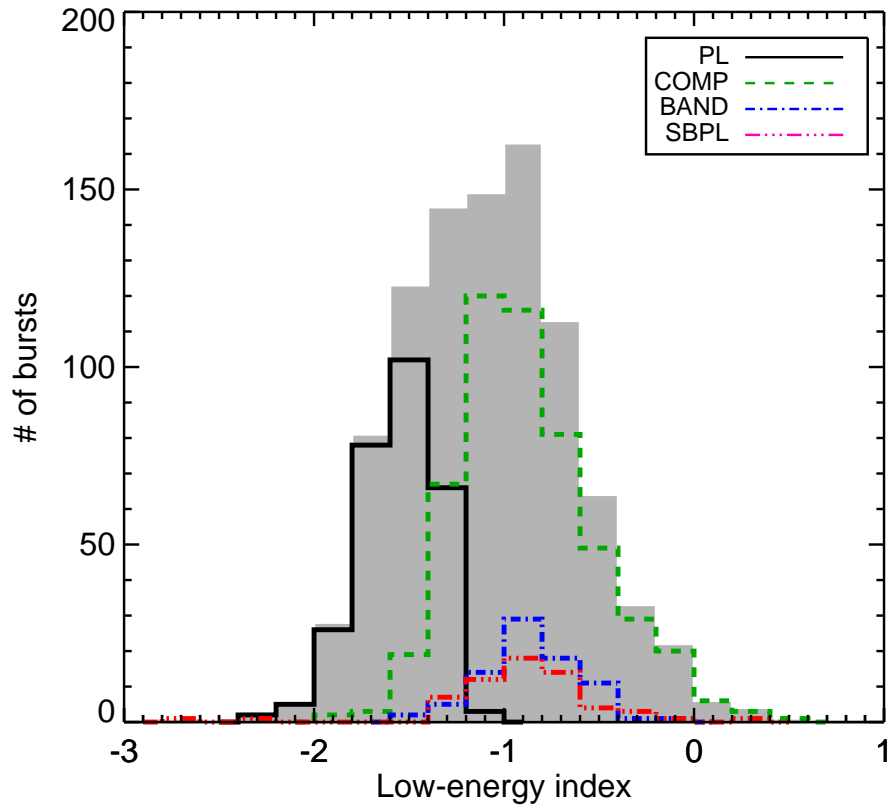


Figure 1.5: The distribution of low-energy spectral index  $\alpha$  for fluence spectra of 943 Fermi-GBM bursts. The gray-filled histogram shows the distribution of the low-energy index of the best model out of four photon models applied, for all spectra. The solid histogram shows the power-law index distribution of the spectra for which the PL model is the best model. Similarly, dashed, dashed-dotted, and dashed-triple dotted histograms represents the low-energy index distributions of COMP, BAND, and SBPL models. Taken from Gruber et al. (2014).

### 1.2.3 Afterglow Phase

The afterglow emission may span the electromagnetic spectrum from X-rays to radio waves and lasts from  $\sim$  hours to years after trigger, with most of the energy is in X-rays. For long GRBs a smooth transition in X-ray spectrum is seen from prompt to afterglow phases which can be composed of segments with different features (Zhang et al. 2006; O'Brien et al. 2006b). Figure 1.6 shows the afterglow emission light curves of three GRBs with different features.

Figure 1.7 shows the schematic of the flux vs time curve in logarithmic scale for various X-ray afterglow phases that are typically observed in GRBs. The phase I is the steep-decay phase  $F_X \propto t^{-\alpha}$  with a temporal index  $3 \lesssim \alpha \lesssim 5$ , and the energy spectrum  $F_\nu \propto \nu^{-\beta}$  has a spectral index  $1 \lesssim \beta \lesssim 2$ . This phase is seen in most of the GRB afterglows and may extend up to  $\sim 200 - 1000$  s. It is usually interpreted as being the high-latitude emission after the central engine stops operating (Kumar & Panaitescu 2000; Zhang et al. 2006). This steep-decay can be followed by a shallower decay, phase II, usually starting within the first hour and may last up to one day and it carries significant amount of energy, with a temporal index  $0.2 \lesssim \alpha \lesssim 0.8$  and spectral index  $0.7 \lesssim \beta \lesssim 1.2$ . The emission has been considered as the forward shock which is fed by late central engine activity (Rees & Mészáros 1998; Zhang et al. 2006). This phase can be also interpreted as the emission coming from the mildly relativistic cone which surrounds a relativistic and narrow jet (responsible for prompt emission) and radiates as it decelerates (Peng et al., 2005). Phase III is the typical afterglow phase observed in most of the GRBs with  $1.1 \lesssim \alpha \lesssim 1.7$  and  $0.7 \lesssim \beta \lesssim 1.2$  being similar to phase II. This phase may extend up to  $\sim 10^5$  s (see section 1.4 for the emission mechanism). The transition from phase III to IV is the expected achromatic jet break (change in temporal decay slope to  $2 \lesssim \alpha \lesssim 3$ ), however it has been observed clearly in a very limited number of GRB afterglow so far (GRB 060526 Dai et al. 2007; GRB 060614 Mangano et al. 2007). This break is a natural outcome from expansion of a relativistic and collimated flow: as the Lorentz factor  $\Gamma$  of the flow decreases and the light-cone angle becomes  $\Gamma^{-1} \gtrsim \theta$  where  $\theta$  is the jet opening angle, the light curve is expected to be steepen in all wavelengths (Sari et al., 1999). Lastly, phase V corresponds to X-ray flares with fast rise and decay structure, which have energies sometimes comparable to burst

itself (Burrows et al. 2005; Falcone et al. 2006). The rise and decay time indices could be very high  $3 \lesssim \alpha \lesssim 6$  as well as the spectral index  $\beta \lesssim 1.5$ . These flares are thought to be due to central engine activity extended to the afterglow phase (Burrows et al., 2007). These feature are mostly for long bursts however some short bursts show similar characteristics.

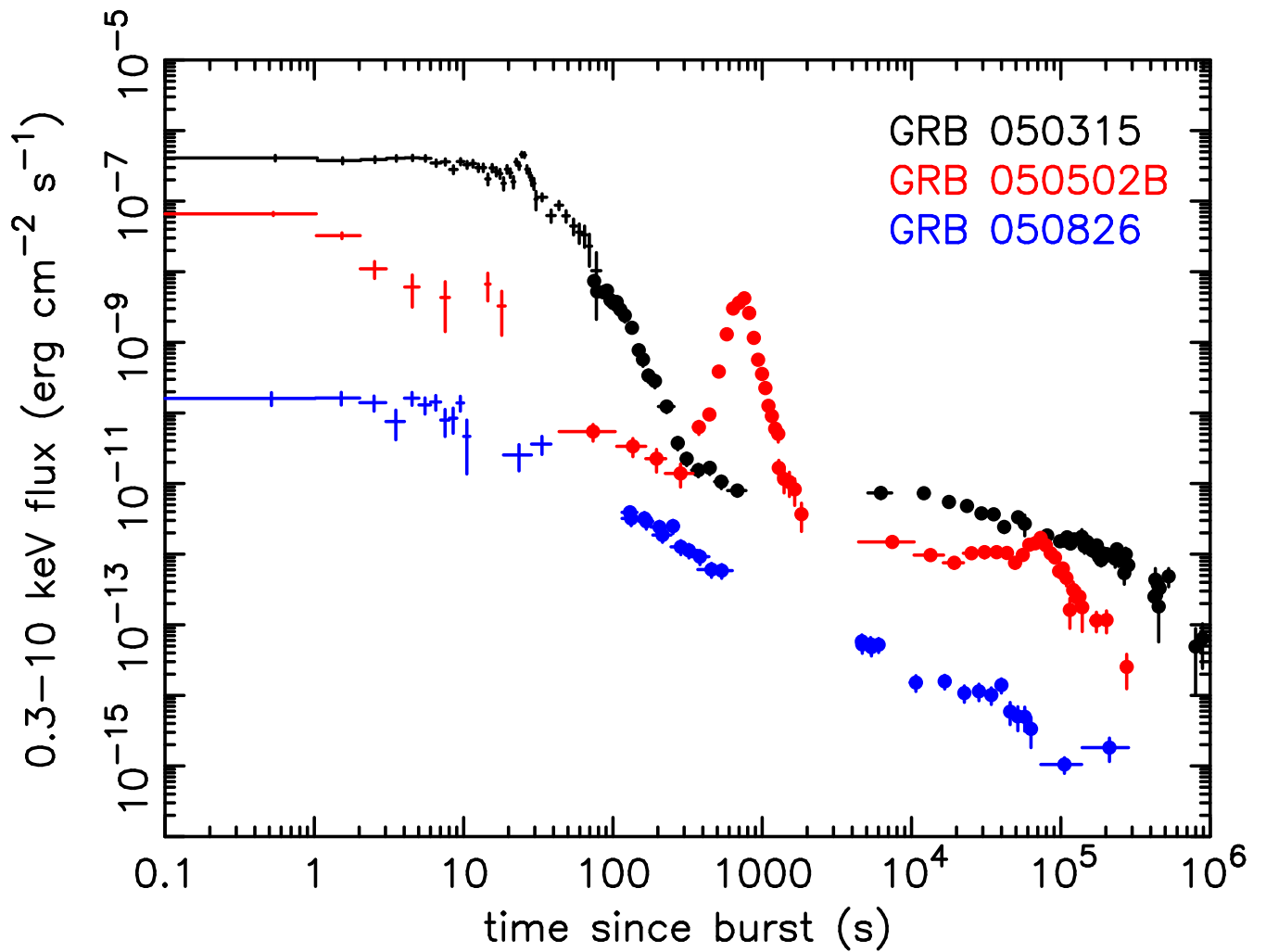


Figure 1.6: Examples afterglow emission. GRB 050315 has a steep-to-shallow transition, GRB 050502B has a large X-ray flare, and GRB050826 has a gradual decline (points are divided by 100 for clarity). Figure is taken from O’Brien et al. (2006a).

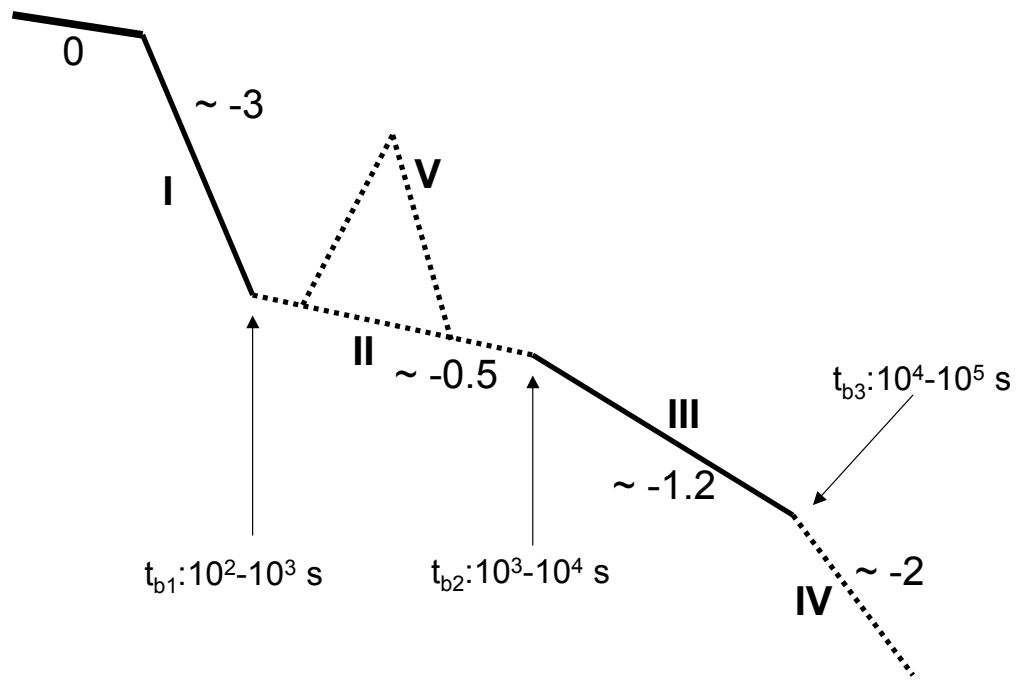


Figure 1.7: The phases of X-ray Afterglow observed in GRBs. The phase 0 represents the prompt emission. I is the steep-decay, II is the shallower decay, III is the typical afterglow, IV is the jet break phases. Phase V is denoting the X-ray flare. Taken from Zhang et al. (2006).

### 1.3 Models of Progenitors

It is believed that short GRBs result from the *compact binary object mergers* (Eichler et al., 1989), whereas long ones result from *core collapse of massive stars*. The proposition of these models are based on the observed properties of these bursts such as: energetics, the host region properties, Supernova (SN) association.

Basically, the long bursts are expected to be in the region where the massive stars are formed, i.e. close to the center of the host galaxies. Indeed, Bloom et al. (2002) studied locations of several long GRBs with optical counterparts within their host galaxies and identified that most of the bursts were positioned in close proximity of the galaxy center. Galama & Wijers (2001) also reported that the inferred column densities from afterglows of 8 bursts were consistent with typical molecular clouds within star-forming regions. Another study, Savaglio et al. (2009) showed that the host galaxies of 46 GRBs are generally small star-forming galaxies.

The very first observational evidence of GRB - SN connection was provided by the localization of a burst GRB 980425 by BeppoSAX on 25 April 1998 (Pian et al., 2000), which was found to be coincident with SN 1998bw (Kulkarni et al., 1998). Several other long GRBs with SN association reported after then (Hjorth et al. 2003; Campana et al. 2006), providing further evidence for the relation of long GRBs with death of massive-stars.

The progenitor should provide huge amount of energy for the GRB, and even more if there is a simultaneous supernova, i.e. non-relativistic ejecta. A recent analysis of Swift energetic bursts indicates an upper bound of  $\sim 10^{52}$  erg for the relativistic jet (Chandra et al. 2008; Cenko et al. 2010), when combined with the possible supernova, the required energy is  $\sim 10^{53}$  erg. Another important model based prediction is that the progenitor star should be a massive star ( $> 20M_{\text{Sun}}$ ; Larsson et al. 2007) without a hydrogen envelope (Woosley, 1993). This was required since the relativistic outflow would not be able to escape the star with a hydrogen envelope within the timescale of typical GRB duration. It is also possible to have a GRB originating from a star with mass  $\lesssim 15M_{\text{Sun}}$  if it has a high rotation rate and low metallicity (Yoon et al., 2006).

It is also suggested that massive stars collapsing into magnetars can be also progenitors of long GRBs. The maximum rotational energy that a magnetar provides

is a few times  $10^{52}$  erg, which is very close to the energy estimates of the most energetic bursts (Ott et al., 2006).

For short GRBs, the picture is more blurry than for the long ones since there are not many afterglow observations. Compact binary mergers are expected to be located in relatively old galaxies and far from the centers of the hosts where the star formation rate is low, and some short GRBs are observed to be from old galaxies. However, some short bursts are observed to be located close to the center of star-forming galaxies, one example is the GRB 050709 (Covino et al., 2006). This lead to consideration of alternative progenitors similar with long GRBs (Metzger et al. 2008; Virgili et al. 2011).

## 1.4 Physics of GRBs

The physical nature of GRB prompt emission is still not very clear. However, there are several observational clues that help us to constrain possible physical processes. In this section, we will examine the Fireball model with internal & external shocks, which is mostly successful in explaining the observational features of GRB prompt and afterglow emission phases.

### 1.4.1 Compactness problem

Compactness problem was raised short time after the discovery of GRBs (Ruderman, 1975). One information in hand is that the observed spectrum is non-thermal and the sub-second variability seen in light curves implies a source size  $R \lesssim c\delta t \approx 10^7$  cm. When we combine these arguments with the observed flux and typical values for other relevant parameters lead to a huge optical depth for electron-positron pair creation,  $\tau \sim 10^{15}$  (Piran 1995). However, having a relativistic motion towards us with a Lorentz factor  $\Gamma$  can decrease the optical depth in the source frame and allows an optically thin emission site consistent with observed spectrum (Fenimore et al., 1993).

### 1.4.2 Internal & External Shock Scenario

The generally accepted theoretical model for GRB emission is the *Fireball* with internal and external shocks model (a schematic of the model can be seen in Figure 1.8). In this model, the energy coming from the inner engine (e.g. a stellar mass black hole with a thick disc around it) is initially confined in a small region, consisting of photons, electron-positron pairs and some baryons. Then this Fireball expands under its own thermal pressure, converting most of its thermal energy into kinetic energy, until the flow reaches its maximum Lorentz factor, i.e., producing the relativistic jet (Paczynski 1986; Goodman 1986). The remaining thermal energy is released when the flow becomes optically thin to Thomson scattering, i.e. at photospheric radius (Mészáros & Rees, 2000). The kinetic energy of the flow is then converted into radiation in internal and external shocks via synchrotron radiation of electrons (Mészáros & Rees, 1993), giving rise to prompt and afterglow emission,

respectively (Piran & Sari, 1998). Also, when the jet starts interacting with environment a reverse shock can be formed, in which a shock front propagates back through the ejecta.

#### 1.4.2.1 Internal Shocks

The dynamical time scale of the relativistic disc around the black hole (the inner engine) can be as short as  $\sim$  ms. For a relativistic jet launched from this system is suggested to have a highly non-uniform Lorentz factor distribution (Rees & Mészáros, 1994). This inhomogeneity produces shocks within the flow, i.e. internal shocks, when faster shells catch up and collide with the slower ones. Then, the dissipated energy at these shocks accelerates electrons which radiate gamma rays via synchrotron radiation or inverse Compton.

Indeed, Daigne & Mochkovitch (1998) studied the evolution of such a variable wind assuming the emission mechanism as the electron synchrotron radiation. The main spectral and temporal properties of typical GRBs were reproduced. Such as; the 'FRED' shape of the pulses, short variability scale of time-profiles, the duration-hardness relation, and the synthetic spectra with conventional BAND shape with typical observed parameters. One major problem with the IS model is the low efficiency of energy extraction. The energy of prompt emission photons are larger than or comparable to afterglow (Fan & Piran 2006; Granot et al. 2006), but internal shocks energy dissipation efficiency is only a  $\sim$  few percent (Daigne & Mochkovitch, 1998). However, high efficiency can be achieved if the relative velocity of shells are large (Beloborodov, 2000).

**Acceleration mechanism:** The electrons are assumed to be accelerated via Fermi mechanism at the shocks. Electrons cross the shock front back and forth multiple times. In each crossing the energy of the particle increases by  $\Delta E \sim E$ .

**Emission Mechanism:** The strongest candidate is the synchrotron emission, in which the shock accelerated electrons interacts with the magnetic field and radiate gamma rays (Rybicki & Lightman, 1979). Within the flow, strong magnetic fields can be produced via Weibel instabilities (Weibel, 1959). For a single electron in a random magnetic field and with Lorentz factor  $\gamma_e$ , the emitted power in the local

frame is:

$$P_{\text{sync}} = \frac{4}{3} \sigma_{\text{T}} c U_{\text{B}} \gamma_e^2 \quad (1.1)$$

where  $\sigma_{\text{T}}$  is the Thomson cross section,  $c$  is the speed of light, and  $U_{\text{B}}$  is the magnetic energy density. The corresponding observed cooling timescale is given by:

$$t_{\text{sync}}(\nu) = \frac{3}{\sigma_{\text{T}}} \sqrt{\frac{2\pi c m_e q_e}{B^3 \Gamma}} \nu^{-1/2} \quad (1.2)$$

so higher energy electrons are expected to cool down rapidly until they reach the Lorentz factor of an electron that cools on a hydrodynamic timescale, i.e., due to adiabatic expansion,  $\gamma_{e,c}$ . The observed spectrum will be the integral of photons coming from all electrons with individual Lorentz factors, distributed in a power law, with an index  $p$ :  $N(\gamma_e) \sim \gamma_e^{-p}$  for  $\gamma_e > \gamma_{e,\text{min}}$  (Sari, Piran, & Narayan, 1998). This minimum Lorentz factor defines the “typical” synchrotron frequency,  $\nu_{\text{m}} \equiv \nu_{\text{sync}}(\gamma_{e,\text{min}})$ , which together with the  $\gamma_{e,c}$  determines whether the electrons are in the fast or slow cooling regime. For fast cooling;  $\gamma_{e,c} < \gamma_{e,\text{min}}$  or  $\nu_c < \nu_{\text{m}}$  where  $\nu_c = \nu_{\text{sync}}(\gamma_{e,c})$ . For slow cooling;  $\gamma_{e,c} > \gamma_{e,\text{min}}$  or  $\nu_c > \nu_{\text{m}}$ . In the fast cooling case all the electrons, whereas in the slow cooling case only the high energy electrons cool down to  $\gamma_{e,c}$ . In the internal-shock synchrotron model a random magnetic field and an isotropic pitch angle distribution of electrons are assumed. Also, the effects of inverse Compton scattering or absorption of the synchrotron photons are ignored. Within this frame the expected spectrum  $f$  for fast and slow cooling regimes shown in Figure 1.9.

From efficiency requirements for the prompt phase, the electrons are expected to cool fast (Cohen et al., 1997). As seen in the bottom panel of Figure 1.9 the expected spectrum of internal-shock synchrotron radiation is composed of four segments. As stated in Sari et al. (1998) the steep cutoff seen at low energies is due to self-absorption. It is shown on the figure for completeness but ignored in the model since its effect in the interested energy range is not significant. Then, the spectrum is given by;

$$f_{\nu,\text{fast}} \propto \begin{cases} \nu^{-2/3}, & \nu < \nu_c \\ \nu^{-3/2}, & \nu_c < \nu < \nu_{\text{m}} \\ \nu^{-p/2-1}, & \nu_{\text{m}} < \nu \end{cases} \quad (1.3)$$

When we fit the GRB prompt spectrum with conventional BAND photon model (which is composed of only two power laws, see section 3.1.2.1), the low and high energy power law indices are expected to be  $-3/2 \lesssim \alpha \lesssim -2/3$  and  $-p/2 - 1 \lesssim \beta \lesssim -2/3$  (Tavani 1996; Preece et al. 1998b; Preece et al. 1998a; Preece et al. 2002), and the peak of the  $\nu F_\nu$  spectrum is  $E_{\text{peak}} \sim \nu_m$ .

#### 1.4.2.2 External Shocks

The external shocks are formed when the relativistic ejecta interacts with the external medium well after the prompt emission is produced via internal shocks. As mentioned, at this stage a reverse shock can also be formed. In both reverse and forward shocks the kinetic energy of the flow is dissipated, some portion of the available energy is converted into magnetic energy (via Weibel instability) and also particles are accelerated via Fermi process as they move back and forth across the shock front (Spitkovsky, 2008) being similar to prompt emission phase. The observed GRB afterglow spectra is consistent with slow cooling electron synchrotron radiation (Mészáros & Rees, 1993). The reverse shock has relatively less energetic electrons than the forward shock, then the radiation is expected to be in optical/UV (Mészáros & Rees, 1993), and the radiation can be overlapped with prompt emission phase.

This internal & External Shock Synchrotron model is a convincing model since it can produce the variable light curves, wide range of durations and the typical spectral properties observed in prompt phase, as well as the main features of observed afterglow spectrum. However, some observed prompt emission spectra are posing several serious problems to this model, as will be discussed in the following section.

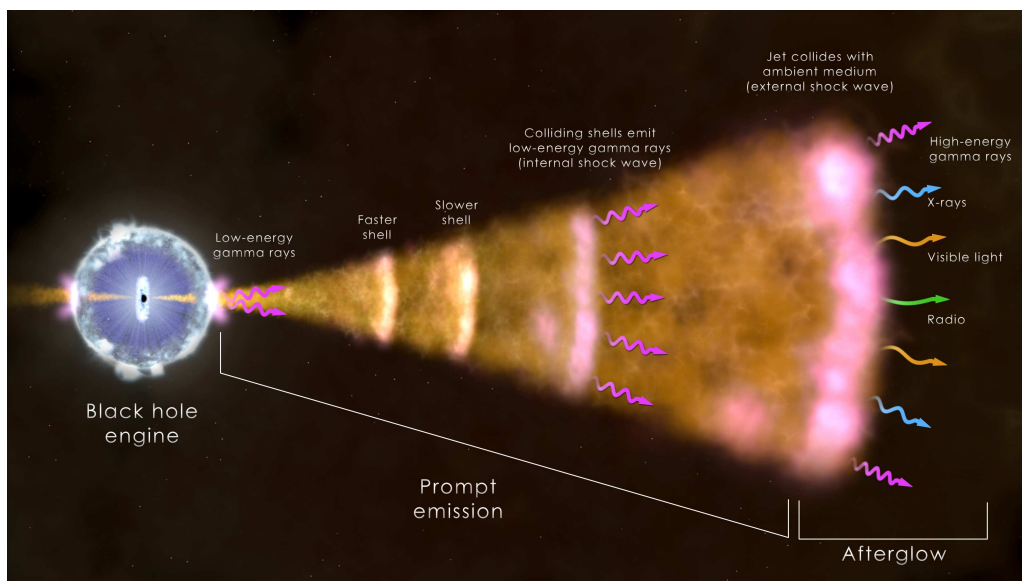


Figure 1.8: The inner engine releases huge amount of energy  $\sim 10^{53}$  erg. Most of this energy is used to produce the relativistic jet and the remaining energy decouples from the flow at photospheric radius. The kinetic energy of the jet is dissipated within internal and external shocks which accelerates the electrons to relativistic speeds and gives rise to observed prompt and afterglow emission via synchrotron radiation . Credit: NASA's Goddard Space Flight Center.

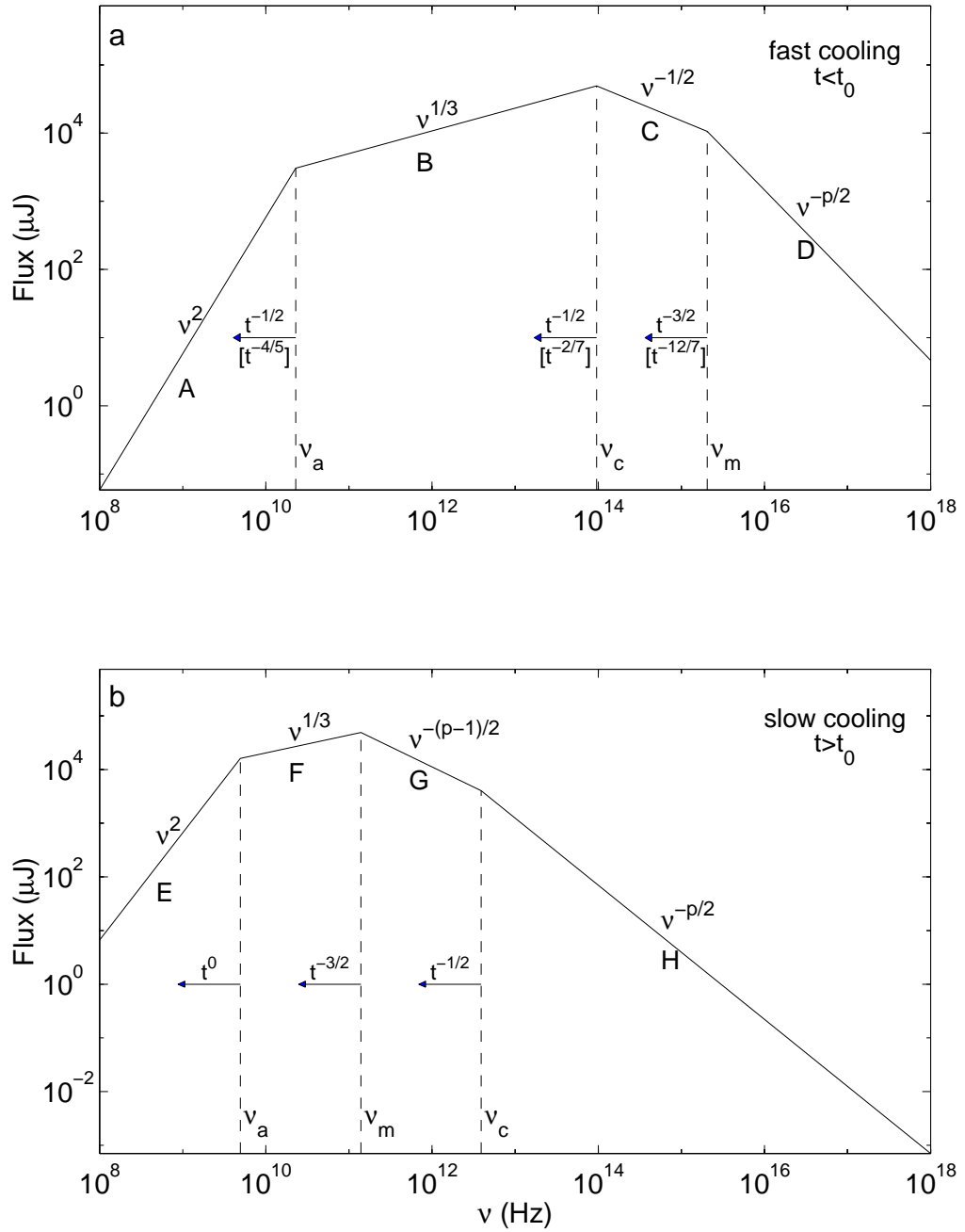


Figure 1.9: The expected energy flux spectrum of power law distributed electrons synchrotron radiation in fast (a) and slow cooling (b) regimes. Taken from Sari et al. (1998).

## 1.5 Observational Constraints on Synchrotron Emission

Independent from the presumed electron energy distribution there are *lines of death* for synchrotron radiation of fast and slow cooling electrons, i.e., upper limits for the low energy spectral index  $\alpha_{\text{fast}} \leq -3/2$  and  $\alpha_{\text{slow}} \leq -2/3$  (Rybicki & Lightman 1979; Katz 1994). There have been several studies which showed that there are significant number of GRB spectra which have inconsistent (harder/larger) low energy indices with (than) these synchrotron limits, either fluence or time-resolved (Preece et al. 1998a; Kaneko et al. 2006). This is the main problem of the synchrotron radiation model and the main point of interest in our work.

To probe this problem, a recent study has taken into account the decrease in the magnetic field with radius, due to flux conservation (Uhm & Zhang, 2014). In this case, the low energy index for the synchrotron emission in the fast-cooling regime has a distribution between  $\sim -1.5$  to  $< -0.8$ , clustering around  $-1$ .

In Kaneko et al. (2006), one of the comprehensive GRB spectral studies catalog, time-integrated and time-resolved spectra of 350 bright BATSE bursts were analyzed. It is shown that 5% of the time-resolved spectra are violating the  $-2/3$  limit. There, several modifications or alternative non-thermal emission mechanisms to shock synchrotron model; synchrotron self-absorption, anisotropic electron pitch-angle distribution (Lloyd-Ronning & Petrosian, 2002), and jitter radiation (Medvedev, 2000) were discussed. It was concluded that a combination of shock-synchrotron and jitter radiation is more promising than synchrotron alone (Kaneko et al., 2006). It is also noted that there is still some spectra (0.2%) with very hard low energy indices  $\alpha > 0$ , which are even beyond the limit of jitter radiation model. These very hard spectra have also been studied in terms of a thermal emission component (Ghisellini et al. 2000; Ryde 2004).

In addition to the low energy index problem, synchrotron-shock model also suffers from variable and highly dispersed high energy index values. The expected post-shock Fermi accelerated electron distribution index is  $p = 2.2 - 2.3$  (Gallant, 2002) and is not supposed to change much. The observed high energy index distribution has most probable values between  $\sim -2.8$  to  $-1.9$ , corresponding to  $1.8 \leq p \leq 3.6$ , and for the half of the spectra the high energy index is highly variable (Kaneko et al., 2006).

Besides those non-thermal emission mechanisms, thermal emission originating from photospheric radius, where relativistic flow becomes optically thin to electron Thomson scattering, can be effective during prompt phase (Mészáros & Rees 2000; Daigne & Mochkovitch 2002) and may help to explain the observed spectral diversities that challenge the non-thermal emission mechanisms. Now, I will focus on this expected thermal component in GRB prompt spectrum.

## 1.6 Photospheric Emission in GRBs

As mentioned most of the GRB spectra are non-thermal. A thermal component originating from photospheric radius is identified in a limited number of GRB spectra and in very different forms. Ryde (2004 & 2005), presented a sample of BATSE bursts, in which the spectra are well modelled by a dominant thermal component (blackbody) along with a non-thermal (power-law) component throughout the prompt phase. Another form is the evolving photospheric emission component as in the case of GRB 090902B. Initially the spectrum is very similar to a pure blackbody (BB), then it is broadened due to subphotospheric dissipation and become BAND-like in later times (Ryde et al., 2011). The thermal emission has also been identified as a sub-dominant component in spectra, along with a dominant non-thermal component, e.g., GRB 100724B (Guiriec et al., 2011), GRB 120323A (Guiriec et al., 2013), GRB 110721A (Axelsson et al., 2012). Now, I present these different forms of thermal emission component and discuss their implications.

### 1.6.1 Dominant Thermal Emission

In Ryde (2004), 5 BATSE GRBs which have well defined pulses in their time profiles and have unusually hard low energy spectral indices were taken and their time resolved spectra were modelled with a BB function. In 3 of them a pure black body component was enough to represent the data well, whereas for the other two bursts an additional sub-dominant power law component is needed to well model the high energy part of the spectrum. Interestingly, the BB temperature (kT) evolution of all bursts have a similar broken power law behaviour; initially a constant or a weakly decaying power law, and then a relatively fast decay with a power law index  $\sim -2/3$ . An example is shown in figure 1.10. In a following study Ryde (2005),

for a specific sample of bursts consisting of 25 strong pulses, not necessarily having hard low energy indices all the time, have been modelled with the hybrid model; a power law (PL) and a blackbody (BB) function. The fits were compared with the conventional BAND model fits (the hybrid and BAND models have same number of free parameters). In 10 of them, the hybrid model was better than BAND and for the others these two models were statistically indistinguishable. Similar to the previous results of Ryde (2004), the thermal component was dominant over or comparable to the non-thermal one, and the temperature evolution has a broken power law behaviour within pulses. The common trend observed in the temperature evolution is interpreted as follows; until the break time,  $\sim$  a few seconds, we observe photons mostly coming from close proximity of line of sight, after this break the inner engine activity decreases (or stops) and what we see is the high latitude emission (Pe'er, 2008).

A similar kind of analysis further extended to a sample of 56 long BATSE bursts (Ryde & Pe'er, 2009). Similar temperature evolution for individual bursts were obtained, as before. This time the evolution of thermal flux were also studied and shown that the variation pattern is very similar to temperature evolution. Here the evolution of a quantity,  $\mathcal{R} = \left( \frac{F_{\text{BB}}}{\sigma T_{\text{BB}}^4} \right)^{1/2}$ , which could be directly related to photospheric radius, was also studied. It was shown that  $\mathcal{R}$  is monotonically increasing throughout the individual pulses, sometimes even during the whole prompt phase. In some cases,  $\mathcal{R}$  remained constant, and these were the cases in which  $F_{\text{BB}} \propto T_{\text{BB}}^\delta$  where  $\delta$  were  $\sim 4$ , which is expected from a blackbody emitter.

GRB 990413 is another BATSE burst whose light curve is composed of two pulses with a duration of  $\sim 14$  sec. Unlike the other smoothly pulsed thermal GRBs, the temporal structure is variable, i.e., more typical. Time resolved analysis showed that the spectrum is well fit with a hybrid model of dominant thermal component in addition to a non-thermal one (Bosnjak et al., 2006). Interestingly, for this burst a correlation between light curve and relative strengths of the spectral components was seen, during the dips of the light curve the non-thermal component dominated the spectrum, whereas for the rest the thermal emission was dominant.

Another burst detected by Fermi, GRB 100507, was shown to have a spectrum compatible with a pure thermal emission throughout its duration (Ghirlanda et al.,

2013). This burst was selected from Fermi-GBM burst catalog of the first 2 years (Goldstein et al., 2012), as being the only burst whose fluence spectrum has a low energy spectral index harder than  $\alpha = 0$  limit ( $\alpha = 0.41 \pm 0.09$ ,  $\sim 4.4\sigma$ ). The temperature evolution of this burst does not have a broken power-law behaviour as in case of Ryde (2004 & 2005). The kT seems to be constant around 30 – 40 keV during the whole prompt phase.

### 1.6.2 Modified Thermal Emission

Dissipation of jet kinetic energy is required in order to have a non-thermal spectrum as observed for most of the GRBs. Depending on the physical properties of the flow, the nature of the dissipation may vary. For example, internal shocks are effective when the flow has a highly variable Lorentz Factor (Rees & Mészáros 1994; Daigne & Mochkovitch 2002), on the other hand in highly magnetized flows shock formation is suppressed and the energy dissipation is expected to occur by magnetic reconnections (Giannios & Spruit 2005; Hascoët et al. 2013). In Pe’er et al. (2005) it is proposed that; regardless of the type of the dissipation, the accelerated electrons cool rapidly via synchrotron radiation and inverse Compton scattering with thermal photons. Numerical simulations show that the observed thermal (Planck) spectrum is significantly modified, i.e. the thermal peak broadens and becomes a non-thermal peak (BAND like shape) if the following conditions are met; dissipation occurs below the photosphere where the optical depth  $\tau \sim$  a few, the energies of thermal photons and accelerated electrons are comparable, and strong magnetic fields,  $U_B/U_{th} \sim$  tens%, are present (Pe’er & Waxman 2005; Pe’er et al. 2006).

This modified thermal emission was proposed to be observed in the spectrum of GRB 090902B, which is a bright and long burst, observed by both GBM (Bissaldi & Connaughton, 2009), and LAT (de Palma et al., 2009) instruments onboard Fermi, lying at a redshift  $z = 1.822$  (Cucchiara et al., 2009). More than 200 photons above 100 MeV, one of them having an energy of  $\sim 33.4$  GeV, were detected (de Palma et al., 2009). Its prompt emission spectrum showed a significant deviation from BAND function, and best fitted with a two component model consisting of a BAND and a PL functions (Abdo et al., 2009). Time resolved analysis of prompt spectrum shows an interesting behaviour. While the PL photon index remains relatively

steady, the BAND model parameters  $E_{\text{peak}}$ ,  $\alpha$ , and  $\beta$  show a significant change half way through the burst. During the first half of the prompt phase, the spectrum is close to a Planck shape, with unusually hard  $\alpha$  and  $\beta$  indices and narrow peaks. For the second half, the peak broadens and indices become softer with average values of  $\alpha \sim -0.6$  and  $\beta \sim -2.5$ , being a more typical non-thermal BAND shape (Ryde et al., 2011). The change in spectral shape can be seen in Figure 1.11.

The evolution of GRB 090902B spectrum is interpreted as follows (Ryde et al., 2011); initially, there is very weak dissipation or no sub-photospheric dissipation at all, and the slight broadening observed in the spectrum is due to geometrical effects (Pe'er 2008). Later on the main spectral component, i.e., the MeV peak, still has thermal origin, but now it is subjected to strong sub-photospheric dissipation, which in turn modifies the spectrum significantly as proposed in (Pe'er et al., 2005). The evolution in the dissipation pattern can be attributed to a variable Lorentz factor due to a change of the inner engine activity. The locations of photospheric ( $R_{\text{ph}}$ ) and dissipation radii ( $R_{\text{dis}}$ ) depend strongly on the Lorentz factor of the flow  $R_{\text{diss}}/R_{\text{ph}} \sim \Gamma^5$  (Mészáros et al. 2002; Rees & Mészáros 2005). If the Lorentz factor decreases half way through, the  $R_{\text{ph}}$  becomes larger than the  $R_{\text{diss}}$  that leads to a strong sub-photospheric dissipation. Since the peak energy of the  $\nu F_{\nu}$  spectrum is determined by the temperature  $kT$ , and  $kT$  scales as  $\Gamma \propto T^{0.5}$  (Pe'er et al., 2007), a decrease in  $\Gamma$  is expected to be seen in temperature evolution also, which is indeed observed.

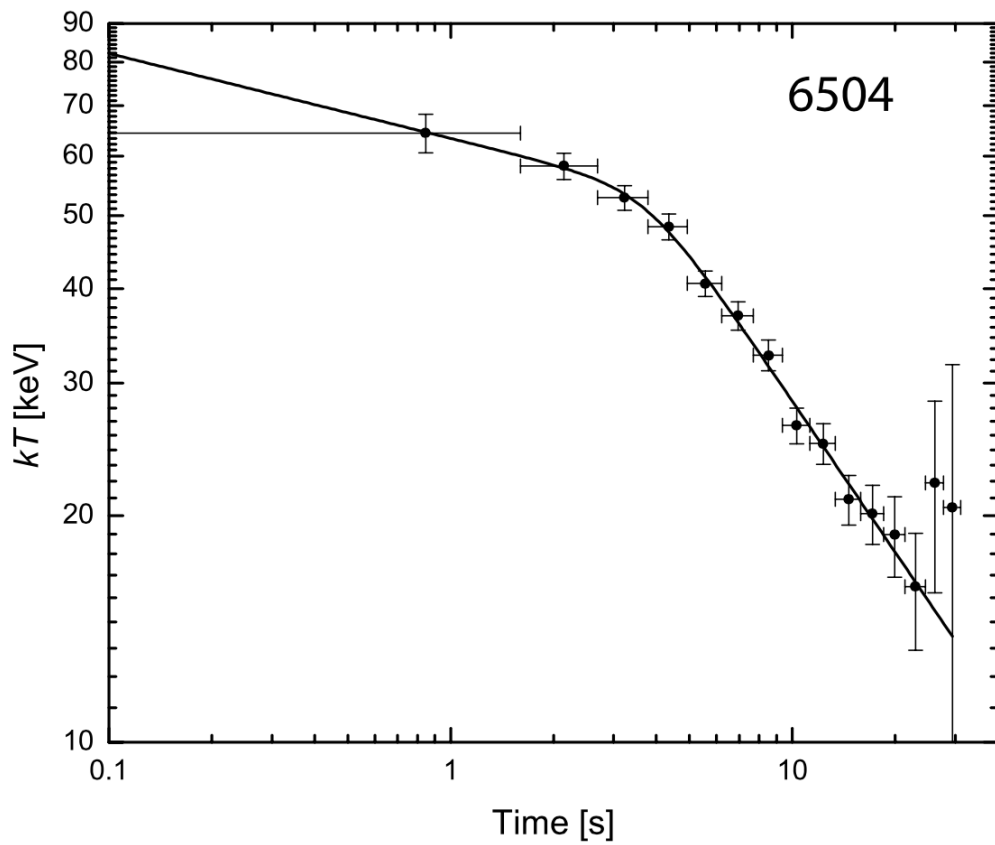


Figure 1.10: The temperature evolution of the blackbody component in the spectrum of a BATSE burst GRB 971127. Taken from Ryde (2004).

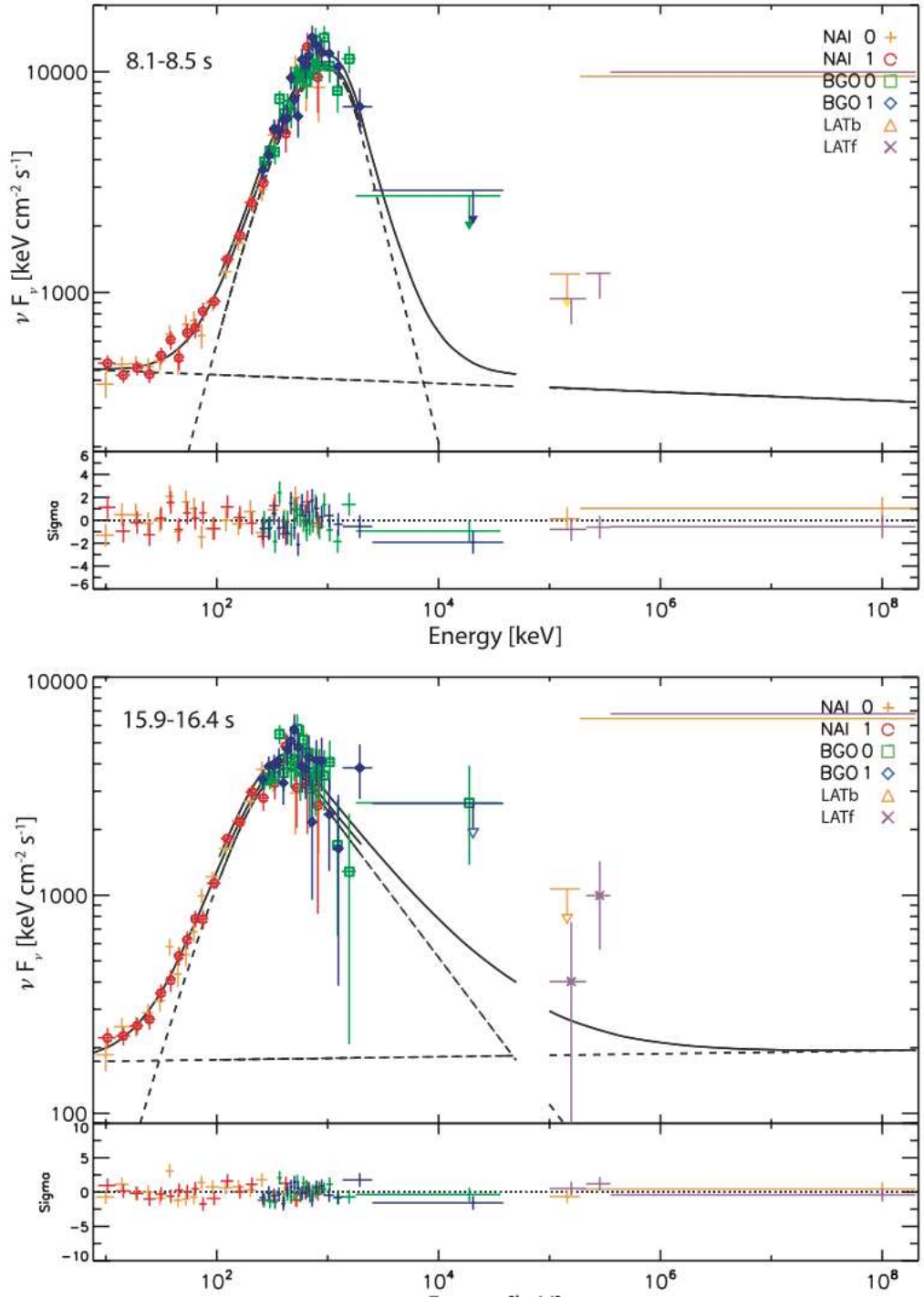


Figure 1.11: The  $\nu F_\nu$  spectra of two time intervals,  $t = 8.1 - 8.5$  s and  $t = 15.9 - 16.4$  s, belonging to first and second half of the prompt emission phase for GRB 090902B. Different symbols are referring to different detectors aboard on Fermi. The broadening in the spectrum is clear. Taken from Ryde et al. (2011).

### 1.6.3 Sub-dominant Thermal Emission

The photospheric emission in the burst spectrum can also be present as a sub-dominant component along with the dominant, non-thermal one. The energy flux of this thermal component is at most  $\sim$  a few tens % of the total flux. Several example cases are summarized below.

GRB 100724B is one of the most intense bursts detected by Fermi-GBM. Its prompt spectrum shows a significant deviation from BAND model both at low & high energies, even though BAND has typical spectral parameters (Guiriec et al., 2011). Among several relevant hybrid models, BAND model along with a blackbody gives the best fit results and is statistically preferred over BAND only fits.

GRB 110721A is another very bright, single pulsed (FRED), long burst observed by both GBM and LAT instruments on board Fermi. Both the time integrated and time resolved analysis of GBM and LAT joint data showed that, the spectra have a significant deviation from BAND model, and addition of a blackbody function significantly improves the fit (Axelsson et al., 2012). A multicolor blackbody (integral of different kT blackbody) function further improves the fit (Pe'er & Ryde, 2011). The energy flux of this thermal component is  $\sim$  5% of total flux. The temperature kT decreases as broken power law, similar to the evolution previously reported for BATSE bursts (Ryde, 2004). It is also interesting to mention that the very first time bin of this burst has an unusually high peak energy  $E_{\text{peak}} = 15 \pm 1.7$  MeV, whereas after a few seconds the  $E_{\text{peak}}$  value drops to  $\sim$  few hundred keV, typical values observed for GRBs (Kaneko et al., 2006).

GRB 120323A is an intense short burst detected by Fermi-GBM, showing a double peak structure in its light curve above 20 keV. Guiriec et al. (2013) studied its prompt emission phase in detail and obtained following results. The analysis of both time-integrated and time-resolved spectra revealed the existence of a secondary curvature in the spectrum with high statistical significance. This secondary (and sub-dominant) hump is consistent with the expected spectral shape of photospheric emission from a relativistically expanding jet. The evolution of the parameters was very interesting. When a single component model, i.e., BAND, is applied there appears a simultaneous discontinuity at  $\sim$  0.1 s in all parameters. As seen in the Figure 1.12, the  $\alpha$  index is initially very hard, i.e.,  $\alpha \gtrsim 0$ , then  $\sim$  0.1 sec it drops to

a value  $\sim -1.5$ . Similarly, the high energy power law index  $\beta$  has values  $\sim -2$  until  $\sim 0.1$  sec, then it has only upper limits of  $\sim -2.7$ . The peak energy  $E_{\text{peak}}$  has an intensity tracking pattern. When two component model is applied  $\alpha$  takes values  $\sim -1.3$ , the  $E_{\text{peak}}$  has hard to soft evolution (having values of  $\sim$  MeV initially),  $\beta$  has only upper limits of  $\sim -2.4$  throughout the burst. The discontinuity almost disappears and parameters evolve smoothly when the additional blackbody model is applied to the spectrum. Figure 1.13 shows the  $\nu F_\nu$  spectra of two time intervals; one from before and the other from after the observed discontinuity. The single and two component model fits are seen. Initially the single component model (BAND) mimics the shape of the lower energy hump (i.e., blackbody, which is more prominent initially) of two component model where it mimics the higher energy hump later. This demonstrates the reason of having discontinuity in BAND model parameters evolution, and how the discontinuity disappears when the blackbody function takes care of the secondary hump structure in the spectrum.

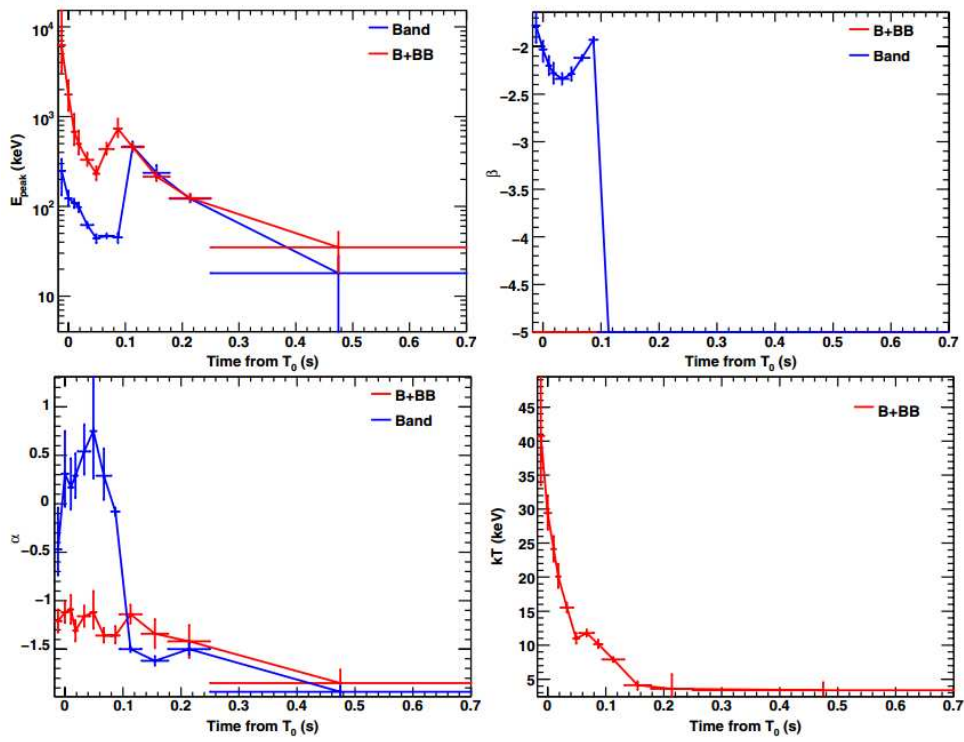


Figure 1.12: The evolution of parameters with and without blackbody function for the prompt emission phase of GRB 120323A. Taken from Guiriec et al. (2013).

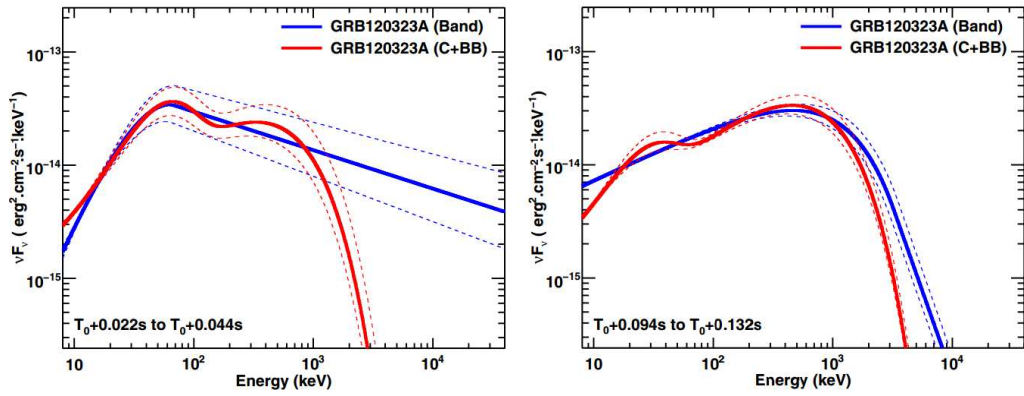


Figure 1.13: The  $\nu F_\nu$  spectrum of two different time intervals, before and after the observed discontinuity. Initially the single hump model (BAND) mimics the blackbody component, where later it mimics the non-thermal component of the hybrid model. Taken from Guiriec et al. (2013).

Now, by combining the theoretical model ingredients and the observations mentioned above, we can draw the following generalized picture; the observed GRB spectra are non-thermal and most of them can be well represented by empirical BAND model whose parameters can be related to non-thermal emission processes. However, there are some spectra which challenges those non-thermal processes. The thermal emission originating from the photospheric radius of the flow is a natural expectation of the basic theoretical framework, and the existence have been reported in some GRB prompt emission spectra. Therefore, there appears two ways; either the main emission mechanism in GRBs is photospheric and it undergoes strong sub-photospheric dissipation in order to be consistent with the observed spectra, i.e., modified Planck spectrum (e.g., GRB 090902B, Ryde et al. 2011), or the dominant mechanism is non-thermal (internal shocks or magnetic reconnection models) and accompanied by thermal emission whose strength depends on the properties of the relativistic flow.

Interpreting the spectrum as a modified Planck spectrum might have a potential problem: the extremely hard peak energies observed in some bursts. For example, for a very hard burst GRB 110721A, it is claimed that the observed  $E_{\text{peak}} = 15 \pm 1.7$  MeV cannot have a photospheric origin (Zhang et al., 2012). In their work an upper limit for the peak energy of the spectrum which is dominated by the dissipative photospheric emission was obtained as follows:

$$E_{\text{peak}} \leq \eta k T_0 \simeq 1.2 \text{ MeV} \eta L_{52}^{1/4} R_{0,7}^{-1/2} \quad (1.4)$$

Here,  $T_0$  is the initial temperature of the hot Fireball,  $\eta$  is a factor depending on the shape of the spectrum. Therefore, this equation defines a death line in  $E_{\text{peak}}$  and Luminosity plane for a photospheric emission model, and this death line is calculated for GRB 110721A and for bright GRBs which are detected by Fermi and have redshift measurements, as seen in Figure 1.14. It is seen that the initial time bins'  $E_{\text{peak}}$  values are above the death line, i.e., violating this limit, indicating that the main emission component in the spectrum of GRB 110721A should be originating from optically thin regions of the flow.

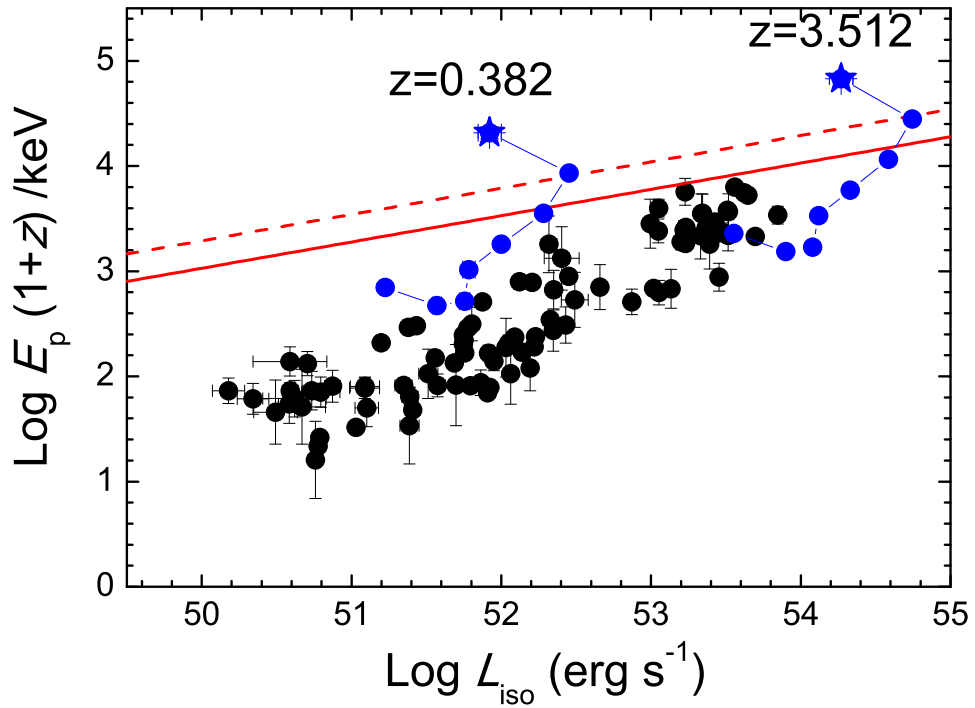


Figure 1.14: The rest frame peak energy  $E_{\text{peak}}(1+z)$  versus observed isotropic luminosity  $L$  graph for Fermi GRBs with redshift measurement (Lu et al., 2012) and GRB 110721A. The solid and dashed lines correspond to death lines of two candidate redshift measurements for GRB 110721A. The two stars are representing the initial time interval of GRB110721A, which are well above the limits. Taken from Zhang et al. (2012).

**Magnetized Fireball:** Daigne & Mochkovitch (2002) showed that in the pure thermal Fireball scenario, which is powered by neutrino-antineutrino annihilation (Zalamea & Beloborodov, 2011), the expected photospheric emission should be quite hot and luminous, and should be clearly seen in spectrum. A more generalized form of conventional *Fireball* model can be achieved by taking into account the presence of magnetic energy, as well as thermal energy in the flow (Spruit et al. 2001; Giannios 2008).

It is suggested that, the diverse appearance of photospheric emission in GRB prompt emission can be explained by the level of initial magnetization at the central engine (Drenkhahn & Spruit, 2002). If the magnetization is low; then the photospheric emission would be bright (e.g., GRB 090902B), if it is moderate; the photospheric component accompanies the dominant nonthermal component (e.g., GRB 100724B), and if it is very high; the prompt spectrum is pure non-thermal.

In another study Hascoët et al. (2013) the expected shape of thermal and non-thermal components for different physical conditions of the flow were produced. It is possible to change the relative strengths of thermal and non-thermal components observed in the spectrum by changing the physical parameters of the flow. In addition, in order to make the photospheric component more visible in spectrum, one needs to increase the amount of initial thermal energy  $\epsilon_T$  and the average Lorentz factor of the flow  $\Gamma$ , or decrease the isotropic luminosity  $\dot{L}_{\text{iso}}$  and the contrast in the distribution of the Lorentz factor of the flow.

#### 1.6.4 Inferring Parameters of the Expanding Fireball

Once the thermal component originating from photosphere is identified in a GRB spectrum, the initial size ( $R_0$ ) and the bulk Lorentz factor of the flow ( $\Gamma$ ) can be calculated by using only the observed flux and temperature of the thermal component, if the redshift of the burst is known (Pe'er et al., 2007). If the photospheric radius ( $R_{\text{ph}}$ ) is reached in the coasting phase of the flow (acceleration is completed before  $R_{\text{ph}}$ ), it is also possible to calculate the photospheric and saturation radius ( $R_{\text{sat}}$ ) of the flow. There are advantages of calculating  $R_0$  and  $\Gamma$  from observed blackbody parameters. It gives a direct measurement of Lorentz factor  $\Gamma$ , not only a lower limit as in the case of energetic photon annihilation condition (Krolik & Pier, 1991).

Hascoët et al. (2013) extended this work in the case of initial magnetic energy presence in the flow under several assumptions such as; flow expands adiabatically from  $R_0$  to  $R_{\text{ph}}$ , the acceleration is completed at photospheric radius (i.e.  $R_{\text{sat}} < R_{\text{ph}}$ ), if the magnetization ( $\sigma$ ) at the end of acceleration phase ( $\sigma$ ) is assumed to be small then it is taken as  $\sigma = 0$ .

Identification of a blackbody component in the spectrum may provide us a better understanding of the inner engine, the energy form, the dynamics of the jet, the emission mechanism of GRBs. Determining the initial radius of the flow  $R_0$  and the Lorentz factor  $\Gamma$  (depends on the mass ejection rate) helps us to characterize the GRB progenitors. The relative strengths of thermal and nonthermal components in the spectrum gives an indication of the thermal and magnetic energy densities of the jet, which in turn enlightens the acceleration and emission mechanism. In these respects it is very important to find more, if possible all, GRBs with thermal signature in their spectra and then to identify its form and evolution throughout the burst.

## 1.7 Motivation of Our Work

Identification of thermal emission component in GRB spectra helps us to better characterize the nature of GRB prompt emission phase. It is also important to probe the thermal emission, when and how it appears in GRB spectrum. So far, the thermal emission have been reported for a limited number of bursts. These bursts are either very bright bursts, or have extremely hard low energy indices ( $\alpha \geq 0$ ) in their time integrated spectrum. It is known that GRB spectrum can show strong spectral evolution throughout its prompt phase, and there is no theoretical reason for thermal component to show up only in spectra of bright GRBs. Within these respects it is crucial to identify more bursts with thermal component in their spectrum. Since the form, intensity, and the evolution of thermal emission differs a lot from burst to burst, it is not an easy task to identify thermal GRBs in an automated manner. However, one can make use of a possible implication of thermal emission, i.e., hard low energy index.

To this extent, we performed a systematic time resolved spectral analysis of all 611 GRBs detected by Fermi, during its first 2, 5 years of operation. We selected a

thermal-candidate sample of bursts based on their time resolved spectral properties. Then, we applied an additional blackbody model to the fluence spectrum of these candidate bursts. The final sample of thermal-candidate bursts is formed based on a certain level the statistical improvement. For the bursts in our final sample, we identify the individual pulse structures in the time profiles of each GRB, and we simulate each pulse to evaluate the statistical significance of the additional thermal component. Then, we performed extensive time-resolved modelling to examine the evolution of thermal and non-thermal components. Finally, we inferred several basic Fireball parameters (e.g.,  $\Gamma$ ,  $R_0$ ) from thermal emission parameters.

## Chapter 2

# GAMMA-RAY BURST MONITOR

Gamma-ray Burst Monitor (GBM) is one of the two experiments onboard Fermi Gamma-Ray Space Telescope (formerly called GLAST), and is specifically designed for GRB detection (Meegan et al., 2009). Fermi was launched on 11 July 2008 and placed into an orbit of 565 km. The other instrument is the Large Area Telescope (LAT). GBM detects and localizes a GRB and sends this information to the LAT and to the ground immediately, for re-orientation of the spacecraft and further observation of the burst by the LAT. GBM observes gamma-rays between  $\sim 8$  keV to  $\sim 40$  MeV, and LAT observes from  $\sim 20$  MeV to  $> 100$  GeV. Altogether, GBM and LAT, make GRB observations possible in broadband ( $\sim$  seven decades of energy). For the spectral analysis in this thesis, we used data obtained from GBM. In this chapter we focus on the detectors on the GBM, performance of the detectors, and data types available for spectral analysis.

There are 12 thallium-activated sodium iodide (NaI(Tl)) scintillation detectors and 2 bismuth germanate (BGO) scintillation detectors on GBM, which are operating at different energy ranges (Meegan et al., 2009). First, we describe the working principles of scintillation detectors briefly, then look closely to the GBM detectors.

### 2.1 Scintillation Detectors

Detection of gamma-rays requires their interaction with matter in gaseous, liquid, or solid phase placed in the detector. This interaction can be in various ways depending on the energy of the incident photon. The three main interaction processes that are utilized for gamma-ray detectors are; photoelectric effect, Compton scattering, and pair production. Figure 2.1 shows the cross sections for these interactions

in a NaI crystal as a function of energy.

In photoelectric interactions the incident photon is totally absorbed in an atom and as a result an electron is released. The kinetic energy of this free electron is related to the energy of the incoming photon and the electron binding energy. Then, this electron loses its energy by ionizing or exciting other atoms. Afterwards, these charges are collected in the detector and a corresponding signal is generated. This type of interaction is dominant at photon energies  $\lesssim$  a few hundreds of keV. The feature seen at 33 keV is called as K-edge, which is the binding energy of the K shell electrons. Incoming photons with energies above this edge can also interact with inner K shell electrons resulting in an increase in cross section of the photoelectric absorption.

In Compton scattering the incoming photon interacts mostly with an outer shell electron. The binding energy of the electron is negligible. After scattering, the photon and the electron are scattered at different directions. Some portion of the incident photon is given to the electron. The amount of this transferred energy depends on the initial energy of the photon and scattering angle. Again, the electron loses its energy by ionizing or exciting other atoms. Here, also the scattered photon can go through other interactions in the material, at the end it can be absorbed by or it can escape from the material. The Compton interaction is the dominant process for photon energies between  $\sim$  a few hundreds of keV -  $\sim$  several MeV.

In pair production process, the incoming photon, with energy at least 1.02 MeV, is converted into an electron-positron pair, in the vicinity of an atomic nucleus (within the Coulomb field of the nucleus). The photon energy exceeding 1.02 MeV is transferred to created pair as kinetic energy. Both the electron and the positron lose their energy by interacting with other atoms in the material. After losing their energy they annihilate and radiate two photons with 511 keV energies. Pair production is a dominant process for photon energies  $\gtrsim$  several MeV.

Through these processes, the energy of the incoming photon is converted into a flash of light (scintillation) via primary and secondary interactions within the detector material. Afterwards, this light pulse is detected by a photomultiplier tube (PMT), in which it is converted into an electrical signal. Since the intensity of the light pulse, and in turn, the amplitude of the electrical signal is a measure of

the incident gamma-ray photon energy, the amplitude distribution of these signals provides us the corresponding source spectrum. This analysis is done by the pulse height analyzer unit.

### 2.1.1 NaI(Tl) Detectors

Thallium activators (impurities) are implemented to pure NaI crystal in order to shift the energy range of the incoming photon to the visible light energies for PMT detection. NaI(Tl) is one of the most common inorganic scintillator material for two reasons. First, the efficiency of conversion process of photon energy to light is relatively high for NaI(Tl) and second, the intensity of the output light is linear over a broad gamma-ray energy range.

Each of the twelve identical NaI(Tl) detectors onboard GBM has crystal disks with a diameter of 12.7 cm and a thickness of 1.27 cm, which are connected to a single PMT. NaI detectors have an energy range of  $\sim 10$  keV to  $\sim 1$  MeV. The positions and the orientations of the NaI detectors of GBM are shown in Figure 2.2. The detectors are placed on the spacecraft in such a way to maximize the sky coverage for monitoring purposes, and to obtain the GRB sky coordinates onboard, from the relative count rates of each NaI detector measures. The onboard software has the information of relative count rates for detectors which are calculated for 1634 different directions ( $\sim 5$  deg resolution). When a burst is triggered, the detector counts are fit to these pre-determined values and the best direction in terms of declination and right ascension is obtained. The error in location calculated with this method is usually a few degrees.

### 2.1.2 BGO Detectors

$\text{Bi}_4\text{Ge}_3\text{O}_{12}$  is an inorganic scintillator with relatively high density,  $7 \text{ g/cm}^3$ . Together with the large atomic number of Bi ( $Z=83$ ), BGO has a relatively large cross section for gamma-ray absorption. The length and the diameter of the BGO crystal are both 12.7 cm, and there are two PMTs placed on both sides of the crystal. Using two PMTs per crystal increases the light collection efficiency. The BGO has an energy range of  $\sim 200$  keV to  $\sim 40$  MeV, which provides an overlap energy range with NaI data for cross-calibration. There are two BGO detectors placed on

opposite sides of the spacecraft, as seen in Figure 2.2. Therefore, a burst is visible to at least one of them if there is no Earth occultation, i.e., if the burst is not behind Earth.

## 2.2 Detector Response Matrices

For any detector, it is not possible to perfectly process the energy of the incoming photon. During the interaction of photon with the scintillation material it is very likely that some part of the incident energy is lost or re-distributed. Therefore, the true spectrum of the source and the observed spectrum by the detector are not exactly the same. A detector response matrix (DRM) is the representative of a detector and helps us to reconstruct the original source spectrum. The DRMs are produced by calibration measurements with well known radioactive sources and by simulations which takes into account the geometry of the detector, the angle to the source, energy dispersion, background radiation, detector shielding, and incoming photon energy. For example, Figure 2.3 shows the energy resolution of a NaI and a BGO detector as a function of energy. The energy resolution of a detector is measured as follows; a monochromatic light is send to the detector and the detector response, i.e., output signal (photopeak) is analyzed, which is similar to a Gaussian shape. Then, the full width at half maximum of the photopeak (FWHM) defines a measure for the energy resolution of the detector at the energy of the monochromatic light. Another important effect that is analyzed and included in DRMs is the energy dependence of the detector effective area. Figure 2.4 shows the effective area of NaI and BGO detectors as a function of energy, assuming normal incidence. It is seen that the sensitivity of NaI detectors starts to decrease for photon energies above  $\sim 100$  keV up until  $\sim 1$  MeV, where BGO has a much better sensitivity. For each triggered burst, for each of the GBM detector a corresponding DRM is generated and made available for spectral analysis.

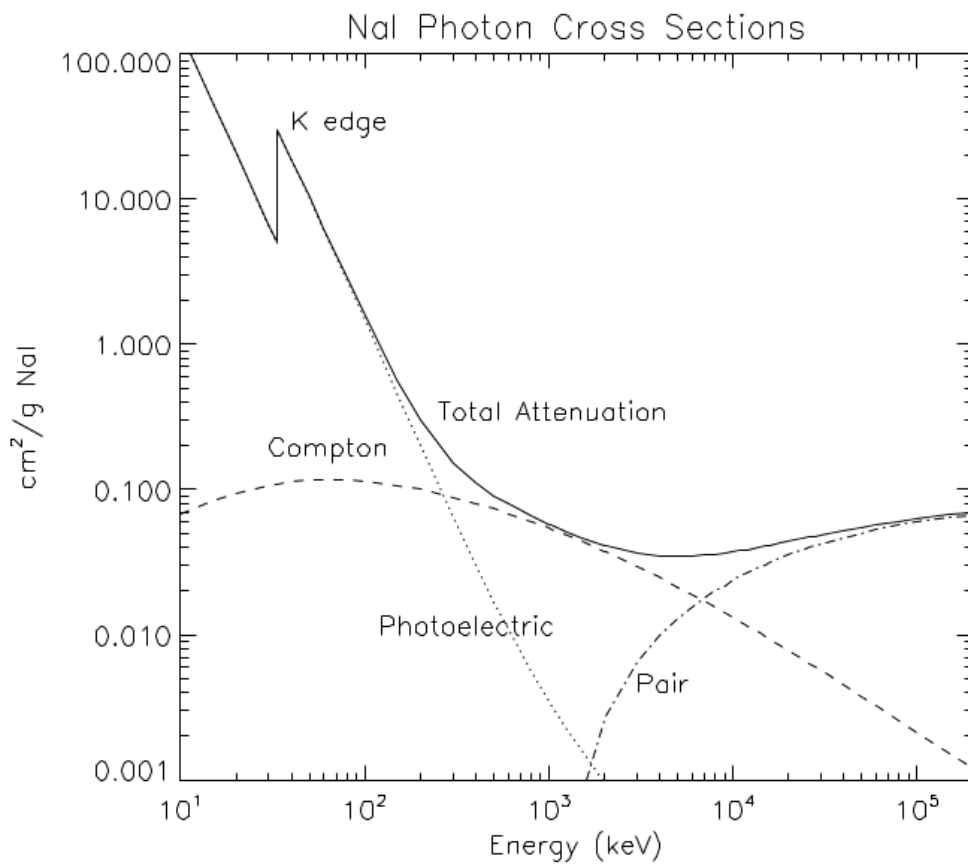


Figure 2.1: The cross sections for gamma-ray interaction processes in a NaI Crystal. Taken from Kaneko et al. (2006).

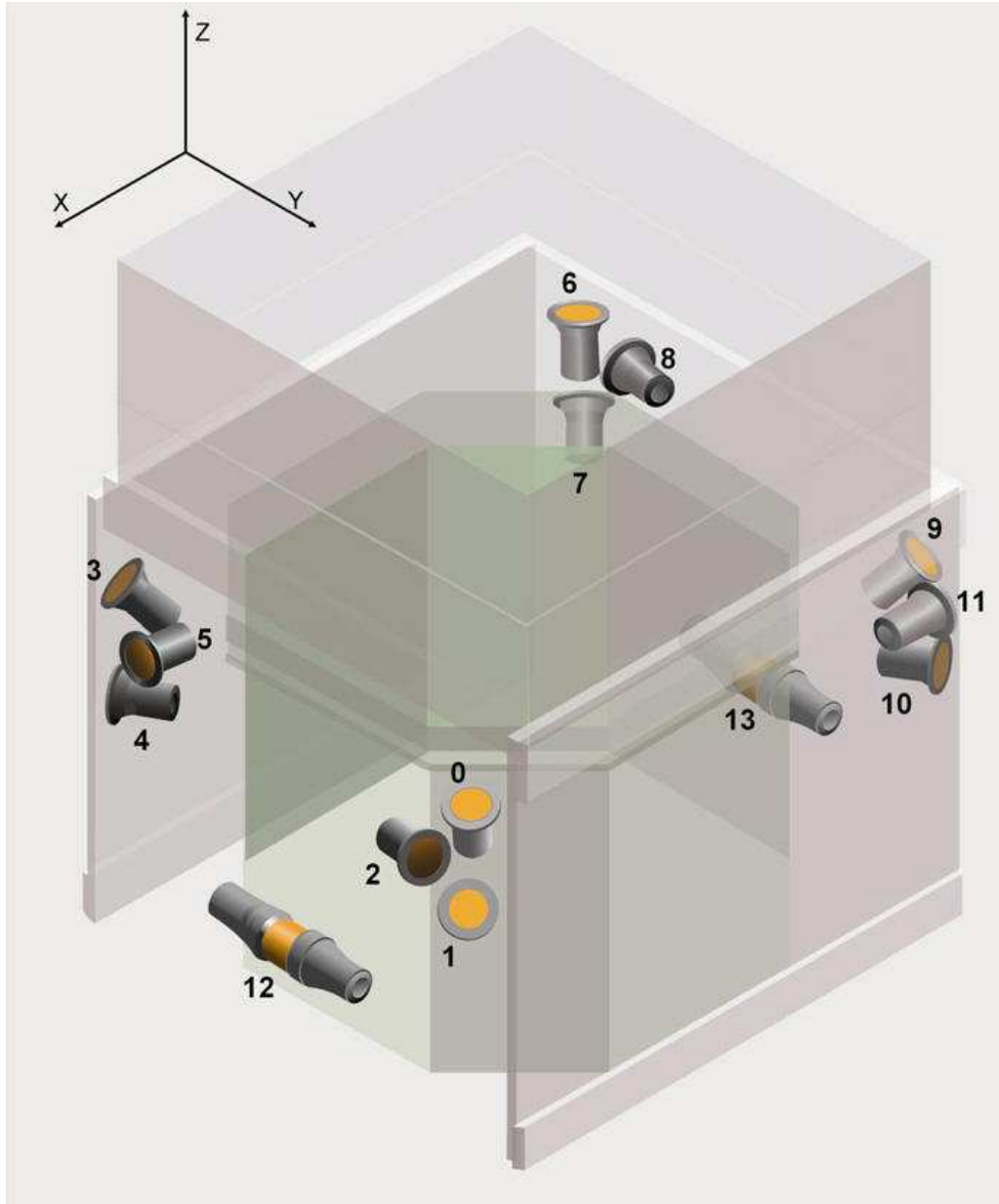


Figure 2.2: The positions and orientations of GBM detectors. Numbers from zero to eleven representing the twelve NaI detectors, and numbers 12 and 13 are showing two BGO detectors. The block on top is the LAT. Taken from Meegan et al. (2009).

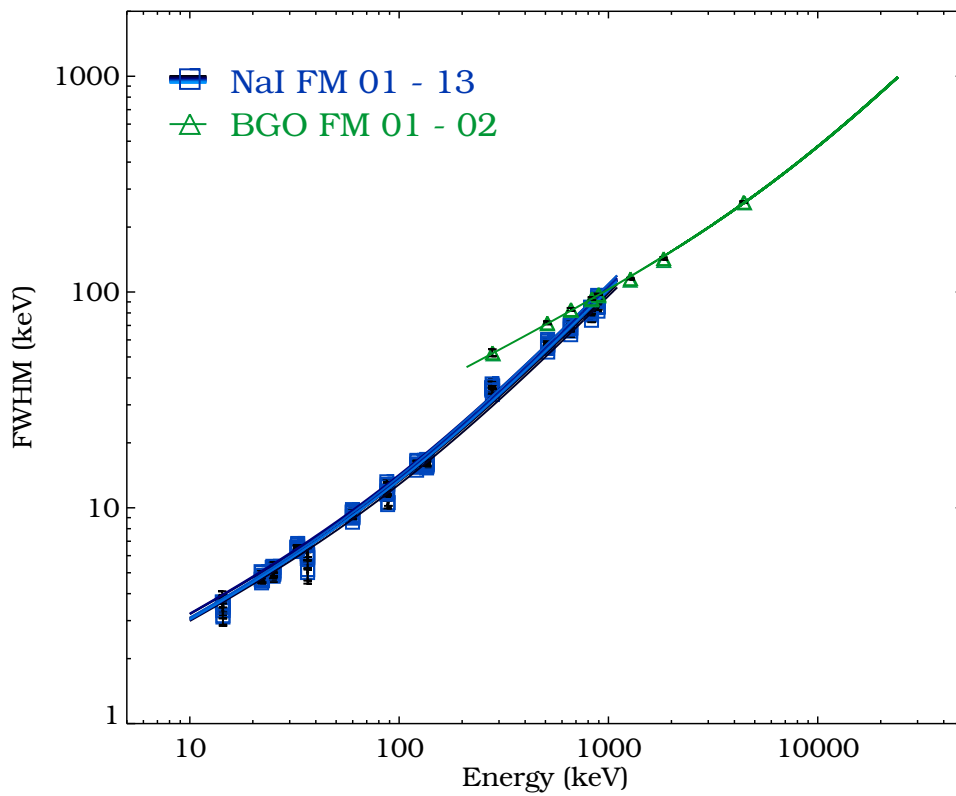


Figure 2.3: The energy resolution of a NaI (squares) and a BGO (triangles) detector as a function of energy. Taken from Bissaldi et al. (2009).

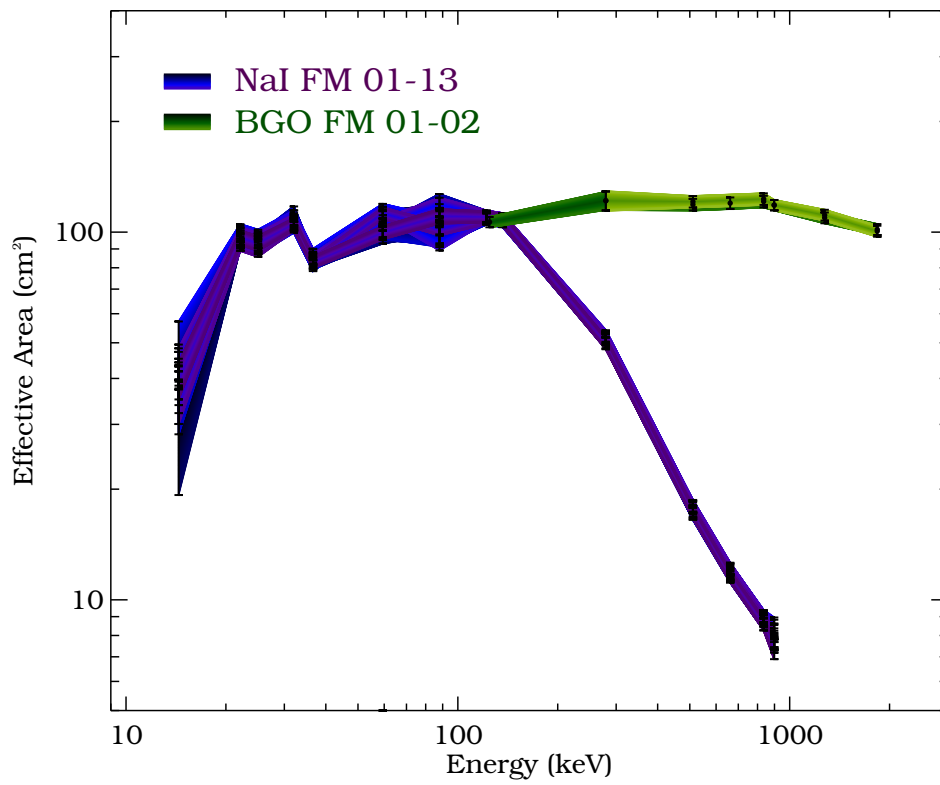


Figure 2.4: The effective area of NaI and BGO detectors as a function of energy, assuming normal incidence. Taken from Bissaldi et al. (2009).

### 2.3 GBM Data Types

GBM provides both daily (continuous) and burst (for triggers) data which are all publicly available. The daily data is continuously produced, whereas the burst data is produced when the onboard software detects count rates above the threshold ( $0.74 \text{ photons cm}^{-2} \text{ s}^{-1}$ ) in at least two of the NaI detectors. The CSPEC (Continuous high spectral resolution) and CTIME (Continuous high time resolution) burst data types provide 4000 sec pre and post burst trigger data, whereas TTE (Time-tagged event) data type provides 30 sec pre and 300 sec post burst trigger data. Each data type is produced for each detector. The types of data with several basic properties are summarized in Table 2.1.

In this work we used TTE data due to its high time and energy resolution. TTE has an absolute time-resolution of  $2\mu\text{s}$  which is significantly higher than all other data types, as can be seen in Table 2.1. However, the duration of pre and post burst data intervals is relatively short which may limit the background modelling.

Table 2.1: GBM data types. Each type of data is produced for each GBM detector.

Name	Type*	Energy Resolution (number of channels)	Temporal Resolution
CSPEC <sup>a</sup>	Daily	128	4.096 s
CTIME <sup>b</sup>	Daily	8	0.256 s
CSPEC		128	1.024 s
CTIME	Burst	8	0.064 s
TTE <sup>c</sup>	Burst	128 <sup>d</sup>	2 $\mu$ s

\* Daily data is continuously produced, whereas burst data is produced when trigger occurs.

<sup>a</sup> Continuous high spectral resolution.

<sup>b</sup> Continuous high time resolution.

<sup>c</sup> Time-tagged events.

<sup>d</sup> Energy edges are same as CSPEC.

## Chapter 3

# METHODOLOGY

We have a two-step approach to identify and investigate GRBs with thermal signatures. We first performed a time-resolved spectral analysis using conventional non-thermal models for all bursts detected with Fermi-GBM in its first  $\sim 2.5$  years of operation (from mid-July, 2008 to the end of December, 2010). From the time-resolved spectral model parameters we determined a sample of GRBs with a potential blackbody signature in their spectra (primary candidates). Then, we used an additional blackbody function to model these primary candidate GRBs' time-integrated spectra, and obtained our thermal candidate GRBs sample based on a certain level of statistical improvement that this additional blackbody component has provided. We then performed extensive spectral analysis and simulations for these thermal candidate bursts. Finally, we used the observed thermal flux and temperature to estimate physical parameters of the relativistic outflow (Lorentz factor, initial and photospheric radius).

At the time of this analysis, another Fermi-GBM burst, GRB 110721A, was reported as having a sub-dominant thermal emission component in its spectrum (Axelsson et al., 2012). This burst is also included in our analysis even though it was detected in 2011, since it will provide an additional test for the validity of the selection and analysis method we used here.

Now, we describe each step of this comprehensive spectral analysis in sections, § 3.1 and § 3.2. In the first section, the methodology that is followed in order to obtain the thermal candidate bursts sample is explained. In the second section, the detailed spectral analysis of these thermal candidate bursts and deduced physical parameters of their outflows are presented. For all of the spectral analysis presented

in this thesis, I used lightcurve and spectral analysis software RMFIT version 4.0rc1 (Mallozzi, R.S., Preece, R.D. & Briggs, M.S., 2005).

### 3.1 Systematic Time Resolved Analysis

Fermi-GBM detected 611 GRBs in the first  $\sim 2.5$  years of operation, from 14 July, 2008 to 12 December, 2010. For this part of the analysis, only the data produced by Sodium Iodide (NaI) detectors of GBM are used, in order to avoid any discrepancy that might exist between different types of detectors. NaI detectors are sensitive between energy range  $\sim 8$  keV –  $\sim 1$  MeV, capturing most of the GRB prompt emission photons.

#### 3.1.1 Detectors, Data Type and Time Binning

As explained in chapter 2, the 12 NaI detectors are located all around the spacecraft in order to maximize the sky coverage. A burst can be seen by multiple detectors but with different zenith angles, and therefore different brightness. In this study, for each burst, the brightest two or three NaI detectors, with an angle to the source less than  $60^\circ$  are used, since these detectors have larger effective area therefore, have the best signal for spectral analysis (Goldstein et al., 2012). Time-tagged event (TTE) data type is preferred for this work because it has the highest temporal ( $2 \mu\text{s}$ ) and spectral resolution (128 channels), hence, most appropriate for time-resolved spectral analysis.

For a given burst, for each of the NaI detectors; the energy range is selected from  $\sim 8$  keV to  $\sim 900$  keV (excluding the highest channels), background level is modelled, and burst interval is selected. For the background modelling, we select time intervals from pre and post burst phases. The TTE provides 30 s of pre-trigger and 300 s of post-trigger data. These background intervals are chosen to be as long as possible depending on the burst duration, mostly  $\sim 10$  s pre and  $\sim 150$  s post the trigger. Then, we fit the background lightcurve with a first or second order polynomial function, which is extrapolated to the source interval. The source interval of the burst is determined by looking at each NaI detector's light curve and background level. The *start time* is mostly consistent with trigger time, but sometimes there were some pre-trigger activity, then the counts above the background level are also

included. The *end time* is determined where the signal drops back to background level. This might slightly differ from one detector to another. In such a case we have taken the widest time interval as the burst interval and made it same for all detectors.

In order to perform the systematic time resolved analysis, the prompt emission phase was divided into fine time intervals (bins) in an optimized manner. Our main objective for the time-resolved analysis is to see the spectral evolution within a burst with highest possible resolution. On the other hand, we also have to have enough signal in each bin to be able to constrain the model parameters. Therefore, for a given burst; the dimmest NaI detector’s data is binned with a signal-to-noise ratio (SNR) of 15, and the last bin is excluded since it may have SNR less than 15. The remaining NaI detectors time intervals are defined according to this dimmest one to make sure that each time bin has a SNR of at least 15. The number 15 for SNR is reached as follows; a burst is taken and its source interval is binned with many different SNRs. We start with  $\text{SNR} = 3.5$  (this is the lower limit where source signal is distinguishable from background fluctuations (Goldstein et al., 2012), and increased the SNR by 0.5 or 1 unit at each step up to  $\sim 20$ . For each value of the SNR binning, we fit various time intervals within the given burst with the Comptonized model (this is the photon model that is used for time-resolved analysis, see § 3.1.2 for the model details). We then noted the value of SNR at which the parameters of the Comptonized model started to be constrained. We repeated this test, for other bursts with different fluences, and concluded that  $\text{SNR} = 15$  is plausible for our purposes here.

After the time binning process, 448 bursts had at least two time bins (each with  $\text{SNR} \geq 15$ ) during their prompt emission phases, and this is the GRB sample that we performed the systematic time-resolved analysis to obtain our primary candidate bursts sample. We excluded the others (bursts with only one time bin) since, in addition to identify thermal component we also want to see the evolution of it within the burst.

### 3.1.2 Spectral Photon Models

Most of GRB spectra are well described by the empirical BAND model (Band et al., 1993). As mentioned earlier, this model consists of two power laws (i.e., low and high) joining at a break energy. In cases where there is no significant emission at high energies a low-energy power law with an exponential cutoff, i.e., Comptonized model is preferred over the BAND model. We modelled non-thermal emission component in GRB spectra with either BAND or Comptonized photon models. For modelling the thermal emission component in the spectrum we used the Planck (blackbody) function. Figure 3.1 shows the shape of the three spectral models in  $\nu F_\nu$  representation. Now, we explain these spectral photon models in detail. The photon model  $f$  is the photon number flux in photons  $\text{s}^{-1} \text{cm}^{-2} \text{keV}^{-1}$ .

- Band Model (BAND)

This model is the so called *Gamma ray burst* function (Band et al., 1993). It has been widely used to model GRB spectrum.

$$f_{\text{BAND}}(E) = \begin{cases} A \left(\frac{E}{100}\right)^\alpha \exp\left(\frac{-E(2+\alpha)}{E_{\text{peak}}}\right), & \text{if } E < \frac{(\alpha-\beta)E_{\text{peak}}}{2+\alpha} \\ A \left(\frac{(\alpha-\beta)E_{\text{peak}}}{100(2+\alpha)}\right)^{\alpha-\beta} \exp(\beta - \alpha) \left(\frac{E}{100}\right)^\beta, & \text{if } E \geq \frac{(\alpha-\beta)E_{\text{peak}}}{2+\alpha} \end{cases} \quad (3.1)$$

The model has four parameters:  $A$  is the amplitude in photons  $\text{s}^{-1} \text{cm}^{-2} \text{keV}^{-1}$ , low energy index  $\alpha$ , high energy index  $\beta$ , and peak energy of the  $\nu F_\nu$  spectrum  $E_{\text{peak}}$  in keV.  $\nu F_\nu$  spectrum is the power density spectrum, showing the total energy flux per energy band.

- Comptonized Model (COMP)

This model is what BAND model converges to in the limit  $\beta \rightarrow -\infty$ , i.e., without high energy power law component.

$$f_{\text{COMP}}(E) = A \left(\frac{E}{E_{\text{pivot}}}\right)^\alpha \exp\left(\frac{-E(2+\alpha)}{E_{\text{peak}}}\right) \quad (3.2)$$

There are three model parameters:  $A$  is the amplitude in photons  $\text{s}^{-1} \text{cm}^{-2} \text{keV}^{-1}$ , low energy index  $\alpha$ , and peak energy of the  $\nu F_\nu$  spectrum  $E_{\text{peak}}$  in keV.  $E_{\text{pivot}}$  is the pivot energy which normalizes the energy at which the amplitude

is evaluated, and it is fixed at 100 keV in the fitting process here. The naming of this model is such because in the case of  $\alpha = -1$ , the model represents the expected spectrum from a Comptonized thermal emitting region. In the case of  $\alpha = +1$ , the shape of the model is similar to black body function (see below).

- Blackbody Model (BB)

The following Planck function is used to model the thermal emission component in the spectrum:

$$f_{\text{BB}}(E) = A \frac{E^2}{\exp\left(\frac{E}{kT}\right) - 1} \quad (3.3)$$

Model has only two free parameters:  $A$  is the amplitude in photons  $\text{s}^{-1} \text{cm}^{-2} \text{keV}^{-1}$  and  $kT$  is the temperature in keV. In the  $\nu F_\nu$  spectrum the peak energy of the black body function is  $\sim 3 kT$ .

These three spectral models are applied in a single; BAND or COMP or in a hybrid; BAND+BB (BANDBB) or COMP+BB (COMPBB), form to the GRB spectra at different stages of our analysis.

### 3.1.3 Castor Statistics

The parameters of the applied photon models are determined by using Castor C-Statistics (CSTAT), which is a likelihood technique with a slightly different parametrization than the widely used  $\chi^2$  statistics (Cash 1979). Application of CSTAT is as easy as  $\chi^2$  minimization method and importantly, in the low count regime it gives much tighter error intervals for model parameters than  $\chi^2$  statistics. In the high count (Gaussian) regime, the two statistics are the same. So, it is more appropriate to use CSTAT method especially for time-resolved analysis where we may have counts of a few tens only. However, this technique does not give a direct measurement for goodness of fits, i.e., cannot be used for model comparison. In order to overcome this problem we performed extensive spectral simulations as described in Section 3.2.1.

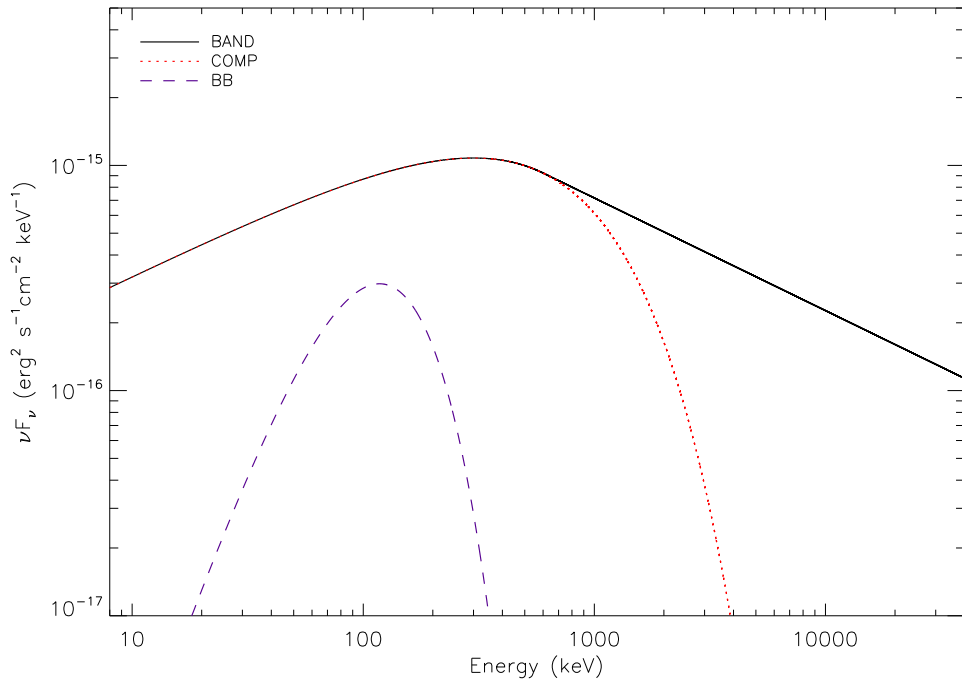


Figure 3.1: The spectral shapes of the COMP ( $\alpha = -1.5$  and  $E_{\text{peak}} = 300 \text{ keV}$ ), BAND ( $\alpha = -1.5$ ,  $E_{\text{peak}} = 300 \text{ keV}$ , and  $\beta = -2.5$ ), and BB ( $kT = 30 \text{ keV}$ ) models in  $\nu F_\nu$  representation.

### 3.1.4 Primary Candidate Bursts Selection

An underlying thermal component in the spectrum possibly affects the low energy power law index of the non-thermal model  $\alpha$ , e.g. makes it larger/harder. As mentioned in § 1.5, the synchrotron emission of fast cooling electrons in a decaying magnetic field can have a maximum  $\alpha = -0.8$  (Uhm & Zhang, 2014). We made use of this potential hard alpha signature. As presented in § 3.1.2, COMP model is similar to BAND with very steep  $\beta$ . For fine time bins there may not be enough counts above the peak of the spectrum to constrain the high energy spectral index  $\beta$  well. Also, since we are interested in low-energy index, we preferred to use COMP instead of BAND for time-resolved analysis here.

The time resolved spectra of each of the 448 GRBs are fit with COMP model. The selection of our primary candidate sample is based on error-weighted means of the model parameters, i.e.,  $\alpha$  and  $E_{\text{peak}}$ . We identified the bursts which have  ${}^1\bar{\alpha}_w \geq -0.8$ , and  $\bar{E}_{\text{peak,w}} \geq 400$  keV for at least two consecutive bins throughout the prompt phase. There are two reasons for selecting bursts with relatively high  $E_{\text{peak}}$ . First is to have enough photons below  $E_{\text{peak}}$  to constrain the  $\alpha$  well. Second, it has been observed that the temperature of thermal component is at most  $\sim 100$  keV (Ryde 2004 & 2005), this corresponds to a peak energy of  $\nu F_\nu$  spectrum  $\sim 300$  keV, and if the thermal and non-thermal peaks are well-separated it is robust to identify thermal component by statistical means. Otherwise, if the thermal component is embedded in the non-thermal one, the thermal emission has to be strong enough to be able seen on top of the non-thermal emission (which is very unlikely for magnetically dominated flows Hascoët et al. 2013). At the end, 268 and 60 bursts passed  $\alpha$  and  $E_{\text{peak}}$  selection, respectively. Where, in common there are 51 bursts, and these are the bursts which call as the primary candidate bursts sample.

### 3.1.5 Thermal Candidate GRBs Sample

We then applied four spectral models to these 51 primary candidates' time integrated spectrum: single (nonthermal) models; COMP and BAND, and hybrid

---


$${}^1\bar{\alpha}_w = \frac{\sum_{j=i}^{i+1, i+2, \dots} \frac{\alpha(j)/\alpha_{\text{err}}(j)^2}{1/\alpha_{\text{err}}(j)^2}}{\text{number of bins of a given burst}}. \quad \text{The summation can run at most up to total}$$

models; COMPBB and BANDBB. Then, we compare single and hybrid model fit results to identify thermal components. We looked for GRBs which show an improvement of  $\geq 10$  units in CSTAT per additional degree of freedom, i.e., 20 units for COMP & COMPBB and BAND & BANDBB comparisons, and 10 units for BAND & COMPBB comparison. Among 51 bursts in the sample, 11 bursts (including the test burst, GRB 110721A) have shown an improvement at or above our criteria. These bursts are listed in Table 3.1 with several observational properties. In these 11 bursts, the thermal characteristics of the spectrum of four of them have been previously reported in literature: GRB 080916C (Guiriec et al., 2015), GRB 090902B (Ryde et al., 2011), GRB 100724B (Guiriec et al., 2011), GRB 110721A (Axelsson et al., 2012), which are indicated in Table 3.1. The remaining seven bursts, form our thermal candidate GRB sample, will be investigated for the first time. The detailed analysis of the bursts in this sample is described in the following section. We also analyzed GRB 110721A in the same way as thermal candidate bursts to compare with reported results and check the consistency and validity of our analysis method.

Table 3.1: Several basic properties of the bursts in thermal candidate GRBs sample.

GRB Name	GBM trigger name	Trigger time (UT)	$T_{90}^a$ (s)	Redshift	Peak photon flux <sup>b</sup>	Detectors used <sup>c</sup>	Number of time bins <sup>d</sup>	Reference*
080817A	080817161	03:52:10.5	60	....	$17.44 \pm 1.04$	n1, n2, n5, b0	15	
080916C <sup>†</sup>	080916009	00:12:45.6	63	...	$16.40 \pm 1.65$	...	...	1
081215A	081215784	18:48:36.8	6	....	$148.47 \pm 2.13$	n9, n10, b1	23	
090217	090217206	04:56:42.5	33	....	$13.06 \pm 1.05$	n6, n7, n9, b1	7	
090323A	090323002	00:02:42.6	135	$3.57^1$	$14.33 \pm 0.84$	n6, n7, b1	19	
090902B <sup>†</sup>	090902462	11:05:08.3	19	$1.822^2$	$100.37 \pm 1.92$	...	...	2
100414A	100414097	02:20:21.9	26	$1.368^3$	$28.16 \pm 1.05$	n7, n11, b1	21	
100724B <sup>†</sup>	100724029	00:42:05.9	115	....	$27.07 \pm 1.25$	...	...	3
100918A	100918863	20:42:18.0	86	....	$10.94 \pm 0.79$	n8, n11, b1	45	
101123A	101123952	22:51:34.9	104	....	$50.27 \pm 2.43$	n9, n10, b1	42	
110721A	110721200	04:47:43.7	22	$0.382/3.512^4$	$34.32 \pm 1.55$	n6, n7, n9, b1	17	4

<sup>a</sup> Taken from von Kienlin et al. (2014).

<sup>b</sup> in units of photon  $\text{cm}^{-2} \text{s}^{-1}$  and calculated in the 10–1000 keV range with 64-ms resolution.

<sup>c</sup> n is for NaI, and b is for BGO detectors.

<sup>d</sup> with  $\text{SNR} \geq 25$

<sup>†</sup> These bursts were not analyzed in this thesis.

\* 1. Guiriec et al. (2015), 2. Ryde et al. (2011), 3. Guiriec et al. (2011), 4. Axelsson et al. (2012).

<sup>1</sup> Chornock et al. (2009) <sup>2</sup> Cucchiara et al. (2009) <sup>3</sup> Cucchiara & Fox (2010) <sup>4</sup> Berger (2011)

## 3.2 Analysis of Thermal Candidate GRBs

For the detailed analysis of these thermal candidate bursts we also include the data of BGO detectors of Fermi-GBM. Combining the data of NaI and BGO detectors extends the high energy end of the spectrum significantly, up to  $\sim 40$  MeV. As explained in Chapter 2, there are two BGO detectors on opposite sides of the GBM. A burst is usually in the field of view of only one BGO detector, which is used in the analysis. For the chosen BGO detector, the TTE data type is also used and the energy range is selected from  $\sim 200$  keV to  $\sim 40$  MeV (excluding the highest energy channels) for the analysis. Background is modelled in the same way as NaI detectors, and the source interval is selected as to be exactly same as the NaI detectors.

*K-edge issue:* For the NaI detectors, at 33 keV, there appears a systematic feature due to the K-edge in Iodine (see § 2.1), which is affecting the data between  $\sim 30$  to  $\sim 40$  keV. Excluding this energy range does not change the fit model parameters significantly since there is a similar excess in residuals both below and above the model fit (Goldstein et al., 2012). However, the goodness of fits, i.e. CSTAT values are affected. For the reliability of the spectral simulation that we perform in this part of the analysis we excluded the data of NaI detectors between 30 to 40 keV range. Now, we describe the analysis methodology in detail.

### 3.2.1 Time Resolved Analysis

For the time resolved analysis of thermal candidate bursts we increased the signal to noise ratio of each time-bin to at least 25 in order to better constrain the model parameters. As a result, the number of time-bins (listed in Table 3.1) in the time profiles is decreased with respect to the ones used in systematic time-resolved analysis, but it was required because the hybrid models that we apply here has two more free parameters than the single models. The spectrum of each time interval of each burst are fit with the same four models; COMP, BAND, COMPBB, and BANDBB. We have two main objectives for this time-resolved analysis. First; identifying the evolution of thermal and non-thermal components throughout the prompt phase. Second; observing how the additional thermal component effects the

non-thermal model parameters. In order to achieve these we examined the evolution of model parameters and compare non-thermal model parameters ( $\alpha$  and  $E_{\text{peak}}$ ) of single and hybrid models for each GRB in the sample. Furthermore, for all time bins of each burst, we calculated thermal and non-thermal energy flux by using hybrid model fit results for the energy range 8 keV - 40 MeV. We calculated the errors in flux values manually, by propagating errors in model parameters. Here, we ignored covariances.

### 3.2.2 Spectral Simulations

As discussed in § 3.1.3, the use of CSTAT is more appropriate when constraining applied model parameters even in the low-count regime (as might be the case for time-resolved analysis), but it does not give a direct measurement for the goodness of fits. In order to test the statistical significance of the improvement that the additional blackbody component provides, and to check the reliability of the parameters obtained from model fits, we performed Monte Carlo simulations. In an ideal case, the simulations needs to be done for each time bin modelled as described in § 3.2.1, but due to lack resources and time limitation we did the simulations for each pulse structure seen in the time profiles of each GRB. The pulses are identified visually based on the light curve photon counts (with 64 ms resolution) and background levels for each burst in the sample. For cases in which the GRB light curve is very complex, i.e., individual pulses are not easily separable (GRBs 090217, 100414A, 100918A) we simulated the whole source interval spectrum (fluence spectrum).

We fit the spectrum of individual pulses and determine the best single and best hybrid models out of our four spectral models mentioned in § 3.1.2, i.e., COMP or BAND, and COMPBB or BANDBB, respectively. For each pulse and for each detector used in the spectral analysis; a set of 20,000 synthetic spectra is generated for both the best single and hybrid model. The background model of actual pulse (with additional Poisson fluctuations) and the photon model (parameters obtained from single and hybrid models) are taken and folded through the detector response matrix in order to obtain a simulated count rate spectrum. After that, Poisson fluctuations are again added to the total count rate. The duration of each synthetic spectrum is exactly same with the pulse duration. Then, these two sets of spectra

are fit by both the single and hybrid models in the exactly same way the real data analysis are done. The distributions of model parameters and the  $\Delta CSTAT$  (the difference in  $CSTAT$  values of the single and hybrid models) are analyzed.

Now, we give an example that we mostly see in our analysis which is the simulation results for one of the pulses seen in the light curve of one of our thermal candidate burst, GRB090323A. For convenience, we call the single and hybrid models as S and H, respectively. Here, the single model is actually BAND, and hybrid model is BANDBB. The H model has two more free parameters than S model, and the  $CSTAT$  value of H model is less than S model  $CSTAT$  value by 23.8 units. We name the parameters of these models as “real fit results”, and the  $\Delta CSTAT$  as  $\Delta CSTAT_{\text{real}}$  ( $\Delta CSTAT_{\text{real}} = 23.8$ ). One set of 20,000 synthetic spectra is produced by using the real fit results of S, i.e., S as the input photon model, and similarly another set of spectra for H model. Then each set is modelled with S and H models, then the distributions of fit results are compared to the real fit results. Figure 3.2 shows the distribution of S and H model parameters resulting from fitting of synthetic spectra produced by taking H model as the input model. The distributions of parameters obtained from fitting H model to the spectra produced from H model are consistent with real fit results of H model, i.e., the H model is re-constructable. Also, the distributions of parameters obtained from fitting S model to the spectra produced from H model are consistent with real fit results of S model. Figure 3.3 shows the distribution of S and H model parameters resulting from fitting of synthetic spectra produced by taking S model as the input model. The distributions of parameters obtained from fitting S model to the spectra produced from S model are consistent with real fit results of S model, i.e., the S model real fit results are re-constructable. However, the distributions of parameters obtained from fitting H model to the spectra produced from S model are mostly *not* consistent with real fit results of H model. Therefore, in this case we say that the H model is a *better representative of the data* since when it is taken as the true model (i.e. input model) we can obtain consistent results for both S and H model fits, but not the other way around.

In order to determine the level of significance of the improvement in the H model fit over S model (i.e., decrease in  $CSTAT$ ), we check the difference in  $CSTAT$  values

obtained from S and H fits to the set of spectra produced from S model real fit results, and compare with  $\Delta CSTAT_{\text{real}}$ . Figure 3.4 shows the CSTAT difference obtained from BAND and BANDBB fits of synthetic spectra produced by taking S model as the input model. None of the 20,000 spectra showed an improvement greater or equal to  $\Delta CSTAT_{\text{real}} = 23.8$ . So, the probability (p value) of getting an improvement in CSTAT more than or equal to  $\Delta CSTAT_{\text{real}}$  by chance is  $< \frac{1}{20000}$ , then we say the improvement in actual pulse spectrum provided by additional blackbody component is statistically significant, i.e., it is not due to statistical fluctuations. The p values obtained from simulations of other bursts are not always as low as for the case of GRB090323A. We say that for a spectrum the BB component is statistically significant if the corresponding p value is  $< 0.0027$  (*or*  $< 0.27\%$ ). This means  $\Delta CSTAT_{\text{real}}$  is lying out of  $3\sigma$  range of the mean of the  $\Delta CSTAT$  distribution of the synthetic spectra. If the BB component is significant in a pulse, we conclude that the BB component found in the time-resolved analysis within the pulse is statistically significant.

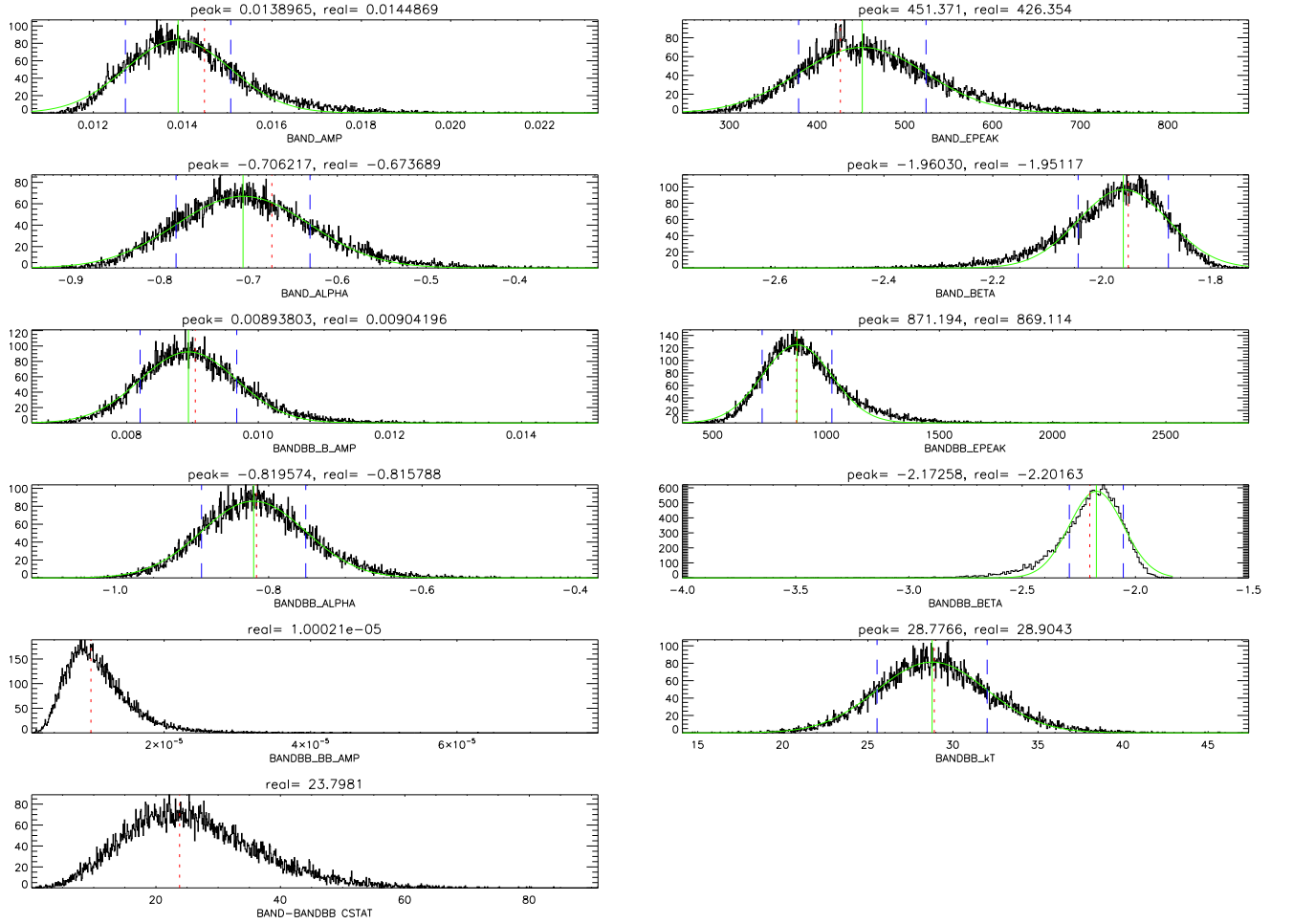


Figure 3.2: The parameter distributions of single (BAND) and hybrid (BANDBB) models resulting from fitting of synthetic spectra produced with BANDBB hybrid model parameters for GRB 090323A. The red dashed lines indicate the real-fit parameters. The green curves are Gaussian fits to distribution of parameters and the peak values are shown by green solid lines. The blue-long dashed lines are showing the  $1\sigma$  error intervals.

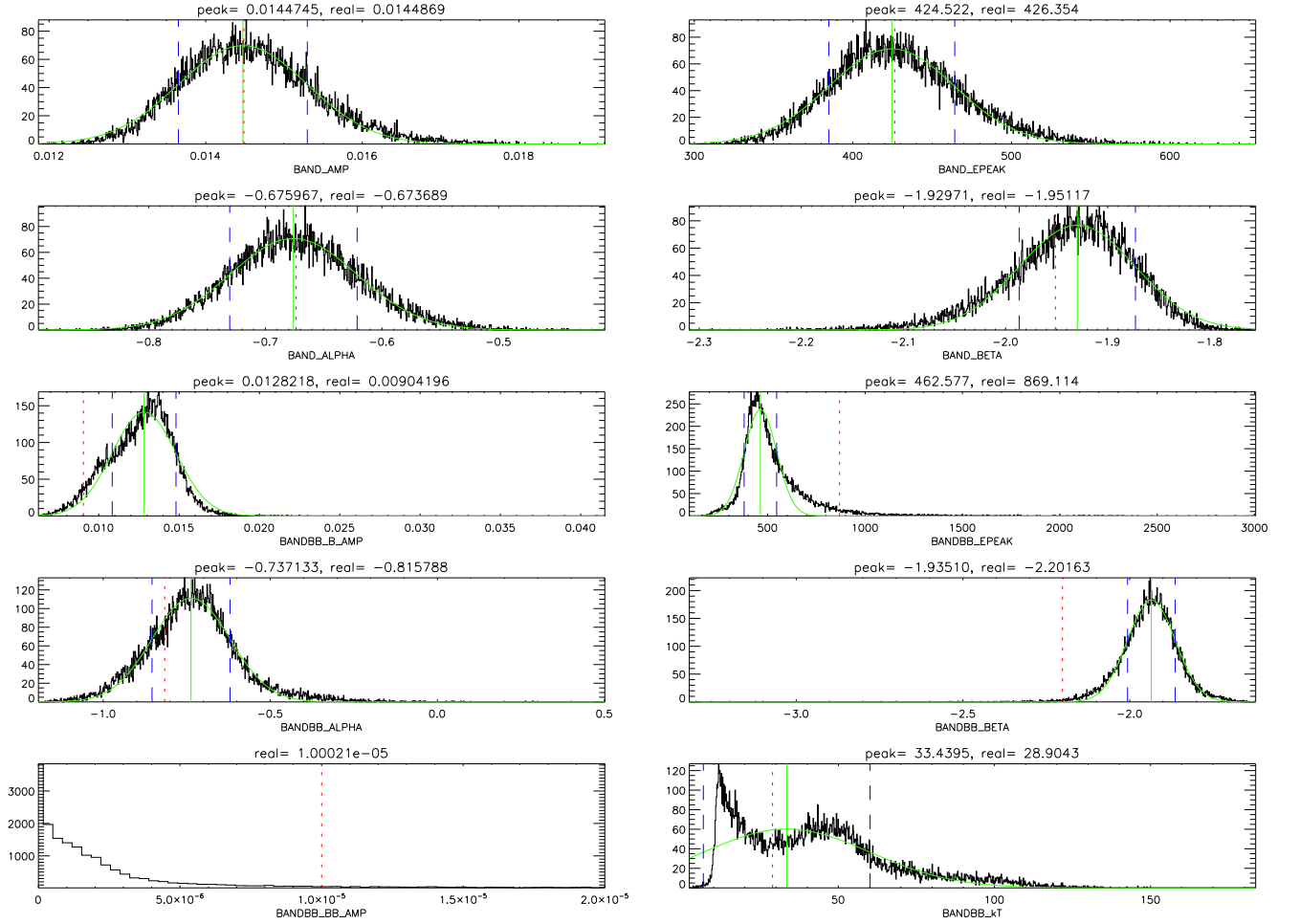


Figure 3.3: The parameter distributions of single (BAND) and hybrid (BANDBB) models resulting from fitting of synthetic spectra produced with single BAND model parameters for GRB 090323A. The red dashed lines indicate the real-fit parameters. The green curves are Gaussian fits to distribution of parameters and the peak values are shown by green solid lines. The blue long-dashed lines are showing the  $1\sigma$  error intervals.

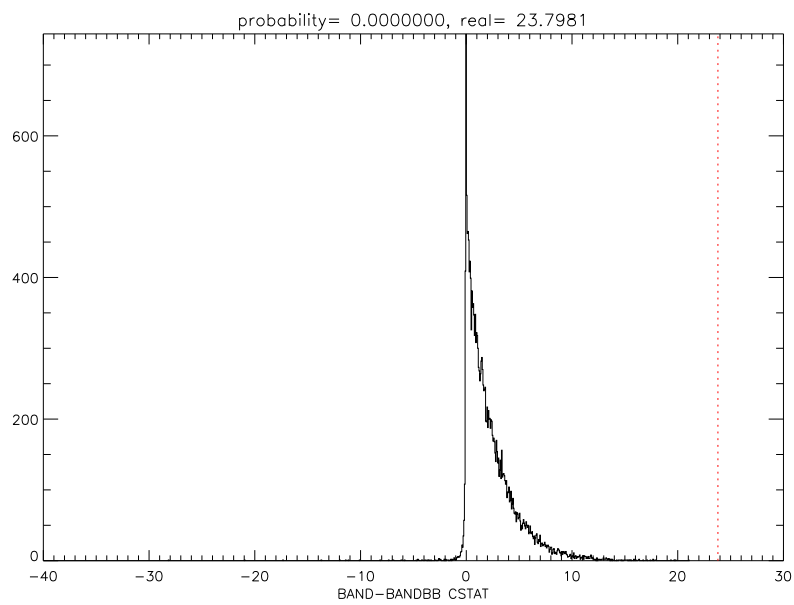


Figure 3.4: The distribution of CSTAT difference obtained from single (BAND) and hybrid (BANDBB) model fits of synthetic spectra produced with single BAND model parameters for GRB 090323A. The red dashed line indicates the real-fit CSTAT improvement obtained by BANDBB model fit over BAND-only model.

## Chapter 4

# RESULTS

We analyzed the seven bursts in our thermal candidate GRB sample as described in § 3.2. Spectral simulation results revealed that there is a statistically significant BB signature in the integrated spectra of six of the bursts. Here, we present the results of the time-resolved analysis and spectral simulation for each of the seven bursts. We also give the time-resolved analysis results of test burst, GRB 110721A, at the very end.

For most of the time bins of each of the burst BAND-only model parameters are all constrained. However, there are some bins in which  $\beta$  of BAND-only model either has very negative value with unconstrained error interval, or it has only upper limit. For these bins, the other BAND-only model parameters, i.e.,  $\alpha$  and  $E_{\text{peak}}$  are very similar to COMP-only model. For the hybrid model fits; BANDBB model parameters are constrained for a limited number of time bins, whereas the COMPBB model parameters are constrained for most of the bins. However, for some cases we needed to combine several bins in order to obtain constrained COMPBB model parameters, as indicated below for each burst. In summary, in fit results table of each of the seven burst, we present BAND-only and COMPBB model fit results for the all defined time bins. In addition, we present BANDBB model fit results for the bins in which its parameters are well constrained. In order to see how the non-thermal component in the spectrum is affected by the presence of thermal component, we plotted  $\alpha$  and  $E_{\text{peak}}$  parameters of both BAND-only and COMPBB models as a function of time. We also plotted the kT of COMPBB model to see how the thermal component evolves. For the energy flux calculations we used COMPBB model fit results. While calculating energy flux ratio of thermal to non-thermal we

ignored the errors.

## 4.1 GRB 080817A

GRB 080817A was detected by Fermi-GBM on 17 August 2008 at 03:52:10.5 UT (Bissaldi et al., 2008). It is a long burst with duration  $T_{90} \sim 60$  s and peak flux  $(17.44 \pm 1.04)$  photon  $\text{cm}^{-2} \text{s}^{-1}$  in the energy range 10 – 1000 keV. Figure 4.1 shows the count rate history of the burst as seen by the brightest GBM detector, NaI5. Figure 4.1 also shows the time intervals of the pulses that are used for spectral simulations. The detectors, NaI1, NaI2, NaI5, and BGO0 are used for the spectral analysis.

### 4.1.1 Parameter Evolutions

The prompt emission phase is divided into 15 time intervals with  $\text{SNR} \geq 25$  as seen in Figure 4.2. For each time bin the time intervals and the fit results of all relevant models are listed in Table 4.1. In almost all time bins high energy power law index  $\beta$  of BAND model is constrained, whereas the  $\beta$  of the BANDBB model could be constrained only in 2 of them. For the 9th bin the blackbody parameters of COMPBB model could not be constrained, then we combined this bin with the consecutive, 10th bin.

Figure 4.2 shows the evolution of BAND and COMPBB model parameters. The peak energies are mostly between 500 - 1000 keV. The  $E_{\text{peak}}$  of COMPBB model fits are higher than BAND-only fits, especially for the bins 3, 5, 9&10, and 15. The spectral low energy index  $\alpha$  is variable for the BAND-only fits, taking values between  $-0.4$  to  $-1.2$ , whereas for the COMPBB hybrid model  $\alpha$  values have relatively low values and are clustered at around  $\sim -1$ , especially during first  $\sim 25$  s. The kT is ranging between  $\sim 10$  - 100 keV, and does not seem to have a particular trend. During the first pulse kT is almost constant around 50 keV, and then decreases for the plateau phase around 8 s. Afterwards, it shows an increase at the beginning of the second pulse and after decreases again.

#### 4.1.1.1 Flux Evolutions

Figure 4.3 top and middle panels are showing the evolution of energy flux for non-thermal and thermal components of COMPBB model. Non-thermal energy flux is following photon flux and thermal flux seems to be decreasing overall, however the errors in BB energy flux are relatively high to conclude a definite trend. The bottom panel of Figure 4.3 shows the ratio of the thermal energy flux to total energy flux, which is always less than 10%. Thermal to total flux ratio is relatively high for the bins 3, 4, 5, 6, and 8, and these are the bins in which  $\alpha$  of non-thermal component is significantly lowered when thermal component is included in fits. The thermal to total energy flux ratio is ranging between  $\sim 1\%$  and  $\sim 9\%$  throughout the burst with an average ratio of  $\sim 5\%$ .

Figure 4.4 shows the  $\nu F_\nu$  spectrum of BAND and COMPBB models with photon counts and residuals, for the time interval 7.94 - 12.16 s, including time bins 5 and 6. When BB is included in fits, the  $E_{\text{peak}}$  of non-thermal component is shifted from  $\sim 220$  keV to  $\sim 670$  keV, and  $\alpha$  is lowered from  $\sim -0.6$  to  $\sim -1$ . The peak of the BB is  $\sim 90$  keV. It is clear that when the spectrum is modelled with a BAND-only model,  $E_{\text{peak}}$  is in between thermal and non-thermal peak energies of COMPBB model, with a relatively high  $\alpha$ . Figure 4.5 shows the evolution of BAND and COMPBB models in  $\nu F_\nu$  representation for GRB 080817A.

#### 4.1.2 Pulse Simulations

We performed spectral simulations for the two pulse structures in the light curve as described in § 3.2.2. We selected the time intervals of 1st and 2nd pulses as;  $-3.20 - 9.408$  s and  $9.408 - 71.04$  s as shown in Figure 4.1. The spectrum of each pulse has enough emission above  $E_{\text{peak}}$  to be able to constrain the high energy power law index  $\beta$  of the BAND model, with and without BB component. Therefore, the simulations are performed with BAND and BANDBB models. The additional BB model improved the BAND-only fits by  $\Delta CSTAT_{\text{real}} = 6.5$  and  $\Delta CSTAT_{\text{real}} = 15.4$  units for the 1st and 2nd pulses, respectively.

The distributions of fit model parameters of both sets of synthetic spectra showed that; for both pulses *BANDBB model is a better representative of the data* than BAND only model, i.e., the fit results of the synthetic spectra produced with

BANDBB model parameters are consistent with real fit results of both BAND and BANDBB models. The probabilities of getting an improvement of  $\geq \Delta CSTAT_{\text{real}}$  in synthetic spectra of individual pulses by chance are; 3.5% and 0.16%, respectively. Here, we find that the BB component is statistically significant for the second pulse. For the first pulse, the improvement in CSTAT is relatively low, i.e.,  $\Delta CSTAT_{\text{real}} = 6.5$ . However, as can be seen in Table 4.1, for the 5th and 6th bins (where we have significant lowering in  $\alpha$ ), there is a CSTAT improvement of 10 and 8 units, respectively, and the improvement is even higher (18 units) when we combine these two bins. So, we conclude that for the whole first pulse the level of CSTAT improvement does not let us to confirm the thermal component statistically significantly. However, based on the parameter recovery of the simulations, the spectrum is better represented with a hybrid model, i.e., double hump structure, and there are time intervals in which we have significant improvement when thermal component is included in fits.

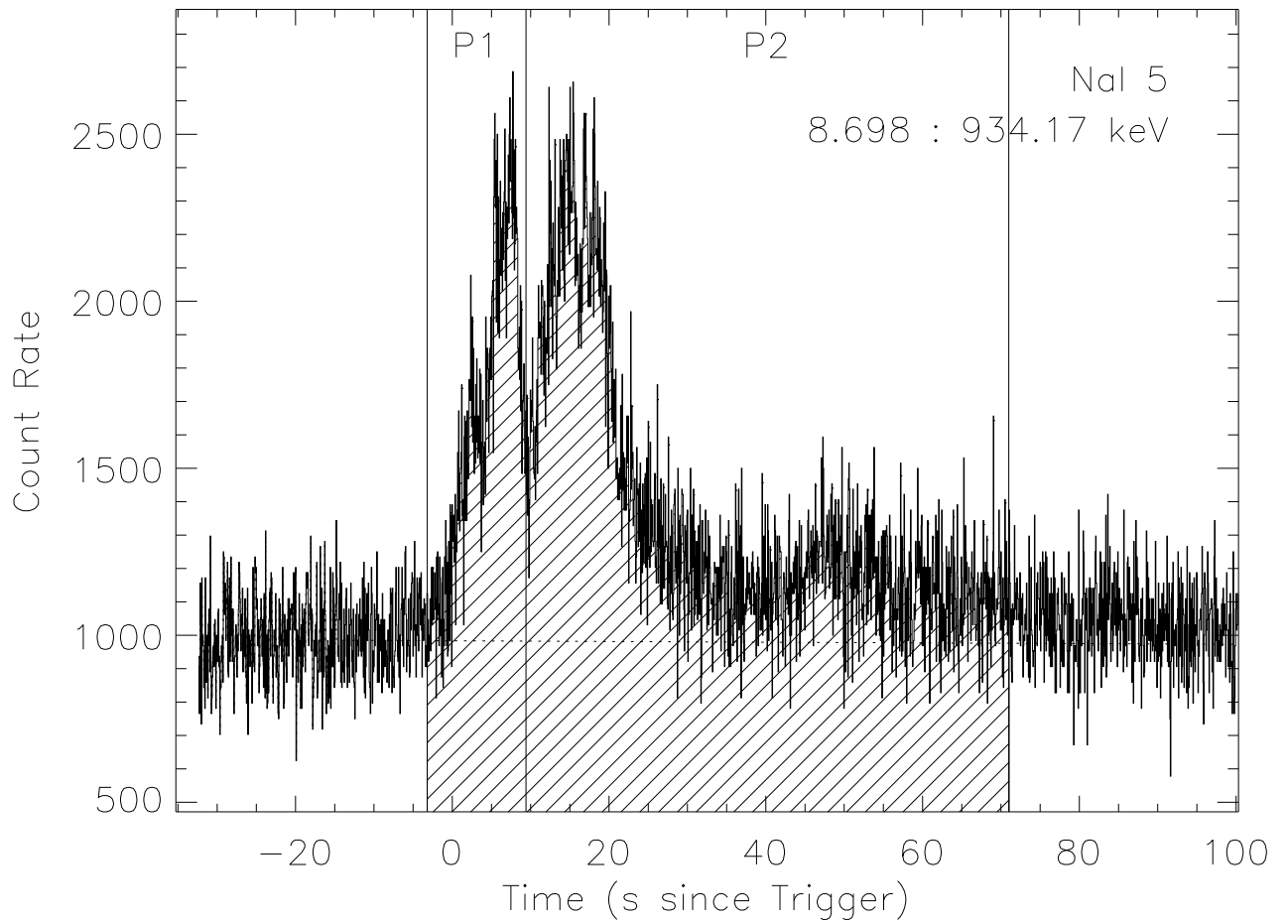


Figure 4.1: The light curve of GRB 080817A with 64 ms resolution. The solid vertical lines define the pulse intervals as used in pulse simulations. First and second pulses are indicated as P1 and P2, respectively.

Table 4.1: Fine time interval fit results for GRB 080817A. Best parameter values with their  $1\sigma$  uncertainties.

Bin number	Time interval since trigger		Model	$E_{\text{peak}}$ (keV)	$\alpha$	$\beta$	$kT$ (keV)	Cstat/dof
	$T_{\text{start}}(s)$	$T_{\text{stop}}(s)$						
1	-0.32	3.84	BAND	$529_{-56}^{+66}$	$-0.70 \pm 0.06$	$-2.46_{-0.81}^{+0.25}$	...	587/464
			COMPBB	$605_{-187}^{+98}$	$-0.69_{-0.29}^{+0.11}$	...	$23_{-9}^{+80}$	587/463
			BANDBB	$571_{-226}^{+108}$	$-0.68_{-0.30}^{+0.12}$	$-2.52_{-1.04}^{+0.29}$	$23_{-10}^{+81}$	586/462
2	3.84	5.70	BAND	$609_{-70}^{+84}$	$-0.80_{-0.05}^{+0.06}$	$-2.61_{-1.49}^{+0.32}$	...	492/464
			COMPBB	$798_{-84}^{+99}$	$-0.89(\text{fixed})$	...	$47_{-14}^{+25}$	492/463
3	5.70	6.91	BAND	$469_{-64}^{+76}$	$-0.77 \pm 0.07$	$-2.08_{-0.16}^{+0.12}$	...	514/464
			COMPBB	$1594_{-401}^{+539}$	$-1.09_{-0.07}^{+0.06}$	...	$46 \pm 7$	515/463
			BANDBB	$780_{-268}^{+865}$	$-0.94_{-0.17}^{+0.14}$	$-2.20_{-0.70}^{+0.18}$	$40_{-34}^{+11}$	512/462
4	6.91	7.94	BAND	$464_{-47}^{+50}$	$-0.74 \pm 0.06$	$-2.38_{-0.28}^{+0.19}$	...	523/464
			COMPBB	$736_{-438}^{+305}$	$-0.93_{-0.12}^{+0.14}$	...	$50_{-18}^{+14}$	526/463
5	7.94	9.86	BAND	$225_{-43}^{+67}$	$-0.61_{-0.15}^{+0.16}$	$-1.87_{-0.13}^{+0.08}$	...	476/464
			COMPBB	$802_{-166}^{+280}$	$-0.10 \pm 0.08$	...	$26 \pm 3$	466/463
6	9.86	12.16	BAND	$220_{-30}^{+46}$	$-0.57 \pm 0.12$	$-2.01_{-0.16}^{+0.09}$	...	510/464
			COMPBB	$572_{-452}^{+147}$	$-0.95 \pm 0.09$	...	$28 \pm 4$	501/463
5+6	7.94	12.16	BAND	$222_{-26}^{+35}$	$-0.59_{-0.09}^{+0.10}$	$-1.94_{-0.09}^{+0.06}$	...	532/464
			COMPBB	$664_{-92}^{+126}$	$-0.97 \pm 0.06$	...	$27 \pm 2$	514/463
7	12.16	13.57	BAND	$553_{-84}^{+95}$	$-0.87 \pm 0.06$	$-2.08_{-0.18}^{+0.13}$	...	485/464
			COMPBB	$702_{-76}^{+94}$	$-0.90(\text{fixed})$	...	$21_{-10}^{+21}$	496/463
8	13.57	14.66	BAND	$567_{-53}^{+66}$	$-0.80 \pm 0.05$	$-3.62_{-Inf}^{+0.95}$	...	522/464
			COMPBB	$843_{-166}^{+230}$	$-0.97_{-0.08}^{+0.09}$	...	$51 \pm 9$	517/463
9	14.66	15.68	BAND	$444_{-58}^{+68}$	$-0.81_{-0.06}^{+0.07}$	$-2.06_{-0.15}^{+0.11}$	...	493/464
10	15.68	16.96	BAND	$371_{-56}^{+72}$	$-0.88 \pm 0.07$	$-2.01_{-0.17}^{+0.11}$	...	509/464
			COMPBB	$1808_{-1010}^{+818}$	$-1.24_{-0.06}^{+0.15}$	...	$39_{-5}^{+6}$	513/463
9+10	14.66	16.96	BAND	$412_{-43}^{+51}$	$-0.85 \pm 0.05$	$-2.04_{-0.11}^{+0.08}$	...	494/464
			COMPBB	$727_{-130}^{+2000}$	$-1.01_{-0.28}^{+0.08}$	...	$34_{-8}^{+14}$	512/463
11	16.96	18.18	BAND	$436_{-50}^{+59}$	$-0.87 \pm 0.06$	$-2.62_{-1.54}^{+0.33}$	...	523/464
			COMPBB	$575_{-55}^{+67}$	$-0.96(\text{fixed})$	...	$33_{-8}^{+12}$	522/463
12	18.18	19.52	BAND	$406_{-62}^{+69}$	$-0.89_{-0.06}^{+0.07}$	$-2.11_{-0.22}^{+0.15}$	...	478/464
			COMPBB	$655_{-134}^{+320}$	$-1.00_{-0.11}^{+0.10}$	...	$27_{-8}^{+10}$	482/463

13	19.52	23.10	BAND	$502^{+73}_{-75}$	$-1.10^{+0.05}_{-0.04}$	$-6.02 \pm Inf$	...	523/464
			COMPBB	$706^{+250}_{-165}$	$-1.19 \pm 0.07$	...	$29 \pm 7$	519/463
14	23.10	38.27	BAND	$162^{+58}_{-44}$	$-0.97^{+0.20}_{-0.14}$	$-1.89^{+0.10}_{-0.17}$	...	645/464
			COMPBB	$452^{+198}_{-385}$	$-1.25^{+0.10}_{-0.09}$	...	$19^{+6}_{-4}$	645/463
15	38.27	55.04	BAND	$209^{+108}_{-76}$	$-1.06^{+0.21}_{-0.13}$	$-1.79^{+0.08}_{-0.12}$	...	635/464
			COMPBB	$2183^{+2160}_{-1170}$	$-1.39^{+0.07}_{-0.06}$	...	$23^{+5}_{-4}$	634/463

---

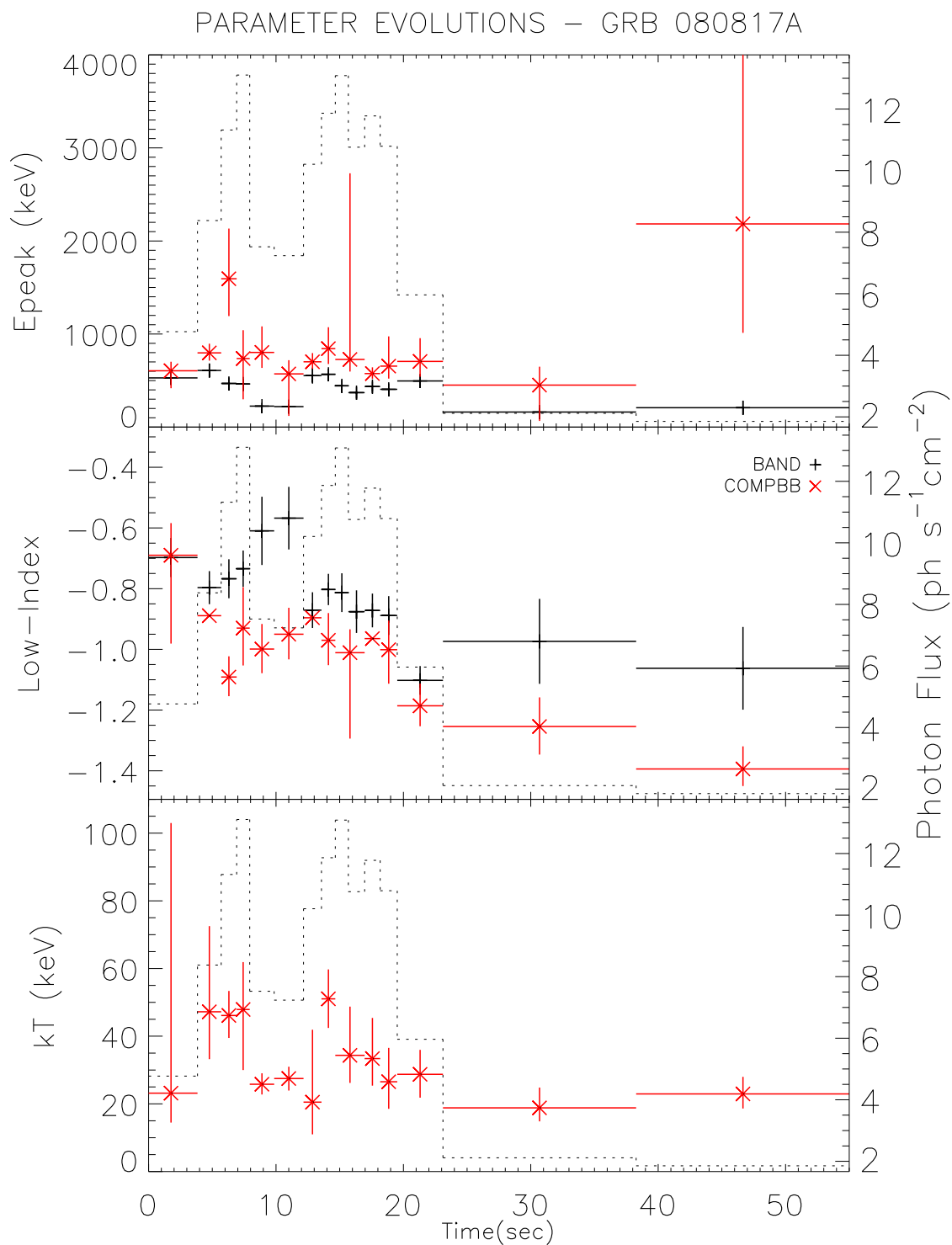


Figure 4.2: The evolution of BAND and COMPBB model parameters for GRB 080817A. The dashed histograms represents the photon fluxes for each time interval (right axis).

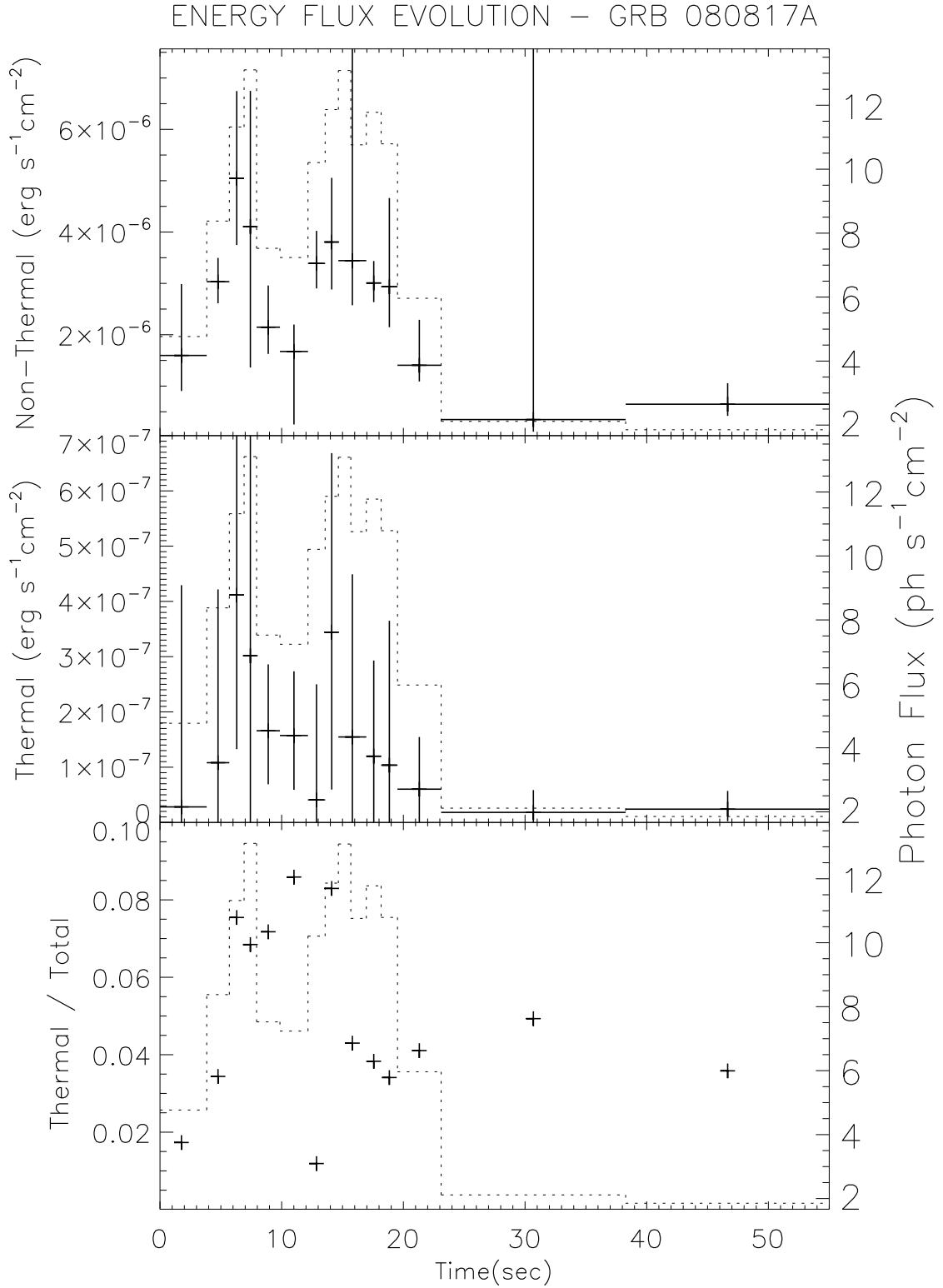


Figure 4.3: The energy flux evolutions of thermal and non-thermal components of COMPBB model for GRB 080817A. The top and middle panels show the energy flux evolutions of COMP and BB models, respectively. The energy flux ratio of thermal to total is seen in the bottom panel. The fluxes are calculated for the energy range 8 keV to 40 MeV. Errors in flux ratio of thermal to total are ignored. The dashed histograms represents the photon fluxes for each time interval (right axis).

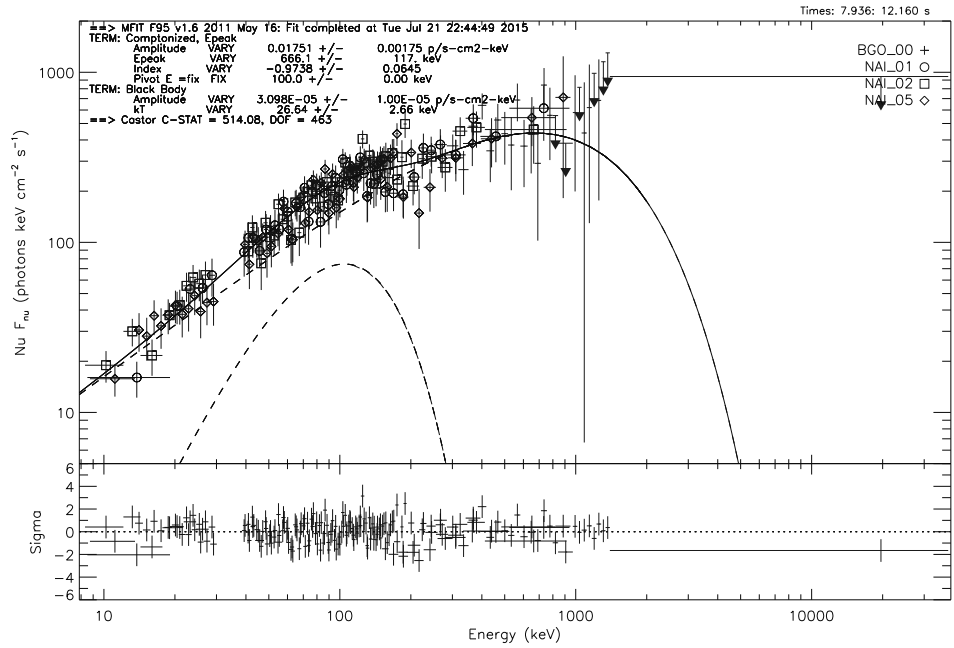
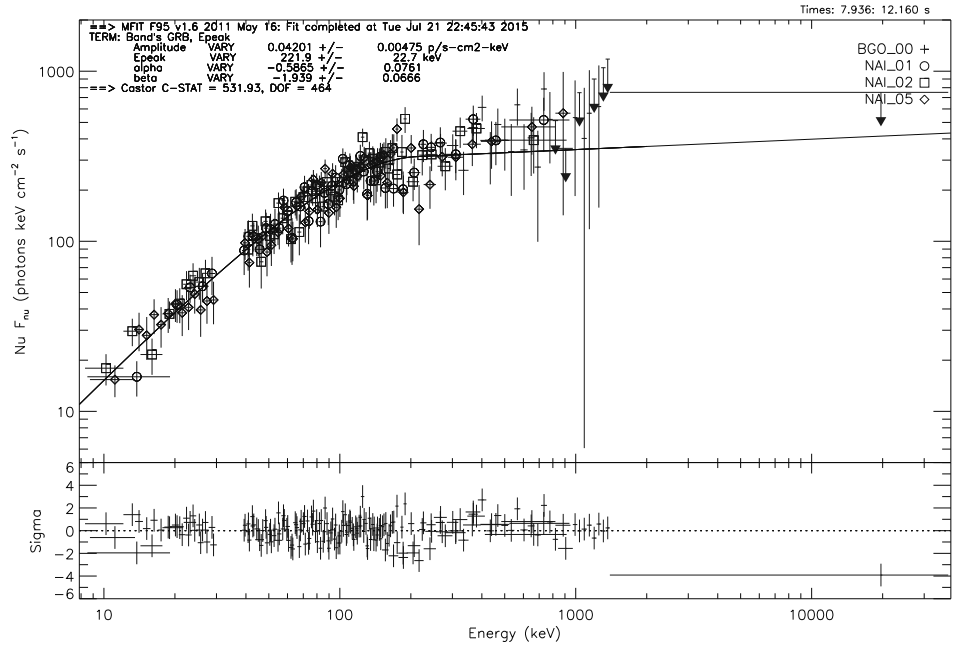


Figure 4.4: The  $\nu F_\nu$  spectrum of BAND and COMPBB models with photon counts and residuals, for the time interval 7.94 - 12.16 s of GRB 080817A, including time bins 5 and 6.

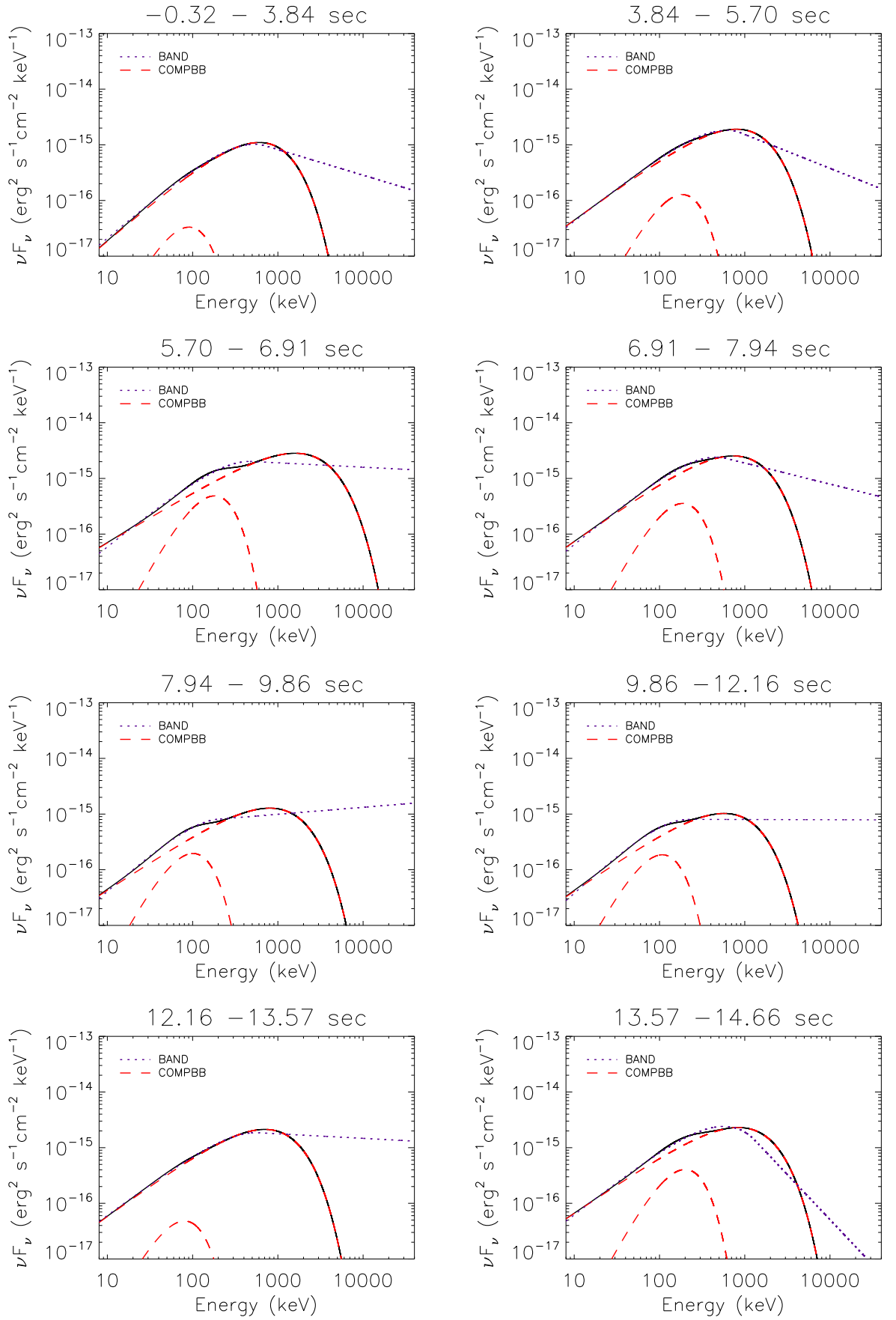


Figure 4.5: The model evolutions for GRB 080817A in  $\nu F_\nu$  representation. The solid line represents the COMPBB model where the dashed lines show the COMP and BB components separately. The dotted line is denoting the BAND model.

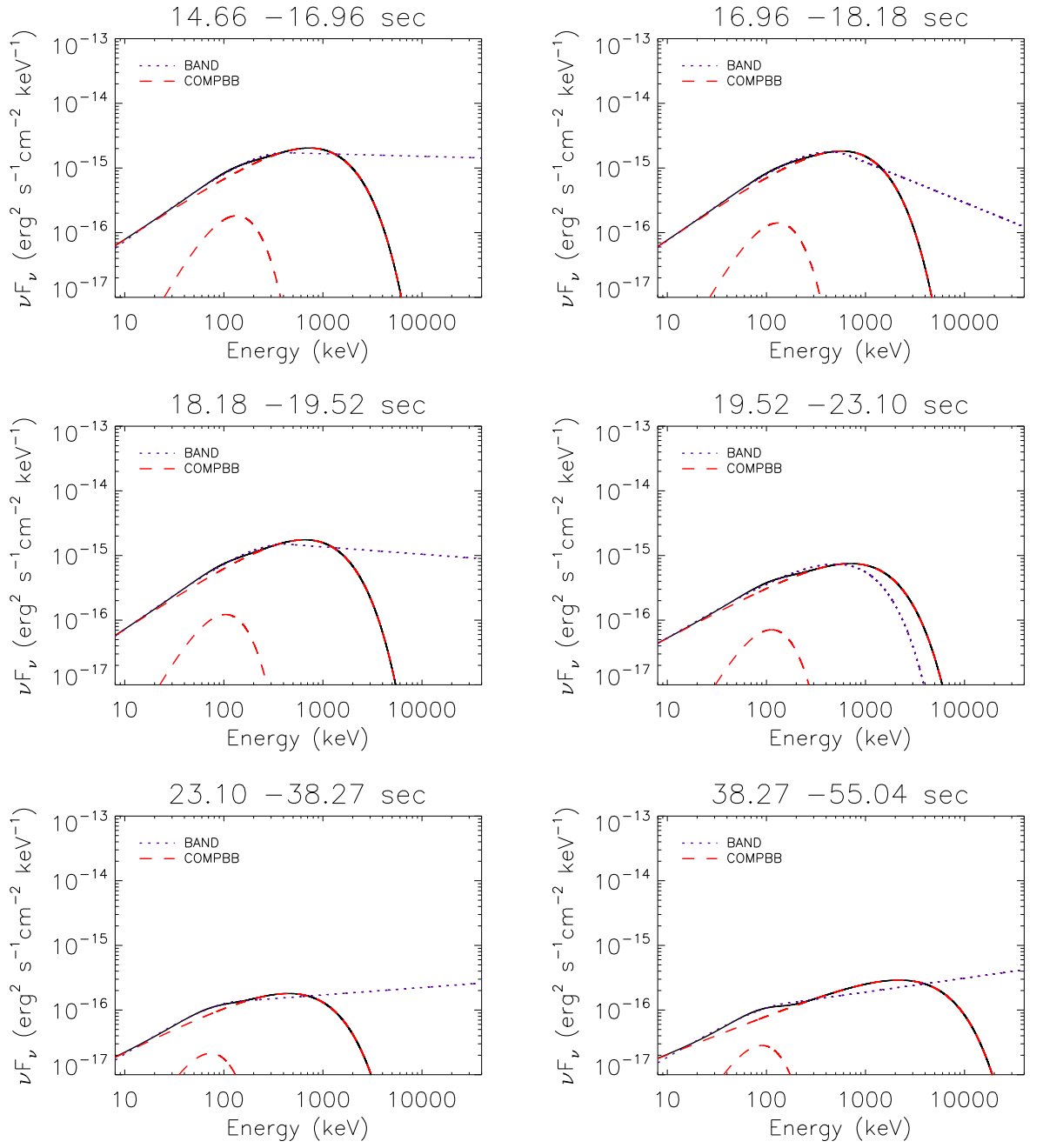


Figure 4.5 Continued.

## 4.2 GRB 081215A

GRB 081215A was detected by Fermi-GBM on 15 December 2008 at 18:48:36.8 UT (Preece, 2008). It is a long burst with duration  $T_{90} \sim 6$  s and peak flux  $(148.47 \pm 2.13)$  photon  $\text{cm}^{-2} \text{s}^{-1}$  in the energy range 10 – 1000 keV. Figure 4.6 shows the count rate history of the burst as seen by the brightest GBM detector NaI10. Figure 4.6 also shows the time intervals of the pulses that are used for spectral simulations. Also, McEnergy (2008) reported detection of more than 100 photon counts with energies less than 200 MeV by Large Area Telescope (LAT) on board FERMI, simultaneously with the first peak seen in Figure 4.6. The detectors, NaI9, NaI10, and BGO1 are used for the spectral analysis.

### 4.2.1 Parameter Evolutions

The prompt phase is divided into 23 time intervals as seen in Figure 4.7. For each time bin the time intervals and the fit results of all relevant models are listed in Table 4.2. In most of the time bins high energy power law index  $\beta$  of BAND model is constrained, whereas the  $\beta$  of the BANDBB model could be constrained only in 8 of them.

Figure 4.7 shows the evolution of BAND and COMPBB model parameters. The peak energy of the spectrum is between a few hundreds to  $\sim 2500$  keV throughout the burst.  $E_{\text{peak}}$  shifts to higher energies when the BB model is added, especially during the 1st pulse. Within the same pulse  $\alpha$  is  $\sim -0.3$  for BAND-only. When the BB model is added the  $\alpha$  values of COMP model are clustered at  $\sim -0.8$ . For the rest of the burst COMPBB  $\alpha$  has large errors but mostly consistent with BAND-only  $\alpha$ . The temperature  $kT$  is  $\sim 120$  keV for the initial few seconds then decays, and shows sudden increases simultaneously with the peaks of the 2nd and 3rd pulses.

#### 4.2.1.1 Flux Evolutions

Figure 4.8 top two panels are showing the evolution of energy flux for thermal and non-thermal components of COMPBB model. Non-thermal energy flux is following the photon flux history of the burst. Thermal energy flux mostly has relatively large errors to conclude a definite trend. For the peak bins of the 1st pulse both the

COMP and BB energy fluxes are the strongest among all, and these are the time bins in which  $\alpha$  is significantly shifted to lower values and  $E_{\text{peak}}$  to higher energies when BB model is included in fits. The bottom panel shows the energy flux ratio of thermal to total, and it is ranging from  $\sim 4\%$  to  $\sim 21\%$  throughout the burst with an average ratio of  $\sim 9\%$ .

Figure 4.9 shows the  $\nu F_\nu$  spectrum of BAND and COMPBB models with photon counts and residuals, for the time interval 1.41 - 1.47 s, time bin 3. When BB is included in fits, the  $E_{\text{peak}}$  of non-thermal component is shifted from  $\sim 990$  keV to  $\sim 2150$  keV, and  $\alpha$  is lowered from  $\sim -0.4$  to  $\sim -0.8$ . The peak of the BB is  $\sim 400$  keV. It is seen that when the spectrum is modelled with a BAND-only model,  $E_{\text{peak}}$  is in between thermal and non-thermal peak energies of COMPBB model, with a relatively high  $\alpha$ .

Figure 4.10 shows the evolution of BAND and COMPBB models in  $\nu F_\nu$  representation throughout the burst. For most of the time bins the thermal component is embedded in non-thermal component of COMPBB model. Only for several initial bins during the first pulse the peak of the BB component is seen above the COMP model left shoulder, and these are the bins where the low energy spectral index  $\alpha$  is shifted significantly to lower values and the  $E_{\text{peak}}$  values are shifted to higher values, as mentioned. Another interesting point is that the peak of the BAND only model is in between thermal and non-thermal peaks of the COMPBB model if BB component is relatively strong. If not, the BAND only model mimics the COMP component of COMPBB model.

#### 4.2.2 Pulse Simulations

We selected the time intervals of 1st, 2nd, and 3rd pulses as;  $-0.064 - 2.752$  s,  $2.752 - 4.352$  s,  $4.352 - 9.664$  s, respectively, as shown in Figure 4.6. The spectrum of each of these pulses has enough emission above  $E_{\text{peak}}$  to be able to constrain the high energy power law index  $\beta$  of the BAND model, with and without BB component. Therefore, the simulations are performed with BAND and BANDBB models. The additional BB model improved the BAND-only fits by  $\Delta CSTAT_{\text{real}} = 4.9, 14.7,$  and 6 units for 1st, 2nd, and 3rd pulses, respectively.

The distributions of fit model parameters of both sets of synthetic spectra showed

that; for all three pulses *BANDBB model is a better representative of the data* than BAND only model, i.e., the fit results of the synthetic spectra produced with BANDBB model parameters are consistent with real fit results of both BAND and BANDBB models. The probabilities of getting an improvement of  $\geq \Delta CSTAT_{\text{real}}$  in synthetic spectra of individual pulses by chance are; 22.6%, 0.075%, 4.8%, respectively. So, the BB component is statistically significant for the second pulse. However, for the 1st and 3rd pulses the chance probabilities are relatively high, especially for the first one. This can be due to the fact that the pulse is a sum of all time bins within, and thus spectral features present in each time-resolved spectrum can be smeared out in the pulse spectrum. It is still possible that the BB components are quite significant in some of the time-resolved spectra. Therefore, we performed spectral simulations with BAND and COMPBB models for the 3rd bin, one of the peak bins of the first pulse, where  $\Delta CSTAT_{\text{real}} = 9$  units (see Table 4.2). We simulate this bin's spectrum in the same way as we did for the pulse simulation, except we produced 5000 spectra instead of 20000. The results showed that the probability of getting an improvement of  $\geq \Delta CSTAT_{\text{real}}$  in synthetic spectra is 0.9% which is significantly lower than the chance probability of the whole 1st pulse, but still not at  $3\sigma$  level. Therefore, we conclude that for the 1st and 3rd pulses (also for the 3rd bin) the level of CSTAT improvement does not let us to confirm the thermal component statistically significantly. However, the spectra is better represented with a hybrid model, i.e., double hump structure.

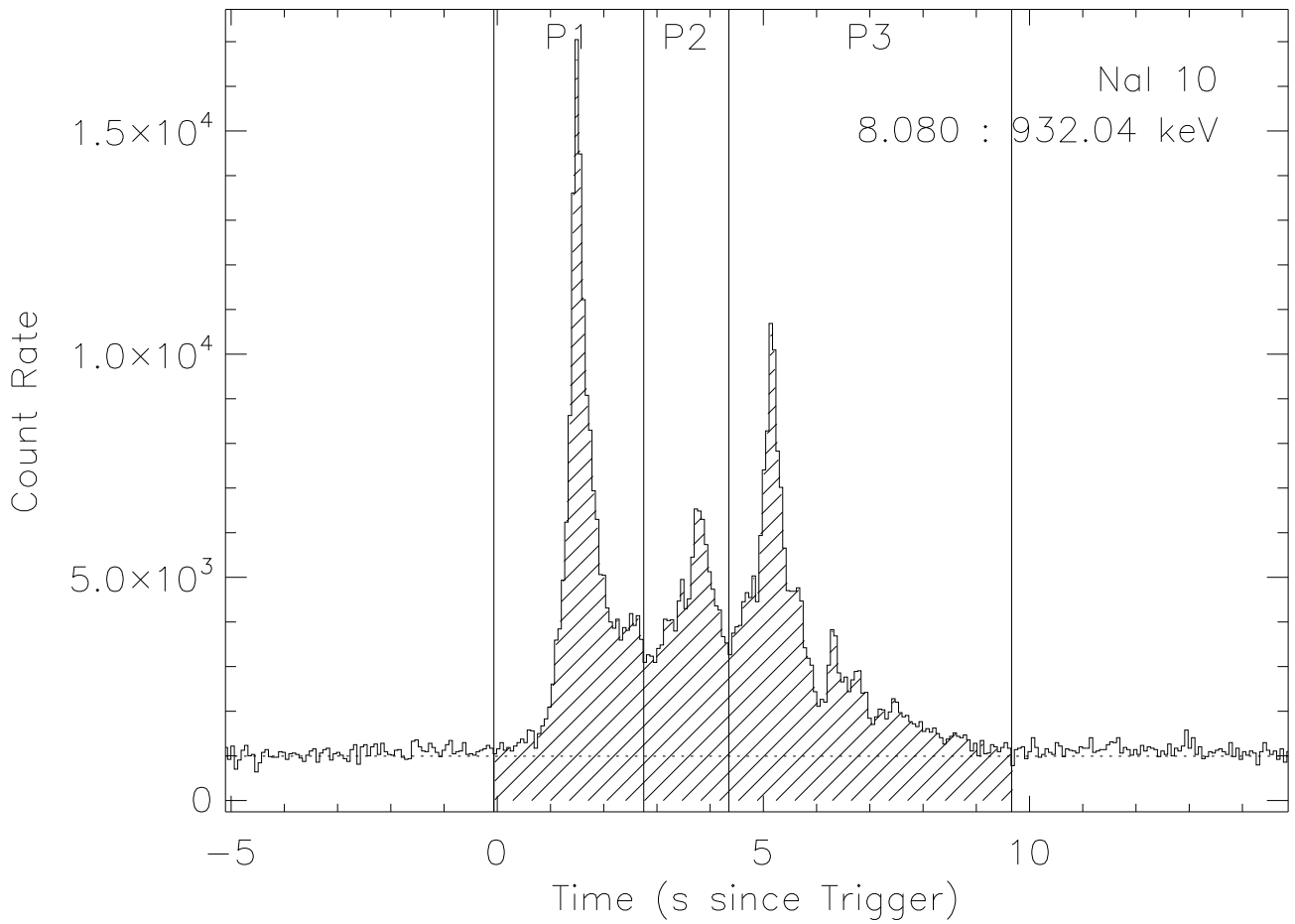


Figure 4.6: The light curve of GRB 081215A with 64 ms resolution. The solid vertical lines define the pulse intervals as used in pulse simulations. First, second, and third pulses are indicated as P1, P2, and P3, respectively.

Table 4.2: Fine time interval fit results for GRB 081215A. Best parameter values with their  $1\sigma$  uncertainties.

Bin number	Time interval since trigger		Model	$E_{\text{peak}}$ (keV)	$\alpha$	$\beta$	$kT$ (keV)	Cstat/dof
	$T_{\text{start}}(s)$	$T_{\text{stop}}(s)$						
1	-0.06	1.34	BAND	$1130 \pm 148$	$-0.70 \pm 0.05$	$-2.61^{+0.33}_{-0.96}$	...	380/358
			COMPBB	$1844 \pm 285$	$-0.91 \pm 0.07$	...	$123 \pm 21$	379/357
2	1.34	1.41	BAND	$1121 \pm 126$	$-0.45 \pm 0.06$	$-2.47 \pm 0.20$	...	398/358
			COMPBB	$2455 \pm 267$	$-0.75 \pm 0.05$	...	$113 \pm 14$	401/357
			BANDBB	$1425 \pm 314$	$-0.54 \pm 0.10$	$-2.60^{+0.84}_{-0.24}$	$88.5 \pm 31$	396/356
3	1.41	1.47	BAND	$988 \pm 82$	$-0.38 \pm 0.05$	$-2.59 \pm 0.18$	...	348/358
			COMPBB	$2144 \pm 233$	$-0.77 \pm 0.06$	...	$127 \pm 11$	339/357
4	1.47	1.54	BAND	$686 \pm 52$	$-0.24 \pm 0.06$	$-2.37 \pm 0.11$	...	362/358
			COMPBB	$1822 \pm 157$	$-0.73 \pm 0.05$	...	$92 \pm 7$	382/357
			BANDBB	$947 \pm 186$	$-0.41 \pm 0.12$	$-2.50 \pm 0.16$	$72 \pm 15$	359/356
5	1.54	1.60	BAND	$696 \pm 64$	$-0.42 \pm 0.06$	$-2.48 \pm 0.16$	...	344/358
			COMPBB	$1887 \pm 232$	$-0.91 \pm 0.06$	...	$99 \pm 7$	347/357
			BANDBB	$1117 \pm 275$	$-0.71 \pm 0.12$	$-2.70 \pm 0.30$	$95 \pm 12$	341/356
6	1.60	1.66	BAND	$483 \pm 52$	$-0.33 \pm 0.09$	$-2.24 \pm 0.12$	...	355/358
			COMPBB	$1132 \pm 169$	$-0.74 \pm 0.08$	...	$62 \pm 7$	372/357
7	1.66	1.79	BAND	$448 \pm 44$	$-0.56 \pm 0.07$	$-2.46 \pm 0.19$	...	362/358
			COMPBB	$672^{+133}_{-93}$	$-0.74 \pm 0.11$	...	$44 \pm 14$	366/357
8	1.79	1.98	BAND	$314 \pm 35$	$-0.44 \pm 0.09$	$-2.20 \pm 0.12$	...	328/358
			COMPBB	$446^{+81}_{-43}$	$-0.55^{+0.14}_{-0.17}$	...	$23^{+20}_{-8}$	341/357
9	1.98	2.37	BAND	$239 \pm 31$	$-0.59 \pm 0.10$	$-2.15^{+0.13}_{-0.13}$	...	438/358
			COMPBB	$454^{+166}_{-63}$	$-0.77^{+0.15}_{-0.22}$	...	$18^{+11}_{-4}$	440/357
			BANDBB	$224 \pm 43$	$+0.2 \pm 0.8$	$-2.17 \pm 0.1$	$11 \pm 1$	431/356
10	2.37	2.75	BAND	$314 \pm 45$	$-0.77 \pm 0.08$	$-2.20^{+0.17}_{-0.17}$	...	362/358
			COMPBB	$448 \pm 49$	$-0.72 \pm 0.13$	...	$14 \pm 2$	363/357
			BANDBB	$311 \pm 56$	$-0.37 \pm 0.34$	$-2.23 \pm 0.18$	$11 \pm 2$	354/356
11	2.75	3.26	BAND	$298 \pm 38$	$-0.82 \pm 0.08$	$-2.46^{+0.31}_{-0.62}$	...	417/358
			COMPBB	$390 \pm 46$	$-0.80 \pm 0.12$	...	$15 \pm 3$	412/357
12	3.26	3.58	BAND	$346 \pm 32$	$-0.62 \pm 0.07$	$-3.11^{+0.40}_{-5.0}$	...	412/358
			COMPBB	$361 \pm 27$	$-0.33 \pm 0.22$	...	$13 \pm 2$	406/357
13	3.58	3.84	BAND	$474 \pm 35$	$-0.56 \pm 0.06$	$-3.36^{+0.48}_{-Inf}$	...	334/358
			COMPBB	$549^{+40}_{-37}$	$-0.68(\text{fixed})$	...	$60^{+20}_{-15}$	334/357

14	3.84	4.03	BAND	283 ± 27	-0.48 ± 0.09	-2.70 <sup>+0.32</sup> <sub>-1.10</sub>	...	305/358
			COMPBB	378 ± 38	-0.45 ± 0.15	...	20 ± 3	296/357
15	4.03	4.35	BAND	188 ± 18	-0.45 ± 0.11	-2.69 <sup>+0.25</sup> <sub>-0.55</sub>	...	388/358
			COMPBB	222 ± 14	-0.23 ± 0.30	...	10 ± 2	386/357
16	4.35	4.74	BAND	259 ± 27	-0.59 ± 0.09	-2.48 <sup>+0.24</sup> <sub>-0.24</sub>	...	382/358
			COMPBB	373 <sup>+135</sup> <sub>-50</sub>	-0.74 <sup>+0.14</sup> <sub>-0.25</sub>	...	23 <sup>+17</sup> <sub>-7</sub>	386/357
17	4.74	4.93	BAND	255 ± 26	-0.48 ± 0.10	-2.82 <sup>+0.36</sup> <sub>-0.70</sub>	...	380/358
			COMPBB	290 ± 22	-0.24 ± 0.27	...	13 ± 2	378/357
			BANDBB	229 ± 33	0.45 ± 0.96	-2.63 ± 0.30	11 ± 2	374/356
18	4.93	5.12	BAND	387 ± 29	-0.36 ± 0.07	-2.77 <sup>+0.29</sup> <sub>-0.29</sub>	...	347/358
			COMPBB	490 ± 35	-0.35 ± 0.12	...	24 ± 5	344/357
			BANDBB	403 ± 38	-0.1 ± 0.24	-2.82 ± 0.31	18 ± 3	340/356
19	5.12	5.18	BAND	665 ± 64	-0.56 ± 0.06	-3.08 <sup>+0.36</sup> <sub>-0.84</sub>	...	370/358
			COMPBB	945 ± 137	-0.71 ± 0.08	...	57 ± 12	365/357
20	5.18	5.31	BAND	401 ± 27	-0.40 ± 0.07	-3.35 <sup>+0.60</sup> <sub>-Inf</sub>	...	333/358
			COMPBB	462 <sup>+34</sup> <sub>-30</sub>	-0.46( <i>fixed</i> )	...	37 <sup>+9</sup> <sub>-7</sub>	331/357
21	5.31	5.50	BAND	268 ± 29	-0.55 ± 0.09	-2.49 <sup>+0.24</sup> <sub>-0.24</sub>	...	346/358
			COMPBB	386 ± 45	-0.63 ± 0.12	...	21 ± 4	343/357
			BANDBB	337 ± 60	-0.54 ± 0.20	-2.70 ± 0.44	19 ± 5	341/356
22	5.50	5.89	BAND	210 ± 23	-0.56 ± 0.10	-2.34 <sup>+0.18</sup> <sub>-0.18</sub>	...	345/358
			COMPBB	405 ± 72	-0.90 ± 0.11	...	26 ± 4	339/357
23	5.89	6.66	BAND	175 ± 19	-0.81 ± 0.09	-2.92 <sup>+0.37</sup> <sub>-1.19</sub>	...	416/358
			COMPBB	221 <sup>+52</sup> <sub>-105</sub>	-1.02 <sup>+0.17</sup> <sub>-0.16</sub>	...	27 <sup>+7</sup> <sub>-9</sub>	415/357

---

PARAMETER EVOLUTIONS – GRB 081215A

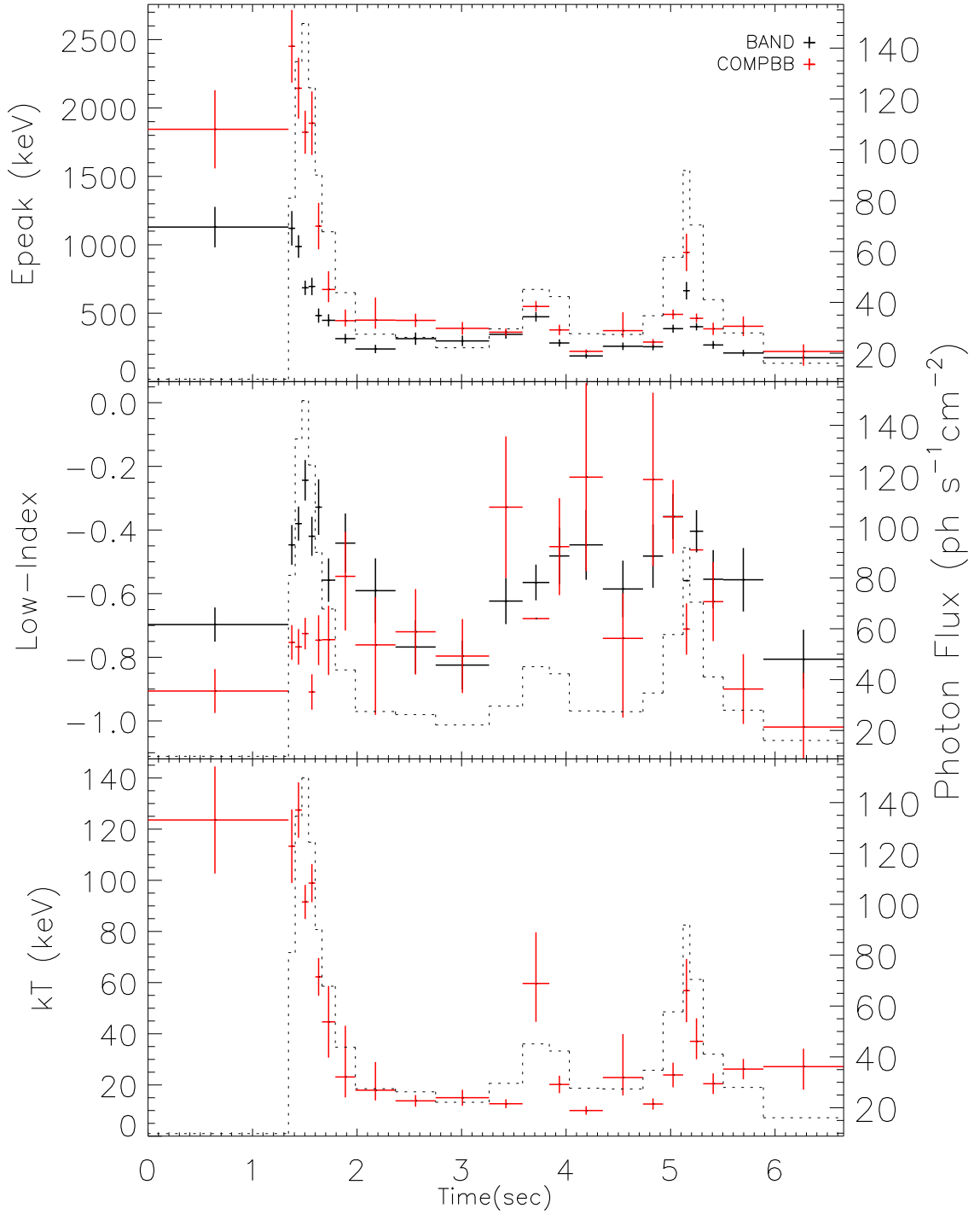


Figure 4.7: The evolution of BAND and COMPBB model parameters for GRB 081215A. The dashed histograms represents the photon fluxes for each time interval (right axis).

ENERGY FLUX EVOLUTION – GRB 081215A

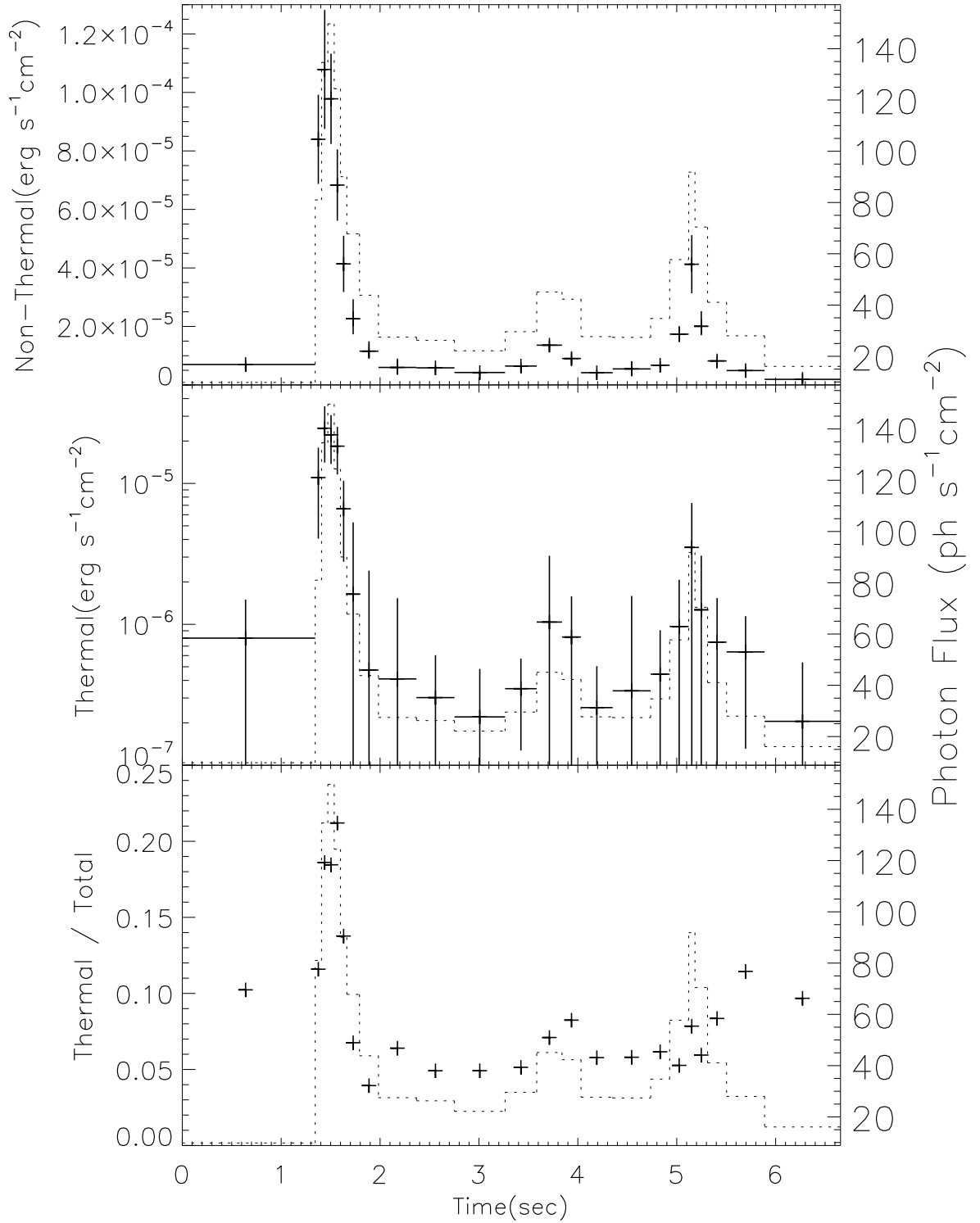


Figure 4.8: The energy flux evolutions of thermal and non-thermal components of COMPBB model for GRB 081215A. The top and middle panels show the energy flux evolutions of COMP and BB models, respectively. The energy flux ratio of thermal to total is seen in the bottom panel. The fluxes are calculated for the energy range 8 keV to 40 MeV. Errors in flux ratio of thermal to total are ignored. The dashed histograms represents the photon fluxes for each time interval (right axis).

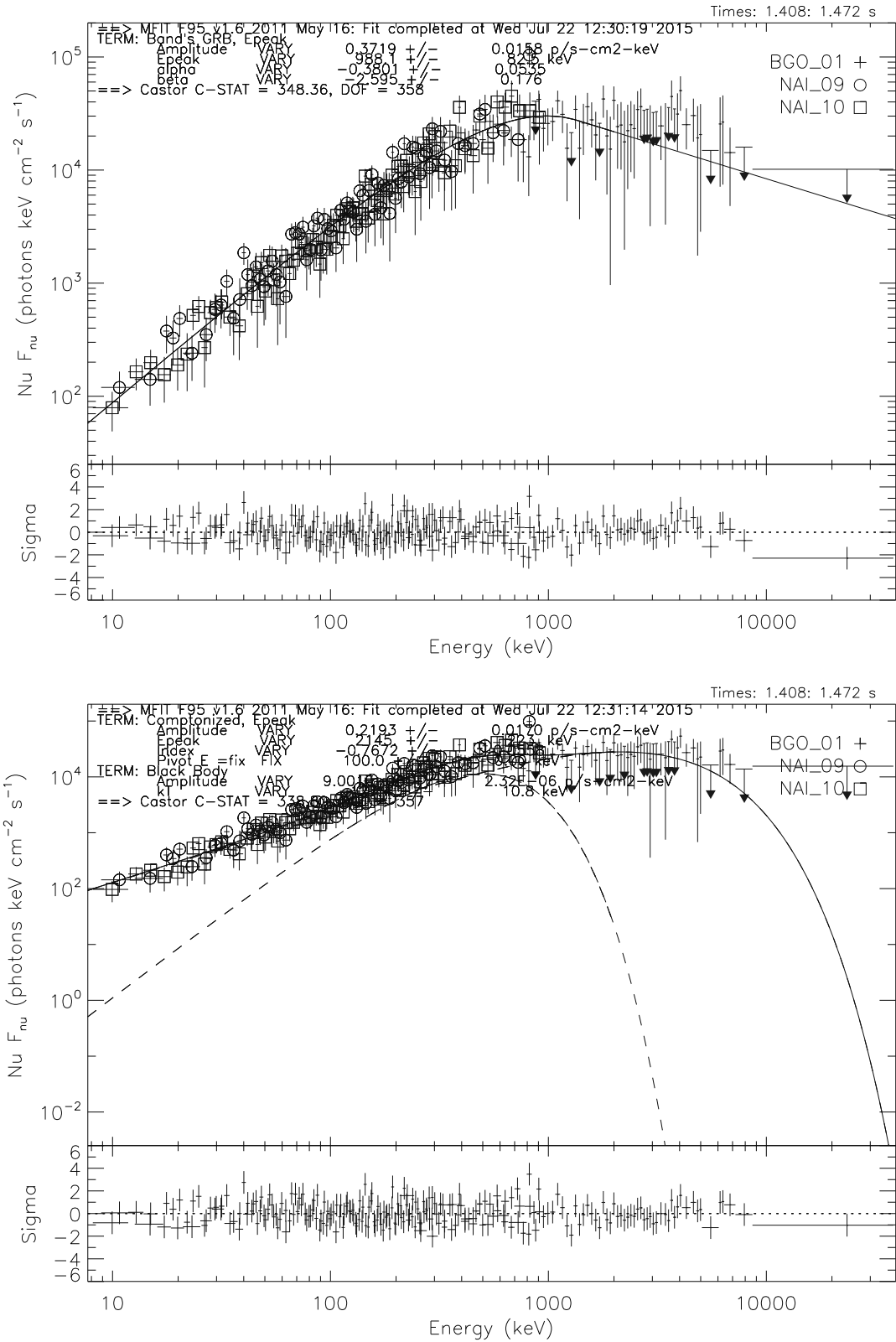


Figure 4.9: The  $\nu F_\nu$  spectrum of BAND and COMPBB models with photon counts and residuals, for the time interval 1.41 - 1.47 s of GRB 081215A, time bin 3.

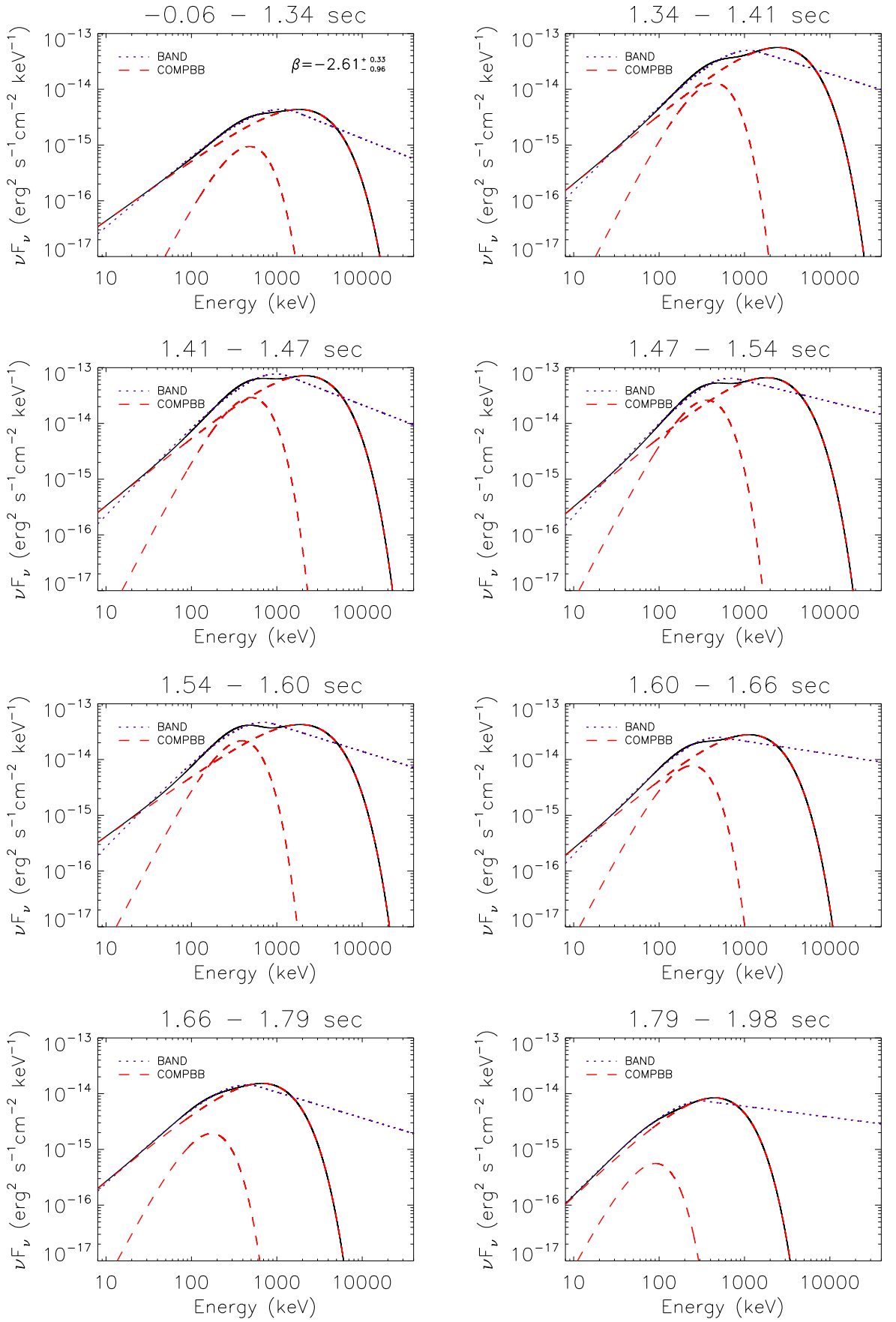


Figure 4.10: The model evolutions for GRB 081215A in  $\nu F_\nu$  representation. The solid line represents the COMPBB model where the dashed lines show the COMP and BB components separately. The dotted line is denoting the BAND model.

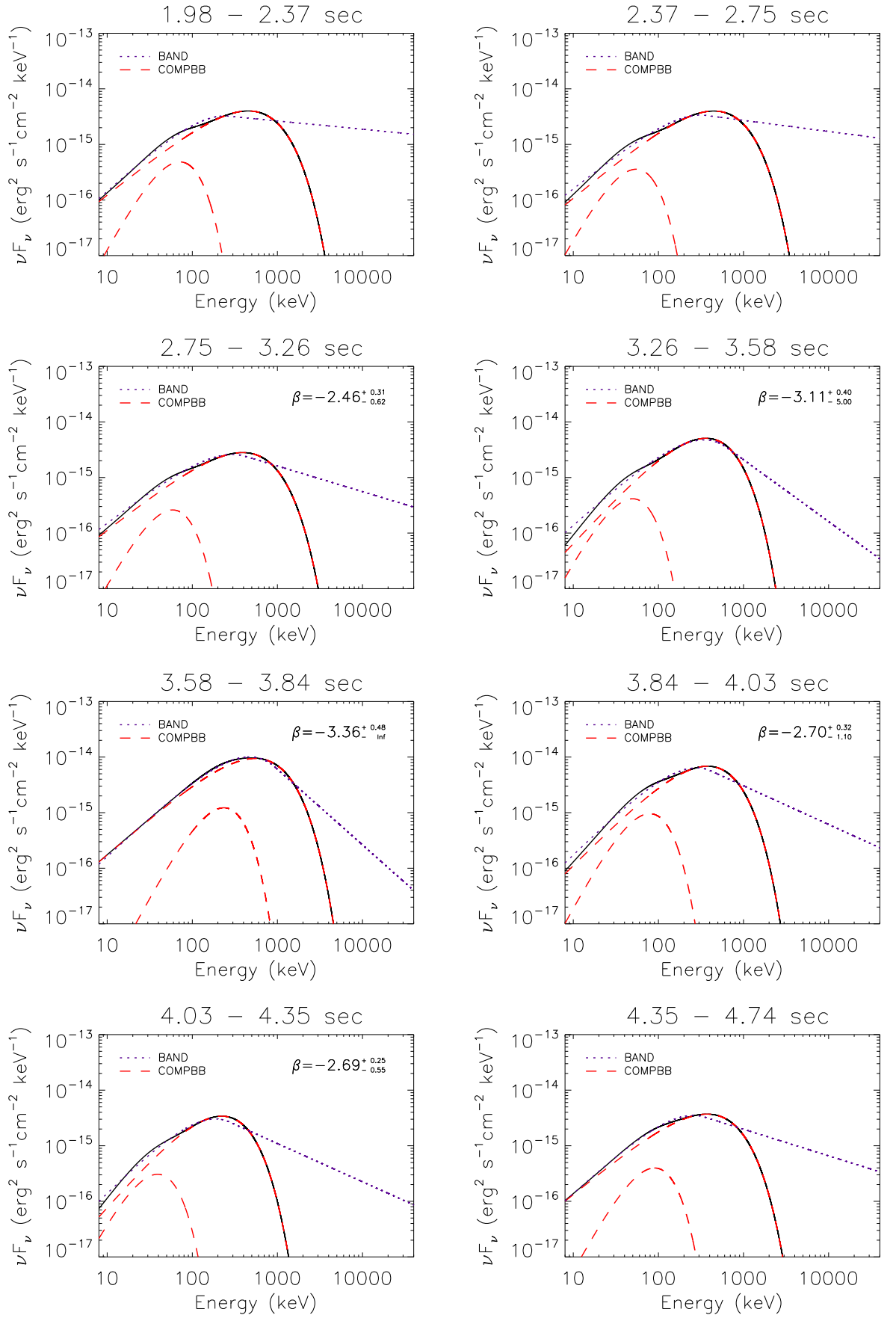


Figure 4.10 Continued.

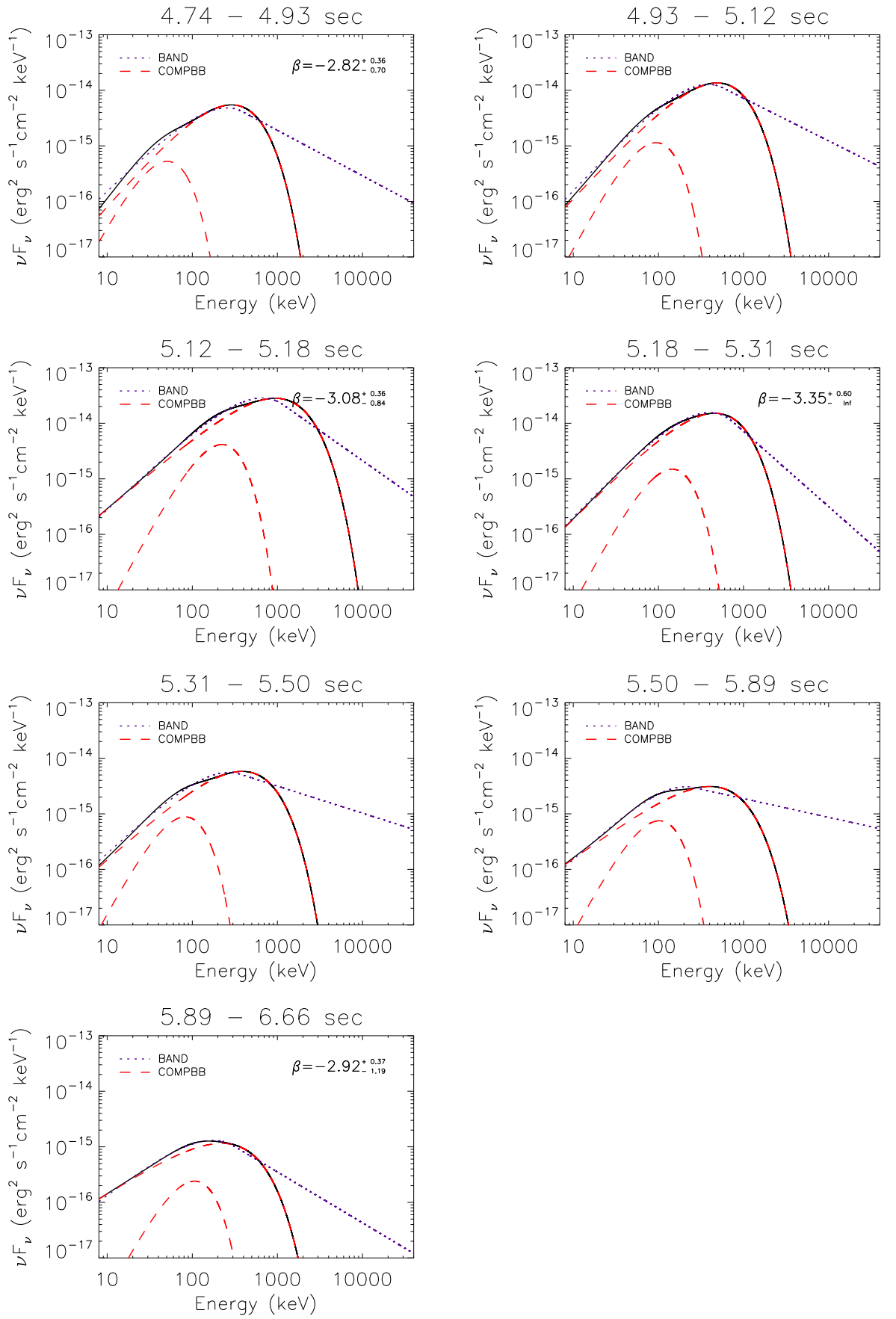


Figure 4.10 Continued.

### 4.3 GRB 090217

GRB 090217 was detected by Fermi-GBM on 17 February 2009 at 04:56:42.5 UT (von Kienlin, 2009). It is a long burst with duration  $T_{90} \sim 33$  s and peak photon flux  $(13.06 \pm 1.05)$  photon  $\text{cm}^{-2} \text{s}^{-1}$  in the energy range 10 – 1000 keV. Ohno et al. (2009b) reported high energy emission from this burst detected by LAT at 04:56:51. Figure 4.11 shows the count rate history of the burst as seen by the brightest GBM detector NaI9. Figure 4.11 also shows the time interval selected for the single pulse structure used for the spectral simulations. The detectors, NaI6, NaI7, NaI9, and BGO1 are used for the spectral analysis.

#### 4.3.1 Parameter Evolutions

The prompt phase of this burst is divided in 7 time bins as seen in Figure 4.12. For each time bin the time intervals and the fit results of all relevant models are listed in Table 4.3. In almost all time bins the  $\beta$  of BAND-only model has only upper limits, and BANDBB model parameters could be constrained only for one time bin, 5th bin.

Figure 4.12 shows the evolution of BAND and COMPBB model parameters. The peak energy of the  $\nu F_\nu$  spectrum is ranging between  $\sim 400$  -  $\sim 900$  keV.  $E_{\text{peak}}$  values of BAND-only and COMPBB models are similar to each other for a given time bin. The  $\alpha$  values are ranging between  $\sim -0.9$  -  $\sim 0$ . For time bins 4, 6, and 7  $\alpha$  shifts to higher values when BB component is included in fits, whereas in other bins  $\alpha$  values of two models are similar. The temperature kT is between  $\sim 50$  to  $\sim 10$  keV, the highest at initial bin, then remains relatively steady at around 10 keV. A slight increase is seen during the 3rd bin where there is a significant increase in photon flux.

##### 4.3.1.1 Flux Evolutions

Figure 4.13 top and middle panels are showing the evolution of energy flux for thermal and non-thermal components of COMPBB model. The non-thermal energy flux is clearly following the photon intensity, whereas the thermal one remains relatively steady throughout the burst. Bottom panel of Figure 4.13 shows the

energy flux ratio of thermal to total, and it is always less than  $\sim 4\%$ . In the second half of the burst (the last 4 bins) the thermal to total flux ratio is relatively high, and for the same bins  $\alpha$  is shifted to higher values significantly, and  $E_{\text{peak}}$  to lower values. The thermal to total energy flux ratio is ranging from  $\sim 1\%$  to  $\sim 4\%$  throughout the burst with an average ratio of 2.6%.

Figure 4.14 shows the  $\nu F_\nu$  spectrum of BAND and COMPBB models with photon counts and residuals, for the time interval 6.08 - 7.17 s, time bin 4. When BB is included in fits, the  $E_{\text{peak}}$  of non-thermal component did not change significantly, but  $\alpha$  is increased from  $\sim -0.57$  to  $\sim -0.13$ . The peak of the BB is  $\sim 30$  keV, as can be seen in Table 4.3 also. Figure 4.15 shows the evolution of BAND and COMPBB models in  $\nu F_\nu$  representation throughout the burst.

### 4.3.2 Pulse Simulations

We performed the spectral simulations as described in § 3.2.2 by considering the whole burst as a single pulse. So, the time interval of the pulse is selected as  $-0.832$  -  $19.840$  s, as seen in Figure 4.11. The spectrum of the pulse does not have enough emission above the peak energy of the  $\nu F_\nu$  spectrum to be able to constrain the  $\beta$  of BAND-only and BANDBB models, and the other spectral parameters ( $E_{\text{peak}}$ ,  $\alpha$ ) are almost same with COMP-only and COMPBB models, respectively. Therefore, we performed simulation with COMP-only and COMPBB models. The additional BB component improved the COMP-only fit by  $\Delta CSTAT_{\text{real}} = 28$  units.

The distributions of fit model parameters of both sets of synthetic spectra showed that; *COMPBB model is a better representative of the data* than COMP-only model, i.e., the fit results of the synthetic spectra produced with COMPBB model parameters are consistent with real fit results of both COMP-only and COMPBB models. The probability of getting an improvement of  $\geq \Delta CSTAT_{\text{real}}$  in synthetic spectra is only 0.005% making BB component statistically significant.

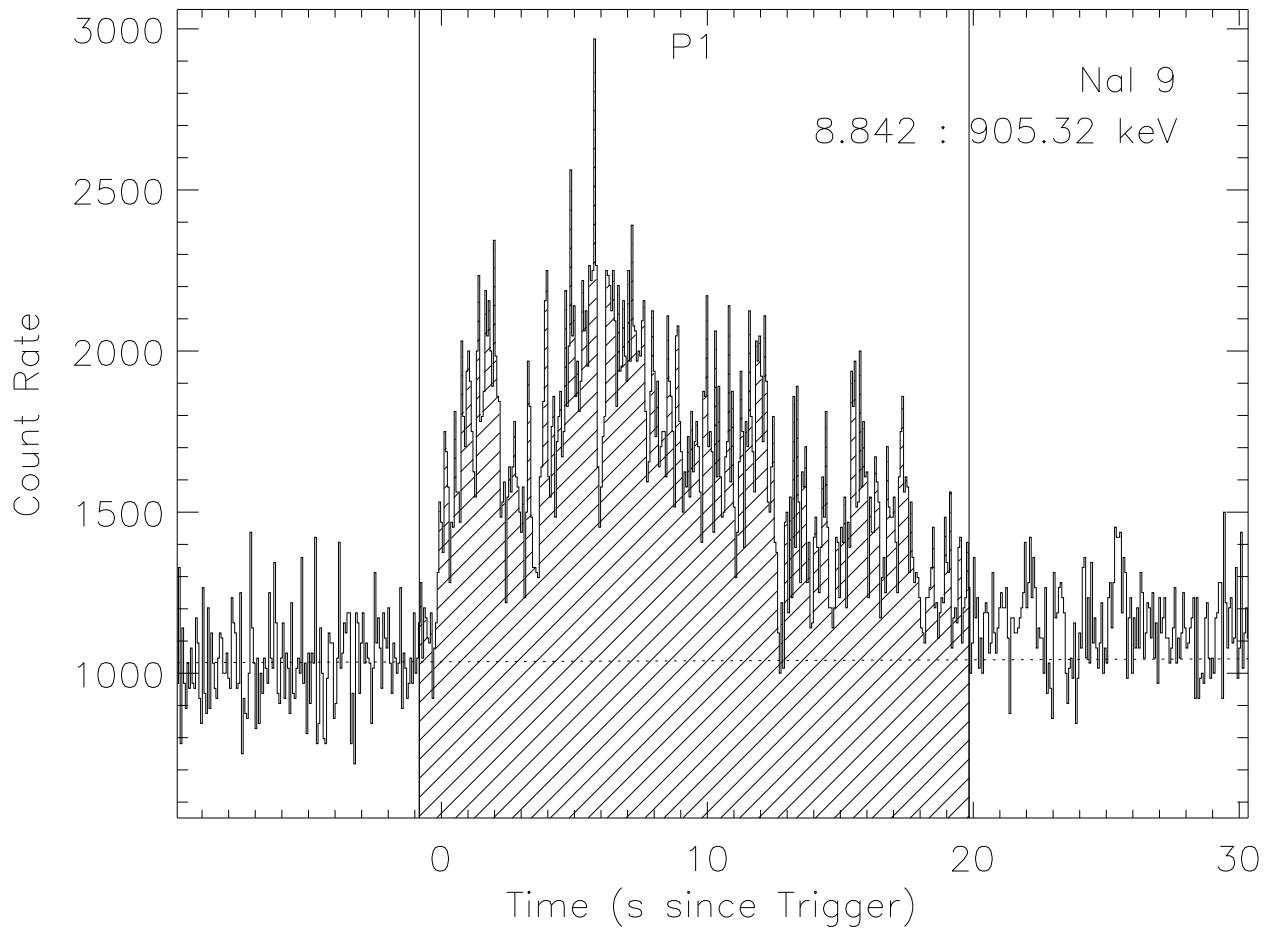


Figure 4.11: The light curve of GRB 090217 with 64 ms resolution. The solid vertical lines define the single pulse interval as used in pulse simulations and indicated as P1.

Table 4.3: Fine time interval fit results for GRB 090217A. Best parameter values with their  $1\sigma$  uncertainties.

Bin number	Time interval since trigger		Model	$E_{\text{peak}}$ (keV)	$\alpha$	$\beta$	$kT$ (keV)	Cstat/dof
	$T_{\text{start}}$ (s)	$T_{\text{stop}}$ (s)						
1	-0.83	2.06	BAND	$614^{+74}_{-76}$	$-0.64^{+0.07}_{-0.06}$	$-3.99^{+1.20}_{-Inf}$	...	437/464
			COMPBB	$725^{+171}_{-113}$	$-0.66^{+0.12}_{-0.11}$	...	$33^{+16}_{-13}$	435/463
2	2.06	4.74	BAND	$580^{+71}_{-59}$	$-0.69 \pm 0.06$	$-2.77^{+0.47}_{-Inf}$	...	494/464
			COMPBB	$543^{+68}_{-53}$	$-0.51 \pm 0.19$	...	$10 \pm 3$	493/463
3	4.74	6.08	BAND	$776^{+80}_{-71}$	$-0.57 \pm 0.06$	$-2.93^{+0.44}_{-1.23}$	...	537/464
			COMPBB	$816^{+82}_{-70}$	$-0.52(\text{fixed})$	...	$26 \pm 11$	537/463
4	6.08	7.17	BAND	$617^{+53}_{-50}$	$-0.57^{+0.07}_{-0.06}$	$-4.15^{+1.14}_{-Inf}$	...	520/464
			COMPBB	$536^{+45}_{-38}$	$-0.13^{+0.22}_{-0.18}$	...	$12 \pm 2$	511/463
5	7.17	8.83	BAND	$658^{+111}_{-88}$	$-0.8 \pm 0.06$	$-3.35^{+0.84}_{-Inf}$	...	513/464
			COMPBB	$569^{+80}_{-62}$	$-0.52^{+0.17}_{-0.51}$	...	$10 \pm 1$	507/463
			BANDBB	$506^{+91}_{-86}$	$-0.41^{+0.26}_{-0.60}$	$-2.65^{0.39}_{-1.31}$	$10 \pm 1$	506/462
6	8.83	10.75	BAND	$781^{+97}_{-83}$	$-0.78 \pm 0.05$	$-7.60 \pm Inf$	...	515/464
			COMPBB	$709^{+98}_{-79}$	$-0.46^{+0.19}_{-0.15}$	...	$14 \pm 2$	507/463
7	10.75	13.57	BAND	$526^{+74}_{-58}$	$-0.85 \pm 0.06$	$-2.71^{+0.43}_{-Inf}$	...	583/464
			COMPBB	$457^{+58}_{-45}$	$-0.46^{+0.18}_{-0.21}$	...	$10 \pm 1$	576/463

PARAMETER EVOLUTIONS – GRB 090217

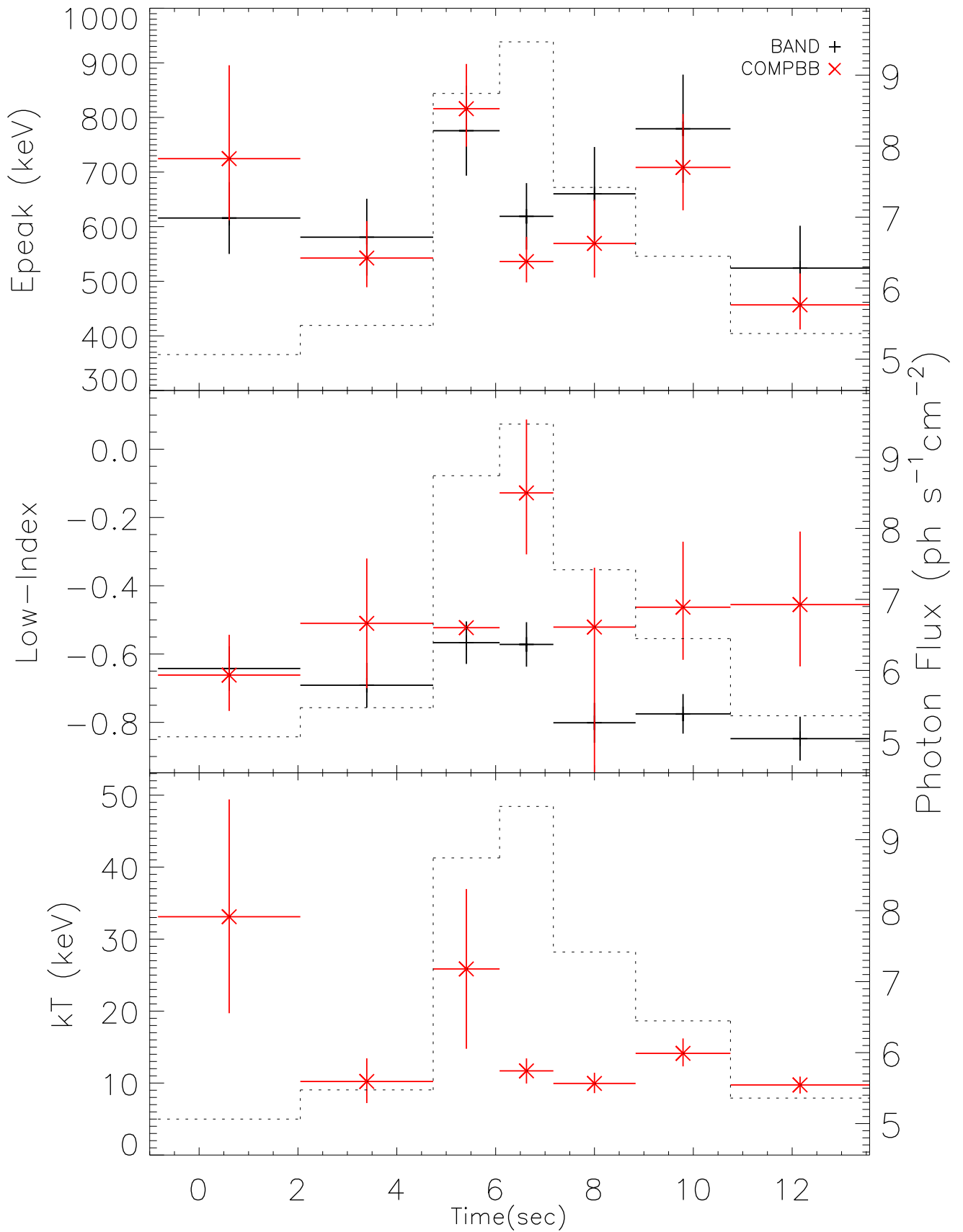


Figure 4.12: The evolution of BAND and COMPBB model parameters for GRB 090217. The dashed histograms represents the photon fluxes for each time interval (right axis).

ENERGY FLUX EVOLUTION – GRB 090217

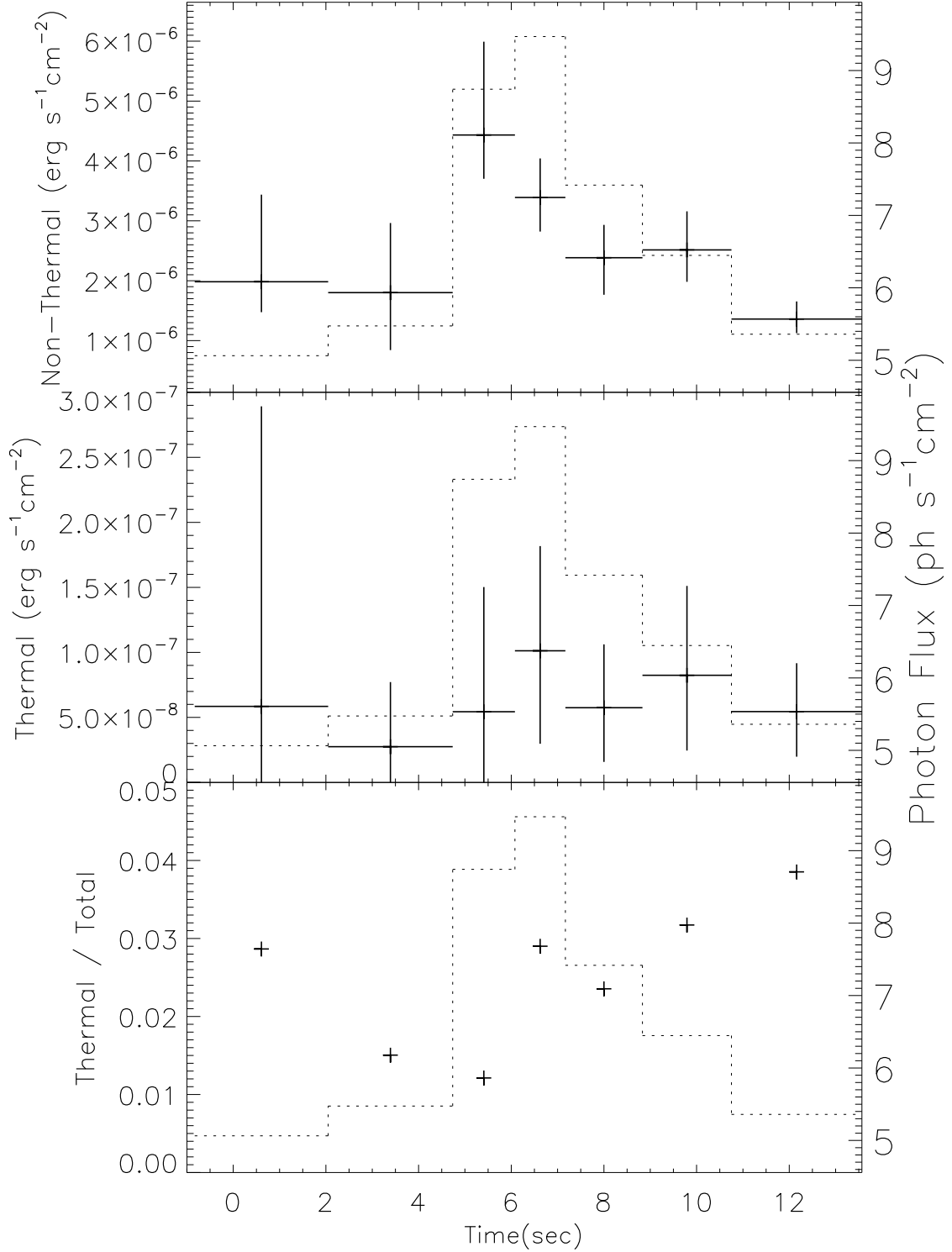


Figure 4.13: The energy flux evolutions of thermal and non-thermal components of COMPBB model for GRB 090217. The top and middle panels show the energy flux evolutions of COMP and BB models, respectively. The energy flux ratio of thermal to total is seen in the bottom panel. The fluxes are calculated for the energy range 8 keV to 40 MeV. Errors in flux ratio of thermal to total are ignored. The dashed histograms represents the photon fluxes for each time interval (right axis).

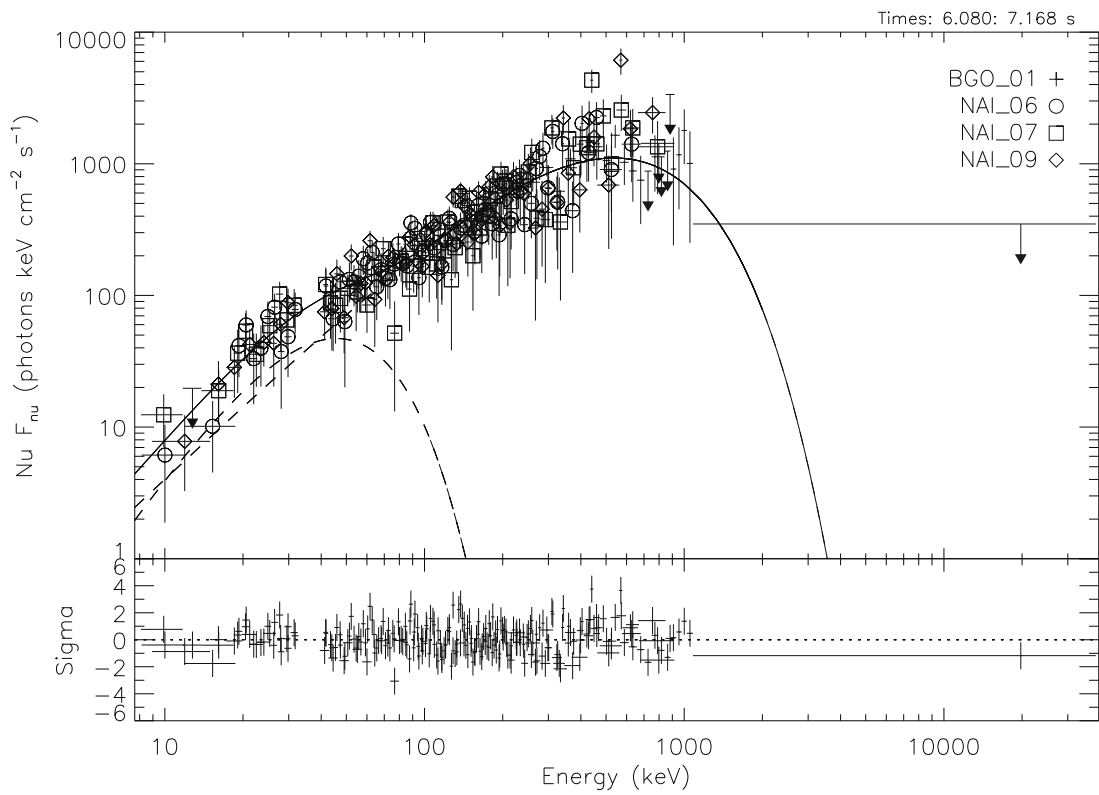
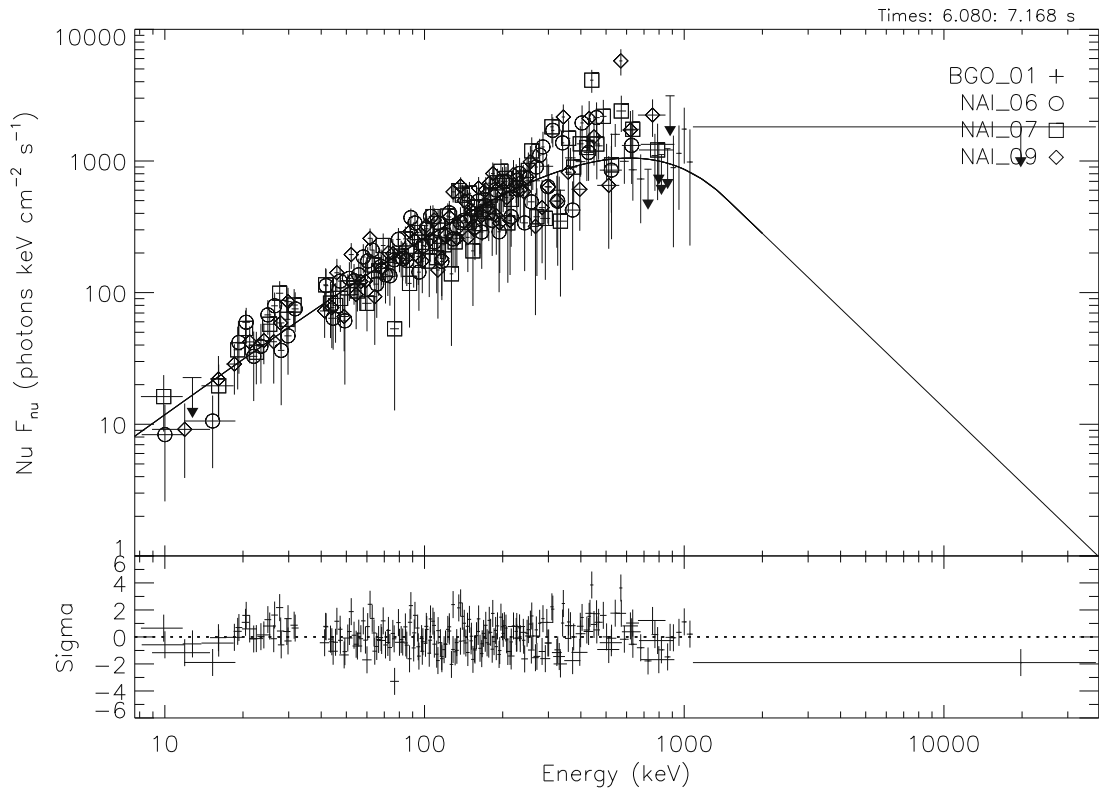


Figure 4.14: The  $\nu F_\nu$  spectrum of BAND and COMPBB models with photon counts and residuals, for the time interval 6.08 - 7.17 s of GRB 090217, time bin 4.

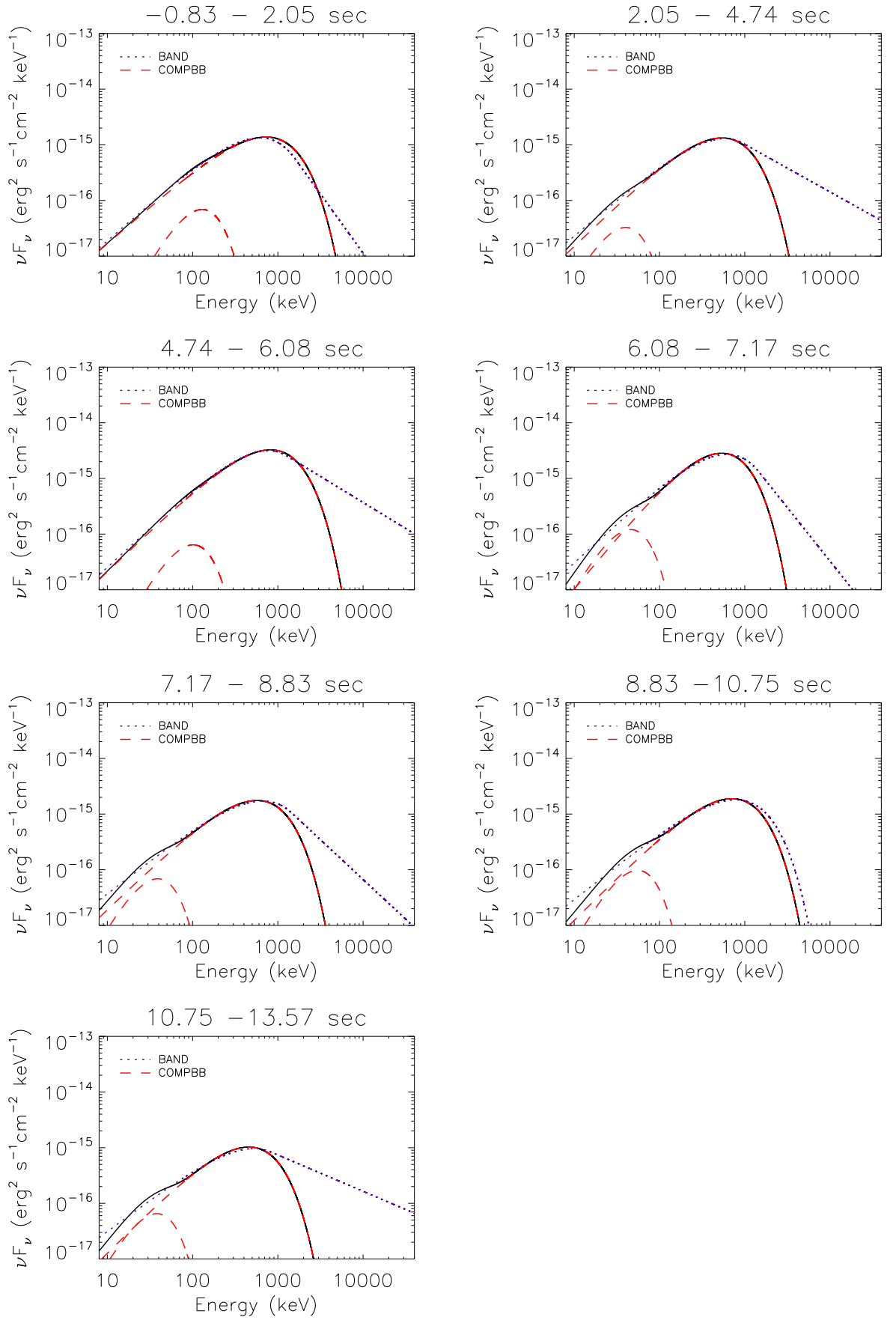


Figure 4.15: The model evolutions for GRB 090217 in  $\nu F_\nu$  representation. The solid line represents the COMPBB model where the dashed lines show the COMP and BB components separately. The dotted line is denoting the BAND model.

## 4.4 GRB 090323A

GRB 090323A was detected by Fermi-GBM and by Fermi-LAT on 23 March 2009 at 00:02:42.6 UT (Ohno et al., 2009a). High energy emission, up to a few GeV, was observed  $\sim$  a few seconds after the GBM trigger up until several kilo-seconds. From the spectroscopic analysis of afterglow emission of the burst, a redshift of  $z = 3.57$  is measured (Chornock et al. 2009). It is a long burst with duration  $T_{90} \sim 135$  s and peak photon flux  $(14.33 \pm 0.84)$  photon  $\text{cm}^{-2} \text{s}^{-1}$  in the energy range 10 – 1000 keV. Figure 4.16 shows the count rate history of the burst as seen by the brightest GBM detector NaI7. In the first  $\sim 80$  s there are two pulse structures possibly overlapping with each other. Then, for about 30 s of quiescence period there appears relatively weak, subsequent several pulse structures lasting for  $\sim 40$  s. Figure 4.16 also shows the selected pulse intervals as used for the spectral simulations. The detectors, NaI6, NaI7, and BGO1 are used for the spectral analysis.

### 4.4.1 Parameter Evolutions

The prompt emission phase is divided into 19 time bins as seen in Figure 4.17. For each time bin the time intervals and the fit results of all relevant models are listed in Table 4.4. For several time bins the  $\beta$  of BAND-only model has only upper limits. For two bins, 14th and 18th,  $\beta$  has very negative values with undetermined error intervals, i.e., BAND being very similar to COMP in shape (with almost same  $E_{\text{peak}}$  and  $\alpha$  values). BANDBB model parameters could be constrained only in 4 time bins.

Figure 4.17 shows the evolution of BAND and COMPBB model parameters.  $E_{\text{peak}}$  values are between  $\sim 150$  -  $\sim 3000$  keV. The peak energies are shifted to higher values when BB component is included in fits, especially during first 40 s. COMPBB  $\alpha$  is either has lower or consistent values with BAND  $\alpha$ , except for one bin at  $\sim 55$  s. The temperature  $kT$  seems to be slowly decreasing overall, however it shows an increase at around 65 s and 120 s, corresponding to the peak photon flux of second pulse and the beginning of the third pulse, respectively.

#### 4.4.1.1 Flux Evolutions

Figure 4.18 shows the evolution of energy flux for thermal and non-thermal components of COMPBB model. Non-thermal energy flux seems to be following the photon flux rate of the burst. The errors of thermal energy flux are relatively large to conclude a clear evolution pattern throughout the burst. The bottom panel of Figure 4.18 shows the thermal energy flux to total energy flux, and the ratio is relatively large during 5th bin ( $\sim 25 - 40$  s), the plateau phase at around 70 - 120 s, and the first two bins of the third pulse  $\sim 120 - 140$ . Thermal to total energy flux ratio is ranging from  $\sim 1\%$  to  $\sim 15\%$  during the burst with an average ratio of 5.5%.

Figure 4.19 shows the  $\nu F_\nu$  spectrum of BAND and COMPBB models with photon counts and residuals, for the time interval 15.10 - 18.37 s, time bin 3. When BB is included in fits, the  $E_{\text{peak}}$  of non-thermal component shifts from  $\sim 500$  keV to  $\sim 1400$  keV, and  $\alpha$  is decreased from  $\sim -0.74$  to  $\sim -0.94$ . The peak of the BB is  $\sim 100$  keV, as can be seen in Table 4.4 also. Figure 4.20 shows the evolution of BAND and COMPBB models in  $\nu F_\nu$  representation throughout the burst.

#### 4.4.2 Pulse Simulations

We selected the time intervals of 1st, 2nd, and 3rd pulses as; 0.0 - 34.240 s, 34.240 - 72.640 s, 115.140 - 153.410 s, respectively, as seen in Figure 4.16. The spectra of first and second pulses have enough emission above  $E_{\text{peak}}$  to be able to constrain the high energy power law index  $\beta$  of the BAND model, with and without BB component. Therefore, the simulations are performed with BAND and BANDBB models. The additional BB component improved the BAND-only fits by  $\Delta CSTAT_{\text{real}} = 23.8$  and  $\Delta CSTAT_{\text{real}} = 13.9$  units for 1st and 2nd respectively. For the third pulse  $\beta$  of BAND-only model was not constrained, and the additional BB model (COMPBB) did not improve the COMP-only fit.

For the first and second pulses the distributions of fit model parameters of both sets of synthetic spectra showed that the *BANDBB model is a better representative of the data* than BAND only model, i.e., the fit results of the synthetic spectra produced with BANDBB model parameters are consistent with real fit results of both BAND and BANDBB models. The probabilities of getting an improvement of that much or

more in synthetic spectra of individual pulses by chance are;  $< 0.005\%$  and  $0.16\%$ , respectively. So, BB component is statistically significant for both 1st and 2nd pulses. For the whole third pulse and for the time bins of this pulse the additional BB component did not improve BAND-only or COMP-only fits significantly. Therefore, without performing bin-wise spectral simulations, we cannot confirm the preference for the BB component (or hybrid model) with confidence, for the individual time bins  $\sim 65$  s after trigger.

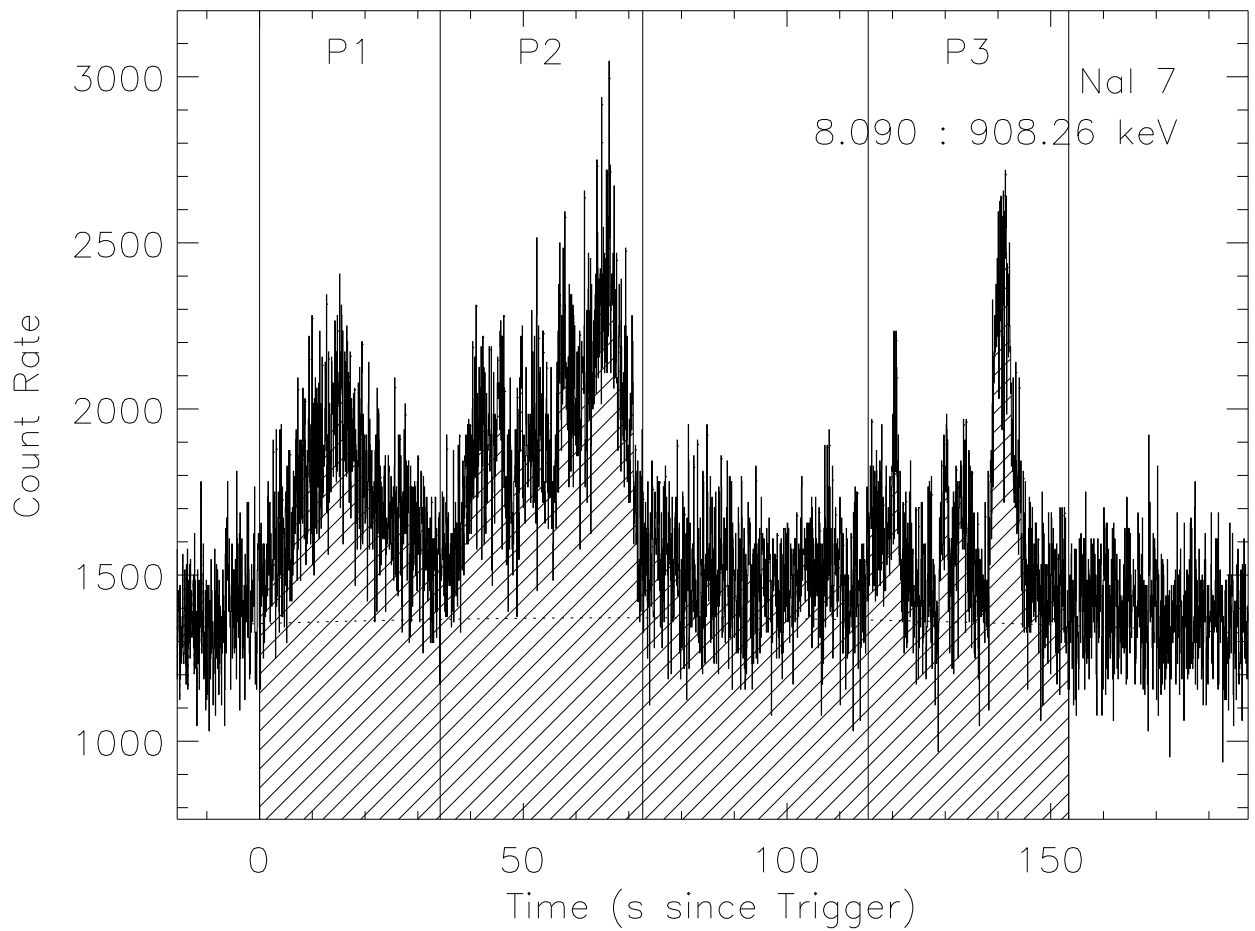


Figure 4.16: The light curve of GRB 090323A with 64 ms resolution. The solid vertical lines define the pulse intervals as used in pulse simulations.

Table 4.4: Fine time interval fit results for GRB 090323A. Best parameter values with their  $1\sigma$  uncertainties.

Bin number	Time interval since trigger		Model	$E_{\text{peak}}$ (keV)	$\alpha$	$\beta$	$kT$ (keV)	Cstat/dof
	$T_{\text{start}}(s)$	$T_{\text{stop}}(s)$						
1	0.06	11.90	BAND	$616_{-151}^{+158}$	$-0.70_{-0.09}^{+0.13}$	$-2.06_{-0.24}^{+0.16}$	...	542/348
			COMPBB	$1466_{-1280}^{+490}$	$-0.86_{-0.08}^{+0.11}$	...	$39_{-7}^{+8}$	540/347
			BANDBB	$1063_{-912}^{+295}$	$-0.78_{-0.09}^{+0.11}$	$-2.27_{-0.32}^{+0.20}$	$35 \pm 8$	535/346
2	11.90	15.10	BAND	$402_{-66}^{+94}$	$-0.50_{-0.13}^{+0.14}$	$-2.03_{-0.20}^{+0.12}$	...	455/348
			COMPBB	$809_{-129}^{+196}$	$-0.53_{-0.15}^{+0.21}$	...	$27_{-3}^{+4}$	445/347
			BANDBB	$717_{-145}^{+207}$	$-0.48_{-0.18}^{+0.27}$	$-2.35_{-0.51}^{+0.23}$	$26_{-3}^{+4}$	442/346
3	15.10	18.37	BAND	$513_{-170}^{+126}$	$-0.74_{-0.09}^{+0.21}$	$-2.23_{-0.42}^{+0.29}$	...	400/348
			COMPBB	$1416_{-457}^{+598}$	$-0.94_{-0.09}^{+0.12}$	...	$35 \pm 6$	392/347
4	18.37	25.86	BAND	$666_{-243}^{+236}$	$-0.96_{-0.08}^{+0.14}$	$-1.95_{-0.17}^{+0.15}$	...	489/348
			COMPBB	$3095_{-523}^{+606}$	$-1.12 \pm 0.05$	...	$30_{-4}^{+6}$	479/347
5	25.86	41.66	BAND	$240_{-42}^{+50}$	$-0.43_{-0.15}^{+0.2}$	$-1.9_{-0.12}^{+0.09}$	...	583/348
			COMPBB	$648_{-136}^{+361}$	$-0.80_{-0.16}^{+0.14}$	...	$28_{-4}^{+5}$	582/347
6	41.66	45.18	BAND	$423_{-83}^{+81}$	$-0.76_{-0.09}^{+0.12}$	$-2.74_{-Inf}^{+0.54}$	...	410/348
			COMPBB	$542_{-81}^{+118}$	$-0.65_{-0.15}^{+0.21}$	...	$20_{-3}^{+4}$	402/347
7	45.18	49.47	BAND	$553_{-101}^{+86}$	$-0.84_{-0.07}^{+0.09}$	$-4.22_{-Inf}^{+0.91}$	...	397/348
			COMPBB	$599_{-180}^{+194}$	$-0.79_{-0.40}^{+0.25}$	...	$20_{-10}^{+18}$	396/347
8	49.47	52.86	BAND	$463_{-61}^{+73}$	$-0.62_{-0.09}^{+0.10}$	$-2.63_{-2.24}^{+0.34}$	...	440/348
			COMPBB	$544_{-89}^{+135}$	$-0.53_{-0.58}^{+0.27}$	...	$21_{-7}^{+12}$	437/347
9	52.86	57.20	BAND	$346_{-31}^{+33}$	$-0.38_{-0.10}^{+0.11}$	$-3.5_{-Inf}^{+0.83}$	...	438/348
			COMPBB	$321_{-24}^{+30}$	$0.17_{-0.37}^{+0.49}$	...	$12 \pm 3$	435/347
			BANDBB	$304_{-30}^{+31}$	$0.37_{-0.44}^{+0.70}$	$-3.22_{-2.1}^{+0.55}$	$12 \pm 2$	434/346
10	57.20	59.20	BAND	$533_{-62}^{+72}$	$-0.59 \pm 0.08$	$-3.26_{-Inf}^{+0.74}$	...	419/348
			COMPBB	$543_{-60}^{+86}$	$-0.45_{-0.51}^{+0.21}$	...	$17_{-5}^{+14}$	417/347
11	59.20	61.76	BAND	$423_{-63}^{+81}$	$-0.48_{-0.11}^{+0.13}$	$-1.86_{-0.09}^{+0.07}$	...	430/348
			COMPBB	$549_{-58}^{+74}$	$-0.33_{-0.66}^{+0.24}$	...	$16_{-3}^{+5}$	455/347
			BANDBB	$358_{-125}^{+68}$	$0.13_{-1.03}^{+3.48}$	$-1.86_{-0.09}^{+0.10}$	$14 \pm 3$	426/346
12	61.76	64.00	BAND	$439_{-40}^{+47}$	$-0.56 \pm 0.08$	$-3.14_{-Inf}^{+0.65}$	...	422/348
			COMPBB	$412_{-35}^{+40}$	$-0.30_{-0.23}^{+0.17}$	...	$10 \pm 2$	419/347
13	64.00	65.47	BAND	$433_{-68}^{+52}$	$-0.40_{-0.10}^{+0.14}$	$-2.66_{-Inf}^{+0.42}$	...	386/348
			COMPBB	$547_{-65}^{+95}$	$-0.41_{-0.14}^{+0.17}$	...	$33_{-7}^{+11}$	383/347

14	65.47	66.69	BAND	$435^{+32}_{-38}$	$-0.41^{+0.10}_{-0.08}$	$-7.4 \pm Inf$	...	365/348
			COMPBB	$414^{+26}_{-23}$	$-0.29(fixed)$	...	$9^{+7}_{-4}$	364/347
15	66.69	68.80	BAND	$336^{+56}_{-46}$	$-0.61^{+0.11}_{-0.10}$	$-2.17^{+0.16}_{-0.28}$	...	360/348
			COMPBB	$502^{+153}_{-86}$	$-0.75 \pm 0.14$	...	$29^{+133}_{-11}$	362/347
16	68.80	120.26	BAND	$105^{+18}_{-15}$	$-0.14^{+0.28}_{-0.22}$	$-1.79^{+0.04}_{-0.05}$	...	1353/348
			COMPBB	$440^{+119}_{-76}$	$-0.79^{+0.15}_{-0.20}$	...	$16 \pm 2$	1354/347
17	120.6	139.78	BAND	$119^{+18}_{-15}$	$-0.75^{+0.16}_{-0.14}$	$-2.27^{+0.26}_{-0.25}$	...	755/348
			COMPBB	$255^{+66}_{-48}$	$-1.28(fixed)$	...	$22 \pm 3$	756/347
18	139.78	141.06	BAND	$154 \pm 14$	$-0.98^{+0.10}_{-0.09}$	$-7.30 \pm Inf$	...	322/348
			COMPBB	$169^{+19}_{-16}$	$-0.60^{+0.51}_{-0.28}$	...	$9^{+2}_{-1}$	318/347
19	141.06	142.14	BAND	$151^{+14}_{-16}$	$-0.92^{+0.12}_{-0.09}$	$-3.68^{+0.94}_{-Inf}$	...	396/348
			COMPBB	$150^{+14}_{-11}$	$-0.57^{+0.42}_{-0.33}$	...	$6 \pm 2$	395/347

---

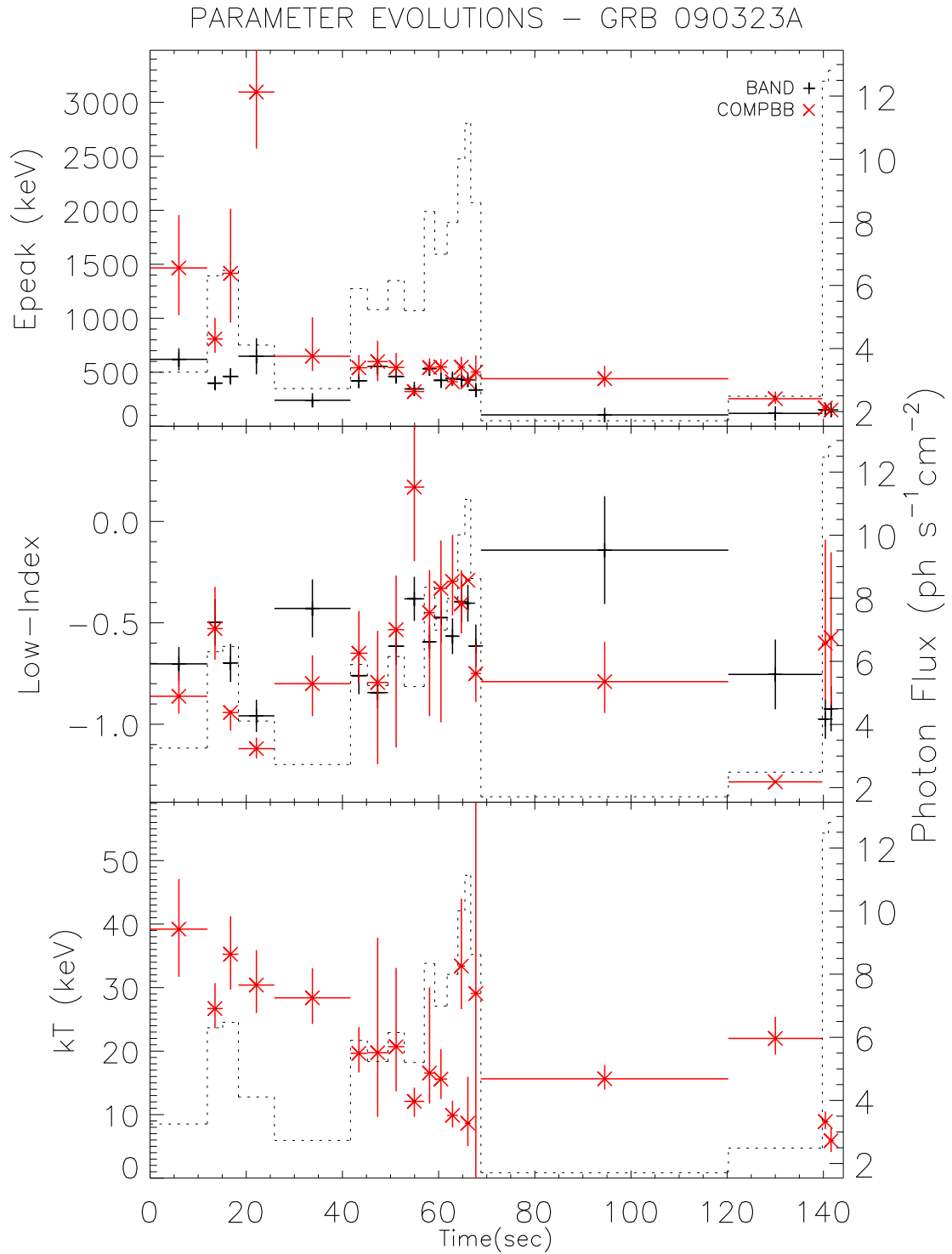


Figure 4.17: The evolution of BAND and COMPBB model parameters for GRB 090323A. The dashed histograms represents the photon fluxes for each time interval (right axis).

ENERGY FLUX EVOLUTION – GRB 090323A

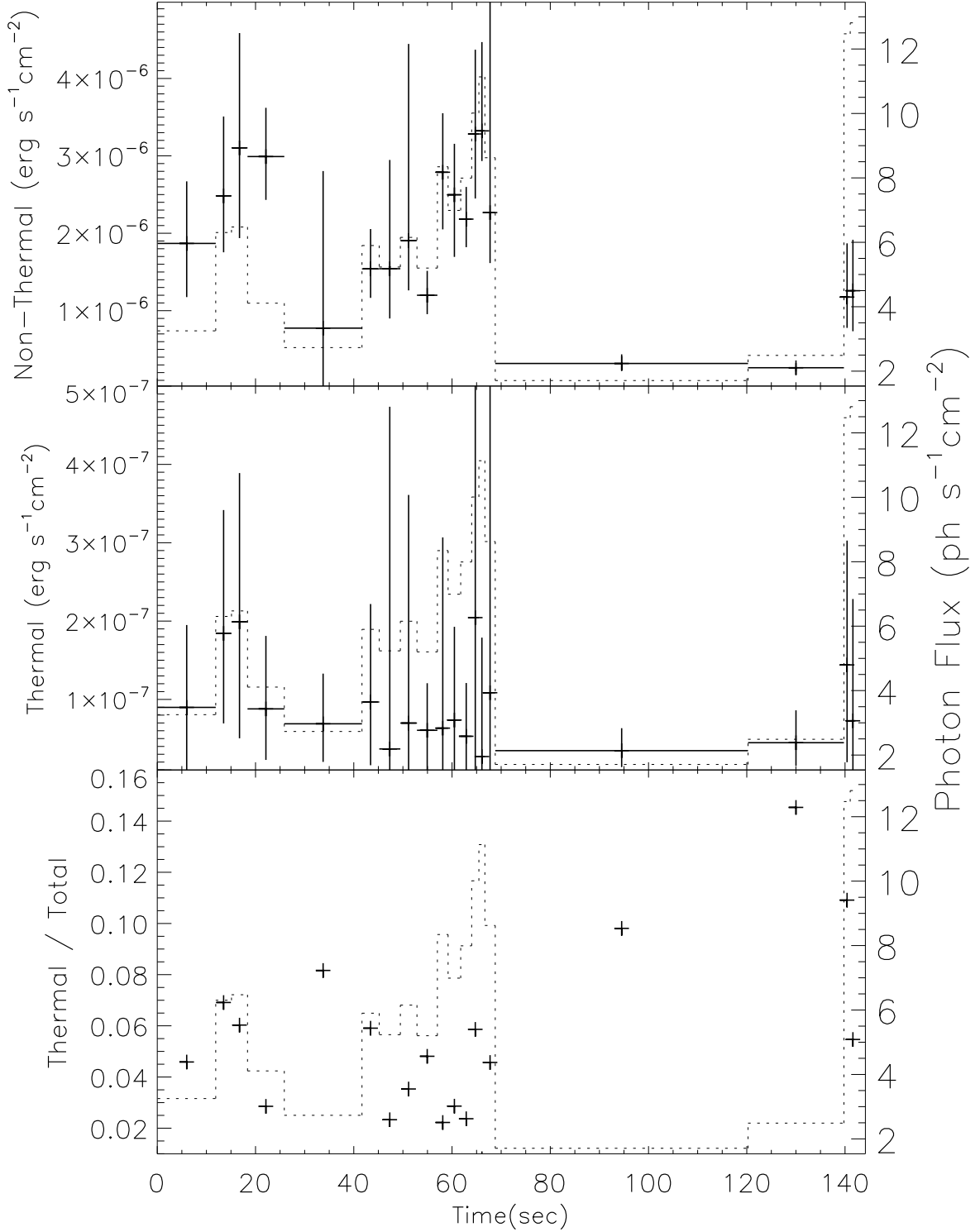


Figure 4.18: The energy flux evolutions of thermal and non-thermal components of COMPBB model for GRB 090323A. The top and middle panels show the energy flux evolutions of COMP and BB models, respectively. The energy flux ratio of thermal to total is seen in the bottom panel. The fluxes are calculated for the energy range 8 keV to 40 MeV. Errors in flux ratio of thermal to total are ignored. The dashed histograms represents the photon fluxes for each time interval (right axis).

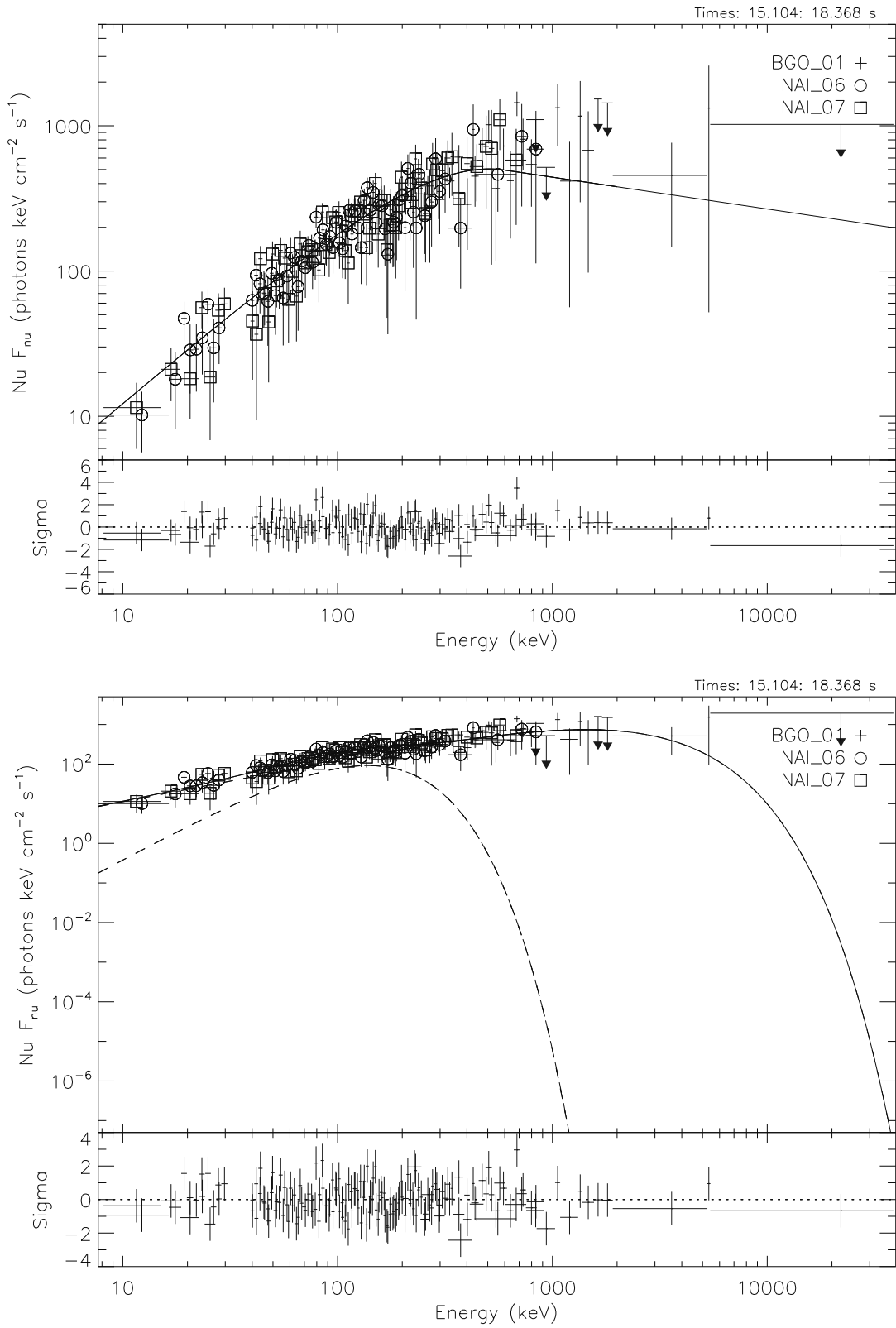


Figure 4.19: The  $\nu F_\nu$  spectrum of BAND and COMPBB models with photon counts and residuals, for the time interval 15.10 - 18.37 s of GRB 090323A, time bin 3.

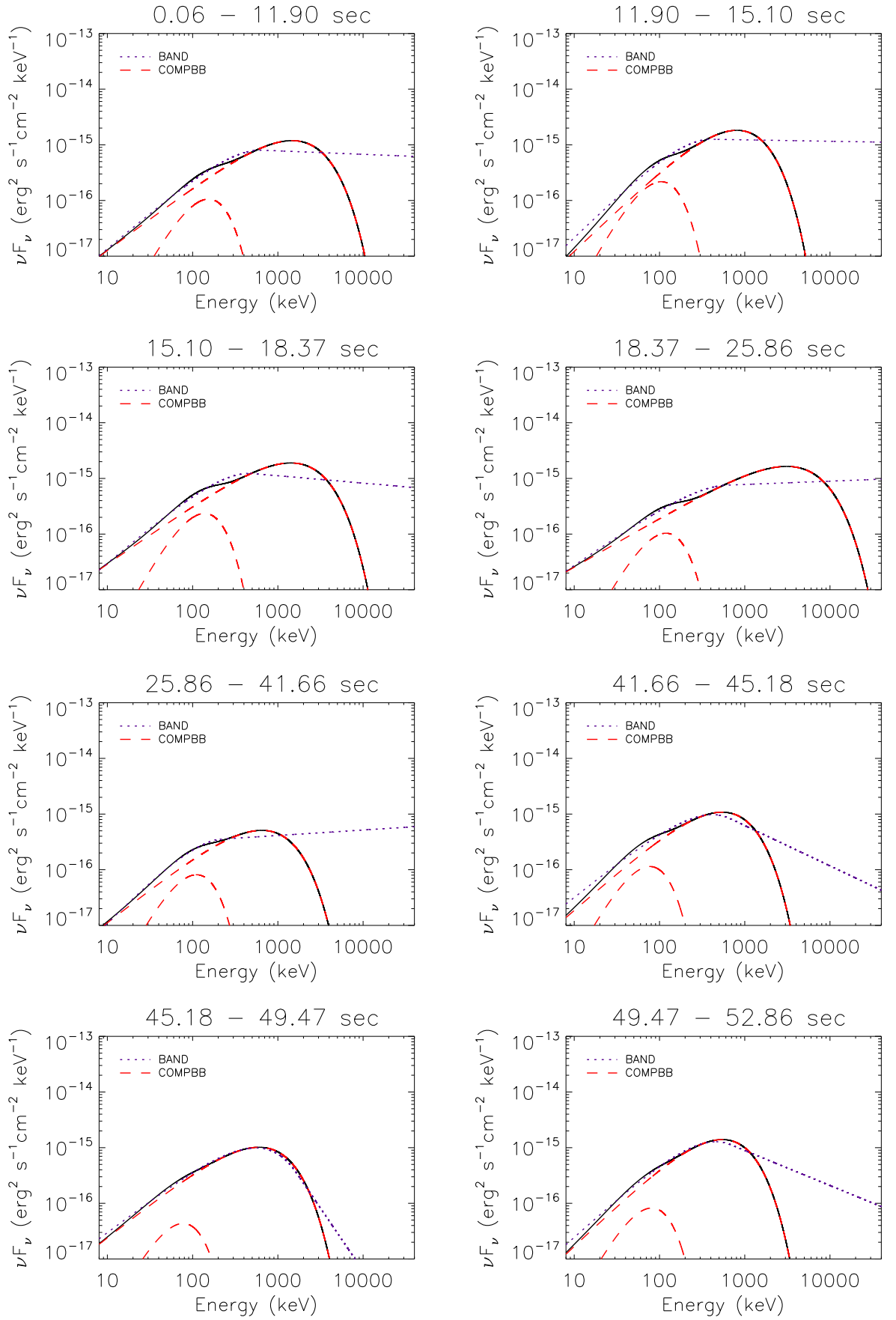


Figure 4.20: The model evolutions for GRB 090323A in  $\nu F_\nu$  representation. The solid line represents the COMPBB model where the dashed lines show the COMP and BB components separately. The dotted line is denoting the BAND model.

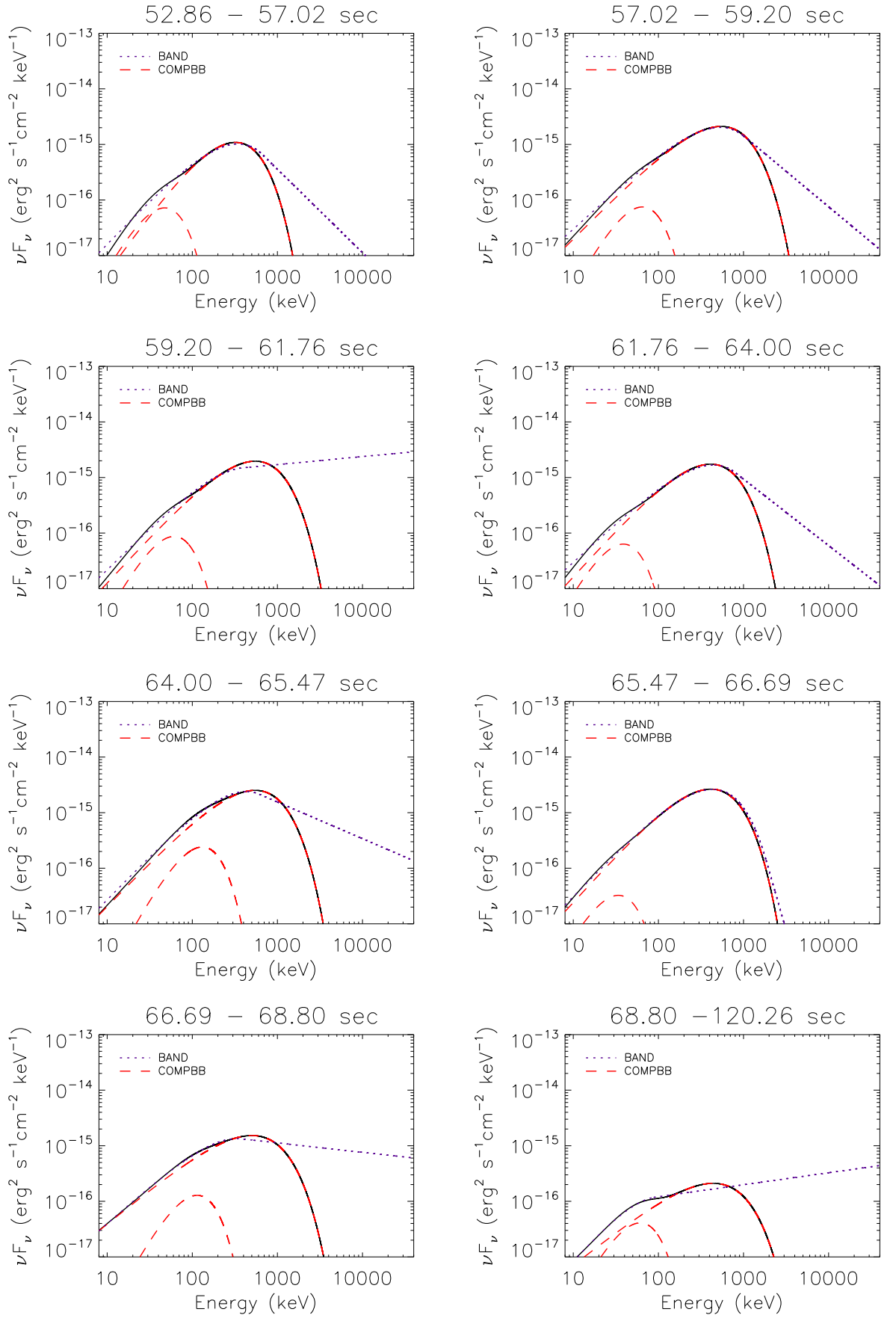


Figure 4.20 Continued.

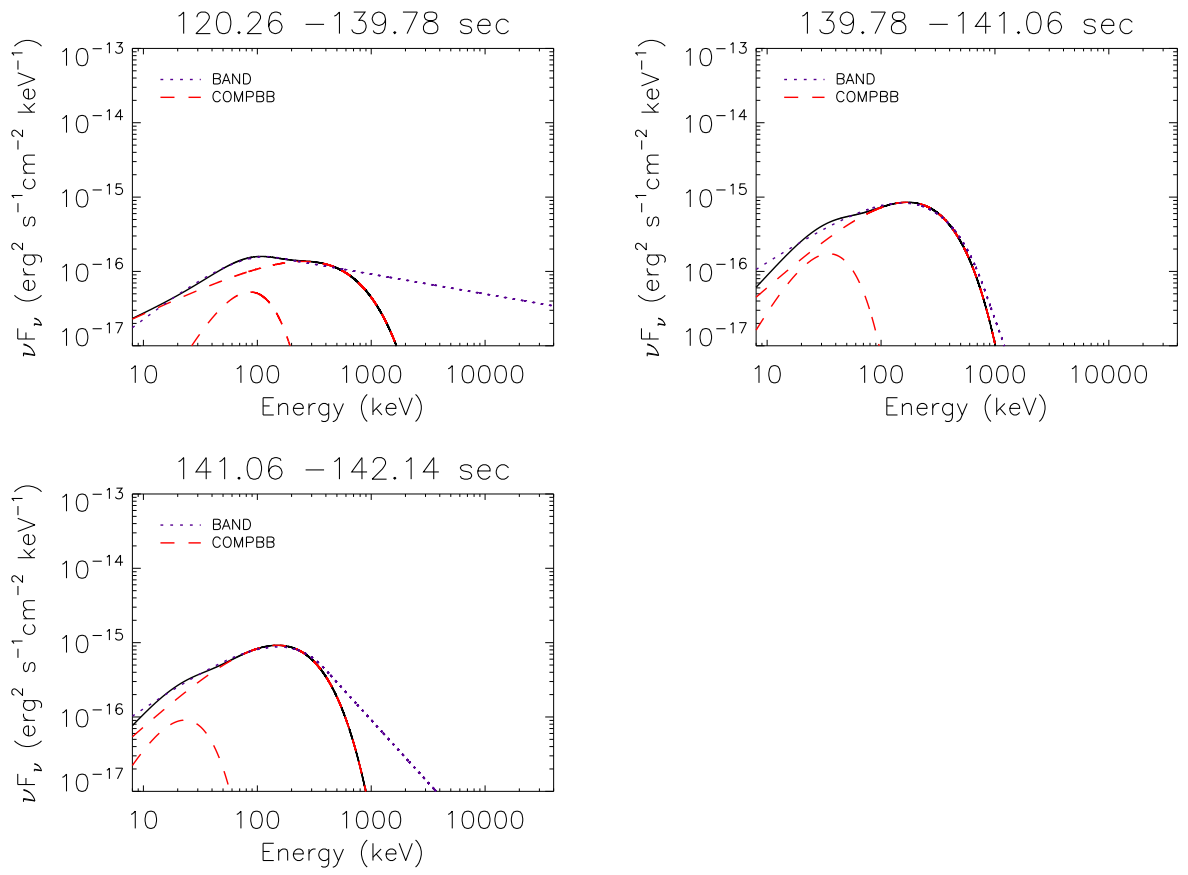


Figure 4.20 Continued.

## 4.5 GRB 100414A

GRB 100414A was detected by Fermi-GBM on 14 April 2010 at 02:20:21.9 UT (Foley, 2010). It is a long burst with duration  $T_{90} \sim 26$  s and peak photon flux  $28.16 \pm 1.05$  photon  $\text{cm}^{-2} \text{s}^{-1}$  in the energy range 10 – 1000 keV. Fermi-LAT also detected a few tens of photons with energies above 100 MeV in the first  $\sim 300$  s after GBM trigger (Takahashi et al., 2010). Cucchiara & Fox (2010) reported redshift measurement of the burst as  $z = 1.368$ . Figure 4.21 shows the count rate history of the burst as seen by the brightest GBM detector NaI11. The detectors, NaI7, NaI11, and BGO1 are used for the spectral analysis.

### 4.5.1 Parameter Evolutions

The prompt emission phase is divided into 21 time intervals as seen in Figure 4.22. For each time bin the time intervals and the fit results of all relevant models are listed in Table 4.5. For 9 time bins  $\beta$  of BAND-only model has only upper limits, and for 4 bins  $\beta$  is relatively steep with undetermined error intervals, i.e., BAND-only being very similar to COMP-only model in shape (with almost same  $E_{\text{peak}}$  and  $\alpha$  values). The BB parameters were not constrained in 2nd and 3rd bins, then we combined these two bins with 4th bin.

Figure 4.22 shows the evolution of BAND and COMPBB model parameters. BAND and COMPBB model fits  $E_{\text{peak}}$  values are between  $\sim 300$  -  $\sim 1000$  keV and they are mostly consistent with each other. Again,  $\alpha$  of single and hybrid model fits of individual time intervals are mostly within their error intervals.  $\alpha$  has a relatively wide range of values and is between  $\sim -1$  -  $\sim 0$ . Only during the first  $\sim 10$  s, additional BB components shifts  $\alpha$  to lower values. Although, for the bins  $\sim 21$  –  $23$   $\alpha$  of COMPBB is higher than that of BAND. kT is relatively steady for the first 9 s at  $\sim 80$  keV, then decreases to  $\sim 10$  keV for later times. There appears increase in kT as the photon flux increases, but the errors are relatively large.

#### 4.5.1.1 Flux Evolutions

Figure 4.23 top and middle panels are showing the evolution of energy flux for thermal and non-thermal components of COMPBB model. Non-thermal flux shows

a slow increase along with the photon count rate. Thermal flux error intervals are relatively high to define a pattern. Bottom panel of Figure 4.23 shows the thermal to total energy flux ratio, and it is ranging from  $\sim 0.4\%$  to  $\sim 37\%$  throughout the burst with an average ratio of  $\sim 7\%$ .

Figure 4.24 shows the  $\nu F_\nu$  spectrum of BAND and BANDBB models with photon counts and residuals, for the time interval 18.30 - 19.46 s, time bin 14. Here, the non-thermal component parameters of BAND-only and BANDBB models, i.e.,  $E_{\text{peak}}$ ,  $\alpha$ , and  $\beta$ , are all consistent with each other, as can be seen in Table 4.5 also. The peak of BB is  $\sim 20$  keV. Figure 4.25 shows the evolution of BAND and COMPBB models in  $\nu F_\nu$  representation throughout the burst.

### 4.5.2 Pulse Simulations

We selected the time interval of the single pulse as;  $-0.512 - 26.240$  s, as seen in Figure 4.21. The spectrum of the pulse has enough emission above  $E_{\text{peak}}$  to be able to constrain the high energy power law index  $\beta$  of the BAND model, with and without BB component. Therefore, the simulations are performed with BAND and BANDBB models. The additional BB component improved the BAND-only fits by  $\Delta CSTAT_{\text{real}} = 15$  units.

The distributions of fit model parameters of both sets of synthetic spectra showed that *BANDBB model is a better representative of the data* than BAND only model, i.e., the fit results of the synthetic spectra produced with BANDBB model parameters are consistent with real fit results of both BAND and BANDBB models. The probability of getting an improvement of  $\geq \Delta CSTAT_{\text{real}}$  in synthetic spectra by chance is 0.1%, which implies the improvement that BB component provides is component statistically significant.

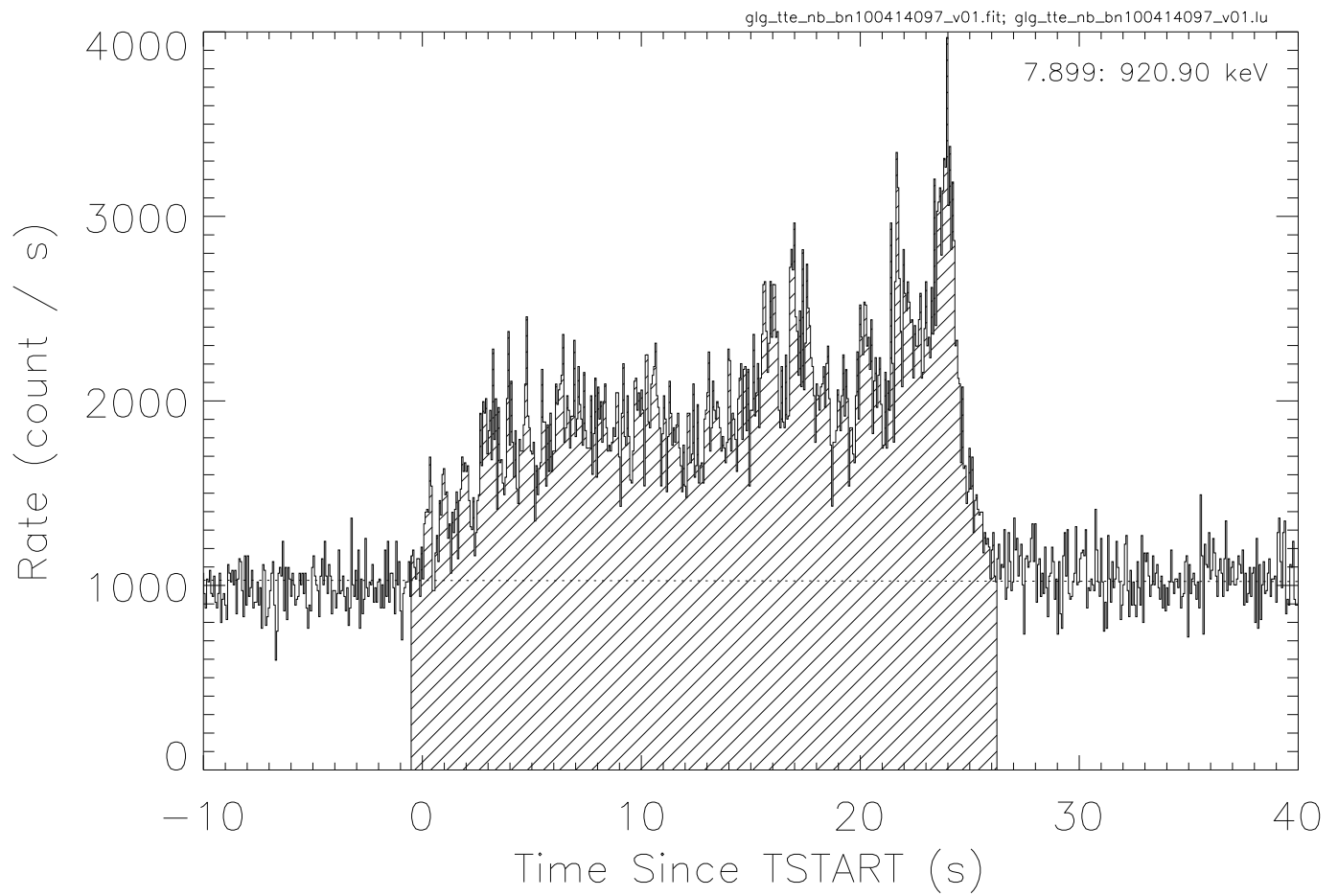


Figure 4.21: The light curve of GRB 100414A with 64 ms resolution. The hatched region represents the time interval of the single pulse used for spectral simulations.

Table 4.5: Fine time interval fit results for GRB 100414A. Best parameter values with their  $1\sigma$  uncertainties.

Bin number	Time interval since trigger		Model	$E_{\text{peak}}$ (keV)	$\alpha$	$\beta$	$kT$ (keV)	Cstat/dof
	$T_{\text{start}}$ (s)	$T_{\text{stop}}$ (s)						
1	-0.51	3.14	BAND	$593^{+52}_{-56}$	$-0.03^{+0.14}_{-0.11}$	$-3.56^{+1}_{-Inf}$	...	405/347
			COMPBB	$790^{+209}_{-147}$	$-0.27^{+0.23}_{-0.22}$	...	$83^{+18}_{-65}$	403/346
2	3.14	4.93	BAND	$452^{+38}_{-31}$	$-0.07 \pm 0.11$	$-3.46^{+1}_{-Inf}$	...	404/347
3	4.93	6.46	BAND	$662^{+55}_{-54}$	$-0.14^{+0.09}_{-0.10}$	$-3.20^{+0.55}_{-Inf}$	...	450/347
4	6.46	7.81	BAND	$509^{+51}_{-48}$	$-0.04^{+0.13}_{-0.11}$	$-2.63^{+0.25}_{-0.46}$	...	377/347
			COMPBB	$785^{+186}_{-449}$	$-0.32^{+0.18}_{-0.17}$	...	$67^{+12}_{-13}$	376/346
2+3+4	3.14	7.81	BAND	$537^{+29}_{-28}$	$-0.11 \pm 0.06$	$-2.97^{+0.28}_{-0.58}$	...	492/347
			COMPBB	$649^{+85}_{-280}$	$-0.26^{+0.12}_{-0.13}$	...	$73^{+14}_{-19}$	493/346
5	7.81	9.15	BAND	$509^{+49}_{-42}$	$-0.13 \pm 0.10$	$-3.8^{+1}_{-Inf}$	...	364/347
			COMPBB	$668^{+213}_{-133}$	$-0.52^{+0.24}_{-0.21}$	...	$79^{+18}_{-18}$	362/346
6	9.15	10.43	BAND	$564^{+29}_{-39}$	$-0.02^{+0.13}_{-0.08}$	$-4.12^{+1}_{-Inf}$	...	429/347
			COMPBB	$520^{+27}_{-24}$	$1.44^{+1.38}_{-1.54}$	...	$29^{+10}_{-14}$	426/346
7	10.43	11.90	BAND	$622^{+43}_{-39}$	$-0.12 \pm 0.09$	$-7.43 \pm Inf$	...	326/347
			COMPBB	$594^{+42}_{-35}$	$0.03^{+0.16}_{-0.48}$	...	$8 \pm 3$	323/346
8	11.90	13.44	BAND	$641^{+52}_{-45}$	$-0.19 \pm 0.09$	$-12 \pm Inf$	...	395/347
			COMPBB	$655(fixed)$	$-0.03^{+0.28}_{-0.39}$	...	$29^{+165}_{-10}$	393/346
9	13.44	14.85	BAND	$598^{+54}_{-53}$	$-0.26^{+0.10}_{-0.09}$	$-3.16^{+0.7}_{-Inf}$	...	383/347
			COMPBB	$581^{+55}_{-45}$	$-0.10^{+0.23}_{-0.24}$	...	$13^{+6}_{-4}$	382/346
			BANDBB	$531^{+71}_{-62}$	$0.06^{+0.36}_{-0.27}$	$-2.83^{+0.36}_{-1.28}$	$13 \pm 4$	381/345
10	14.85	15.74	BAND	$710^{+73}_{-63}$	$-0.58^{+0.07}_{-0.06}$	$-7.63 \pm Inf$	...	366/347
			COMPBB	$672^{+73}_{-61}$	$-0.32^{+0.20}_{-0.44}$	...	$15^{+4}_{-3}$	362/346
11	15.74	16.70	BAND	$590^{+75}_{-68}$	$-0.48^{+0.09}_{-0.08}$	$-2.55^{+0.28}_{-0.64}$	...	359/347
			COMPBB	$609^{+43}_{-39}$	$-0.41(fixed)$	...	$11^{+7}_{-4}$	361/346
			BANDBB	$470^{+94}_{-203}$	$-0.14^{+0.38}_{-0.33}$	$-2.41^{+0.20}_{-0.38}$	$11 \pm 3$	357/345
12	16.70	17.41	BAND	$424^{+37}_{-32}$	$-0.48 \pm 0.08$	$-12 \pm Inf$	...	411/347
			COMPBB	$492^{+51}_{-43}$	$-0.59(fixed)$	...	$50^{+17}_{-11}$	410/346
13	17.41	18.30	BAND	$591^{+68}_{-63}$	$-0.46 \pm 0.08$	$-2.56^{+0.30}_{-0.79}$	...	389/347
			COMPBB	$680^{+101}_{-209}$	$-0.40^{+0.20}_{-0.36}$	...	$28^{+14}_{-10}$	388/346
			BANDBB	$630^{+107}_{-357}$	$-0.35^{+0.25}_{-0.37}$	$-2.63^{+0.30}_{-0.97}$	$25^{+14}_{-9}$	386/345

14	18.30	19.46	BAND	$673^{+67}_{-60}$	$-0.33 \pm 0.09$	$-2.96^{+0.4}_{-1.47}$	...	361/347
			COMPBB	$663^{(fixed)}$	$-0.25^{+0.10}_{-0.25}$	...	$6^{+7}_{-3}$	361/346
			BANDBB	$632^{+72}_{-67}$	$-0.20^{+0.21}_{-0.30}$	$-2.90^{+0.42}_{-1.25}$	$7^{+6}_{-4}$	360/345
15	19.46	20.48	BAND	$481^{+46}_{-52}$	$-0.46^{+0.09}_{-0.08}$	$-3.34^{+0.8}_{-Inf}$	...	369/347
			COMPBB	$551^{+64}_{-52}$	$-0.48^{(fixed)}$	...	$38^{+11}_{-10}$	368/346
16	20.48	21.38	BAND	$564^{+60}_{-56}$	$-0.51^{+0.09}_{-0.08}$	$-2.80^{+0.43}_{-1.69}$	...	381/347
			COMPBB	$510^{+54}_{-42}$	$-0.05^{+0.30}_{-0.25}$	...	$13 \pm 2$	377/346
			BANDBB	$494^{+58}_{-57}$	$-0.02^{+0.36}_{-0.27}$	$-2.91^{+0.49}_{-1.82}$	$13 \pm 2$	376/345
17	21.38	22.08	BAND	$707^{+86}_{-74}$	$-0.72 \pm 0.06$	$-3.48^{+0.80}_{-Inf}$	...	363/347
			COMPBB	$870^{+210}_{-150}$	$-0.82^{+0.34}_{-0.10}$	...	$60^{+22}_{-38}$	361/346
18	22.08	22.78	BAND	$808^{+100}_{-88}$	$-0.74 \pm 0.06$	$-3.37^{+1}_{-Inf}$	...	431/347
			COMPBB	$693^{+88}_{-71}$	$-0.50^{+0.15}_{-0.13}$	...	$8 \pm 2$	427/346
19	22.78	23.55	BAND	$668^{+85}_{-71}$	$-0.70 \pm 0.06$	$-2.61^{+0.30}_{-0.79}$	...	390/347
			COMPBB	$666^{+67}_{-51}$	$-0.60^{(fixed)}$	...	$11^{+95}_{-4}$	391/346
			BANDBB	$626^{+127}_{-313}$	$-0.57^{+0.17}_{-0.13}$	$-2.60^{+0.29}_{-0.68}$	$11^{+110}_{-5}$	389/345
20	23.55	23.94	BAND	$324^{+47}_{-44}$	$-0.43^{+0.13}_{-0.11}$	$-2.35^{+0.20}_{-0.31}$	...	383/347
			COMPBB	$550^{+175}_{-99}$	$-0.65^{+0.19}_{-0.17}$	...	$31 \pm 10$	382/346
21	23.94	24.45	BAND	$589^{+69}_{-60}$	$-0.66^{+0.07}_{-0.06}$	$-2.58^{+0.29}_{-0.71}$	...	388/347
			COMPBB	$431^{+1200}_{-270}$	$-0.77^{+0.28}_{-0.13}$	...	$148^{+28}_{-110}$	386/346
			BANDBB	$211^{+191}_{-86}$	$-0.67^{+0.33}_{-0.18}$	$-1.87^{+0.14}_{-0.25}$	$126^{+15}_{-12}$	381/345

---

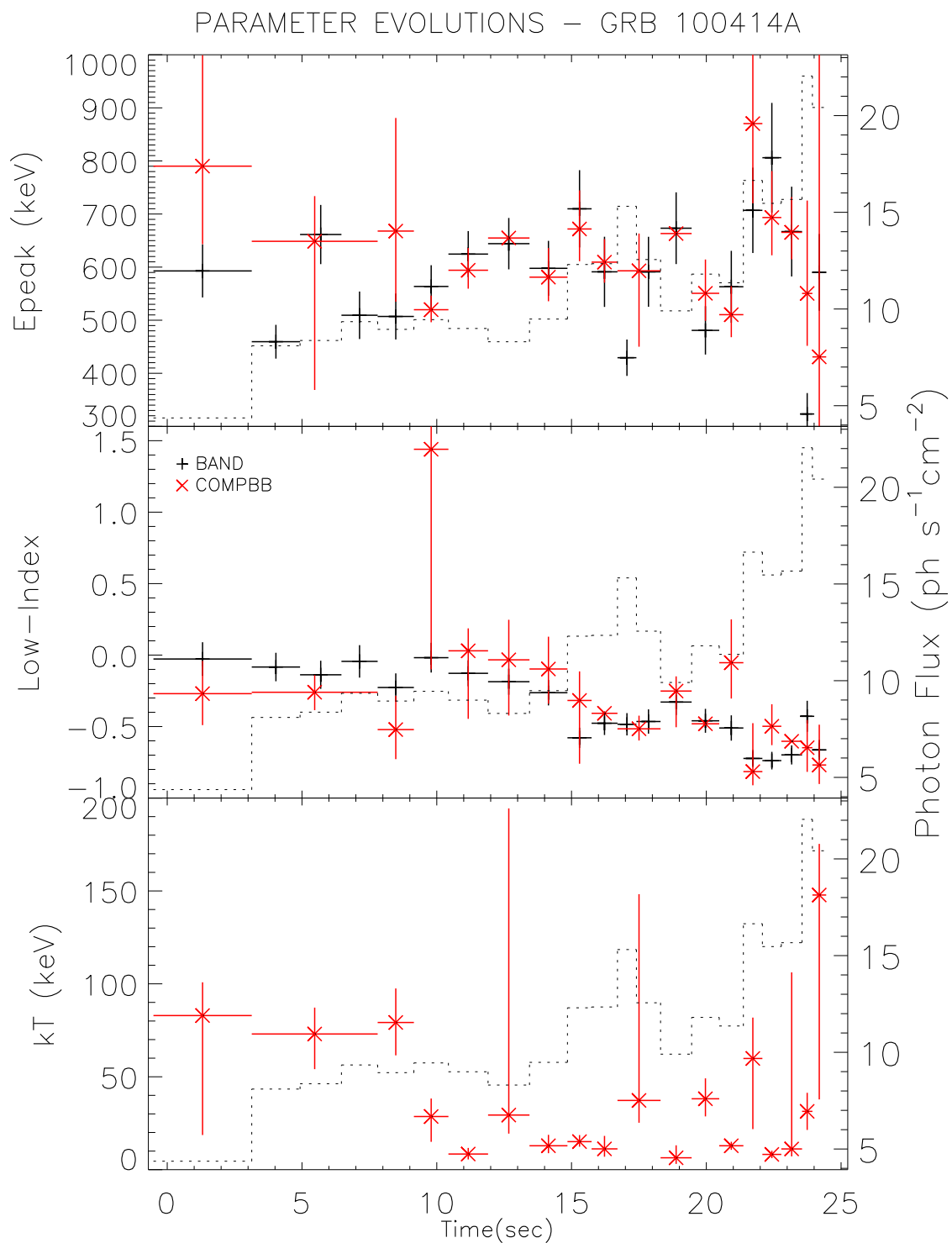


Figure 4.22: The evolution of BAND and COMPBB model parameters for GRB 100414A. The dashed histograms represents the photon fluxes for each time interval (right axis).

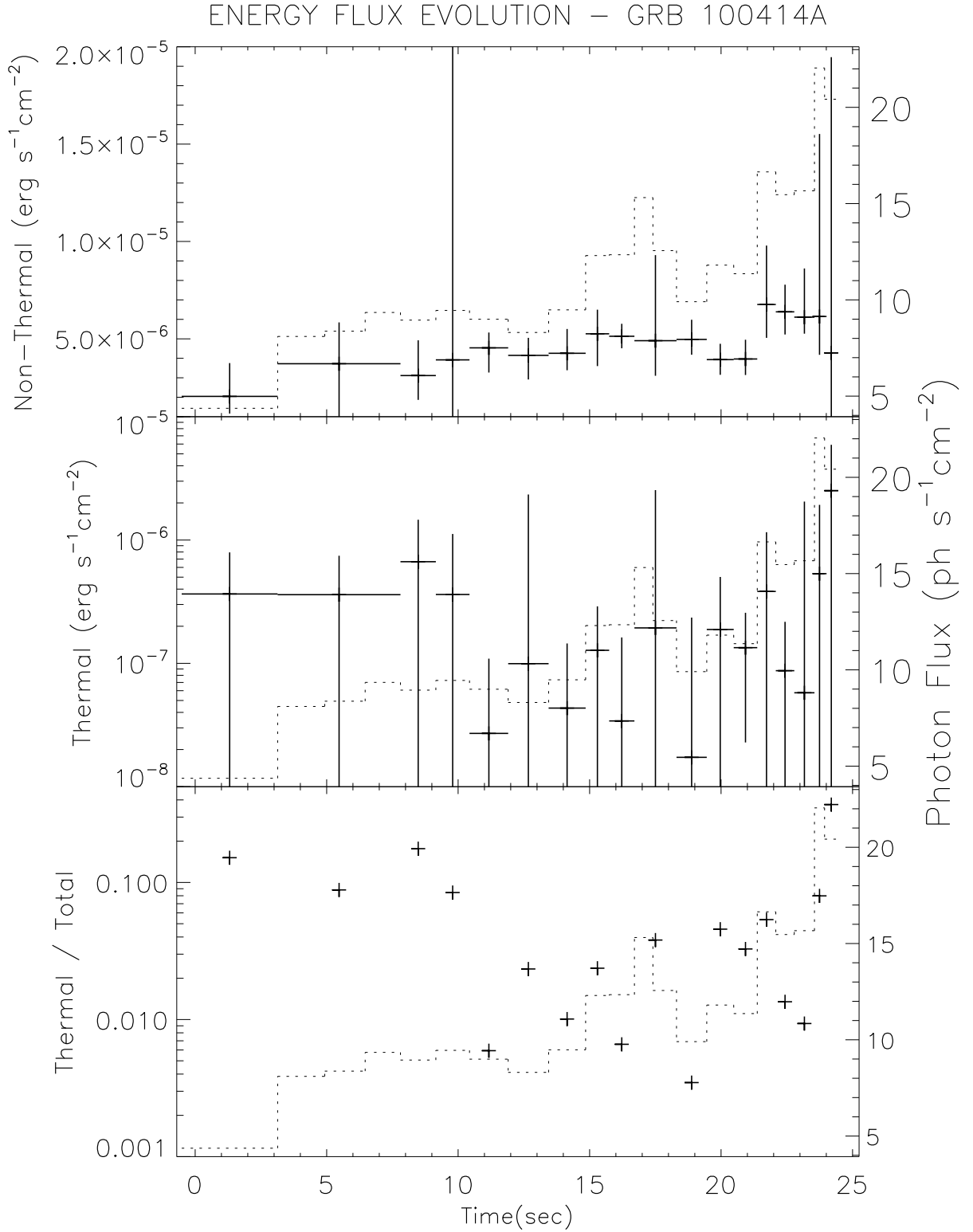


Figure 4.23: The energy flux evolutions of thermal and non-thermal components of COMPBB model for GRB 100414A. The top and middle panels show the energy flux evolutions of COMP and BB models, respectively. The energy flux ratio of thermal to total is seen in the bottom panel. The fluxes are calculated for the energy range 8 keV to 40 MeV. Errors in flux ratio of thermal to total are ignored. The dashed histograms represents the photon fluxes for each time interval (right axis).

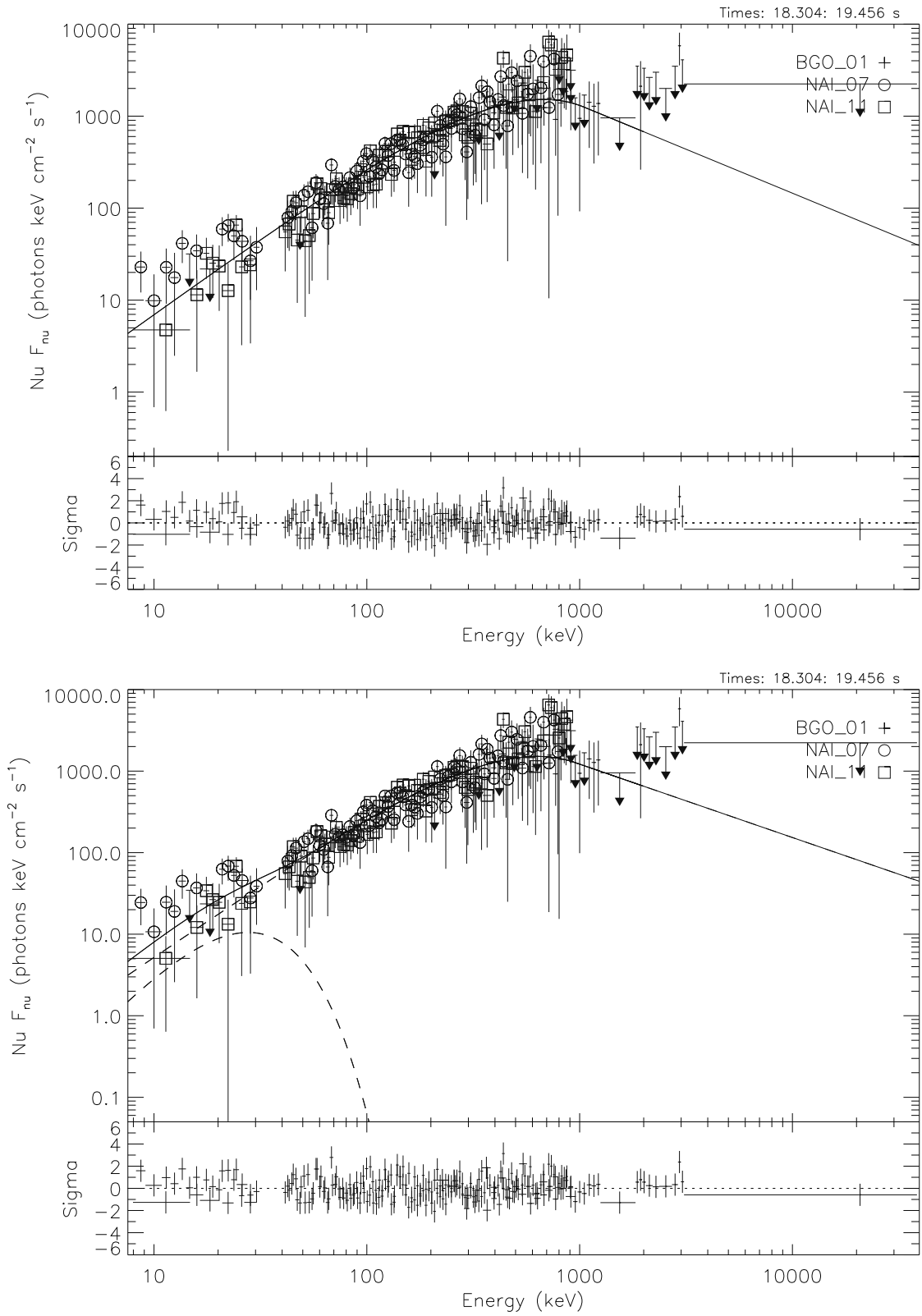


Figure 4.24: The  $\nu F_\nu$  spectrum of BAND and BANDBB models with photon counts and residuals, for the time interval 18.30 - 19.46 s of GRB 100414A, time bin 14.

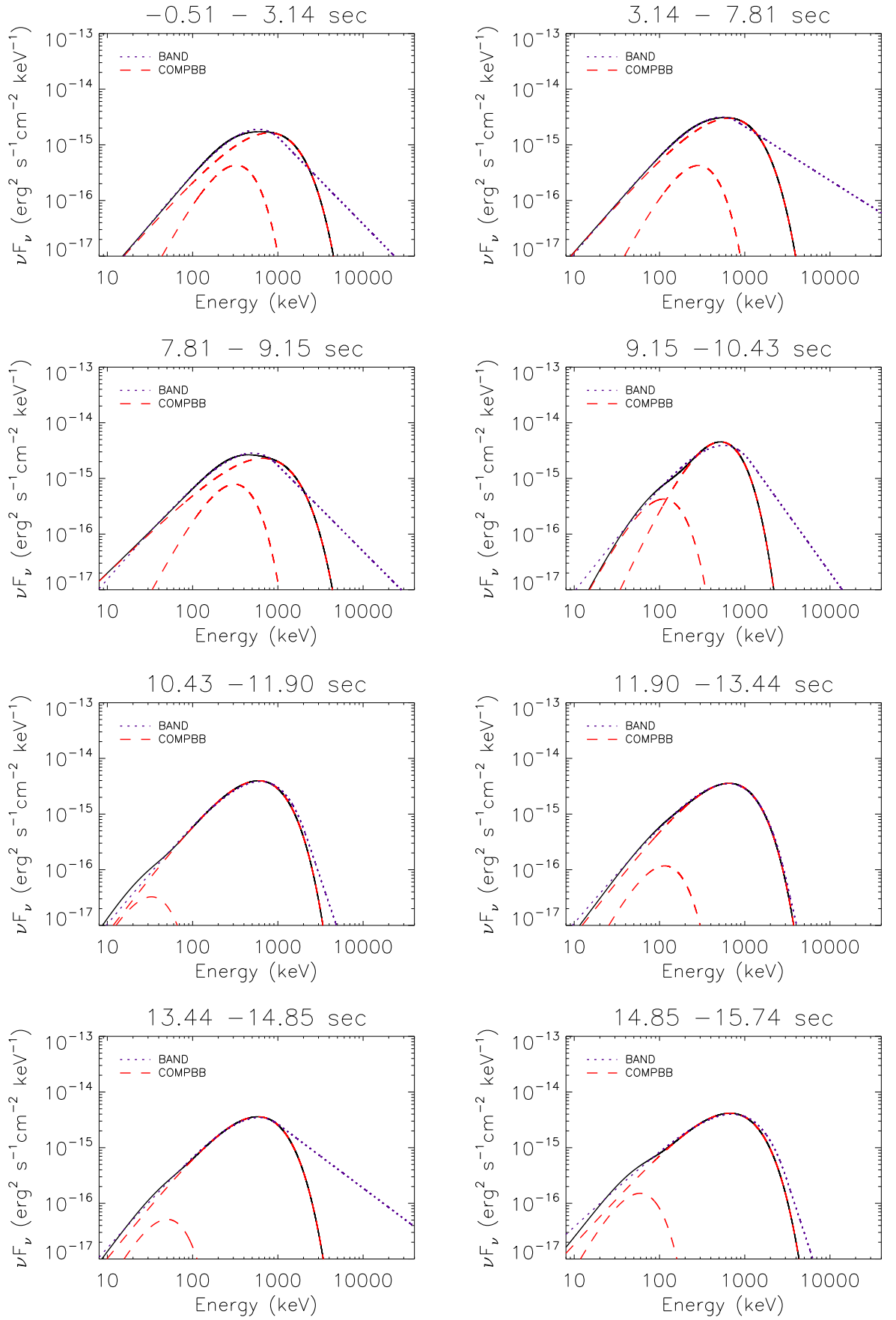


Figure 4.25: The model evolutions for GRB 100414A in  $\nu F_\nu$  representation. The solid line represents the COMPBB model where the dashed lines show the COMP and BB components separately. The dotted line is denoting the BAND model.

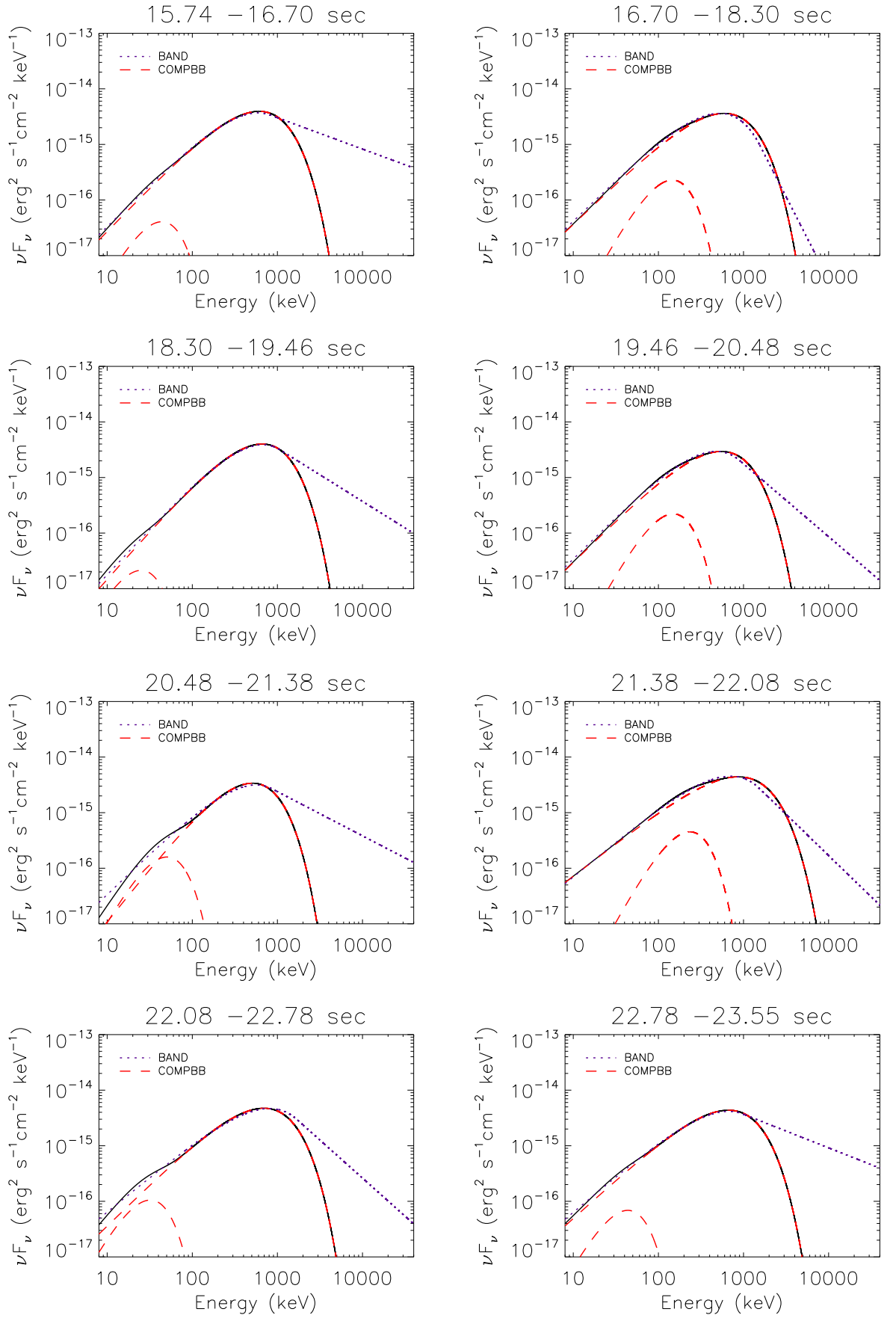


Figure 4.25 Continued.

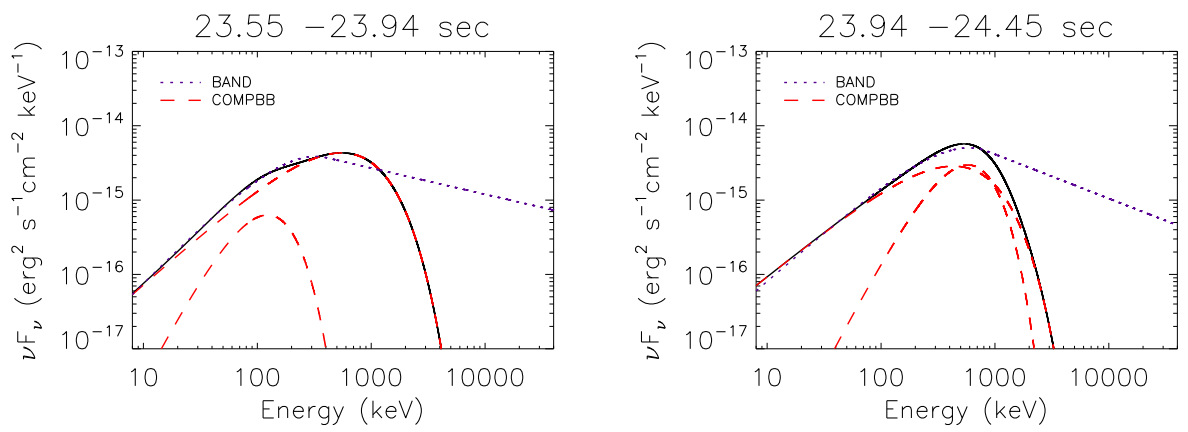


Figure 4.25 Continued.

## 4.6 GRB 100918A

GRB 100918A was detected by Fermi-GBM on 18 September 2010 at 20:42:18.0 UT (von Kienlin et al., 2014). It is a long burst with duration  $T_{90} \sim 86$  s and peak photon flux  $10.94 \pm 0.79$  photon  $\text{cm}^{-2} \text{s}^{-1}$  in the energy range 10 – 1000 keV. Figure 4.26 shows the count rate history of the burst as seen by the brightest GBM detector NaI11, and selected region is the pulse interval used for the spectral simulations. The detectors, NaI8, NaI11, and BGO1 are used for the spectral analysis.

### 4.6.1 Parameter Evolutions

The prompt phase is divided into 45 time intervals as seen in Figure 4.27. For each time bin the time intervals and the fit results of all relevant models are listed in Table 4.6. For 13 time bins  $\beta$  of BAND-only model has only upper limits. For 14 time bins  $\beta$  has very negative values with undetermined error intervals. BB model parameters were not constrained for the bins: 1, 2, 5, 6, 8, 9, 17, 25, 26, 32, 35, 38, and 40. Then, we combined the bins as; 1 and 2 with 3, 5 with 4, 6 with 7, 8 and 9 with 10, 17 with 18, 25 and 26 with 27, 32 with 33, 35 with 36, 38 with 39, and 40 with 41. BANDBB model parameters are constrained for 9 time intervals.

Figure 4.27 shows the evolution of BAND and COMPBB model parameters.  $E_{\text{peak}}$  values are between  $\sim 100$  -  $\sim 2000$  keV. BAND-only and COMPBB peak energies are mostly similar to each other for individual bins, except for the several bins at around 55, 65 and 90 s, where  $E_{\text{peak}}$  of COMPBB is higher than that of BAND-only.  $\alpha$  takes values between  $\sim -1.2$  -  $0.2$ , and it is variable for both single and hybrid models. Including BB component in fits makes  $\alpha$  shift to lower values for some of the bins (e.g. at  $\sim 65$  s), and to higher values for some others (e.g.  $\sim 107$  s).  $kT$  is mostly in the range  $\sim 10$  -  $\sim 50$ , and varying without following any particular trend and seems not to be correlated with photon flux history. For example, for the bins at around 60 s, during which the photon flux shows an increase, the temperature also increases up to  $\sim 150$  keV, but after it sharply and significantly decreases, independently from photon flux history.

#### 4.6.1.1 Flux Evolutions

Figure 4.28 shows the evolution of energy flux for thermal and non-thermal components of COMPBB model. Non-thermal energy flux is mostly following the photon flux history of the burst. Since the errors in energy flux of thermal component are relatively large, it is not possible to assign a particular trend. For the bins  $\sim 65$  the  $\alpha$  is lowered and  $E_{\text{peak}}$  is increased significantly. However for the bin  $\sim 107$   $\alpha$  is significantly increased. The thermal to total energy flux ratio is ranging from  $\sim 0.4\%$  to  $\sim 29\%$  throughout the burst with an average ratio of  $\sim 6\%$ .

Figure 4.29 shows the  $\nu F_\nu$  spectrum of BAND and COMPBB models with photon counts and residuals, for the time interval 57.98 - 59.26 s, time bin 18. When BB included in fits  $E_{\text{peak}}$  shifts from  $\sim 950$  keV to  $\sim 1700$  keV, and  $\alpha$  values of the two models are consistent with each other, as can be seen in Table 4.6 also. The peak of BB is  $\sim 100$  keV. Figure 4.30 shows the evolution of BAND and COMPBB models in  $\nu F_\nu$  representation throughout the burst.

#### 4.6.2 Pulse Simulations

We selected the time interval of the pulse as  $-3.520 - 120.192$  s, as seen in Figure 4.26. The spectrum of each pulse has enough emission above  $E_{\text{peak}}$  to be able to constrain the high energy power law index  $\beta$  of the BAND model, with and without BB component. Therefore, the simulations are performed with BAND and BANDBB models. The additional BB component improved the BAND-only fit by  $\Delta CSTAT_{\text{real}} = 13$  units.

The distributions of fit model parameters of both sets of synthetic spectra showed that *BANDBB model is a better representative of the data* than BAND only model. The probability of getting an improvement of  $\geq \Delta CSTAT_{\text{real}}$  in synthetic spectra of individual pulses by chance is 1.57%. We conclude that the level of CSTAT improvement is not enough to confirm thermal component statistically significantly, however the hybrid model (BANDBB) is a better representative of the data.

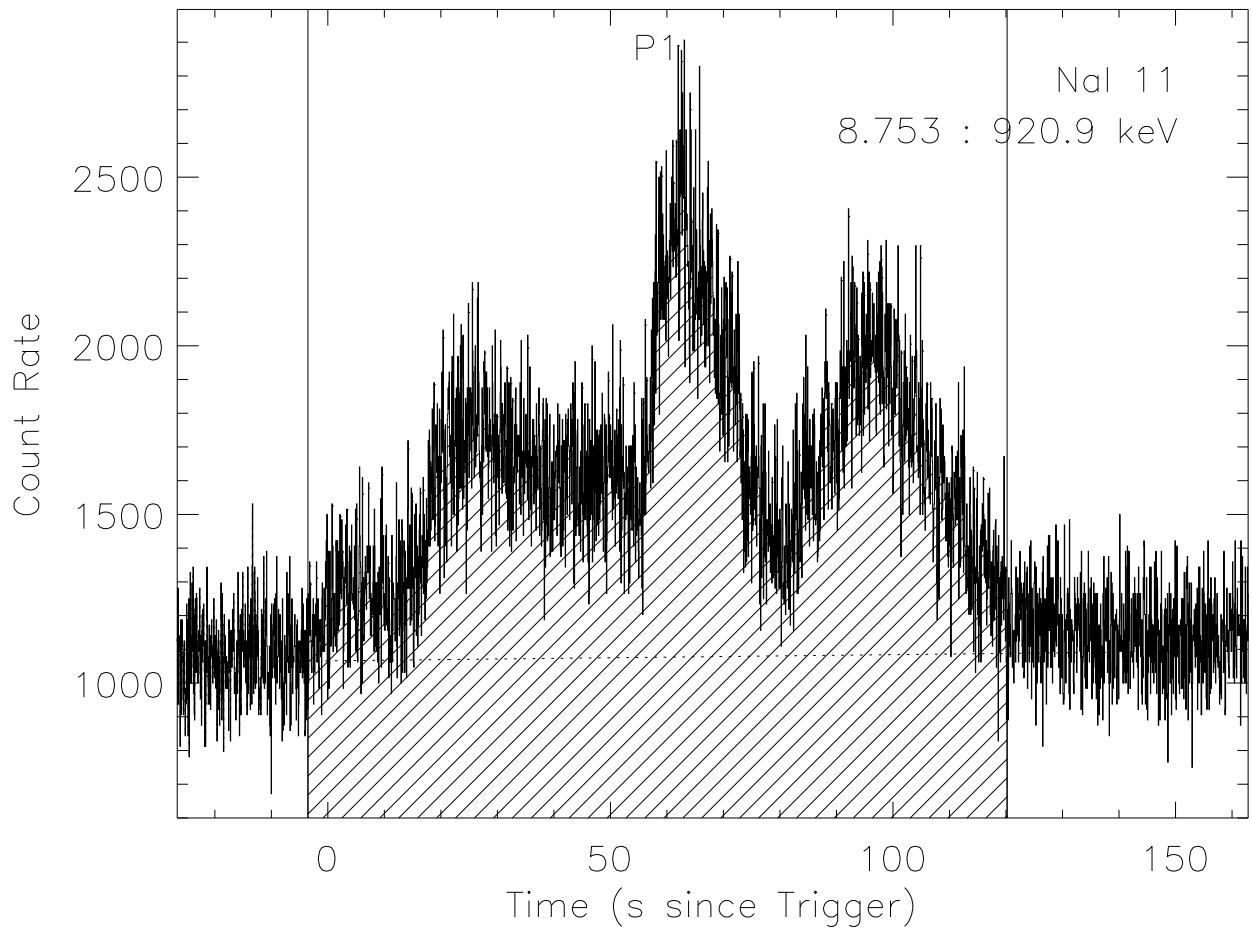


Figure 4.26: The light curve of GRB 100918A with 64 ms resolution. Vertical lines define the interval of the single pulse used for spectral simulations, and indicated as P1.

Table 4.6: Fine time interval fit results for GRB 100918A. Best parameter values with their  $1\sigma$  uncertainties.

Bin number	Time interval since trigger		Model	$E_{\text{peak}}$ (keV)	$\alpha$	$\beta$	$kT$ (keV)	Cstat/dof
	$T_{\text{start}}(s)$	$T_{\text{stop}}(s)$						
1	-3.52	5.57	BAND	$274_{-32}^{+41}$	$-0.13_{-0.23}^{+0.29}$	$-10.8 \pm Inf$	...	518/344
2	5.57	14.27	BAND	$150_{-32}^{+41}$	$-0.46_{-0.26}^{+0.32}$	$-2.12_{-0.42}^{+0.23}$	...	388/344
3	14.27	19.20	BAND	$431_{-61}^{+64}$	$-0.56_{-0.10}^{+0.12}$	$-2.74_{-2.27}^{+0.46}$	...	458/344
1+2+3	-3.52	19.20	BAND	$321_{-30}^{+29}$	$-0.57_{-0.09}^{+0.10}$	$-7.7 \pm Inf$	...	675/344
			COMPBB	$360_{-47}^{+38}$	$-0.58(\text{fixed})$	...	$26_{-7}^{+8}$	673/343
4	19.20	21.95	BAND	$478_{-59}^{+35}$	$-0.52_{-0.07}^{+0.13}$	$-3.8_{-Inf}^{+0.99}$	...	443/344
			COMPBB	$398_{-47}^{+72}$	$-0.07_{-0.48}^{+0.77}$	...	$10_{-4}^{+3}$	437/343
4+5	19.20	24.45	BAND	$428_{-32}^{+22}$	$-0.40_{-0.06}^{+0.09}$	$-4.17_{-Inf}^{+1.07}$	...	507/344
			COMPBB	$389_{-23}^{+26}$	$-0.10_{-0.17}^{+0.20}$	...	$8_{-3}^{+2}$	502/343
6+7	24.45	28.80	BAND	$407_{-33}^{+29}$	$-0.54_{-0.06}^{+0.07}$	$-3.99_{-Inf}^{+1.28}$	...	393/344
			COMPBB	$445_{-69}^{+49}$	$-0.68(\text{fixed})$	...	$66_{-18}^{+34}$	392/343
8+9+10	28.80	37.18	BAND	$382_{-29}^{+32}$	$-0.61 \pm 0.06$	$-2.90_{-1.40}^{+0.31}$	...	456/344
			COMPBB	$459_{-49}^{+65}$	$-0.66_{-0.08}^{+0.09}$	...	$28 \pm 8$	454/343
11	37.18	40.38	BAND	$291_{-97}^{+64}$	$-0.61_{-0.13}^{+0.27}$	$-2.10_{-0.30}^{+0.24}$	...	380/344
			COMPBB	$446_{-63}^{+95}$	$-0.22_{-0.75}^{+0.64}$	...	$17 \pm 2$	370/343
			BANDBB	$394_{-55}^{+61}$	$2.13_{-1.84}^{+4.28}$	$-2.30_{-0.37}^{+0.24}$	$17 \pm 2$	366/342
12	40.38	43.20	BAND	$463_{-146}^{+110}$	$-0.73_{-0.10}^{+0.19}$	$-2.28_{-1.16}^{+0.38}$	...	358/344
			COMPBB	$689_{-150}^{+298}$	$-0.79_{-0.14}^{+0.14}$	...	$29_{-8}^{+9}$	356/343
			BANDBB	$643_{-511}^{+244}$	$-0.78_{-0.13}^{+0.14}$	$-2.36_{-1.30}^{+0.32}$	$30_{-8}^{+9}$	354/342
13	43.20	46.21	BAND	$347_{-111}^{+83}$	$-0.60_{-0.13}^{+0.25}$	$-2.26_{-1.01}^{+0.37}$	...	383/344
			COMPBB	$450_{-206}^{+113}$	$-0.43_{-0.81}^{+0.42}$	...	$18_{-4}^{+6}$	380/343
14	46.21	49.22	BAND	$380_{-72}^{+88}$	$-0.77_{-0.11}^{+0.12}$	$-2.70_{-Inf}^{+0.58}$	...	348/344
			COMPBB	$446_{-64}^{+82}$	$-0.77(\text{fixed})$	...	$20_{-12}^{+13}$	347/343
15	49.22	52.61	BAND	$484_{-99}^{+93}$	$-0.82_{-0.08}^{+0.10}$	$-2.60_{-Inf}^{+0.50}$	...	360/344
			COMPBB	$553_{-215}^{+145}$	$-0.76_{-0.40}^{+0.19}$	...	$19_{-5}^{+11}$	358/343
16	52.61	55.81	BAND	$548_{-119}^{+130}$	$-0.73_{-0.10}^{+0.12}$	$-2.21_{-0.42}^{+0.26}$	...	342/344
			COMPBB	$1304_{-525}^{+675}$	$-0.92_{-0.12}^{+0.18}$	...	$34_{-12}^{+16}$	342/343
17	55.81	57.98	BAND	$975_{-195}^{+223}$	$-0.86_{-0.07}^{+0.08}$	$-2.88_{-Inf}^{+0.61}$	...	340/344

18	57.98	59.26	BAND	$961^{+348}_{-176}$	$-0.85^{+0.07}_{-0.07}$	$-2.46^{+0.28}_{-1.41}$	...	328/344
			COMPBB	$1684^{+381}_{-315}$	$-0.93^{+0.07}_{-0.06}$	...	$39^{+12}_{-10}$	323/343
17+18	57.98	59.26	BAND	$969^{+145}_{-172}$	$-0.86 \pm 0.05$	$-2.61^{+0.32}_{-0.78}$	...	336/344
			COMPBB	$1377^{+304}_{-920}$	$-0.95^{+0.07}_{-0.06}$	...	$65 \pm 030$	336/343
19	59.26	60.54	BAND	$1112^{+165}_{-147}$	$-0.87^{+0.06}_{-0.04}$	$-9.3 \pm Inf$	...	417/344
			COMPBB	$1188^{+319}_{-265}$	$-1.02^{+0.22}_{-0.09}$	...	$146^{+43}_{-25}$	413/343
20	60.54	61.70	BAND	$706^{+113}_{-100}$	$-0.78^{+0.07}_{-0.06}$	$-2.45^{+0.28}_{-0.56}$	...	344/344
			COMPBB	$728^{+131}_{-99}$	$-0.65^{+0.19}_{-0.13}$	...	$15^{+5}_{-3}$	345/343
			BANDBB	$654^{+140}_{-372}$	$-0.58^{+0.25}_{-0.17}$	$-2.43^{+0.25}_{-0.57}$	$14^{+5}_{-3}$	342/342
21	61.70	62.78	BAND	$844^{+145}_{-130}$	$-0.82^{+0.07}_{-0.06}$	$-2.49^{+0.30}_{-0.60}$	...	364/344
			COMPBB	$1027^{+228}_{-172}$	$-0.83^{+0.10}_{-0.20}$	...	$24^{+15}_{-10}$	365/343
			BANDBB	$886^{+193}_{-573}$	$-0.79^{+0.14}_{-0.08}$	$-2.53^{+0.31}_{-0.66}$	$21^{+15}_{-9}$	363/342
22	62.78	63.87	BAND	$947^{+196}_{-134}$	$-0.82^{+0.06}_{-0.06}$	$-2.7^{+0.36}_{-1.98}$	...	325/344
			COMPBB	$979^{+119}_{-100}$	$-0.76(fixed)$	...	$10^{+5}_{-4}$	325/343
			BANDBB	$798^{+152}_{-101}$	$-0.62^{+0.16}_{-0.14}$	$-2.6^{+0.25}_{-0.54}$	$10 \pm 3$	322/342
23	63.87	65.02	BAND	$609^{+128}_{-123}$	$-0.72^{+0.11}_{-0.08}$	$-2.36^{+0.28}_{-0.56}$	...	392/344
			COMPBB	$1156^{+560}_{-325}$	$-0.94^{+0.12}_{-0.11}$	...	$56^{+11}_{-12}$	391/343
24	65.02	66.24	BAND	$621^{+111}_{-89}$	$-0.78^{+0.08}_{-0.07}$	$-2.49^{+0.29}_{-0.58}$	...	334/344
			COMPBB	$1432^{+555}_{-501}$	$-1.04^{+0.12}_{-0.08}$	...	$58^{+13}_{-12}$	334/343
25	66.24	67.58	BAND	$1112^{+207}_{-179}$	$-0.96^{+0.006}_{-0.05}$	$-5.9 \pm Inf$	...	452/344
26	67.58	68.99	BAND	$902^{+145}_{-173}$	$-0.91^{+0.08}_{-0.05}$	$-7.04 \pm Inf$	...	406/344
27	68.99	70.59	BAND	$743^{+165}_{-123}$	$-0.89 \pm 0.07$	$-2.94^{+0.59}_{-Inf}$	...	393/344
			COMPBB	$631^{+136}_{-95}$	$-0.61^{+0.23}_{-0.48}$	...	$10 \pm 2$	390/343
25+26+27	66.24	70.59	BAND	$917^{+98}_{-93}$	$-0.93 \pm 0.03$	$-9.95 \pm Inf$	...	410/344
			COMPBB	$881^{+84}_{-66}$	$-0.89(fixed)$	...	$10^{+11}_{-6}$	409/343
28	70.59	72.13	BAND	$710^{+191}_{-147}$	$-0.92^{+0.09}_{-0.07}$	$-2.60^{+0.44}_{-3.76}$	...	332/344
			COMPBB	$1187^{+673}_{-427}$	$-1.04^{+0.14}_{-0.10}$	...	$46^{+18}_{-27}$	332/343
29	72.13	74.37	BAND	$235^{+62}_{-47}$	$-0.65^{+0.17}_{-0.14}$	$-1.88^{+0.11}_{-0.17}$	...	376/344
			COMPBB	$596^{+500}_{-186}$	$-1.00^{+0.17}_{-0.16}$	...	$31^{+8}_{-11}$	379/343
30	74.37	77.82	BAND	$353^{+72}_{-77}$	$-0.81^{+0.13}_{-0.10}$	$-2.62^{+0.56}_{-Inf}$	...	412/344
			COMPBB	$375^{+77}_{-53}$	$-0.60^{+0.38}_{-0.22}$	...	$13^{+6}_{-3}$	410/343
31	77.82	82.30	BAND	$185^{+124}_{-45}$	$-0.71^{+0.25}_{-0.26}$	$-2.01^{+0.19}_{-Inf}$	...	406/344
			COMPBB	$311^{+71}_{-51}$	$-0.96(fixed)$	...	$27^{+18}_{-8}$	405/343

32	82.30	85.95	BAND	$497 \pm 170$	$-0.98^{+0.09}_{-0.08}$	$-2.36^{+0.4}_{-1.1}$	...	375/344
33	85.95	88.32	BAND	$1251^{+430}_{-310}$	$-0.99^{+0.07}_{-0.06}$	$-2.30^{+0.29}_{-0.65}$	...	367/344
			COMPBB	$1681^{+628}_{-510}$	$-0.98^{+0.14}_{-0.25}$	...	$19^{+13}_{-7}$	367/343
			BANDBB	$1188^{+546}_{-317}$	$-0.89^{+0.17}_{-0.30}$	$-2.27^{+0.25}_{-0.67}$	$15^{+10}_{-5}$	365/342
32+33	82.30	88.32	BAND	$707^{+222}_{-128}$	$-0.99 \pm 0.06$	$-2.13^{+0.18}_{-0.44}$	...	385/344
			COMPBB	$1207^{+270}_{-460}$	$-1.06(\text{fixed})$	...	$28^{+18}_{-9}$	386/343
34	88.32	90.56	BAND	$878^{+161}_{-129}$	$-0.85 \pm 0.07$	$-8.61 \pm Inf$	...	375/344
			COMPBB	$1059^{+187}_{-151}$	$-0.87(\text{fixed})$	...	$38^{+13}_{-10}$	373/343
35	90.56	92.48	BAND	$745^{+156}_{-111}$	$-0.87 \pm 0.07$	$-3.31^{+0.68}_{-Inf}$	...	349/344
36	92.48	94.27	BAND	$1080^{+255}_{-351}$	$-.95^{+0.11}_{-0.06}$	$-5.60 \pm Inf$	...	396/344
			COMPBB	$1492^{+507}_{-373}$	$-1.07^{+0.09}_{-0.08}$	...	$85^{+22}_{-21}$	393/343
35+36	90.56	94.27	BAND	$825^{+195}_{-109}$	$-0.89^{+0.05}_{-0.06}$	$-2.98^{+0.50}_{-Inf}$	...	331/344
			COMPBB	$1083^{+321}_{-574}$	$-1.00^{+0.13}_{-0.08}$	...	$84^{+57}_{-46}$	330/343
37	94.27	95.87	BAND	$848^{+237}_{-121}$	$-0.78^{+0.07}_{-0.09}$	$-3.20^{+0.60}_{-Inf}$	...	359/344
			COMPBB	$1009^{+245}_{-181}$	$-0.74 \pm 0.14$	...	$24^{+10}_{-6}$	356/343
38	95.87	97.41	BAND	$966^{+179}_{-157}$	$-0.92^{+0.06}_{-0.05}$	$-8.40 \pm Inf$	...	361/344
39	97.41	99.20	BAND	$713^{+132}_{-104}$	$-0.87^{+0.07}_{-0.06}$	$-4.5 \pm Inf$	...	390/344
			COMPBB	$646^{+123}_{-88}$	$-0.59^{+0.23}_{-0.44}$	...	$13 \pm 2$	385/343
38+39	95.87	99.20	BAND	$828^{+105}_{-92}$	$-0.90^{+0.05}_{-0.04}$	$-9.43 \pm Inf$	...	394/344
			COMPBB	$794^{+80}_{-69}$	$-0.81(\text{fixed})$	...	$13^{+4}_{-3}$	393/343
40	99.20	101.06	BAND	$538^{+125}_{-102}$	$-0.83^{+0.09}_{-0.08}$	$-2.18^{+0.22}_{-0.46}$	...	391/344
41	101.06	103.23	BAND	$658^{+173}_{-105}$	$-0.95 \pm 0.07$	$-2.76^{+0.66}_{-Inf}$	...	363/344
			COMPBB	$617^{+145}_{-101}$	$-0.76^{+0.24}_{-0.18}$	...	$11^{+4}_{-3}$	362/343
40+41	99.20	103.23	BAND	$609^{+93}_{-84}$	$-0.90^{+0.06}_{-0.05}$	$-2.36^{+0.28}_{-0.77}$	...	408/344
			COMPBB	$607^{+99}_{-75}$	$-0.76^{+0.15}_{-0.12}$	...	$11^{+3}_{-2}$	407/343
			BANDBB	$535^{+104}_{-107}$	$-0.69^{+0.24}_{-0.15}$	$-2.34^{+0.28}_{-0.64}$	$10 \pm 2$	405/342
42	103.23	105.15	BAND	$632^{+171}_{-95}$	$-0.93^{+0.07}_{-0.08}$	$-2.14^{+0.18}_{-0.48}$	...	360/344
			COMPBB	$591^{+161}_{-99}$	$-0.68^{+0.29}_{-0.44}$	...	$10^{+3}_{-2}$	361/343
43	105.15	108.03	BAND	$520^{+109}_{-112}$	$-0.94^{+0.10}_{-0.08}$	$-3.22^{+0.84}_{-Inf}$	...	377/344
			COMPBB	$388^{+76}_{-53}$	$-0.37^{+0.38}_{-0.28}$	...	$8 \pm 2$	370/343
			BANDBB	$330^{+74}_{-47}$	$-0.11^{+0.52}_{-0.39}$	$-2.52^{+0.31}_{-0.94}$	$9 \pm 2$	369/342
44	108.03	111.42	BAND	$338^{+71}_{-57}$	$-0.99^{+0.10}_{-0.09}$	$-7.16 \pm Inf$	...	318/344
			COMPBB	$402^{+99}_{-69}$	$-1.01(\text{fixed})$	...	$19^{+10}_{-7}$	317/343

45	11.42	116.54	BAND	$174^{+55}_{-46}$	$-0.89^{+0.22}_{-0.16}$	$-2.10^{+0.22}_{-0.41}$	...	378/344
			COMPBB	$338^{+129}_{-81}$	$-1.19(\textit{fixed})$	...	$26^{+12}_{-8}$	379/343

---

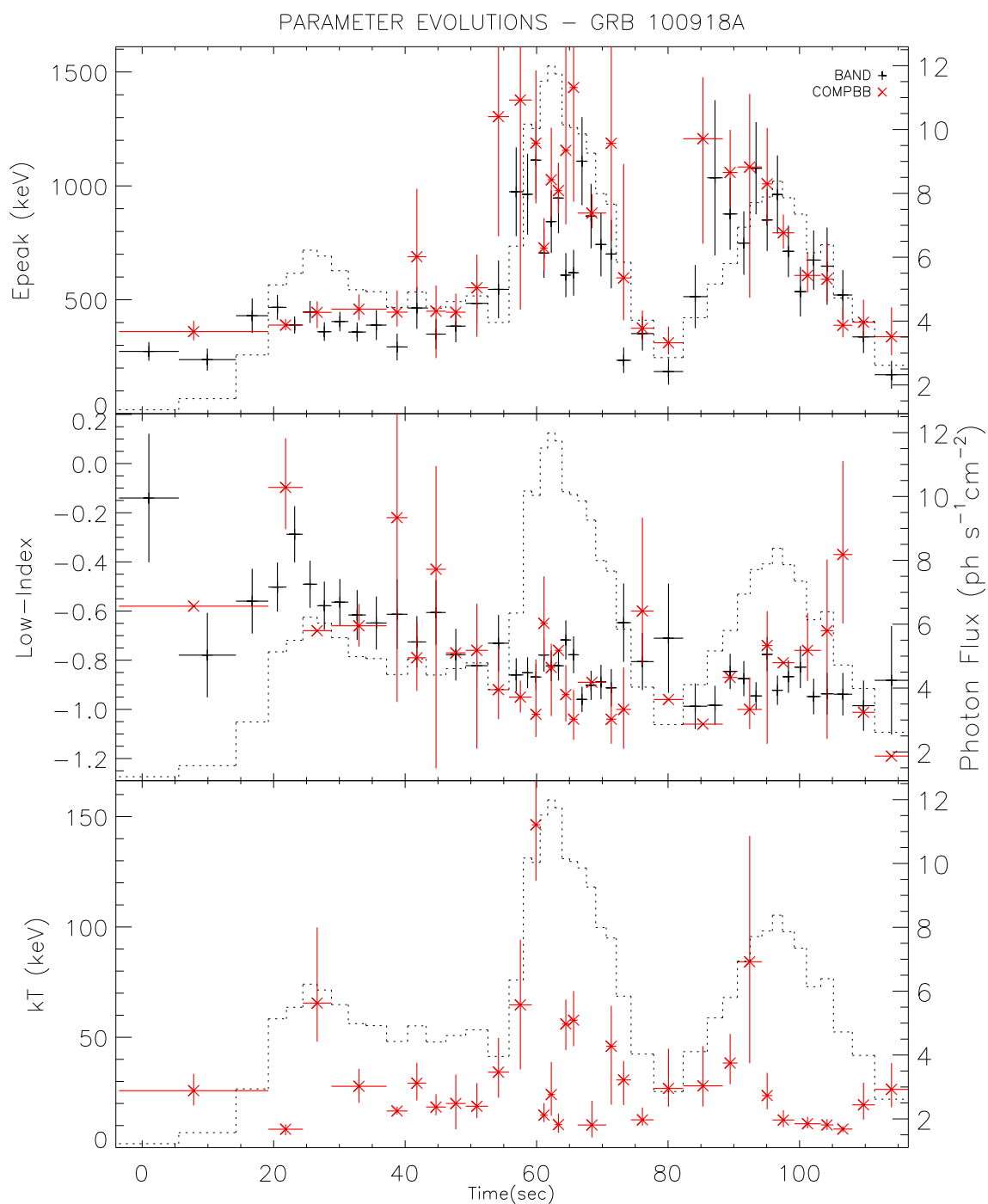


Figure 4.27: The evolution of BAND and COMPBB model parameters for GRB 100918A. The dashed histograms represents the photon fluxes for each time interval (right axis).

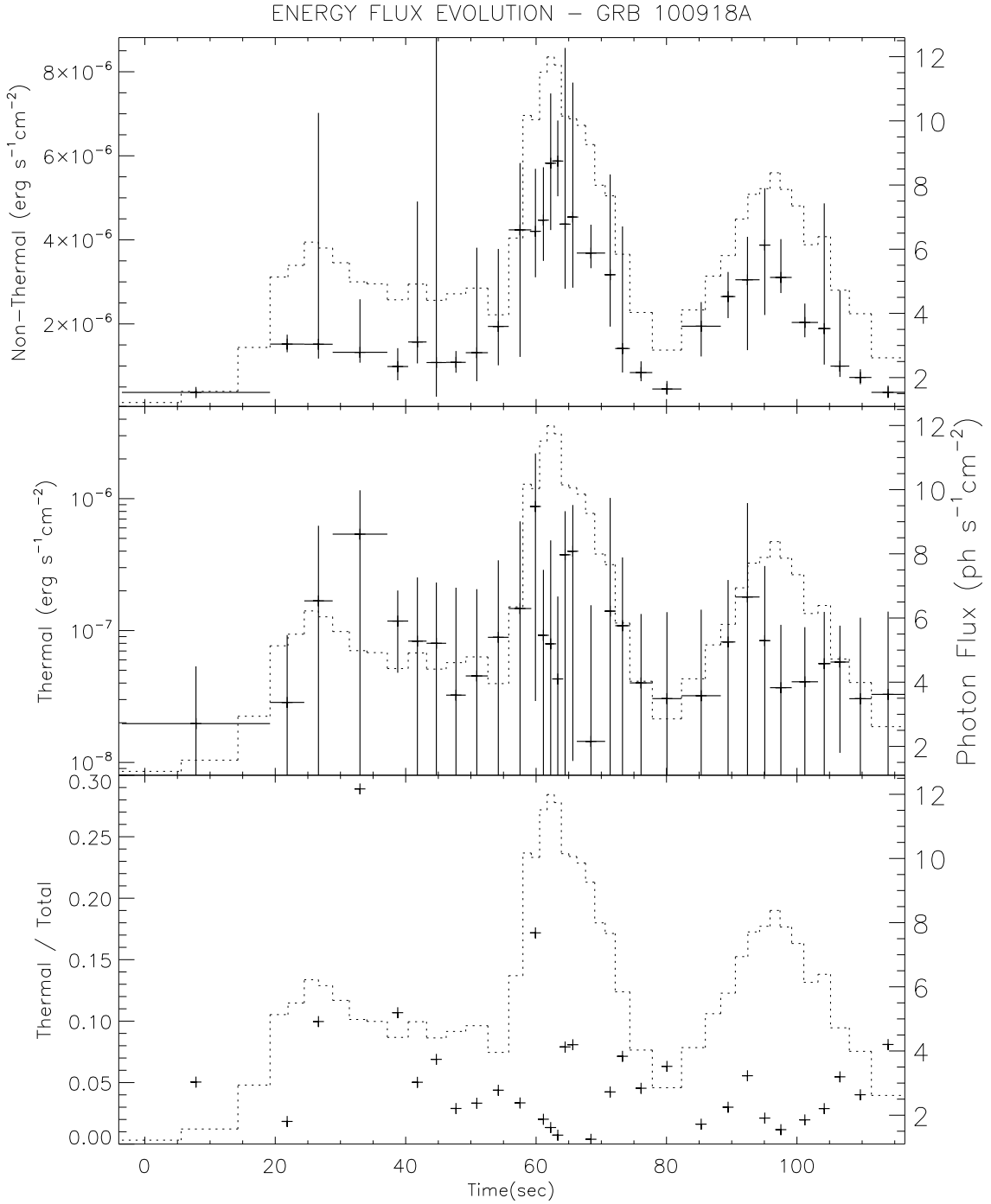


Figure 4.28: The energy flux evolutions of thermal and non-thermal components of COMPBB model for GRB 100918A. The top and middle panels show the energy flux evolutions of COMP and BB models, respectively. The flux ratio of thermal to total is seen in the bottom panel. The fluxes are calculated for the energy range 8 keV to 40 MeV. Errors in flux ratio of thermal to total are ignored. The dashed histograms represents the photon fluxes for each time interval (right axis).

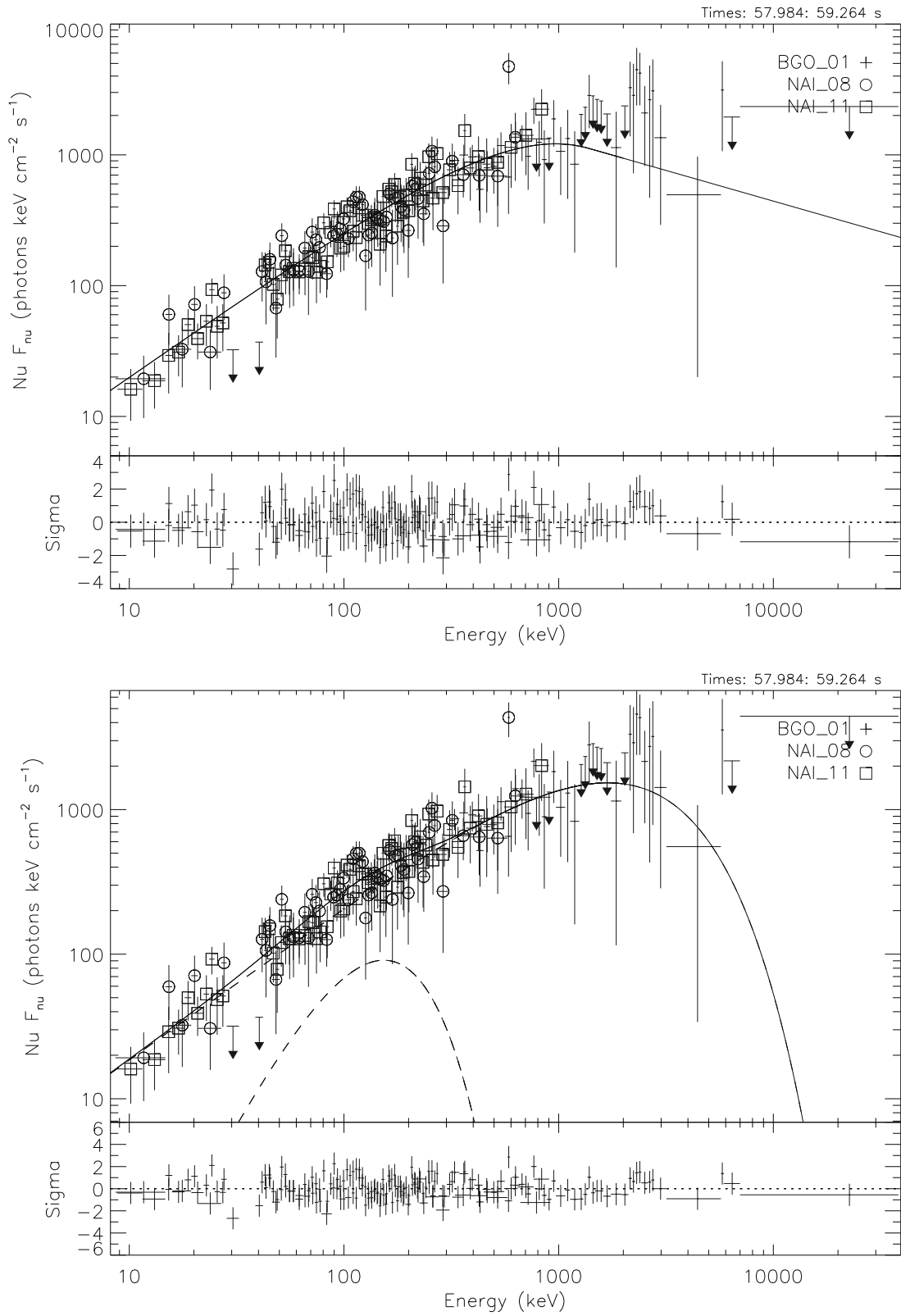


Figure 4.29: The  $\nu F_\nu$  spectrum of BAND and BANDBB models with photon counts and residuals, for the time interval 57.98 - 59.26 s of GRB 100918A, time bin 18.

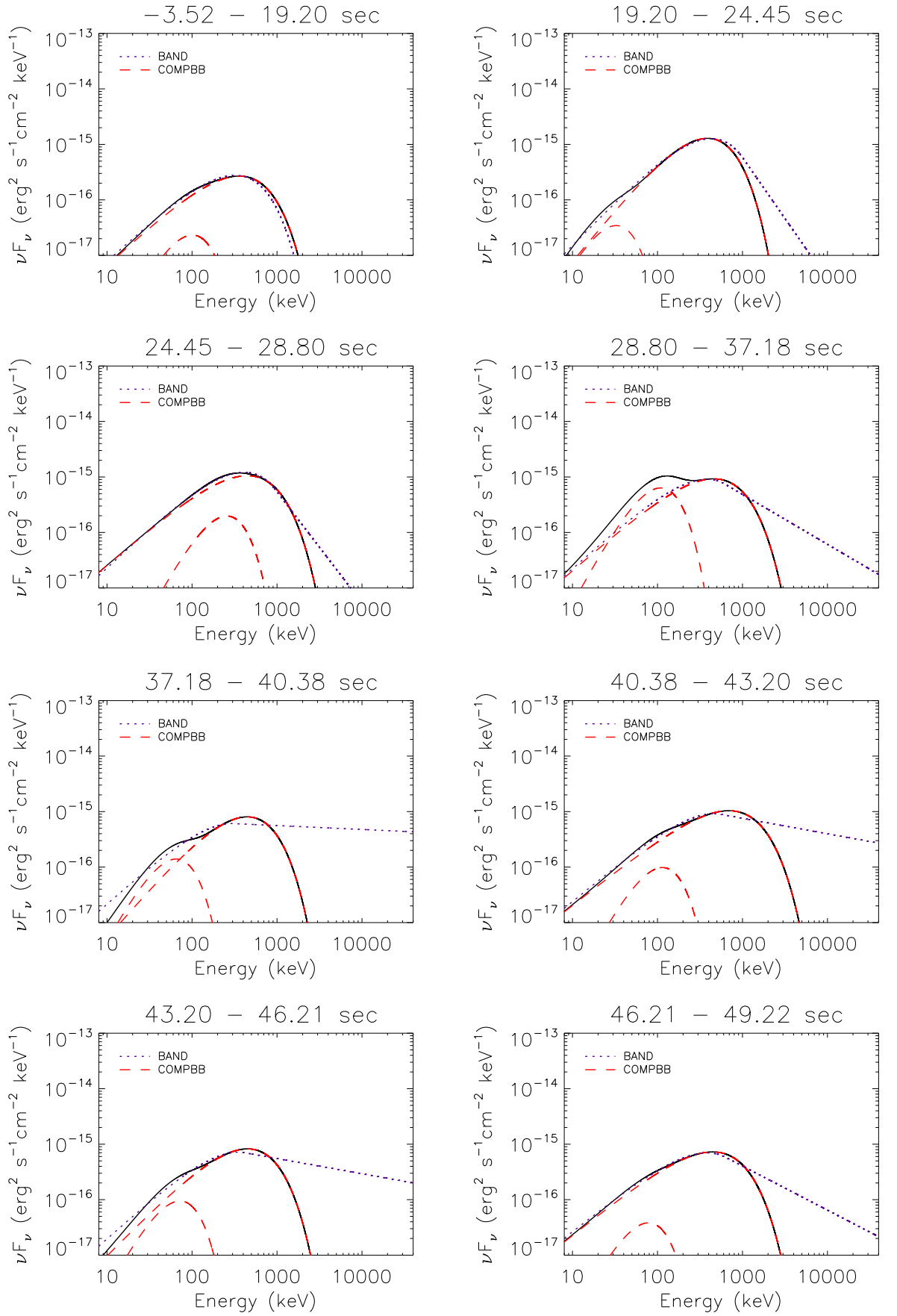


Figure 4.30: The model evolutions for GRB 100918A in  $\nu F_\nu$  representation. The solid line represents the COMPBB model where the dashed lines show the COMP and BB components separately. The dotted line is denoting the BAND model.

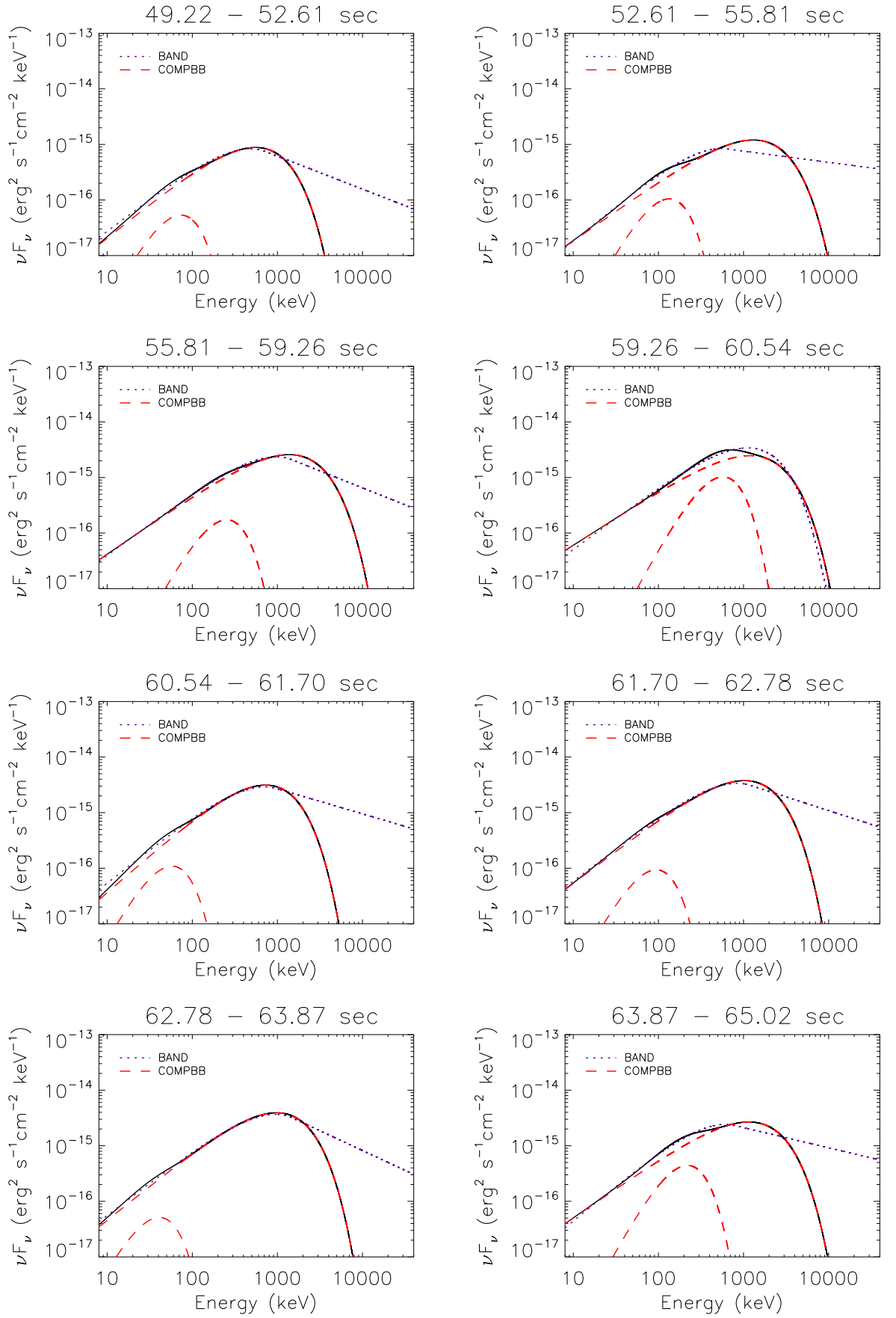


Figure 4.30 Continued.

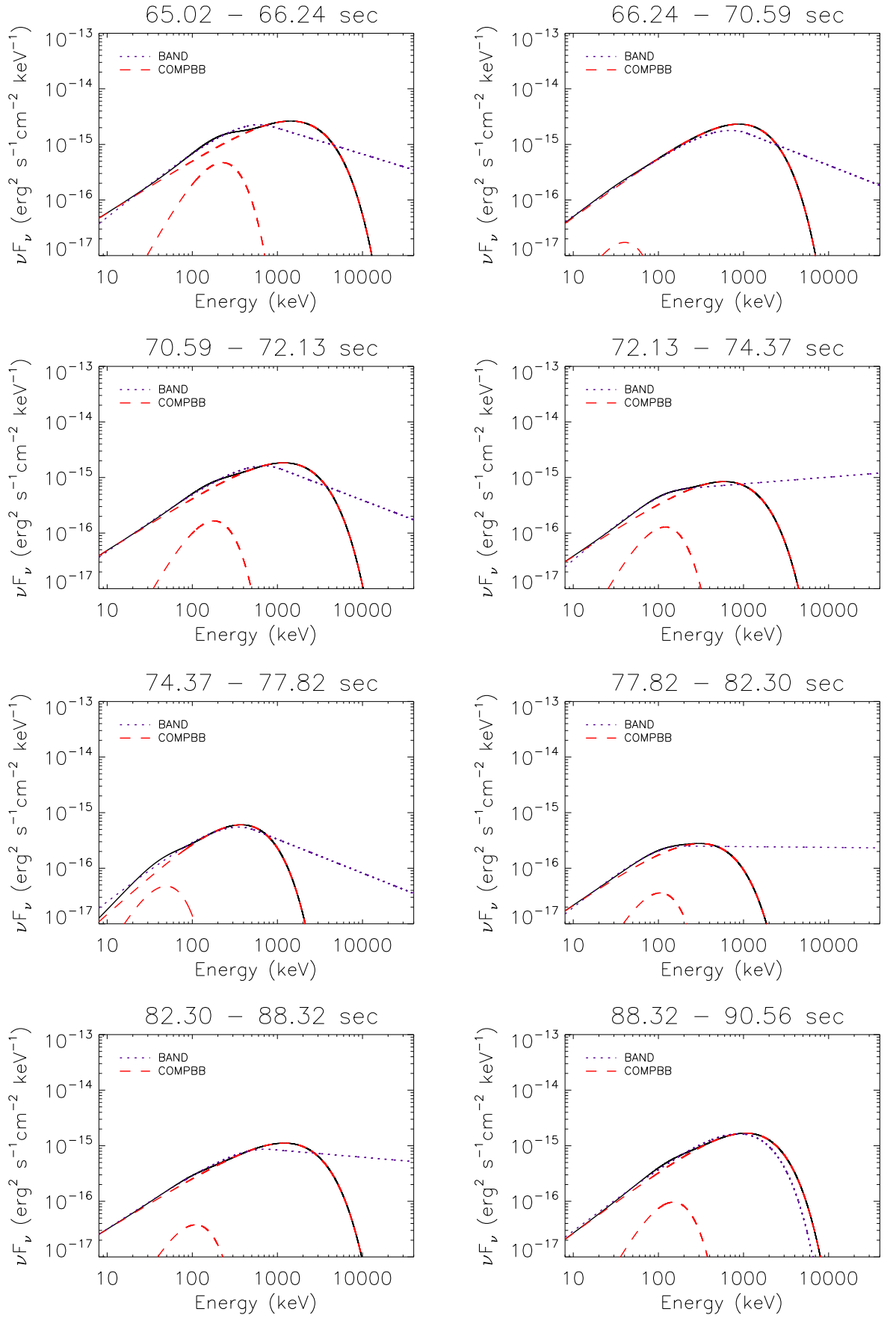


Figure 4.30 Continued.

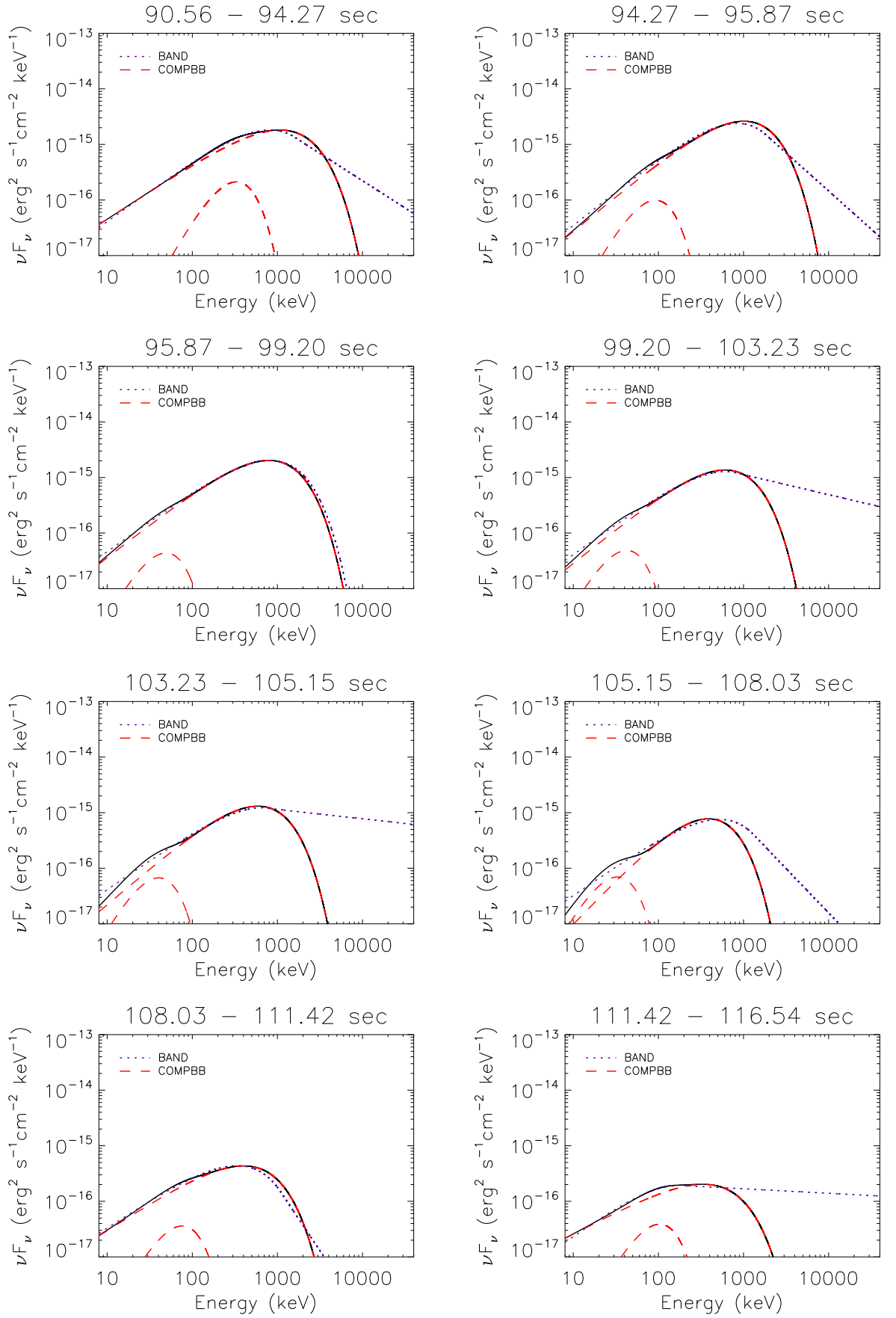


Figure 4.30 Continued.

## 4.7 GRB 101123A

GRB 101123A was detected by Fermi-GBM on 23 November 2010 at 22:51:34.9 UT (Guiriec, 2010). It is a long burst with duration  $T_{90} \sim 104$  s and peak photon flux  $(50.27 \pm 2.43)$  photon  $\text{cm}^{-2} \text{s}^{-1}$  in the energy range 10–1000 keV. Figure 4.31 shows the count rate history of the burst as seen by the brightest GBM detector NaI10. The time intervals of pulses used for the spectral simulations are also shown on Figure 4.31. The detectors, NaI9, NaI10, and BGO1 are used for spectral analysis.

### 4.7.1 Parameter Evolutions

The prompt emission phase is divided into 42 time intervals as seen in Figures 4.32 and 4.33. For each time bin the time intervals and the fit results of all relevant models are listed in Table 4.7. For 5 time bins the BAND-only  $\beta$  has only upper limits. For another 5 bins  $\beta$  has very negative values. The bins from 26 to 30 and 33 to 35 are combined in order to constrain blackbody parameters of COMPBB model. BANDBB model parameters are constrained for 13 time intervals.

Figure 4.32 shows the evolution of BAND and COMPBB model parameters, and Figure 4.33 shows the 1st pulse ( $\sim 30 - \sim 60$  s) in more detail.  $E_{\text{peak}}$  is taking values between a few hundreds to  $\sim 1.5 \times 10^4$  keV. COMPBB model has significantly higher peak energies than BAND model, especially during the first pulse.  $\alpha$  is mostly between  $-1.5$  to  $-0.5$ . Including BB component in fits, most of the time, shifts  $\alpha$  to lower values, which can be clearly seen for the time bins between 30 to 50 s.  $kT$  is relatively variable during the first pulse, taking values between  $\sim 5$  to  $\sim 100$  keV, and the variations seem to be independent from photon flux evolution. During the second pulse, temperature is around 40 keV initially and then decays to 10 keV.

#### 4.7.1.1 Flux Evolutions

Figure 4.34 top and middle panels are showing the evolution of energy flux for thermal and non-thermal components of COMPBB model, and Figure 4.35 shows the 1st pulse ( $\sim 30 - \sim 60$  s) in more detail. Non-thermal energy flux is highest during the initial times of the first pulse,  $\sim 45$  s, then, there seems an increase simultaneously with the increase in photon flux, at around 50 s. Similarly, thermal

flux is highest for the time bins around 45 s (for these time bins  $\alpha$  is decreased and  $E_{\text{peak}}$  is increased significantly), and increasing along with the count rate of the burst at  $\sim 50$  s, but the errors are large for these bins. Bottom panel of Figure 4.34 shows the thermal to total energy flux ratio, and Figure 4.35 shows the ratio for the 1st pulse in more detail. Thermal to total flux ratio is ranging from  $\sim 0.5\%$  to  $\sim 17\%$  throughout the burst with an average ratio of  $\sim 6\%$ .

Figure 4.36 shows the  $\nu F_\nu$  spectrum of BAND and BANDBB models for the time interval 46.53 - 46.78 s, time bin 10. When BB component included in fits,  $E_{\text{peak}}$  shifts to  $\sim 1400$  keV and  $\alpha$  decreases to  $\sim -1$  where  $E_{\text{peak}} \sim 370$  keV and  $\alpha \sim -0.6$  for BAND-only fits, as can be seen in Table 4.7 also. For this time bin BANDBB model parameters were all constrained and the values are consistent with COMPBB model parameter values,  $E_{\text{peak}}$ ,  $\alpha$ , and kT. Figure 4.37 shows the evolution of BAND and COMPBB models in  $\nu F_\nu$  representation throughout the burst.

#### 4.7.2 Pulse Simulations

We selected the time intervals of 1st, 2nd, and 3rd pulses as; 29.248 - 75.712 s, 75.712 - 111.296 s, 111.296 - 154.816 s, respectively, as can be seen in Figure 4.31. The spectra of the first and third pulses have enough emission above  $E_{\text{peak}}$  to be able to constrain the high energy power law index  $\beta$  of the BAND model, with and without BB component. Therefore, the simulations are performed with BAND and BANDBB models. The additional BB component improved the BAND-only fits by  $\Delta CSTAT_{\text{real}} = 25.3$  and  $\Delta CSTAT_{\text{real}} = 13.3$  units for the 1st and 3rd pulses, respectively.

The distributions of fit model parameters of both sets of synthetic spectra showed that *BANDBB model is a better representative of the data* than BAND only model for both of the first and third pulses. The probabilities of getting an improvement of  $\geq \Delta CSTAT_{\text{real}}$  in synthetic spectra of individual pulses by chance are; 0.1% and 2.08% for 1st and 3rd pulses, respectively. So, the improvement in CSTAT when BB model is included in fits is statistically significant for the first pulse, whereas it could be due to statistical fluctuations for the 3rd pulse. For the second pulse, the additional BB component did not improve the fits. Also, for the individual time bins within the second pulse thermal component did not provide any improvement.

Therefore, we conclude that BB component is statistically significant for the first pulse. For the 3rd pulse level of CSTAT improvement does not let us confirm the thermal component significantly however, BANDBB model is a better representative of the data. For the second pulse, since BB did not provide any improvement (also bin-wise) without performing bin-wise spectral simulations, we cannot confirm the preference for the BB component (or hybrid model) with confidence, for the bins from 37 to 41.

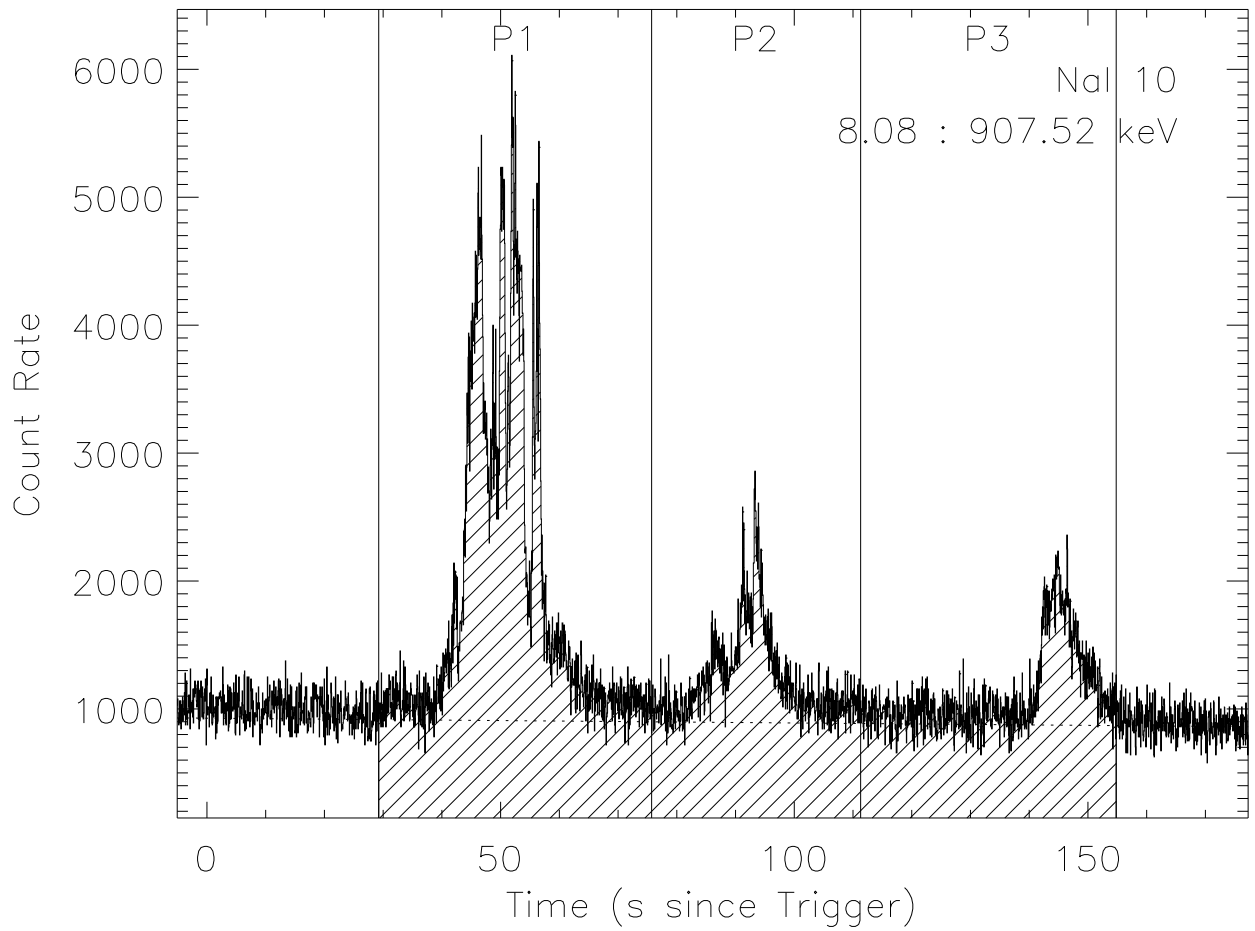


Figure 4.31: The light curve of GRB 101123A with 64 ms resolution. The vertical lines are showing the time intervals of pulses as used for spectral simulations. First, second and third pulses are indicated as P1, P2, and P3.

Table 4.7: Fine time interval fit results for GRB 101123A. Best parameter values with their  $1\sigma$  uncertainties.

Bin number	Time interval since trigger		Model	$E_{\text{peak}}$ (keV)	$\alpha$	$\beta$	$kT$ (keV)	Cstat/dof
	$T_{\text{start}}$ (s)	$T_{\text{stop}}$ (s)						
1	29.25	43.58	BAND	$409_{-99}^{+145}$	$-0.8_{-0.10}^{+0.11}$	$-1.70_{-0.08}^{+0.06}$	...	600/350
			COMPBB	$4620_{-1410}^{+1940}$	$-1.16 \pm 0.06$	...	$38_{-7}^{+8}$	608/349
2	43.58	44.29	BAND	$1569_{-297}^{+496}$	$-0.76 \pm 0.06$	$-1.94_{-0.15}^{+0.09}$	...	364/350
			COMPBB	$4432_{-488}^{+629}$	$-0.90_{-0.05}^{+0.04}$	...	$58_{-13}^{+23}$	366/349
			BANDBB	$2588_{-779}^{+1080}$	$-0.81_{-0.08}^{+0.07}$	$-2.16_{-0.39}^{+0.20}$	$42_{-12}^{+17}$	359/348
3	44.29	44.67	BAND	$754_{-130}^{+158}$	$-0.60_{-0.07}^{+0.08}$	$-1.82_{-0.08}^{+0.07}$	...	376/350
			COMPBB	$5003_{-992}^{+1610}$	$-0.99_{-0.06}^{+0.05}$	...	$68_{-9}^{+12}$	403/349
			BANDBB	$1344_{-373}^{+453}$	$-0.73_{-0.11}^{+0.10}$	$-1.90_{-0.11}^{+0.09}$	$45_{-9}^{+11}$	371/348
4	44.67	44.99	BAND	$526_{-74}^{+95}$	$-0.60 \pm 0.08$	$-1.79_{-0.07}^{+0.06}$	...	387/350
			COMPBB	$6031_{-1420}^{+2320}$	$-1.13 \pm 0.05$	...	$71 \pm 7$	397/349
5	44.99	45.38	BAND	$527_{-81}^{+108}$	$-0.62 \pm 0.08$	$-1.95_{-0.11}^{+0.08}$	...	404/350
			COMPBB	$3428_{-540}^{+675}$	$-1.04 \pm 0.04$	...	$52_{-5}^{+6}$	404/349
			BANDBB	$1088_{-300}^{+498}$	$-0.83_{-0.09}^{+0.10}$	$-2.09_{-0.18}^{+0.12}$	$43 \pm 7$	398/348
6	45.38	45.63	BAND	$380_{-54}^{+66}$	$-0.53_{-0.09}^{+0.10}$	$-2.00_{-0.12}^{+0.09}$	...	352/350
			COMPBB	$3292_{-745}^{+1010}$	$-1.13 \pm 0.05$	...	$57 \pm 5$	349/349
7	45.63	45.95	BAND	$355_{-58}^{+73}$	$-0.53_{-0.10}^{+0.11}$	$-1.77_{-0.06}^{+0.05}$	...	357/350
			COMPBB	$4593_{-1080}^{+1950}$	$-1.12 \pm 0.05$	...	$48_{-4}^{+5}$	380/349
			BANDBB	$926_{-294}^{+315}$	$-0.86_{-0.08}^{+0.12}$	$-1.86_{-0.09}^{+0.08}$	$39_{-6}^{+5}$	353/348
8	45.95	46.21	BAND	$593_{-106}^{+111}$	$-0.81_{-0.06}^{+0.07}$	$-2.24_{-0.26}^{+0.18}$	...	378/350
			COMPBB	$2058_{-487}^{+566}$	$-1.10_{-0.05}^{+0.06}$	...	$48_{-6}^{+7}$	378/349
			BANDBB	$884_{-203}^{+353}$	$-0.93 \pm 0.09$	$-2.31_{-0.32}^{+0.19}$	$42 \pm 10$	374/348
9	45.95	46.21	BAND	$532_{-77}^{+82}$	$-0.72_{-0.06}^{+0.07}$	$-2.09_{-0.14}^{+0.11}$	...	372/350
			COMPBB	$834_{-150}^{+369}$	$-0.82_{-0.12}^{+0.09}$	...	$30_{-8}^{+12}$	386/349
			BANDBB	$641_{-347}^{+143}$	$-0.75_{-0.08}^{+0.10}$	$-2.13_{-0.14}^{+0.11}$	$25_{-8}^{+11}$	369/348
10	45.95	46.78	BAND	$369_{-48}^{+60}$	$-0.55_{-0.09}^{+0.09}$	$-1.94_{-0.09}^{+0.08}$	...	416/350
			COMPBB	$2612_{-549}^{+731}$	$-1.09 \pm 0.05$	...	$49_{-4}^{+5}$	414/349
			BANDBB	$1407_{-575}^{+730}$	$-0.10_{-0.08}^{+0.12}$	$-2.20_{-0.35}^{+0.21}$	$46 \pm 5$	410/348
11	46.78	47.17	BAND	$328_{-48}^{+64}$	$-0.73_{-0.08}^{+0.09}$	$-2.03_{-0.16}^{+0.11}$	...	416/350
			COMPBB	$819_{-195}^{+330}$	$-0.99_{-0.09}^{+0.10}$	...	$30 \pm 8$	414/349
12	47.17	47.62	BAND	$379_{-64}^{+96}$	$-0.81 \pm 0.09$	$-2.02_{-0.18}^{+0.11}$	...	328/350
			COMPBB	$1620_{-484}^{+576}$	$-1.12_{-0.06}^{+0.07}$	...	$33_{-6}^{+8}$	324/349

13	47.61	48.26	BAND	$496^{+116}_{-97}$	$-0.91^{+0.08}_{-0.07}$	$-2.01^{+0.12}_{-0.17}$	...	354/350
			COMPBB	$921^{+493}_{-224}$	$-0.97^{+0.11}_{-0.10}$	...	$18^{+6}_{-4}$	357/349
			BANDBB	$559^{+188}_{-108}$	$-0.83^{+0.14}_{-0.11}$	$-2.04^{+0.12}_{-0.20}$	$14^{+4}_{-2}$	345/348
14	48.26	48.77	BAND	$470^{+125}_{-82}$	$-0.78 \pm 0.08$	$-2.10^{+0.14}_{-0.32}$	...	349/350
			COMPBB	$857^{+245}_{-673}$	$-0.94^{+0.09}_{-0.08}$	...	$36^{+12}_{-16}$	347/349
			BANDBB	$836^{+256}_{-648}$	$-0.94^{+0.10}_{-0.08}$	$-2.46^{+0.29}_{-1.27}$	$37^{+11}_{-14}$	346/348
15	48.77	49.28	BAND	$335^{+52}_{-43}$	$-0.73 \pm 0.08$	$-2.40^{+0.23}_{-0.56}$	...	367/350
			COMPBB	$575^{+195}_{-120}$	$-0.95 \pm 0.10$	...	$34 \pm 6$	364/349
16	49.28	49.92	BAND	$253^{+43}_{-39}$	$-0.65^{+0.11}_{-0.09}$	$-2.12^{+0.13}_{-0.19}$	...	385/350
			COMPBB	$653^{+207}_{-508}$	$-1.00^{+0.10}_{-0.09}$	...	$28^{+5}_{-4}$	380/349
17	49.92	50.11	BAND	$468^{+48}_{-46}$	$-0.41^{+0.08}_{-0.07}$	$-2.59^{+0.25}_{-0.45}$	...	351/350
			COMPBB	$677^{+186}_{-372}$	$-0.61 \pm 0.13$	...	$52^{+11}_{-13}$	351/349
18	50.11	50.37	BAND	$649^{+59}_{-57}$	$-0.66^{+0.05}_{-0.05}$	$-8.33 \pm Inf$	...	364/350
			COMPBB	$621^{+67}_{-56}$	$-0.54^{+0.15}_{-0.12}$	...	$12^{+6}_{-4}$	362/349
19	50.37	50.62	BAND	$533^{+66}_{-75}$	$-0.69^{+0.07}_{-0.06}$	$-2.68^{+0.26}_{-0.89}$	...	399/350
			COMPBB	$735^{+197}_{-127}$	$-0.82^{+0.09}_{-0.10}$	...	$47^{+10}_{-12}$	397/349
			BANDBB	$691^{+194}_{-108}$	$-0.80^{+0.08}_{-0.10}$	$-2.77^{+0.32}_{-1.20}$	$46^{+11}_{-11}$	396/348
20	50.62	50.88	BAND	$320^{+73}_{-59}$	$-0.71^{+0.11}_{-0.10}$	$-1.98^{+0.11}_{-0.16}$	...	357/350
			COMPBB	$534^{+109}_{-75}$	$-0.78^{+0.14}_{-0.42}$	...	$17^{+9}_{-15}$	361/349
21	50.88	51.46	BAND	$349^{+97}_{-62}$	$-0.84 \pm 0.09$	$-2.16^{+0.16}_{-0.43}$	...	375/350
			COMPBB	$919^{+415}_{-253}$	$-1.12 \pm 0.08$	...	$34 \pm 5$	369/349
22	51.46	51.78	BAND	$537^{+82}_{-74}$	$-0.96 \pm 0.06$	$-12 \pm Inf$	...	385/350
			COMPBB	$619^{+168}_{-125}$	$-0.96^{+0.15}_{-0.09}$	...	$20^{+11}_{-14}$	383/349
23	51.78	51.97	BAND	$579^{+106}_{-80}$	$-0.66 \pm 0.08$	$-2.90^{+0.44}_{-Inf}$	...	339/350
			COMPBB	$909^{+205}_{-675}$	$-0.81 \pm 0.09$	...	$43 \pm 11$	331/349
24	51.97	52.29	BAND	$417^{+59}_{-52}$	$-0.72^{+0.07}_{-0.06}$	$-2.30^{+0.17}_{-0.27}$	...	385/350
			COMPBB	$649^{+149}_{-103}$	$-0.87^{+0.08}_{-0.09}$	...	$33^{+11}_{-10}$	385/349
25	52.29	52.48	BAND	$648^{+76}_{-71}$	$-0.73^{+0.06}_{-0.05}$	$-9.00 \pm Inf$	...	395/350
			COMPBB	$727^{+95}_{-92}$	$-0.83(fixed)$	...	$79^{+35}_{-26}$	394/349
26	52.48	52.74	BAND	$509^{+47}_{-42}$	$-0.73 \pm 0.05$	$-9.5 \pm Inf$	...	351/350
			COMPBB	$504^{+42}_{-37}$	$-0.66(fixed)$	...	$12 \pm 6$	351/349
27	52.74	53.06	BAND	$543^{+74}_{-62}$	$-0.71 \pm 0.06$	$-2.66^{+0.32}_{-Inf}$	...	402/350
28	53.06	53.38	BAND	$549^{+77}_{-84}$	$-0.78^{+0.07}_{-0.06}$	$-3.2^{+0.75}_{-Inf}$	...	401/350

29	53.38	53.63	BAND	$425_{-49}^{+100}$	$-0.63_{-0.11}^{+0.08}$	$-2.6_{-Inf}^{+0.30}$	...	349/350
30	53.63	533.89	BAND	$502_{-45}^{+52}$	$-0.69 \pm 0.06$	$-5.8 \pm Inf$	...	335/350
26+27+28 +29+30	52.48	53.89	BAND	$522_{-23}^{+27}$	$-0.72 \pm 0.03$	$-4.2_{-Inf}^{+0.11}$	...	372/350
			COMPBB	$516_{-18}^{+20}$	$-0.68(fixed)$	...	$10_{-3}^{+5}$	371/349
31	53.89	55.36	BAND	$182_{-48}^{+64}$	$-0.93_{-0.12}^{+0.16}$	$-1.84_{-0.12}^{+0.08}$	...	417/350
			COMPBB	$2968_{-1230}^{+1840}$	$-1.39 \pm 0.05$	...	$24_{-4}^{+5}$	422/349
32	55.36	55.68	BAND	$522_{-59}^{+62}$	$-0.53_{-0.07}^{+0.08}$	$-2.63_{-0.63}^{+0.29}$	...	380/350
			COMPBB	$661_{-80}^{+115}$	$-0.54_{-0.10}^{+0.11}$	...	$28_{-7}^{+10}$	377/349
			BANDBB	$618_{-262}^{+118}$	$-0.51_{-0.11}^{+0.12}$	$-2.84_{-1.47}^{+0.38}$	$27_{-6}^{+10}$	376/348
33	55.68	56.19	BAND	$545_{-62}^{+65}$	$-0.82 \pm 0.05$	$-3.11_{-Inf}^{+0.637}$	...	357/350
34	56.19	56.51	BAND	$509_{-76}^{+68}$	$-0.78_{-0.07}^{+0.06}$	$-2.36_{-0.41}^{+0.21}$	...	345/350
35	56.51	56.77	BAND	$383_{-73}^{+65}$	$-0.76 \pm 0.09$	$-2.26_{-0.36}^{+0.20}$	...	349/350
33+34+35	55.68	56.77	BAND	$488_{-44}^{+48}$	$-0.80 \pm 0.04$	$-2.48_{-0.40}^{+0.19}$	...	372/350
			COMPBB	$599_{-55}^{+71}$	$-0.85_{-0.05}^{+0.04}$	...	$30_{-7}^{+9}$	373/349
			BANDBB	$584_{-66}^{+77}$	$-0.85 \pm 0.05$	$-2.63_{-0.43}^{+0.24}$	$30_{-7}^{+9}$	369/348
36	56.77	59.39	BAND	$157_{-23}^{+30}$	$-0.89_{-0.10}^{+0.12}$	$-1.95_{-0.12}^{+0.09}$	...	456/350
			COMPBB	$2441_{-1320}^{+1980}$	$-1.45_{-0.05}^{+0.06}$	...	$25 \pm 3$	454/349
37	59.39	87.62	BAND	$203_{-36}^{+51}$	$-0.92_{-0.09}^{+0.10}$	$-1.71_{-0.06}^{+0.05}$	...	712/350
			COMPBB	$16840_{-8420}^{+3950}$	$-1.44 \pm 0.04$	...	$31 \pm 3$	710/349
38	87.62	91.78	BAND	$324_{-70}^{+110}$	$-1.08 \pm 0.08$	$-2.05_{-0.46}^{+0.17}$	...	378/350
			COMPBB	$923_{-382}^{+543}$	$-1.30 \pm 0.08$	...	$30_{-8}^{+9}$	376/349
39	91.78	93.50	BAND	$275_{-50}^{+59}$	$-1.03_{-0.07}^{+0.08}$	$-2.40_{-1.59}^{+0.31}$	...	428/350
			COMPBB	$450_{-70}^{+91}$	$-1.19(fixed)$	...	$26_{-6}^{+9}$	427/349
40	93.50	95.23	BAND	$151_{-32}^{+38}$	$-0.98_{-0.11}^{+0.15}$	$-2.00_{-0.18}^{+0.12}$	...	383/350
			COMPBB	$422_{-136}^{+345}$	$-1.31_{-0.12}^{+0.14}$	...	$20_{-6}^{+5}$	384/349
41	95.23	145.98	BAND	$221_{-51}^{+57}$	$-1.19_{-0.07}^{+0.09}$	$-1.9_{-0.14}^{+0.10}$	...	771/350
			COMPBB	$272_{-29}^{+35}$	$-1.08(fixed)$	...	$6 \pm 1$	778/349
42	145.98	151.30	BAND	$126_{-20}^{+24}$	$-0.91_{-0.11}^{+0.13}$	$-1.99_{-0.14}^{+0.10}$	...	404/350
			COMPBB	$191_{-21}^{+29}$	$-0.82_{-0.71}^{+0.22}$	...	$8_{-1}^{+2}$	407/349
			BANDBB	$116_{-18}^{+22}$	$0.17_{-0.67}^{+2.25}$	$-2.03_{-0.13}^{+0.10}$	$6 \pm 1$	396/348

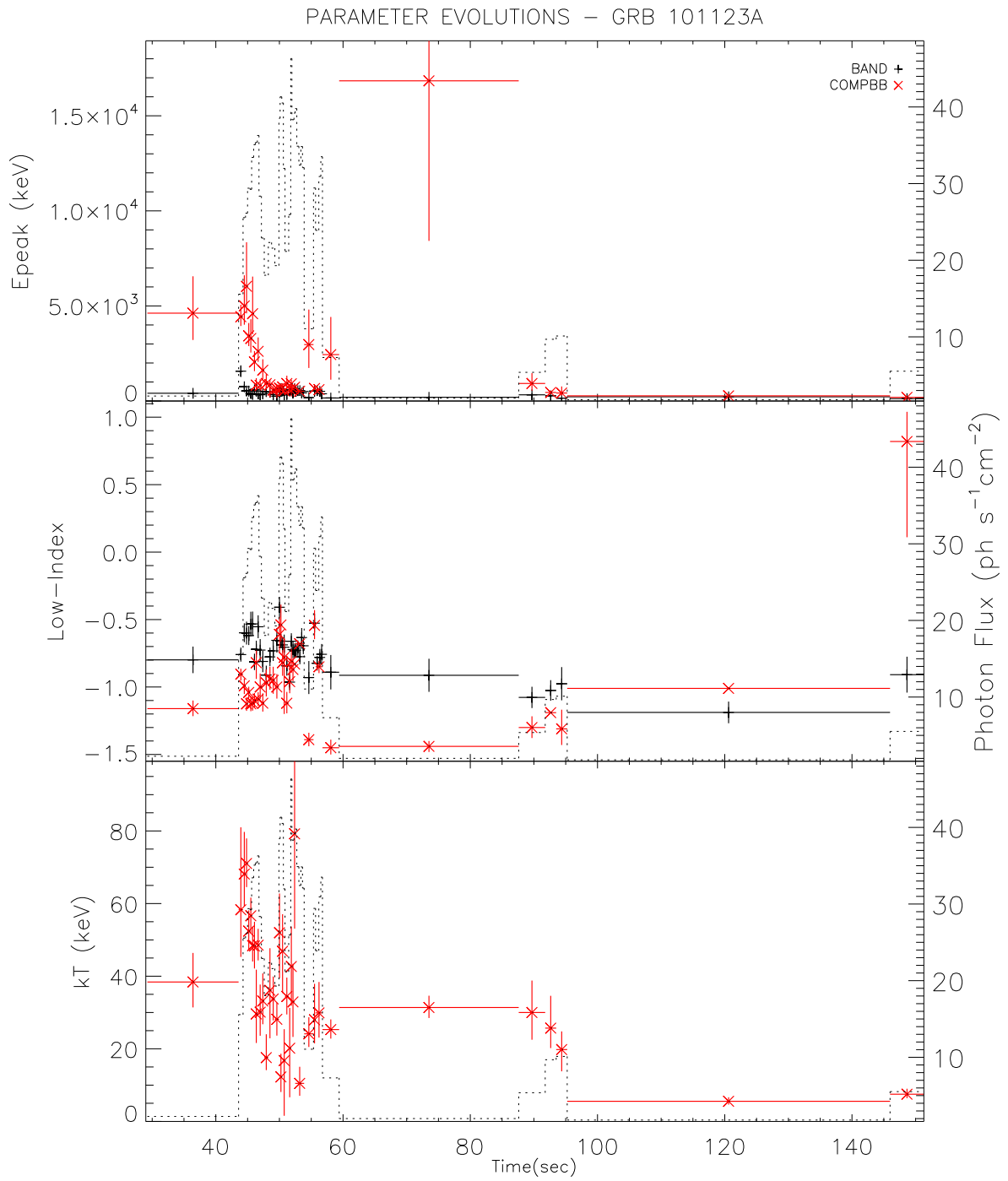


Figure 4.32: The evolution of BAND and COMPBB model parameters for GRB 101123A. The dashed histograms represents the photon fluxes for each time interval (right axis).

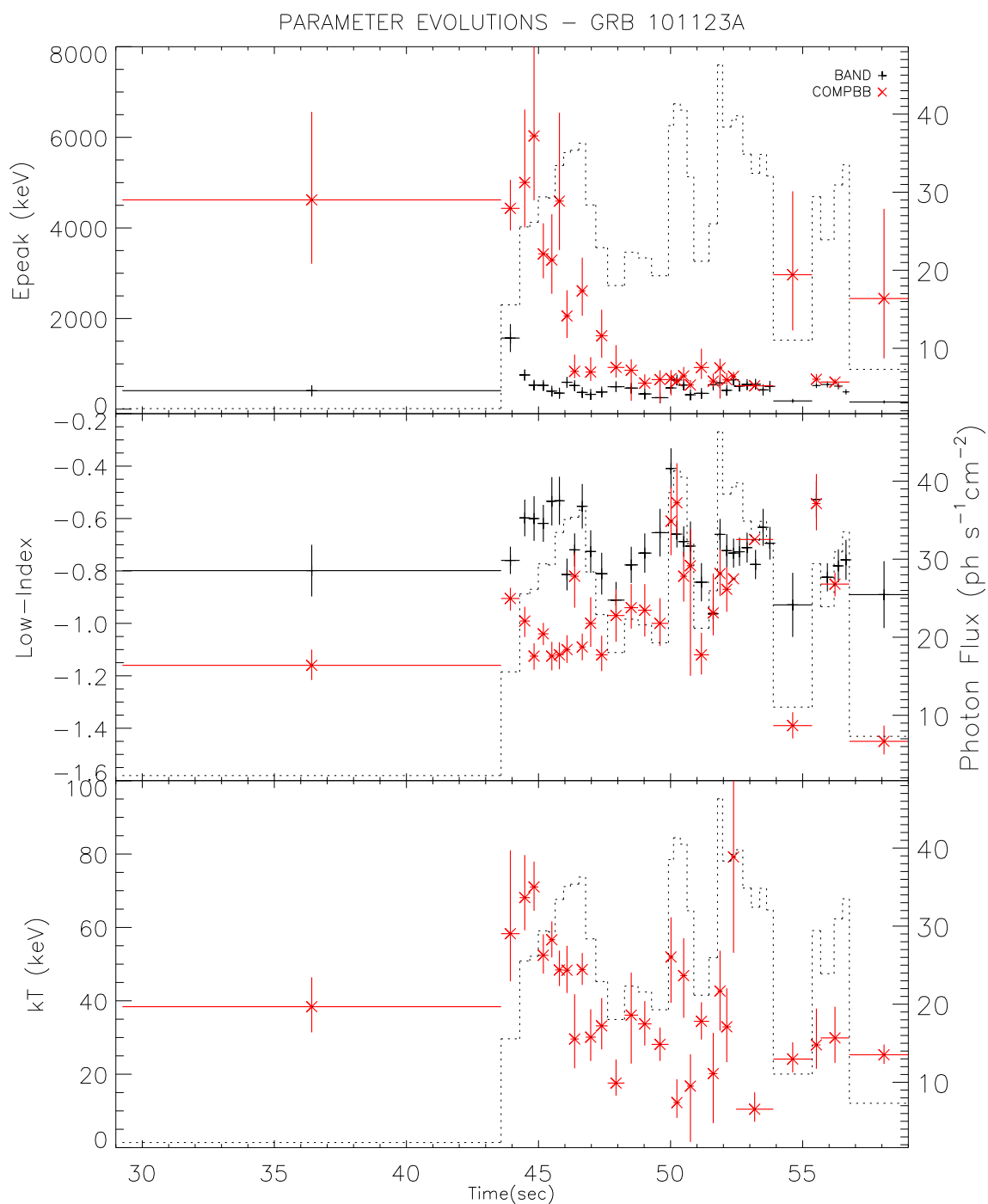


Figure 4.33: The evolution of BAND and COMPBB model parameters during the 1st pulse of GRB 101123A. The dashed histograms represents the photon fluxes for each time interval (right axis).

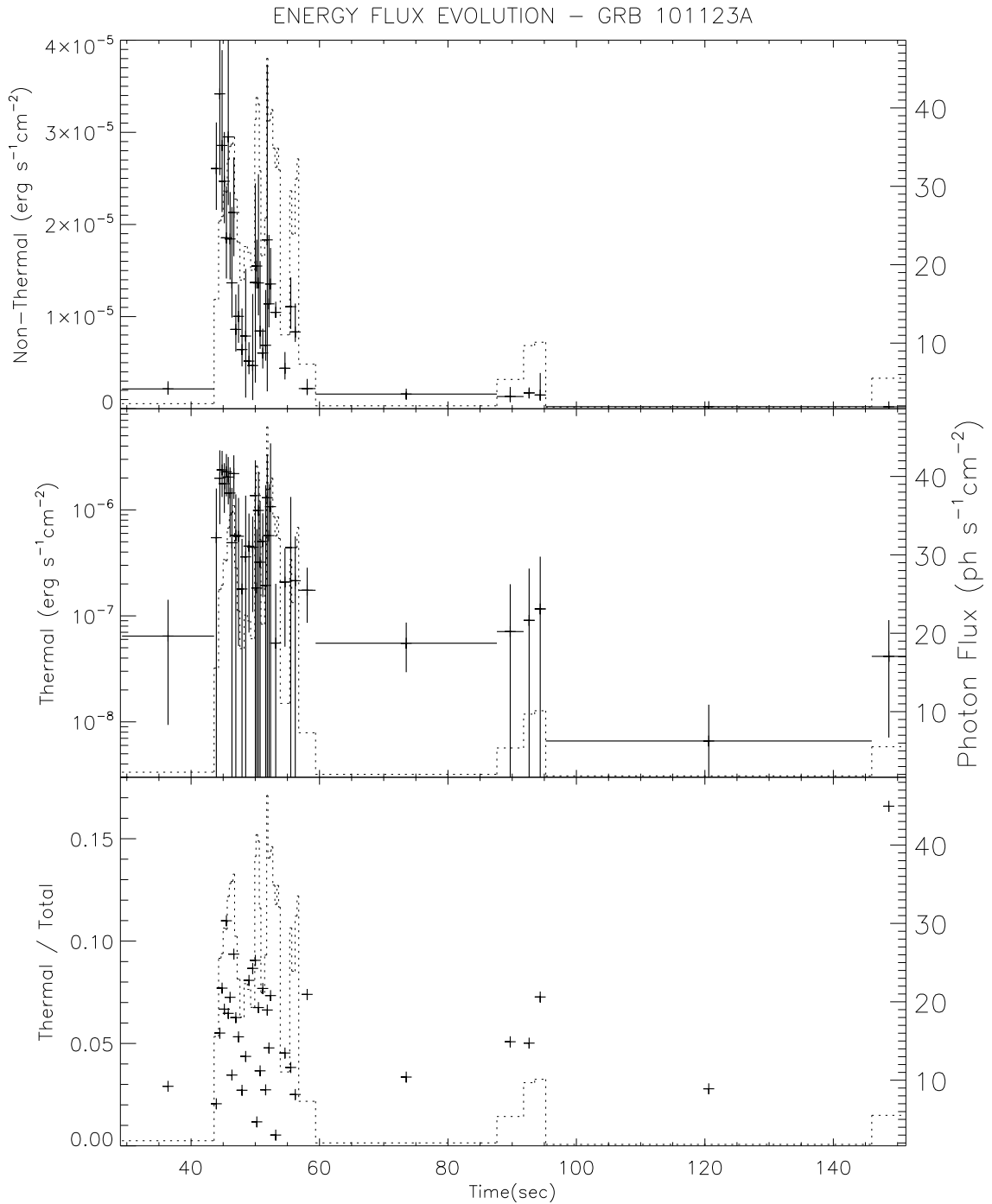


Figure 4.34: The energy flux evolutions of thermal and non-thermal components of COMPBB model for GRB 101123A. The top and middle panels show the energy flux evolutions of COMP and BB models, respectively. The flux ratio of thermal to total is seen in the bottom panel. The fluxes are calculated for the energy range 8 keV to 40 MeV. Errors in flux ratio of thermal to total are ignored. The dashed histograms represents the photon fluxes for each time interval (right axis).

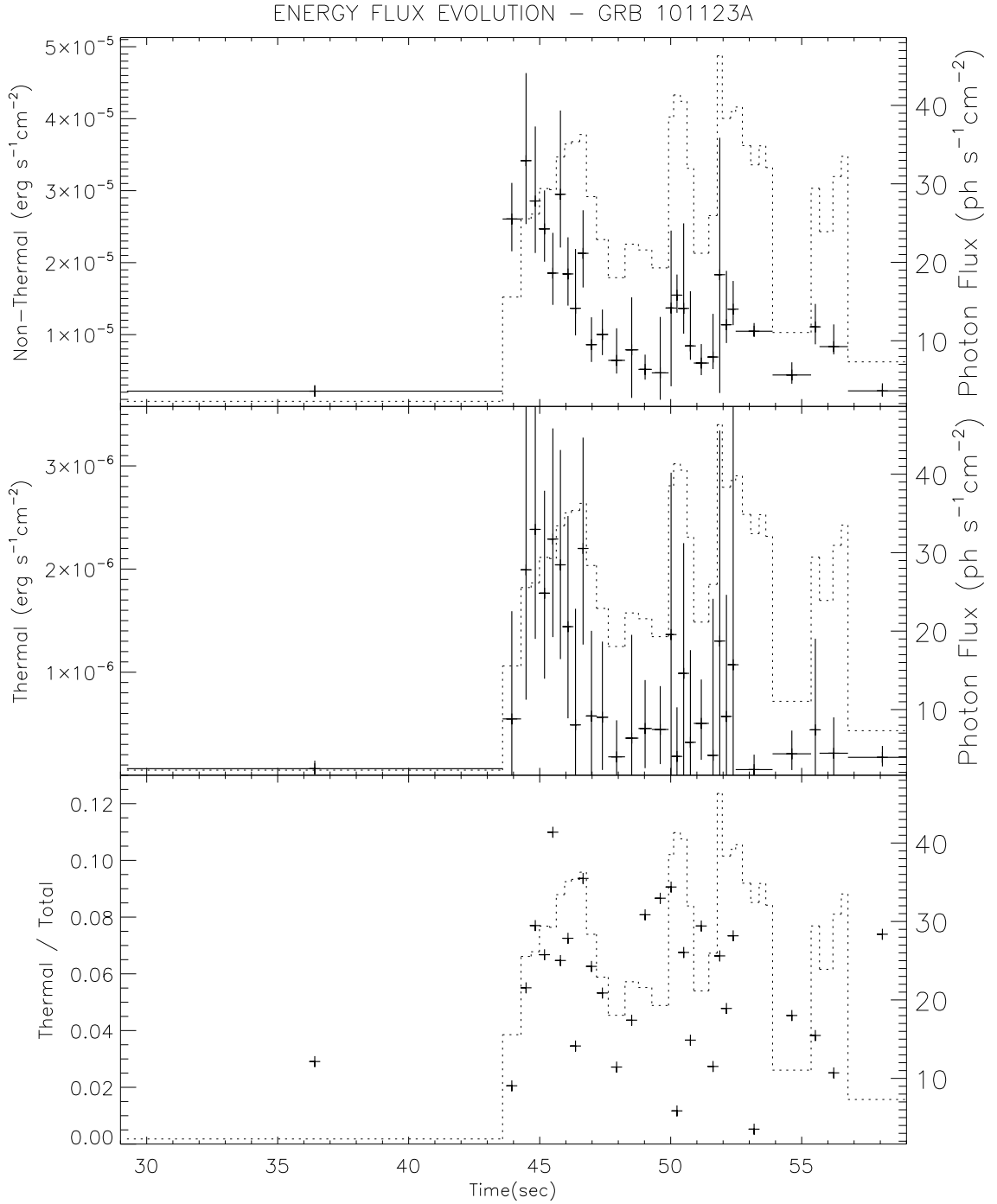


Figure 4.35: The energy flux evolutions of thermal and non-thermal components of COMPBB model during the 1st pulse of GRB 101123A. The top and middle panels show the energy flux evolutions of COMP and BB models, respectively. The flux ratio of thermal to total is seen in the bottom panel. The fluxes are calculated for the energy range 8 keV to 40 MeV. The dashed histograms represents the photon fluxes for each time interval (right axis).

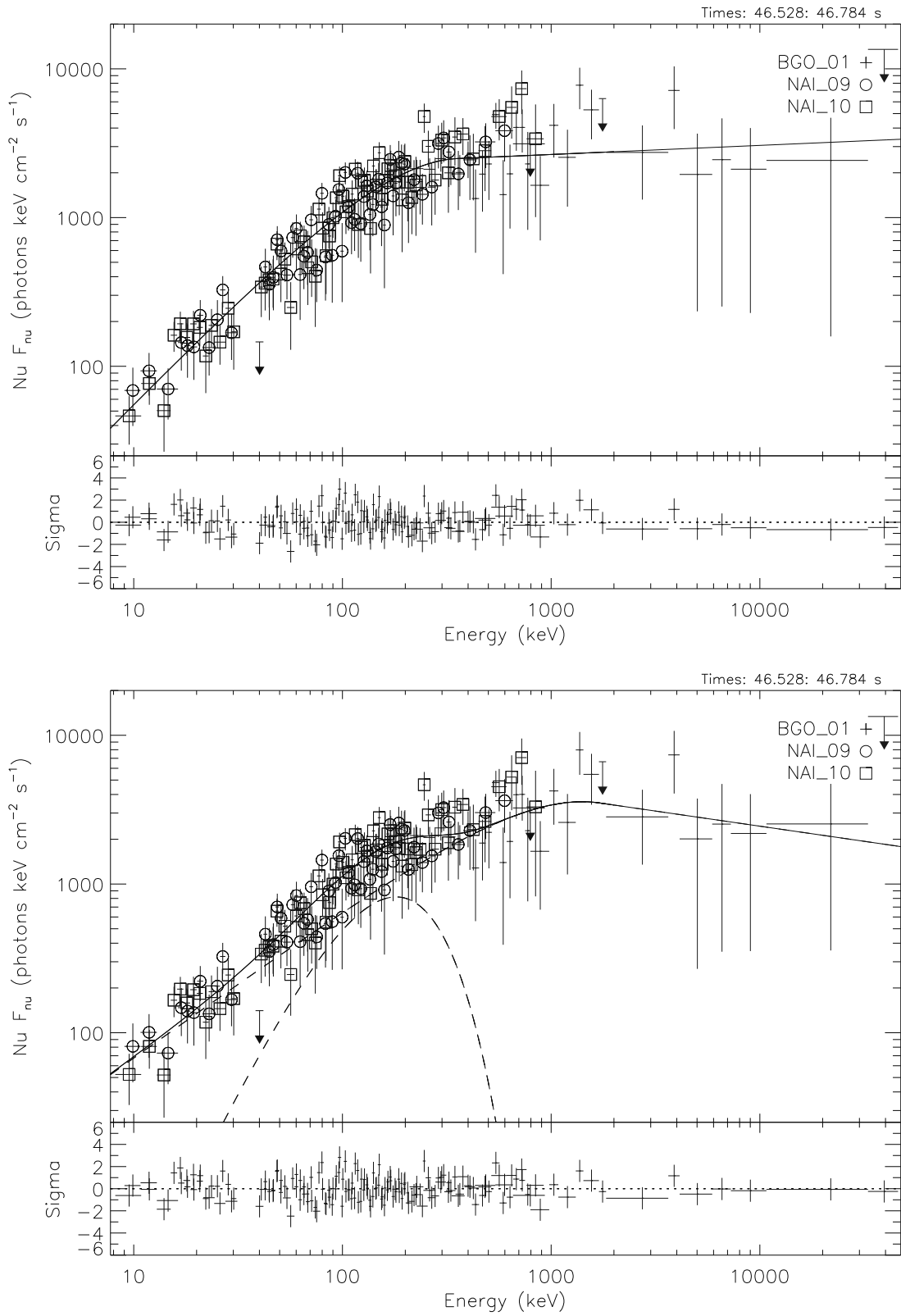


Figure 4.36: The  $\nu F_\nu$  spectrum of BAND and BANDBB models with photon counts and residuals, for the time interval 46.53 - 46.78 s of GRB 101123A, time bin 10.

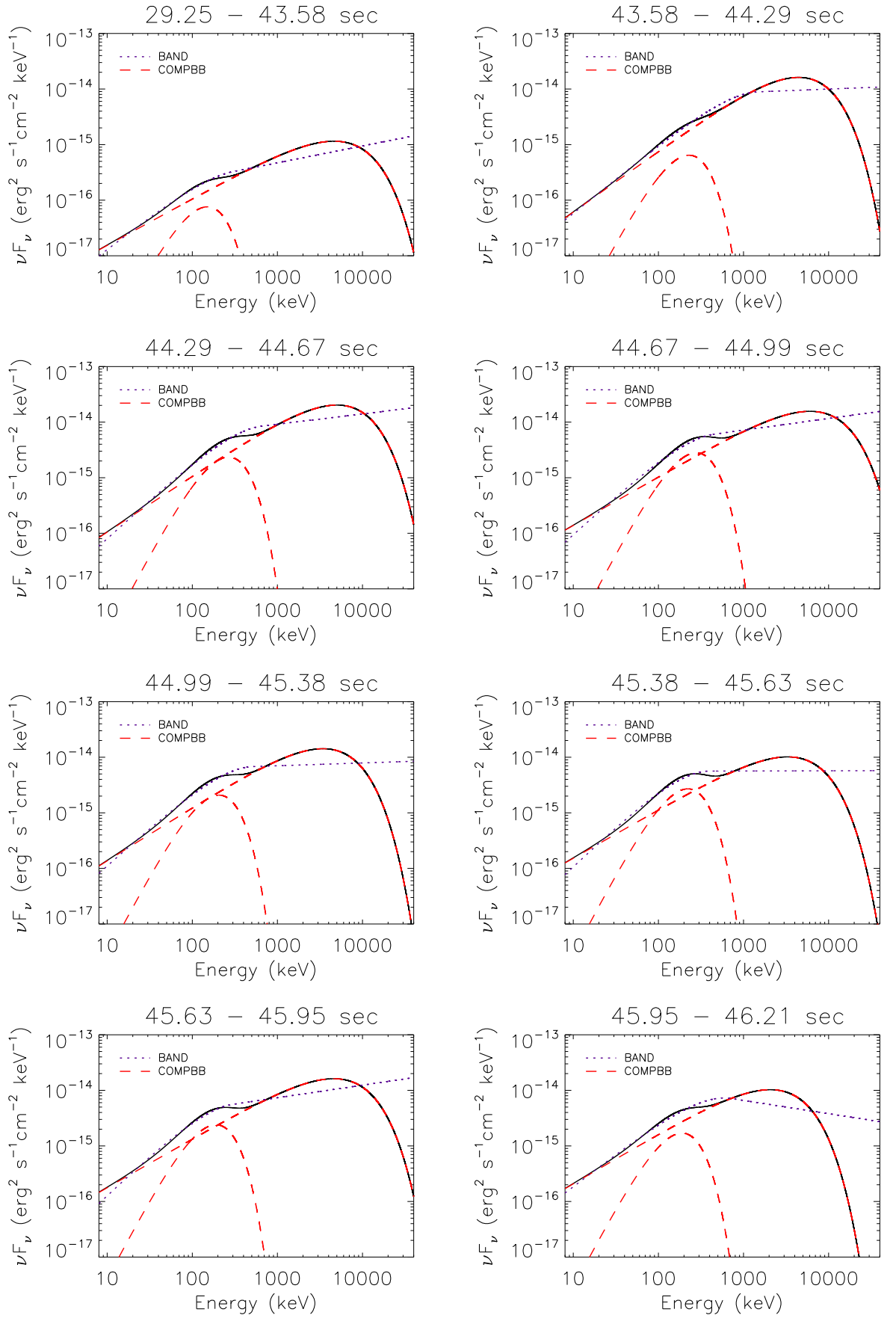


Figure 4.37: The model evolutions for GRB 100918A in  $\nu F_\nu$  representation. The solid line represents the COMPBB model where the dashed lines show the COMP and BB components separately. The dotted line is denoting the BAND model.

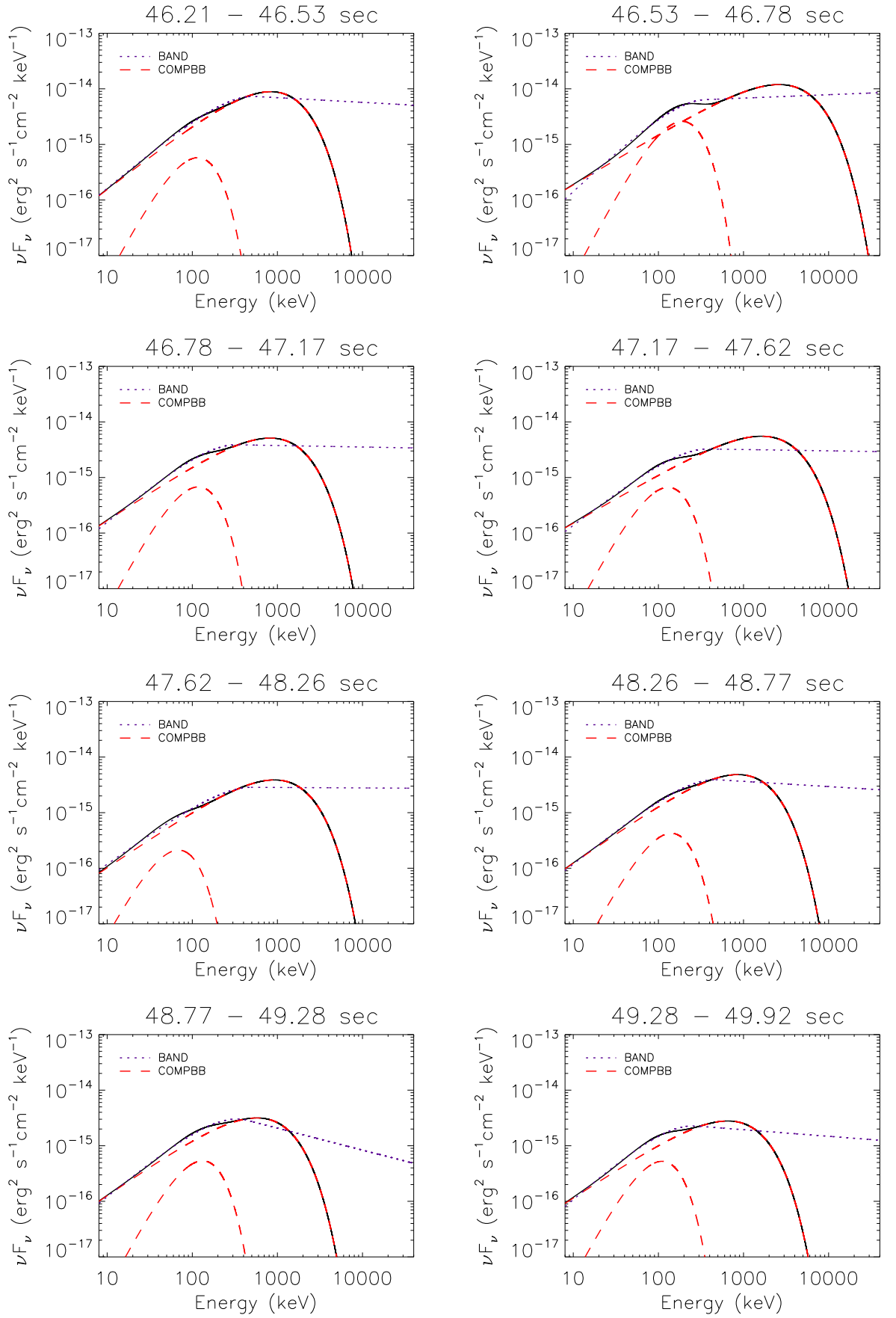


Figure 4.37 Continued.

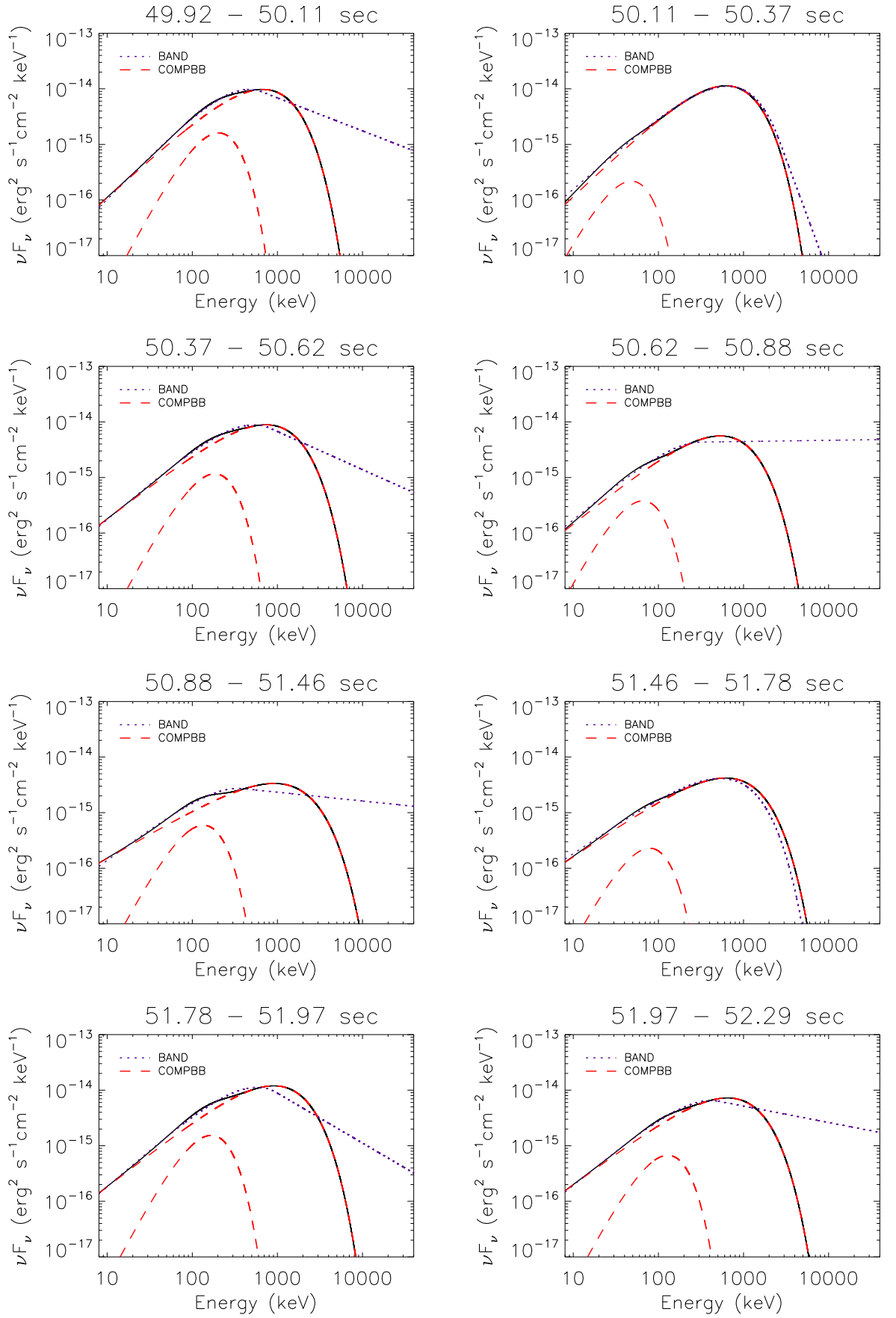


Figure 4.37 Continued.

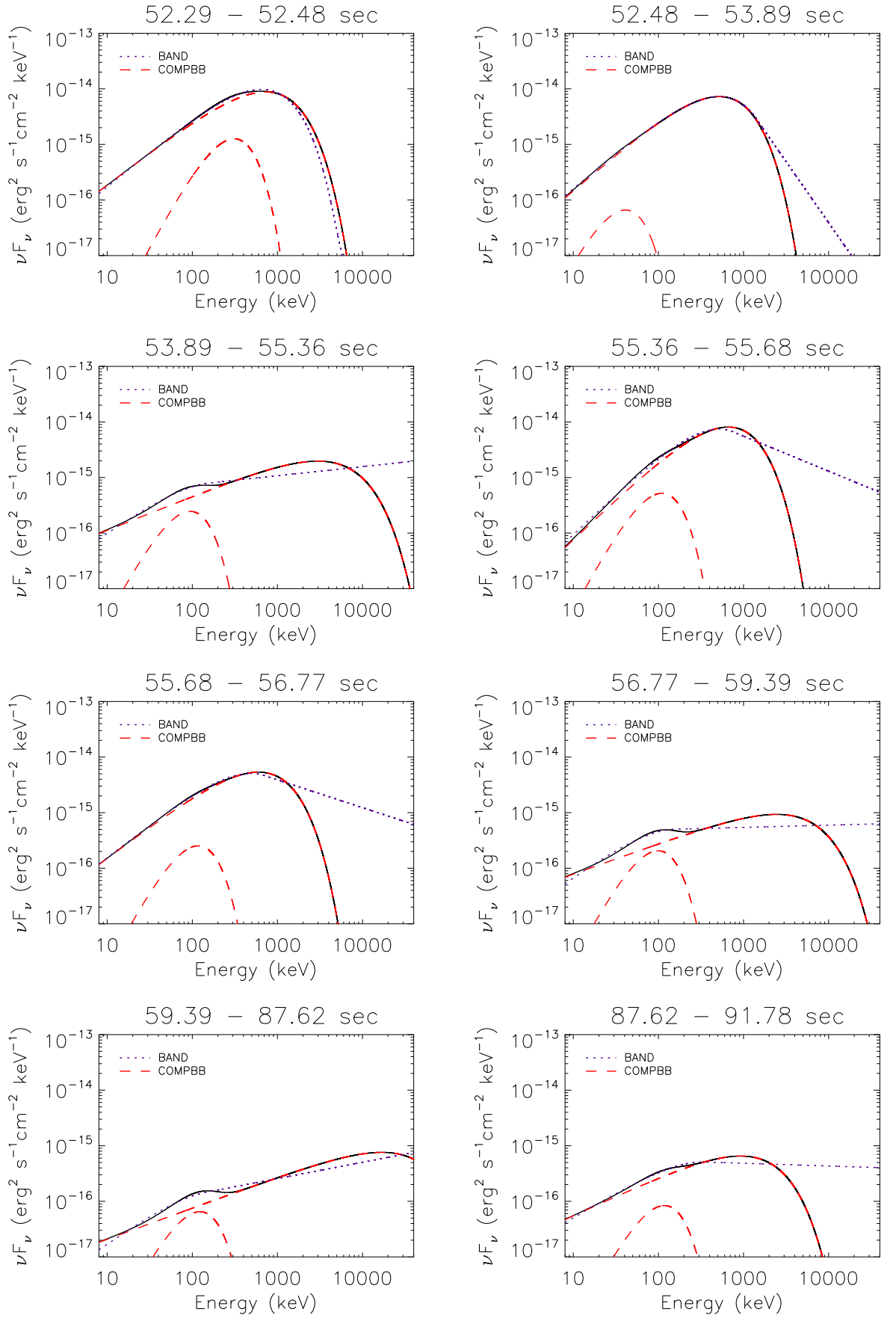


Figure 4.37 Continued.

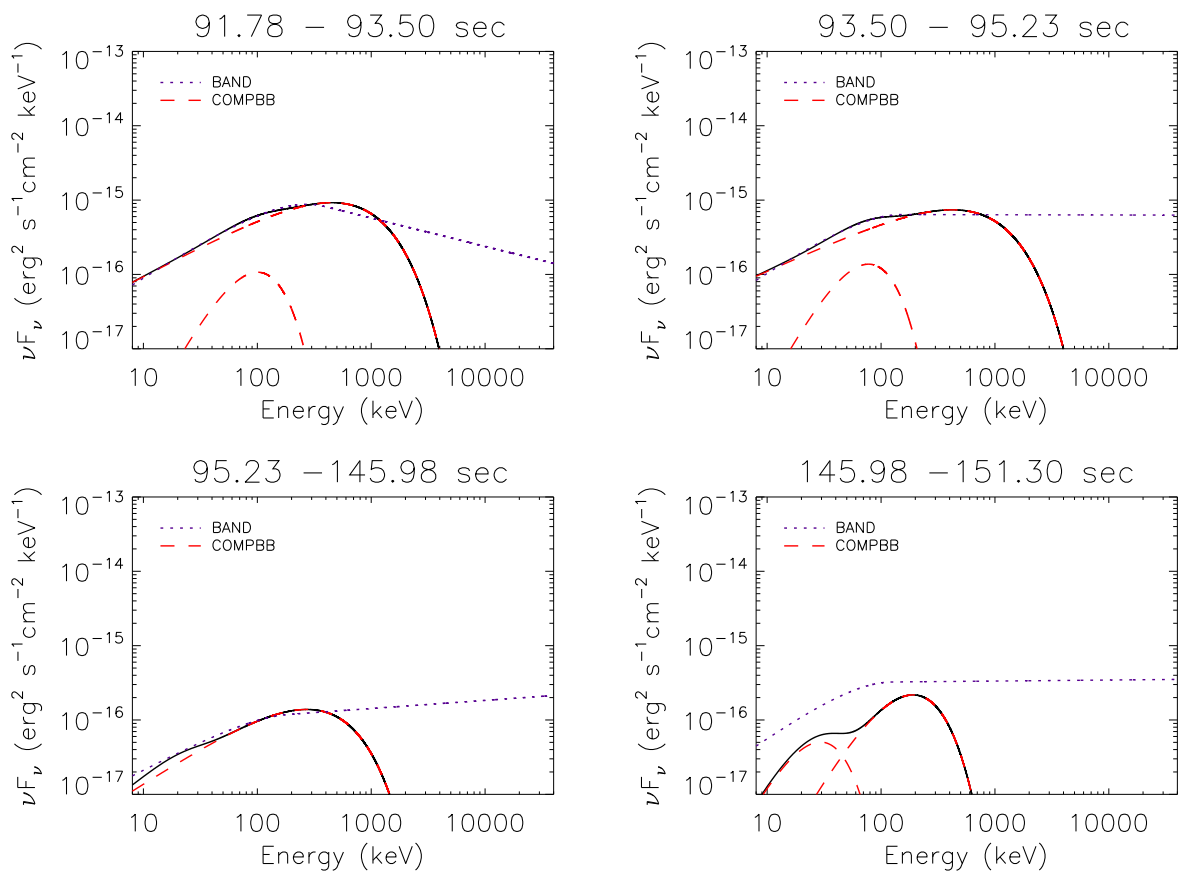


Figure 4.37 Continued.

## 4.8 GRB 110721A

GRB 110721A was detected by Fermi-GBM on 21 July 2011 at 04:47:43.7 UT (Tierney & von Kienlin, 2011). It is a long burst with duration  $T_{90} \sim 22$  s and peak flux  $(34.32 \pm 1.55)$  photon  $\text{cm}^{-2} \text{s}^{-1}$  in the energy range 10 – 1000 keV. Fermi-LAT also detected more than 20 photons with energies above 100 MeV from the burst starting from  $\sim 2$  s after GBM trigger and lasting for about 16 s (Vasileiou et al., 2011). There are two possible redshift measurements,  $z = 0.38$  and  $z = 3.512$ , based on two absorption features at 5487 and 5436 angstrom seen in the optical counterpart of the burst (Berger, 2011). The thermal characteristics of its spectrum and time-resolved analysis have been previously reported (Axelsson et al., 2012). They used GBM detectors, NaI6, NaI7, NaI9, NaI11, BGO1, and LAT-LLE data up to 130 MeV. They divided the prompt phase into 8 time intervals with SNR of 40 in the brightest detector NaI9. They modelled the spectrum of each bin by BAND and BANDBB models. We plot their fit results along with our results in Figure 4.39. Figure 4.38 shows the count rate history of the burst as seen by GBM detector NaI9. We performed time-resolved spectral analysis of this burst in the same way as we did for other bursts. We used GBM detectors, NaI6, NaI7, NaI9, and BGO1. The prompt emission phase is divided into 17 time bins, i.e., we have used finer time intervals. For each time bin the time intervals and the fit results of our analysis are listed in Table 4.8. For only one bin (14th) BAND  $\beta$  has very negative value. BANDBB model parameters are constrained for 3 time intervals.

The Figure 4.39 shows the parameter evolutions from our fit results along with the previously reported hybrid model (BANDBB) results. Both the non-thermal and thermal model parameters are consistent within  $1\sigma$  uncertainties. When we compare our single (BAND) and hybrid model (COMPBB) results we see that  $E_{\text{peak}}$  of COMPBB is relatively higher than that of BAND-only, especially for the first several time bins.  $\alpha$  is evolving throughout the burst for both BAND-only and COMPBB models. Including BB component in fits shifts  $\alpha$  from  $\sim -0.6$  to  $\sim -1$ . during 1 - 3 s.  $kT$  is decreasing throughout the burst.

Figure 4.40 top and middle panels are showing the evolution of energy flux for thermal and non-thermal components of COMPBB model. Non-thermal energy flux is clearly decreasing throughout the burst. Thermal flux seems to be increasing

initially then decreases. Until  $\sim 3$  s the thermal flux values are all within their error intervals, after then it decreases. The thermal to total energy flux ratio is ranging from  $\sim 1\%$  to  $\sim 10\%$  during the burst with an average ratio of 4.7%. The BB energy flux is found to be  $\sim 5\%$  of the total flux in Axelsson et al. (2012), which is consistent with our results.

For spectral pulse simulations, we selected the time interval of the single pulse as  $-0.32 - 30.98$  s, as can be seen in Figure 4.38. The spectrum has enough emission above  $E_{\text{peak}}$  to be able to constrain the high energy power law index  $\beta$  of the BAND model, with and without BB component. Therefore, the simulations are performed with BAND and BANDBB models. The additional BB component improved the BAND-only fits by  $\Delta CSTAT_{\text{real}} = 19.2$ . The distributions of fit model parameters of both sets of synthetic spectra showed that *BANDBB model is a better representative of the data* than BAND only model. The probability of getting an improvement of  $\geq \Delta CSTAT_{\text{real}}$  in synthetic spectra of the pulse by chance is 0.02%. So, the improvement in CSTAT when BB model is included in fits is statistically significant.

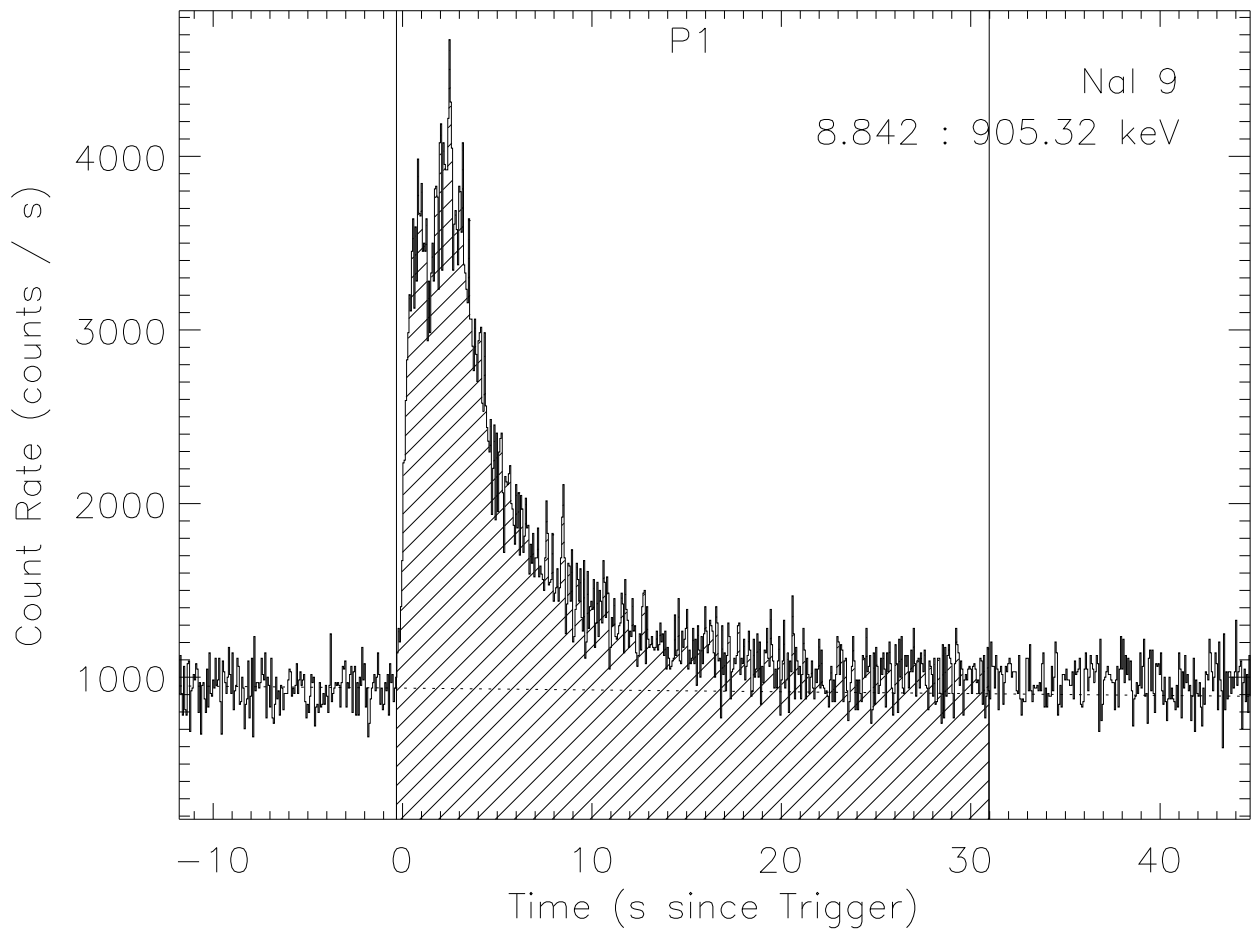


Figure 4.38: The light curve of GRB 110721A with 64 ms resolution. The vertical lines are showing the time interval of the pulse used for spectral simulations.

Table 4.8: Fine time interval fit results for GRB 110721A. Best parameter values with their  $1\sigma$  uncertainties.

Bin number	Time interval since trigger		Model	$E_{\text{peak}}$ (keV)	$\alpha$	$\beta$	$kT$ (keV)	Cstat/dof
	$T_{\text{start}}(s)$	$T_{\text{stop}}(s)$						
1	-0.32	0.51	BAND	$7656 \pm 1060$	$-0.96 \pm 0.02$	$-2.24 \pm 0.25$	...	529/483
			COMPBB	$10260 \pm 1110$	$-0.99 \pm 0.0$	...	$94^{+36}_{-23}$	530/482
2	0.51	0.83	BAND	$2216 \pm 307$	$-0.88 \pm 0.03$	$-2.40^{+0.23}_{-0.42}$	...	561/483
			COMPBB	$3193 \pm 303$	$-0.89 \pm 0.03$	...	$37 \pm 7$	554/482
			BANDBB	$2732 \pm 381$	$-0.86 \pm 0.04$	$-2.7^{+0.32}_{-0.71}$	$33 \pm 7$	550/481
3	0.83	1.09	BAND	$1677 \pm 254$	$-0.87 \pm 0.04$	$-2.42^{+0.27}_{-0.60}$	...	560/483
			COMPBB	$2533 \pm 309$	$-0.91 \pm 0.04$	...	$50 \pm 11$	551/482
4	1.09	1.41	BAND	$1225 \pm 181$	$-0.85 \pm 0.04$	$-2.42 \pm 0.25$	...	542/483
			COMPBB	$1926 \pm 235$	$-0.87 \pm 0.05$	...	$33 \pm 5$	531/482
			BANDBB	$1629 \pm 328$	$-0.84 \pm 0.06$	$-2.6 \pm 0.40$	$32 \pm 5$	525/481
5	1.41	1.73	BAND	$375 \pm 54$	$-0.56 \pm 0.08$	$-1.9 \pm 0.08$	...	572/483
			COMPBB	$1926 \pm 289$	$-0.94 \pm 0.05$	...	$35 \pm 4$	540/482
6	1.73	2.05	BAND	$571 \pm 72$	$-0.89 \pm 0.05$	$-2.6^{+0.33}_{-0.65}$	...	553/483
			COMPBB	$890^{+124}_{-102}$	$-1.02(\text{fixed})$	...	$41 \pm 11$	553/482
7	2.05	2.30	BAND	$291 \pm 36$	$-0.59 \pm 0.08$	$-2.10 \pm 0.13$	...	537/483
			COMPBB	$1013 \pm 241$	$-1.02 \pm 0.07$	...	$35 \pm 4$	529/482
8	2.30	2.56	BAND	$226 \pm 32$	$-0.59 \pm 0.10$	$-1.90 \pm 0.08$	...	525/483
			COMPBB	$1282 \pm 314$	$-1.12 \pm 0.06$	...	$31 \pm 3$	523/482
9	2.56	2.82	BAND	$195 \pm 29$	$-0.62 \pm 0.11$	$-1.94 \pm 0.08$	...	509/483
			COMPBB	$2568^{+1978}_{-1110}$	$-1.32 \pm 0.05$	...	$33 \pm 3$	522/482
10	2.82	3.13	BAND	$185^{+65}_{-39}$	$-0.79 \pm 0.11$	$-1.9^{+0.08}_{-0.12}$	...	510/483
			COMPBB	$727 \pm 169$	$-1.14 \pm 0.07$	...	$19 \pm 3$	497/482
11	3.13	3.46	BAND	$203 \pm 43$	$-0.94 \pm 0.10$	$-1.90^{+0.09}_{-0.22}$	...	485/483
			COMPBB	$697^{+336}_{-190}$	$-1.30 \pm 0.07$	...	$23 \pm 4$	481/482
12	3.46	3.84	BAND	$244 \pm 50$	$-1.06 \pm 0.08$	$-2.10 \pm 0.20$	...	531/483
			COMPBB	$615^{+146}_{-110}$	$-1.26(\text{fixed})$	...	$18^{+5}_{-3}$	532/482
13	3.84	4.29	BAND	$323 \pm 133$	$-1.2^{+0.14}_{-0.08}$	$-1.90^{+0.14}_{-0.21}$	...	483/483
			COMPBB	$662^{+362}_{-160}$	$-1.27 \pm 0.07$	...	$15 \pm 4$	485/482
			BANDBB	$471 \pm 227$	$-1.23 \pm 0.11$	$-1.98 \pm 0.20$	$13 \pm 5$	481/481
14	4.29	4.99	BAND	$633 \pm 134$	$-1.29 \pm 0.04$	$-9.20 \pm Inf$	...	508/483

			COMPBB	$767 \pm 205$	$-1.23 \pm 0.07$	...	$13 \pm 2$	499/482
15	4.99	5.89	BAND	$317 \pm 90$	$-1.18 \pm 0.08$	$-1.94^{+0.13}_{-0.20}$	...	531/483
			COMPBB	$405(\textit{fixed})$	$-1.04^{+0.10}_{-0.09}$	...	$8 \pm 1$	533/482
16	5.89	7.36	BAND	$272 \pm 71$	$-1.10 \pm 0.08$	$-1.90 \pm 0.13$	...	580/483
			COMPBB	$380^{+48}_{-40}$	$-1.12(\textit{fixed})$	...	$5 \pm 2$	584/482
17	7.36	10.05	BAND	$222 \pm 53$	$-1.09 \pm 0.09$	$-1.9^{+0.10}_{-0.24}$	...	527/483
			COMPBB	$751 \pm 80$	$-1.35 \pm 0.12$	...	$24 \pm 4$	531/482

---

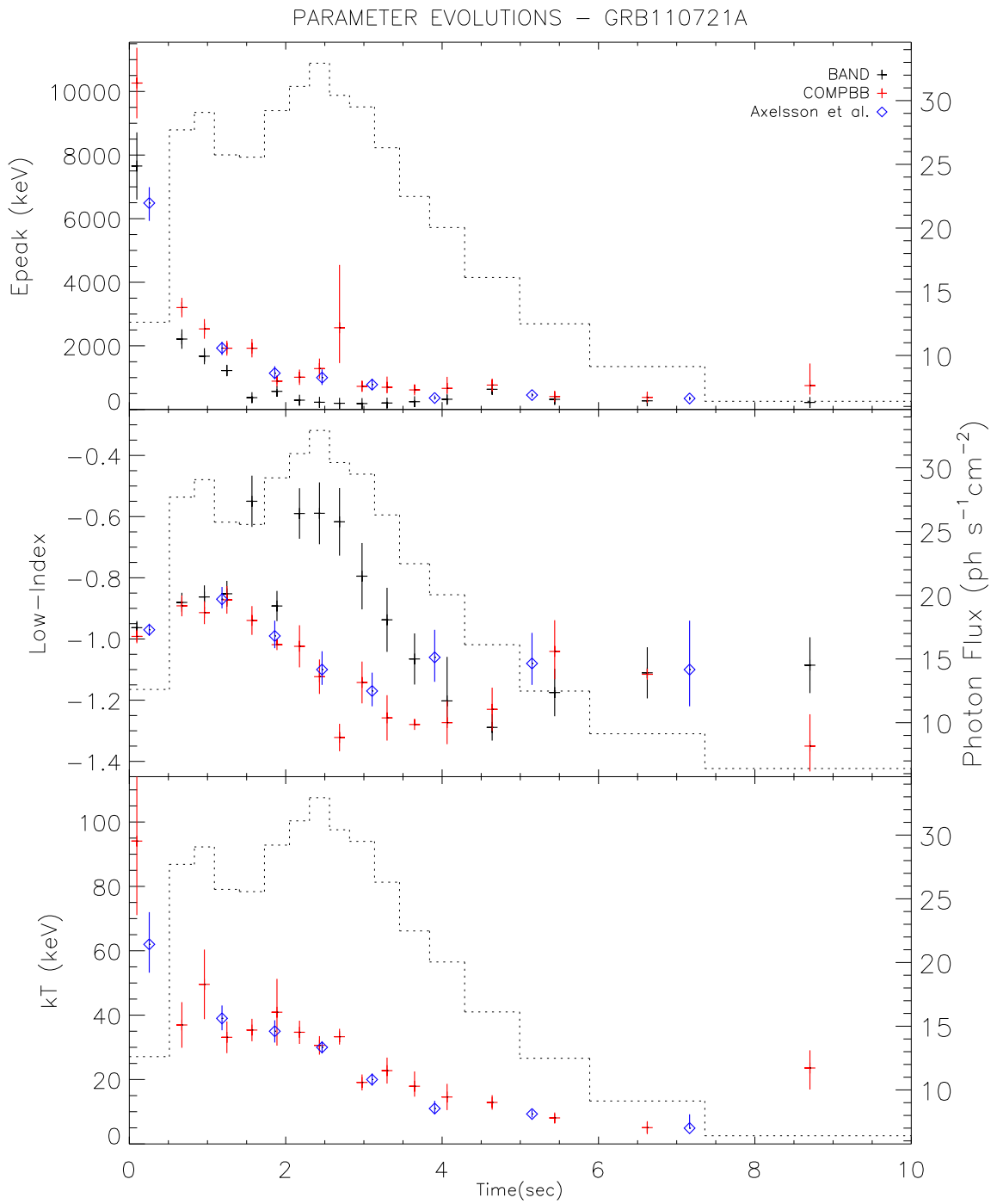


Figure 4.39: The evolution of BAND and COMPBB model parameters for GRB 110721A. The reported values are shown with diamonds (Axelsson et al. 2012), and kT of the very last bin has only upper limit. The dashed histograms represents the photon fluxes for each time interval (right axis).

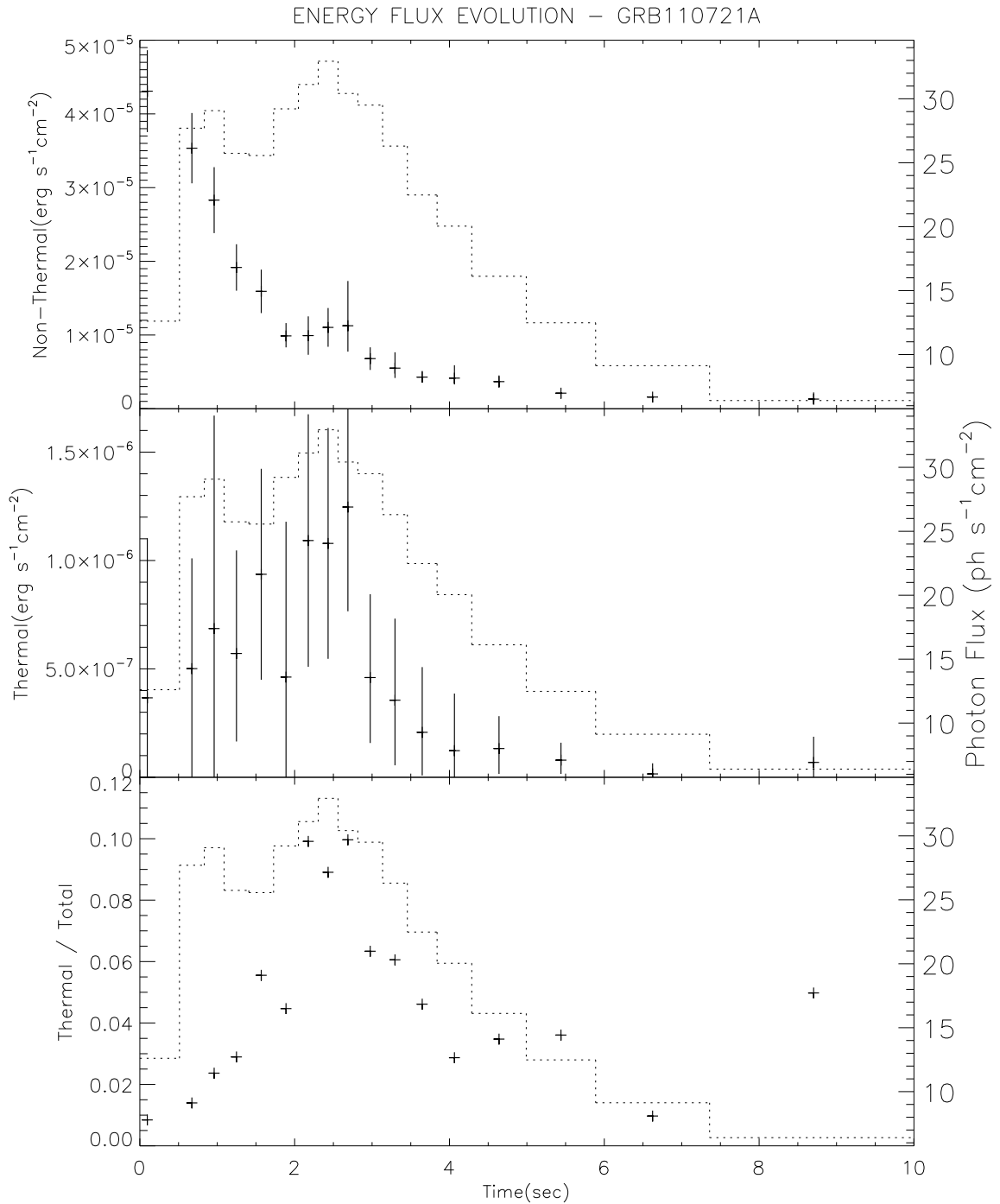


Figure 4.40: The energy flux evolutions of thermal and non-thermal components of COMPBB model for GRB 110721A. The top and middle panels show the energy flux evolutions of COMP and BB models, respectively. The flux ratio of thermal to total is seen in the bottom panel. The fluxes are calculated for the energy range 8 keV to 40 MeV. Errors in flux ratio of thermal to total are ignored. The dashed histograms represents the photon fluxes for each time interval (right axis).

## Chapter 5

### SUMMARY AND DISCUSSION

Most GRB spectra are non-thermal. Thermal emission component have been identified in a very limited number of burst spectra. These bursts are either extremely bright or having relatively simple, single pulse structure in their light curve (Guiriec et al., 2012 & 2013; Ghirlanda et al. 2013, Ryde 2004 & 2005). Here, we performed a systematic search for GRBs with spectral thermal signature for all the GRBs detected by Fermi-GBM in its first 2.5 years of operation (611 bursts). In the first part of this search we made use of hard low-energy spectral index signature, i.e., spectra with  $\alpha \geq -0.8$ . The hard alpha signature had been used in Ryde (2004) and Ghirlanda et al. (2013), but their selections were based on time-integrated spectral properties. In our study, we first performed systematic time-resolved analysis, then selected bursts with hard  $\alpha$  anywhere within burst, which is more appropriate than selecting bursts based on their time-integrated fit results, since it is known that a GRB spectrum can show strong spectral evolution. Also, there is no theoretical prediction that thermal emission should be seen only in bright burst spectra. In our systematic search, we used a set of selection criteria (based on  $\alpha$  and  $E_{\text{peak}}$ ) and identified 11 bursts with high probability of having thermal feature in their spectrum. Indeed, the spectral thermal characteristics for 4 of them have been previously reported. We also analyzed time-resolved spectra one of these four bursts, GRB 110721A, and our results are fully compatible with the reported one (Axelsson et al., 2012). Altogether, our systematic thermal GRB search is performed for a uniform sample of bursts, and takes into account the possible spectral evolution within a given burst. Finally, both identifying previously reported thermal GRBs with our search and yielding similar fit results for GRB 110721A, show the validity

of the method we used and reliability of the analysis presented in this thesis.

We performed detailed spectral analysis for the remaining 7 bursts for which the possible thermal signatures are identified for the first time. These seven bursts have peak fluxes between  $\sim 10$  and  $\sim 150$  photon  $\text{cm}^{-2} \text{s}^{-1}$  in  $10 - 1000$  keV range. The spectral simulations verified the statistical significance of the BB component in the spectra of 6 bursts. The thermal component is found to be sub-dominant in terms of thermal energy typically  $\sim 5\%$  of the total energy of individual bursts, and may go up to  $\sim 20\%$  for some of the individual time bins. The temperature  $kT$  evolution of the thermal component is different from one burst to another, and  $kT$  takes values between  $\sim 10 - \sim 150$  keV. It remains steady for some bursts, decreases monotonically for others. Sometimes,  $kT$  has a very complex evolution which could be due to pulse overlapping. Also, sudden increases in temperature can be observed correlated to the times of peak of photon flux, possibly due to re-heating of the flow by the inner engine activity. Previously, a common evolution pattern for  $kT$ , a relatively steady or slowly decreasing  $kT$  initially, and then a fast decay (also known as a broken power-law shape in logarithmic scale), was reported for single-pulse BATSE bursts (Ryde 2004 & 2005). Figure 5.1 shows the  $kT$  evolutions of the bursts in our sample in logarithmic scale. GRB 110721A also has similar  $kT$  evolution, as reported before (Axelsson et al., 2012). We cannot see a similar BPL evolution in  $kT$  for our bursts, clearly. Here, it is important to note that not all GRBs which are reported to have thermal component in their spectrum with high statistical significance show this broken power-law shape  $kT$  evolution (Guiriec et al. 2011 & 2013).

BAND-only and COMPBB time-resolved fit results showed that the spectral shape of non-thermal component is changed when thermal component is included in fits, not necessarily in the same way for each burst's each time bin. For GRB 080817A, GRB 081215A, and GRB 110323A, when the BB component is relatively strong, non-thermal component's peak is shifted to higher energies and low-energy spectral index is decreased significantly. On the other hand, we have cases where  $E_{\text{peak}}$  is decreased and  $\alpha$  is increased when BB component included in fits (e.g., GRB 090217, GRB 100414A).

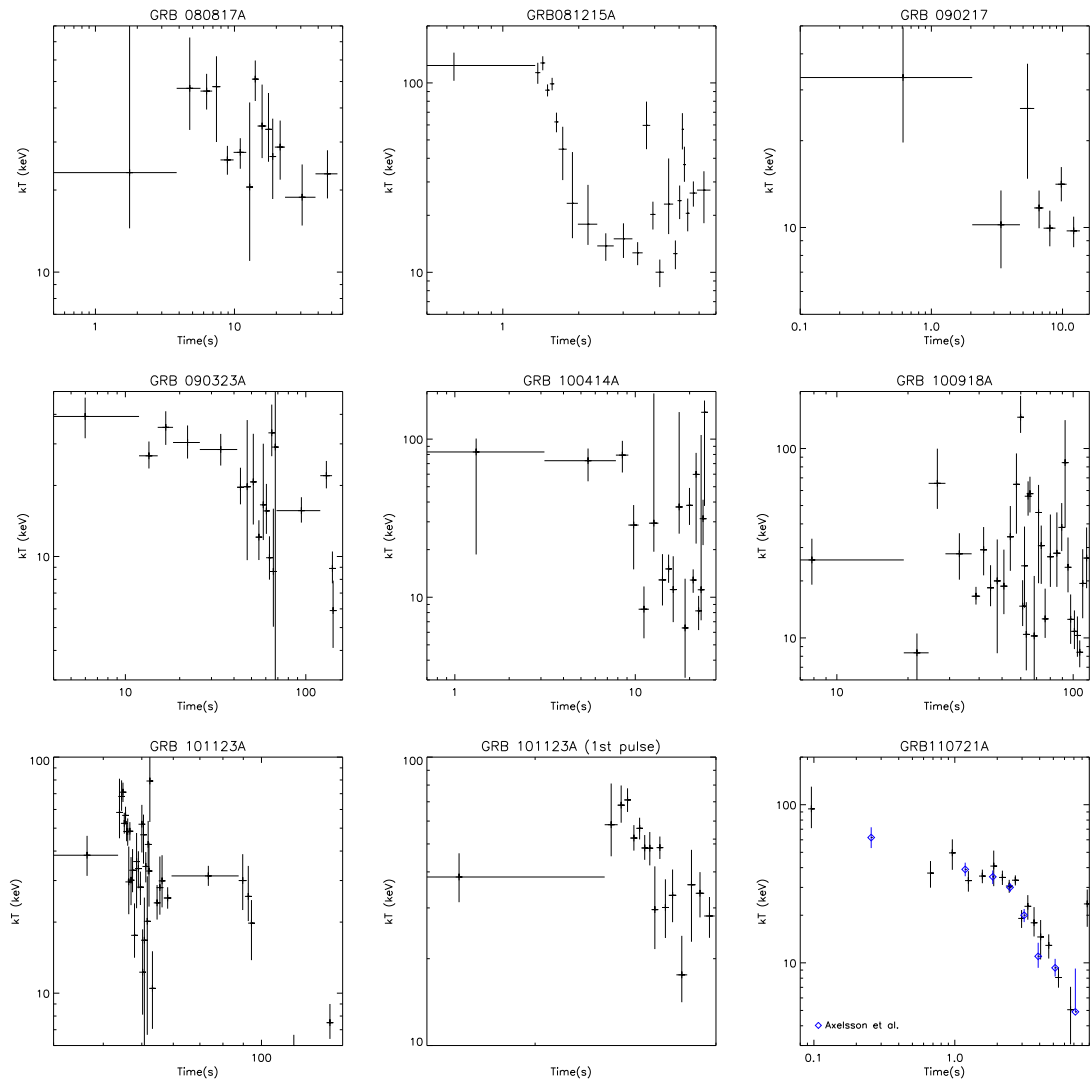


Figure 5.1: Temperature evolutions in logarithmic scale for all the bursts in our thermal candidate sample. The initial times of the GRB 101123A and test burst GRB 110721A are also shown in the last two plots.

## 5.1 Intrinsic Parameters of Expanding Fireball

Using the observed thermal flux and temperature, we calculated the following the physical parameters of the relativistic flow: the initial radius ( $R_0$ ), the bulk Lorentz factor ( $\Gamma$ ), and the photospheric radius ( $R_{\text{ph}}$ ). We have used the method presented in Hascoët et al. (2013), which is the generalized version (under several assumptions) of the original work of Pe'er et al. (2007), as discussed in Section 1.8. This method has been applied to another burst with thermal-like emission in its spectrum, GRB 120323A (Guiriec et al., 2013). We followed a similar procedure for our thermal bursts. The parameters are estimated as follows:

$$R_0 \simeq \left( \frac{D_L \mathcal{R}}{2(1+z)^2} \left( \frac{\phi}{1-\phi} \right)^{3/2} \right) \times \left( \frac{f_{\text{NT}}}{\epsilon_T} \right)^{3/2} \quad (5.1)$$

$$\Gamma \simeq \left( \frac{\sigma_T}{m_p c^3} \frac{(1+z)^2 D_L F_{\text{BB}}}{\mathcal{R}} \frac{1-\phi}{\phi} \right)^{1/4} \times ((1+\sigma)f_{\text{NT}})^{-1/4} \quad (5.2)$$

$$R_{\text{ph}} \simeq \left( \frac{\sigma_T}{16m_p c^3} \frac{D_L^5 F_{\text{BB}} \mathcal{R}^3}{(1+z)^6} \frac{1-\phi}{\phi} \right)^{1/4} \times ((1+\sigma)f_{\text{NT}})^{-1/4} \quad (5.3)$$

The quantity  $\mathcal{R}$  is defined as;  $\mathcal{R} = \left( \frac{F_{\text{BB}}}{\sigma T_{\text{BB}}^4} \right)^{1/2}$ .  $D_L$  and  $z$  are the luminosity distance and the redshift of the given burst.  $F_{\text{BB}}$  and  $T_{\text{BB}}$  are the flux and temperature of the thermal component,  $\phi$  is the ratio of thermal over total flux,  $\phi = F_{\text{BB}}/F_{\text{Tot}}$  for the given time bin of the burst.  $\epsilon_T$  is the fraction of thermal energy initially released.  $f_{\text{NT}}$  is the efficiency of the non-thermal emission process.  $\sigma$  is the amount of magnetization of the outflow at the end of acceleration phase.

The values of  $\epsilon_T$ ,  $f_{\text{NT}}$ , and  $\sigma$  are not directly measurable. So, we calculated the physical parameters by assuming these unknown factors;  $f_{\text{NT}}/\epsilon_T$  and  $(1+\sigma)f_{\text{NT}}$  as equal to 1. Then, we discuss possible scenarios; the form of the energy of the jet and the non-thermal emission process, based on the obtained  $R_0$ ,  $\Gamma$ , and  $R_{\text{ph}}$  values.

It is also good to check the relative locations of thermal and non-thermal emission sites. The internal shock radius  $R_{\text{is}}$  where the non-thermal emission originates is given by  $R_{\text{is}} \approx \Gamma^2 c t_{\text{var}}$ , where  $t_{\text{var}}$  is the characteristic timescale for the Lorentz factor variations (Daigne & Mochkovitch 1998). The internal shock radius is expected to be well above the photospheric radius, otherwise there would be sub-photospheric

dissipation causing modification in thermal emission component spectral shape.

The flow parameters are estimated for all of our candidate GRBs' each time interval by using observed BB flux and temperature of COMPBB model. In addition, we also calculate the same flow parameters by using observed BB parameters of BANDBB model for the time intervals in which BANDBB model parameters are all constrained. For the bursts which do not have redshift measurement we assumed  $z = 1$ , and a corresponding luminosity distance of  $D_L = 2.06 \times 10^{28}$  cm is taken.

Table 5.1 lists the estimated ranges for the parameters of the relativistic flow  $R_0$ ,  $R_{\text{ph}}$ ,  $R_{\text{is}}$ , and  $\Gamma$  for all the bursts in our thermal candidate GRB sample. The estimated values by using COMPBB and BANDBB model parameters are consistent with each other for a given burst. Also, for a given parameter, ranges are very similar for all the bursts listed. When we compare the locations of thermal and non-thermal emission sites, for all the bursts listed, the  $R_{\text{is}}$  is always higher than the  $R_{\text{ph}}$ , implying that the dissipation (non-thermal emission) is occurring well above the photospheric radius (thermal emission site) as expected. The  $\Gamma$  are in the typical range for GRB outflows as inferred from compactness problem, i.e., a few hundreds. For long bursts where the progenitor is believed to be core collapse of a massive star, the initial radius is expected to be  $\sim 300$  km (Hascoët et al., 2013). Our estimated  $R_0$  values are around the typical range. In some cases  $R_0$  can be an order of magnitude more or less than the typical value. As mentioned, the values of  $\epsilon_T$ ,  $f_{\text{NT}}$ , and  $\sigma$  are not directly measurable. The estimated  $R_0$ ,  $R_{\text{ph}}$ , and  $\Gamma$  values (with unknown factors;  $f_{\text{NT}}/\epsilon_T$  and  $(1 + \sigma)f_{\text{NT}}$  as equal to 1) are in the typical ranges. There are two scenarios for non-thermal energy dissipation; internal shocks with  $f_{\text{NT}} \sim 0.01$  (Daigne & Mochkovitch, 1998) and magnetic reconnection with  $f_{\text{NT}} \gtrsim 0.1 - 0.5$  (Zhang & Yan, 2011). In the conventional Fireball scenario ( $\epsilon_T = 1$ ), where we have kinetic acceleration and non-thermal energy is dissipated by internal shocks, is very challenging for our bursts here. Even with a  $f_{\text{NT}} \sim 0.05$ , the initial radius will be decreased by two orders of magnitude, i.e.,  $R_0 < 70$  km. However, in the magnetized outflows, where  $\epsilon_T \sim 0.05$  (since thermal energy flux is mostly  $\sim 5\%$  of total in our sample), we can either have internal shocks ( $f_{\text{NT}} \sim 0.05$ ) or magnetic reconnection ( $f_{\text{NT}} \sim 0.2$ ) as dissipation process. The other parameters are not affected much by variations in non-thermal efficiency, since they are  $\propto f_{\text{NT}}^{-1/4}$ . The last unknown

factor is the amount of magnetization in the flow at the end of acceleration,  $\sigma$ . The existence of magnetic fields affects the formation of shocks in the flow. For  $\sigma \gtrsim 1$  the shock may not be formed at all (Mimica & Aloy, 2010). Then, for highly magnetized flows (still at the end of acceleration) magnetic reconnection is favourable process for energy extraction. Also, an efficient internal shocks formation requires highly variable Lorentz factor of the flow. A variable  $\Gamma$  implies a variable  $kT$  evolution, since  $kT$  is strongly dependent on  $\Gamma$  (Pe'er et al., 2007). For a burst which has a thermal component with relatively steady  $kT$ , again, magnetic reconnection is a better candidate for energy dissipation. From  $kT$  evolutions of our thermal bursts, GRB 081215A and GRB 101123A have relatively variable  $kT$  evolution, and they may have efficient internal shock formation within their relativistic flows.

Table 5.1: Estimated ranges for intrinsic flow parameters for all the bursts in thermal candidate sample.

GRB Name	$z^a$	Model <sup>b</sup>	Initial Radius (cm)	Photospheric Radius (cm)	Internal Shock Radius (cm)	Lorentz Factor
			$R_0 \times \left(\frac{f_{\text{NT}}}{\epsilon_T}\right)^{3/2}$	$R_{\text{ph}} \times ((1 + \sigma)f_{\text{NT}})^{-\frac{1}{4}}$	$R_{\text{is}}$	$\Gamma \times ((1 + \sigma)f_{\text{NT}})^{-\frac{1}{4}}$
080817A	1	C	$1.6 \times 10^6 - 3.8 \times 10^7$	$8.7 \times 10^8 - 1.9 \times 10^9$	$2.2 \times 10^{12} - 9.5 \times 10^{12}$	183 - 399
080817A		B	$9.8 \times 10^5 - 4.7 \times 10^6$	$1.3 \times 10^9 - 1.9 \times 10^9$	$5.6 \times 10^{12} - 9.8 \times 10^{12}$	305 - 404
081215A	1	C	$5.8 \times 10^6 - 2.0 \times 10^8$	$5.9 \times 10^8 - 7.8 \times 10^9$	$1.9 \times 10^{12} - 4.0 \times 10^{13}$	179 - 812
081215A		B	$4.7 \times 10^6 - 2.7 \times 10^8$	$2.3 \times 10^9 - 9.7 \times 10^9$	$2.5 \times 10^{12} - 4.1 \times 10^{13}$	204 - 832
090217	1	C	$1.2 \times 10^6 - 5.0 \times 10^7$	$1.0 \times 10^9 - 4.7 \times 10^9$	$1.6 \times 10^{12} - 7.5 \times 10^{12}$	162 - 354
090217		B	$2.3 \times 10^7$	$4.9 \times 10^9$	$2.2 \times 10^{12}$	193
090323A	3.57	C	$3.8 \times 10^6 - 4.8 \times 10^8$	$1.7 \times 10^9 - 1.4 \times 10^{10}$	$4.2 \times 10^{12} - 3.3 \times 10^{13}$	266 - 738
090323A		B	$2.4 \times 10^6 - 1.6 \times 10^7$	$1.8 \times 10^9 - 7.8 \times 10^9$	$2.2 \times 10^{13} - 5.6 \times 10^{13}$	601 - 774
100414A	1.368	C	$1.7 \times 10^6 - 8.3 \times 10^7$	$5.9 \times 10^8 - 7.7 \times 10^9$	$2.5 \times 10^{12} - 1.6 \times 10^{13}$	206 - 519
100414A		B	$1.7 \times 10^6 - 2.7 \times 10^7$	$3.8 \times 10^9 - 8.8 \times 10^9$	$3.0 \times 10^{12} - 4.0 \times 10^{12}$	223 - 259
100918A	1	C	$1.7 \times 10^6 - 8.3 \times 10^7$	$5.9 \times 10^8 - 7.7 \times 10^9$	$2.5 \times 10^{12} - 1.6 \times 10^{13}$	206 - 519
100918A		B	$1.7 \times 10^6 - 2.7 \times 10^7$	$3.8 \times 10^9 - 8.8 \times 10^9$	$3.0 \times 10^{12} - 4.0 \times 10^{12}$	223 - 259
101123A	1	C	$7.2 \times 10^5 - 6.2 \times 10^8$	$4.5 \times 10^8 - 4.6 \times 10^9$	$1.1 \times 10^{12} - 2.1 \times 10^{13}$	138 - 587
101123A		B	$1.4 \times 10^6 - 1.9 \times 10^8$	$1.3 \times 10^9 - 5.8 \times 10^9$	$1.3 \times 10^{12} - 7.2 \times 10^{12}$	147 - 346

<sup>a</sup> assumed to be 1 when no redshift measurement is available.

<sup>b</sup> C is for COMPBB and B is for BANDBB models.

## 5.2 Remaining Questions

Now, I will discuss several issues related our analysis method and obtained results. *Modeling thermal component with a blackbody function:* We used a pure blackbody function to model thermal emission component in GRB spectrum. However, the observed photospheric thermal emission can be modified due to two main reasons; the complex geometry of the photosphere (angle dependence of the photospheric radius) and existence of strong spectral evolution in kT (Goodman 1986; Beloborodov 2010; Pe'er 2008; Guiriec et al. 2013). However as noted by Pe'er (2008) the geometrical effects should not significant in the observer frame while the inner source is active, since only the line of sight photons characterize the spectrum. Moreover, by performing time-resolved analysis we minimized the second effect. However, for the pulse simulations we performed in this thesis, modeling the thermal component with a multi-color blackbody (Pe'er & Ryde, 2011), which is an integral of blackbodies with different temperatures, could have increased the level of significance of thermal component we identified. This may be especially for the first pulse of GRB 081215A, during which we have a strong evolution in kT (see Figure 4.7).

*Did addition of thermal component resolve the hard alpha issue?:* Our main selection criteria for the thermal GRB search was the hard  $\alpha$  signature. This way we have selected burst with spectra which are challenging non-thermal emission mechanisms. Indeed, additional BB component decreased  $\alpha$  of the non-thermal component most of the time. The most clear examples are GRB 080817A, GRB 081215A, and GRB 110323A. For GRB 080817A BAND-only fits have  $\alpha > -0.8$ , whereas  $\alpha \sim -1$  for COMPBB. Similarly, for GRB 081215A  $\alpha$  shifts from  $\sim -0.3$  to  $-0.8$ , and for GRB 101123A  $\alpha$  is decreased to  $\sim -1.1$  from  $\sim -0.3$ . However, as mentioned, there are cases where additional BB component increases the  $\alpha$  relative to BAND-only fits.

*Time binning issue:* In order to perform a time-resolved analysis we divided the prompt emission phase of individual bursts into time intervals by signal-to-noise ratio method. This method provides us a reproducible and statistically valid way for conducting time-resolved analysis for a sample of bursts. However, using a fixed SNR for a group of bursts might be a problem. Each burst has almost unique light curve as we have seen very clearly in our thermal candidate bursts sample. While binning

each light curve with a fixed SNR, it is highly probable to combine different features seen in light curve, e.g., some portion of decaying part of one pulse and raising part of a consecutive pulse. Also, we might be losing information on spectral evolution, i.e., using single time interval during which strong spectral evolution exists. Despite these potential problems, in order to perform our analysis uniformly among all bursts in the sample, and obtain reproducible results we preferred to use SNR method for time binning.

*Is this the complete sample of thermal GRBs?:* In our analysis, we have selected burst with peak energies higher than 400 keV. Our main motivation was to identify thermal and non-thermal peaks in the spectrum easily, since thermal peak in  $\nu F_\nu$  spectrum is expected to be at most  $\sim 300$  keV. Here, our assumption was that the BB component is sub-dominant, and when we apply COMP-only model to spectrum it will converge to non-thermal peak. However, if the thermal component is strong enough it can make COMP-only model to converge the thermal component, i.e., making COMP-only  $E_{\text{peak}} \sim$  a few hundred. Indeed, there is one burst detected by Fermi-GBM, GRB 100517, which has a pure thermal spectrum with  $E_{\text{peak}} \sim 100$  keV (Ghirlanda et al., 2013). This burst actually passed our  $\alpha$  selection, but not the  $E_{\text{peak}}$  one. There is another burst detected by Fermi-GBM, GRB 090926A, which also has a thermal spectral component (Guiriec et al., 2015). This burst has  $E_{\text{peak}} \sim 300$  keV when its spectrum is modelled by a single non-thermal model. Again, we lost this burst during our  $E_{\text{peak}}$  selection. Therefore, our next step to enlarge our thermal GRB sample will be modifying the  $E_{\text{peak}}$  selection criteria. In addition to these bursts, there are several other Fermi-GBM bursts with reported thermal spectral features (e.g., GRB 090820A, Burgess et al. 2011). Further analysis of these missing GRBs is needed to understand their absence in our sample. Also, after the time of the detection of the latest GRB included in our systematic search, from 01 January 2011 to 30 June 2015, Fermi-GBM detected 1035 more GRBs. When we extend our analysis to these bursts, by statistical means, we expect to find  $\sim 18$  more GRBs with sub-dominant thermal component in their spectra. In conclusion, the sample we present in this thesis is not the final thermal GRB sample. As we find bursts with thermal component in their spectrum, I believe we will find better ways to identify more thermal GRBs.

## Chapter 6

### CONCLUSIONS

We presented, for the first time, a very detailed time-resolved spectral analysis of 7 GRBs, where there is a significant thermal emission component in the spectra of 6 of them. The sample is obtained from a systematic time-resolved analysis of more than 600 bursts detected by Fermi-GBM in its first 2.5 years of operation. Time-resolved spectral analysis of these bursts revealed that the evolution of temperature of the thermal component is very different from one burst to another. The thermal energy flux is between 2.6% – 9% of the total energy flux of the burst. This may suggest that the thermal component is present in all GRB spectra (as expected theoretically), but we can only detect it if the thermal energy flux is  $\gtrsim$  a few % of the total energy flux. In some cases  $kT$  follows photon flux history (e.g., GRB 081215A), whereas it remains relatively steady for others (e.g., GRB 080817A). Single and hybrid model fit results showed that including blackbody component in fits may cause significant change in the shape of non-thermal component. The observed hard  $\alpha$  values which are challenging non-thermal emission processes are softened and become compatible with electron synchrotron emission in a decaying magnetic field, clearly, for some portions of prompt emission phases of GRB 080817A, GRB 081215A, and GRB 101123A, but not for all. Assuming that this thermal component is originating from photosphere of the GRB jet, we estimated several physical parameters for our bursts. The inferred parameters suggests an initially magnetized flow, where the energy dissipation mechanism could be either internal shocks or magnetic reconnection.

## 6.1 Prospects for Future Work

Identifying more GRBs with thermal signature in their spectra is required to better understand how and in what type of GRB spectrum the thermal component appears. Detection of this thermal component, if it exists, is also important to model the non-thermal component more properly. To this extent, our next main goal is to enlarge the sample presented in this thesis. First, we will modify the selection criteria that we used in the systematic search to increase our sample size. Then, we will extend this work to bursts detected by Fermi-GBM after 2010.

Our another short term goal is to analyze GRB 090902B. This is one of the bursts in our thermal candidate sample and its thermal nature was previously reported. The reason that we want to re-analyze this burst is that the form of the thermal component in its spectrum. Ryde et al. (2011) claimed that the main emission component of this burst's spectrum is a modified blackbody (broadened Planck function due to subphotospheric dissipation) which is accompanied by a non-thermal power-law component. However, in our analysis we have seen that the time-integrated spectrum of GRB 090902B shows significant improvement when it is modelled with a thermal component along with a non-thermal one, i.e., double curvature model is better than single one. We need to perform time-resolved analysis to verify the existence of two humps in the spectrum, i.e., improvement is not due to spectral evolution throughout the prompt phase.

## Bibliography

- Abdo, A. A., Ackermann, M., Ajello, M., et al. 2009, *ApJL*, 706, L138
- Akerlof, C., Balsano, R., Barthelmy, S., et al. 1999, *Nature*, 398, 400
- Axelsson, M., Baldini, L., Barbiellini, G., et al. 2012, *ApJL*, 757, L31
- Band, D., Matteson, J., Ford, L., et al. 1993, *ApJ*, 413, 281
- Band, D. L. 1997, *ApJ*, 486, 928
- Beloborodov, A. M. 2000, *ApJL*, 539, L25
- . 2010, *MNRAS*, 407, 1033
- Berger, E. 2011, *GRB Coordinates Network*, 12193, 1
- Bissaldi, E., Briggs, M., von Kienlin, A., & McBreen, S. 2008, *GRB Coordinates Network*, 8108, 1
- Bissaldi, E., & Connaughton, V. 2009, *GRB Coordinates Network*, 9866, 1
- Bissaldi, E., von Kienlin, A., Lichti, G., et al. 2009, *Experimental Astronomy*, 24, 47
- Bloom, J. S., Kulkarni, S. R., & Djorgovski, S. G. 2002, *AJ*, 123, 1111
- Bosnjak, Z., Celotti, A., & Ghirlanda, G. 2006, *MNRAS*, 370, L33
- Burgess, J. M., Preece, R. D., Baring, M. G., et al. 2011, *ApJ*, 741, 24
- Burgess, J. M., Preece, R. D., Ryde, F., et al. 2014, *ApJL*, 784, L43
- Burrows, D. N., Romano, P., Falcone, A., et al. 2005, *Science*, 309, 1833
- Burrows, D. N., Falcone, A., Chincarini, G., et al. 2007, *Royal Society of London Philosophical Transactions Series A*, 365, 1213
- Campana, S., Mangano, V., Blustin, A. J., et al. 2006, *Nature*, 442, 1008
- Cenko, S. B., Frail, D. A., Harrison, F. A., et al. 2010, *ApJ*, 711, 641
- Chandra, P., Cenko, S. B., Frail, D. A., et al. 2008, *ApJ*, 683, 924
- Chornock, R., Perley, D. A., Cenko, S. B., & Bloom, J. S. 2009, *GRB Coordinates Network*, 9028, 1

- Cline, T. L., Desai, U. D., Klebesadel, R. W., & Strong, I. B. 1973, *ApJL*, 185, L1
- Cohen, E., Katz, J. I., Piran, T., et al. 1997, *ApJ*, 488, 330
- Colgate, S. A. 1968, *Canadian Journal of Physics*, 46, 476
- Costa, E., Frontera, F., Heise, J., et al. 1997, *Nature*, 387, 783
- Covino, S., Malesani, D., Israel, G. L., et al. 2006, *A&A*, 447, L5
- Cucchiara, A., & Fox, D. B. 2010, *GRB Coordinates Network*, 10606, 1
- Cucchiara, A., Fox, D. B., Tanvir, N., & Berger, E. 2009, *GRB Coordinates Network*, 9873, 1
- Dai, X., Halpern, J. P., Morgan, N. D., et al. 2007, *ApJ*, 658, 509
- Daigne, F., & Mochkovitch, R. 1998, *MNRAS*, 296, 275
- . 2002, *MNRAS*, 336, 1271
- de Palma, F., Bregeon, J., & Tajima, H. 2009, *GRB Coordinates Network*, 9867, 1
- de Pasquale, M., Piro, L., Gendre, B., et al. 2006, *A&A*, 455, 813
- Dingus, B. L., & Catelli, J. R. 1998, in *19th Texas Symposium on Relativistic Astrophysics and Cosmology*, ed. J. Paul, T. Montmerle, & E. Aubourg, 63
- Drenkhahn, G., & Spruit, H. C. 2002, *A&A*, 391, 1141
- Eichler, D., Livio, M., Piran, T., & Schramm, D. N. 1989, *Nature*, 340, 126
- Falcone, A. D., Burrows, D. N., Lazzati, D., et al. 2006, *ApJ*, 641, 1010
- Fan, Y., & Piran, T. 2006, *MNRAS*, 369, 197
- Fenimore, E. E., Epstein, R. I., & Ho, C. 1993, *A&AS*, 97, 59
- Fenimore, E. E., in 't Zand, J. J. M., Norris, J. P., Bonnell, J. T., & Nemiroff, R. J. 1995, *ApJL*, 448, L101
- Foley, S. 2010, *GRB Coordinates Network*, 10595, 1
- Frail, D. A., Kulkarni, S. R., Sari, R., et al. 2001, *ApJL*, 562, L55
- Galama, T. J., & Wijers, R. A. M. J. 2001, *ApJL*, 549, L209
- Gallant, Y. A. 2002, in *Lecture Notes in Physics*, Berlin Springer Verlag, Vol. 589, *Relativistic Flows in Astrophysics*, ed. A. W. Guthmann, M. Georganopoulos, A. Marcowith, & K. Manolakou, 24
- Gehrels, N., Chincarini, G., Giommi, P., et al. 2004, *ApJ*, 611, 1005
- Gehrels, N., Sarazin, C. L., O'Brien, P. T., et al. 2005, *Nature*, 437, 851
- Ghirlanda, G., Pescalli, A., & Ghisellini, G. 2013, *MNRAS*, 432, 3237

- Ghisellini, G., Celotti, A., & Lazzati, D. 2000, MNRAS, 313, L1
- Ghisellini, G., Ghirlanda, G., Nava, L., & Celotti, A. 2010, MNRAS, 403, 926
- Giannios, D. 2008, A&A, 480, 305
- Giannios, D., & Spruit, H. C. 2005, A & A, 430, 1
- Goldstein, A., Burgess, J. M., Preece, R. D., et al. 2012, ApJS, 199, 19
- Goodman, J. 1986, ApJL, 308, L47
- Granot, J., Königl, A., & Piran, T. 2006, MNRAS, 370, 1946
- Greiner, J., Clemens, C., Krühler, T., et al. 2009, A&A, 498, 89
- Gruber, D., Goldstein, A., Weller von Ahlefeld, V., et al. 2014, ApJS, 211, 12
- Guiriec, S. 2010, GRB Coordinates Network, 11423, 1
- Guiriec, S., Connaughton, V., Briggs, M. S., et al. 2011, ApJL, 727, L33
- Guiriec, S., Daigne, F., Hascoët, R., et al. 2013, ApJ, 770, 32
- Guiriec, S., Kouveliotou, C., Daigne, F., et al. 2015, ApJ, 807, 148
- Hascoët, R., Daigne, F., & Mochkovitch, R. 2013, A & A, 551, A124
- Hjorth, J., Sollerman, J., Møller, P., et al. 2003, Nature, 423, 847
- Kaneko, Y., Preece, R. D., Briggs, M. S., et al. 2006, ApJS, 166, 298
- Katz, J. I. 1994, ApJ, 422, 248
- Klebesadel, R. W., Strong, I. B., & Olson, R. A. 1973, ApJL, 182, L85
- Kouveliotou, C., Meegan, C. A., Fishman, G. J., et al. 1993, ApJL, 413, L101
- Krolik, J. H., & Pier, E. A. 1991, ApJ, 373, 277
- Kulkarni, S. R., Frail, D. A., Wieringa, M. H., et al. 1998, ArXiv Astrophysics e-prints
- Kumar, P., & Panaitescu, A. 2000, ApJL, 541, L51
- Larsson, J., Levan, A. J., Davies, M. B., & Fruchter, A. S. 2007, MNRAS, 376, 1285
- Lloyd-Ronning, N. M., & Petrosian, V. 2002, ApJ, 565, 182
- Lu, R.-J., Wei, J.-J., Liang, E.-W., et al. 2012, ApJ, 756, 112
- Mallozzi, R.S., Preece, R.D. & Briggs, M.S. 2005, RMFIT – A Lightcurve and Spectral Analysis Tool, Available through request, ©2011 Robert D. Preece, UNIVERSITY OF ALABAMA IN HUNTSVILLE
- Mangano, V., Holland, S. T., Malesani, D., et al. 2007, A&A, 470, 105

- McBreen, S., Quilligan, F., McBreen, B., Hanlon, L., & Watson, D. 2001, *A&A*, 380, L31
- McEnery, J. 2008, GRB Coordinates Network, 8684, 1
- Medvedev, M. V. 2000, *ApJ*, 540, 704
- Meegan, C., Lichti, G., Bhat, P. N., et al. 2009, *ApJ*, 702, 791
- Meegan, C. A., Fishman, G. J., Wilson, R. B., et al. 1992, *Nature*, 355, 143
- Mészáros, P., Ramirez-Ruiz, E., Rees, M. J., & Zhang, B. 2002, *ApJ*, 578, 812
- Mészáros, P., & Rees, M. J. 1993, *ApJL*, 418, L59
- . 2000, *ApJ*, 530, 292
- Metzger, B. D., Quataert, E., & Thompson, T. A. 2008, *MNRAS*, 385, 1455
- Metzger, M. R., Djorgovski, S. G., Kulkarni, S. R., et al. 1997, *Nature*, 387, 878
- Mimica, P., & Aloy, M. A. 2010, *MNRAS*, 401, 525
- Norris, J. P., Nemiroff, R. J., Bonnell, J. T., et al. 1996, *ApJ*, 459, 393
- O’Brien, P. T., Willingale, R., Osborne, J. P., & Goad, M. R. 2006a, *New Journal of Physics*, 8, 121
- O’Brien, P. T., Willingale, R., Osborne, J., et al. 2006b, *ApJ*, 647, 1213
- Ohno, M., Cutini, S., McEnery, J., Chiang, J., & Koerding, E. 2009a, GRB Coordinates Network, 9021, 1
- Ohno, M., McEnery, J., & Pelassa, V. 2009b, GRB Coordinates Network, 8903, 1
- Ott, C. D., Burrows, A., Thompson, T. A., Livne, E., & Walder, R. 2006, *ApJS*, 164, 130
- Paczynski, B. 1986, *ApJL*, 308, L43
- Pe’er, A. 2008, *ApJ*, 682, 463
- Pe’er, A., Mészáros, P., & Rees, M. J. 2005, *ApJ*, 635, 476
- . 2006, *ApJ*, 642, 995
- Pe’er, A., & Ryde, F. 2011, *ApJ*, 732, 49
- Pe’er, A., Ryde, F., Wijers, R. A. M. J., Mészáros, P., & Rees, M. J. 2007, *ApJL*, 664, L1
- Pe’er, A., & Waxman, E. 2005, *ApJ*, 628, 857
- Pendleton, G. N., Paciesas, W. S., Briggs, M. S., et al. 1997, *ApJ*, 489, 175
- Peng, F., Königl, A., & Granot, J. 2005, *ApJ*, 626, 966

- Pian, E., Amati, L., Antonelli, L. A., et al. 2000, *ApJ*, 536, 778
- Piran, T., & Sari, R. 1998, in *American Institute of Physics Conference Series*, Vol. 428, *Gamma-Ray Bursts, 4th Huntsville Symposium*, ed. C. A. Meegan, R. D. Preece, & T. M. Koshut, 662–666
- Piro, L., Scarsi, L., & Butler, R. C. 1995, in *Society of Photo-Optical Instrumentation Engineers (SPIE) Conference Series*, Vol. 2517, *X-Ray and EUV/FUV Spectroscopy and Polarimetry*, ed. S. Fineschi, 169–181
- Preece, R. 2008, *GRB Coordinates Network*, 8678, 1
- Preece, R. D., Briggs, M. S., Giblin, T. W., et al. 2002, *ApJ*, 581, 1248
- Preece, R. D., Briggs, M. S., Mallozzi, R. S., et al. 1998a, *ApJL*, 506, L23
- Preece, R. D., Pendleton, G. N., Briggs, M. S., et al. 1998b, *ApJ*, 496, 849
- Rees, M. J., & Mészáros, P. 1994, *ApJL*, 430, L93
- . 1998, *ApJL*, 496, L1
- . 2005, *ApJ*, 628, 847
- Ruderman, M. 1975, in *Annals of the New York Academy of Sciences*, Vol. 262, *Seventh Texas Symposium on Relativistic Astrophysics*, ed. P. G. Bergman, E. J. Fenyves, & L. Motz, 164–180
- Rybicki, G. B., & Lightman, A. P. 1979, *Radiative processes in astrophysics*
- Ryde, F. 2004, *ApJ*, 614, 827
- . 2005, *ApJL*, 625, L95
- Ryde, F., & Pe’er, A. 2009, *ApJ*, 702, 1211
- Ryde, F., Pe’er, A., Nymark, T., et al. 2011, *MNRAS*, 415, 3693
- Salvaterra, R., Della Valle, M., Campana, S., et al. 2009, *Nature*, 461, 1258
- Sari, R., Piran, T., & Halpern, J. P. 1999, *ApJL*, 519, L17
- Sari, R., Piran, T., & Narayan, R. 1998, *ApJL*, 497, L17
- Savaglio, S., Glazebrook, K., & Le Borgne, D. 2009, *ApJ*, 691, 182
- Spitkovsky, A. 2008, *ApJL*, 682, L5
- Spruit, H. C., Daigne, F., & Drenkhahn, G. 2001, *A&A*, 369, 694
- Takahashi, H., Ohno, M., & Omodei, N. 2010, *GRB Coordinates Network*, 10594, 1
- Tanvir, N. R., Fox, D. B., Levan, A. J., et al. 2009, *Nature*, 461, 1254
- Tavani, M. 1996, *ApJ*, 466, 768

- Tierney, D., & von Kienlin, A. 2011, GRB Coordinates Network, 12187, 1
- Tierney, D., McBreen, S., Preece, R. D., et al. 2013, *A&A*, 550, A102
- Uhm, Z. L., & Zhang, B. 2014, *Nature Physics*, 10, 351
- Vasileiou, V., Piron, F., Tierney, D., et al. 2011, GRB Coordinates Network, 12188, 1
- Virgili, F. J., Zhang, B., O'Brien, P., & Troja, E. 2011, *ApJ*, 727, 109
- von Kienlin, A. 2009, GRB Coordinates Network, 8902, 1
- von Kienlin, A., Meegan, C. A., Paciesas, W. S., et al. 2014, *ApJS*, 211, 13
- Weibel, E. S. 1959, *Phys. Rev. Lett.*, 2, 83
- Woosley, S. E. 1993, *ApJ*, 405, 273
- Yoon, S.-C., Langer, N., & Norman, C. 2006, *A&A*, 460, 199
- Zalamea, I., & Beloborodov, A. M. 2011, *MNRAS*, 410, 2302
- Zhang, B., Fan, Y. Z., Dyks, J., et al. 2006, *ApJ*, 642, 354
- Zhang, B., Lu, R.-J., Liang, E.-W., & Wu, X.-F. 2012, *ApJL*, 758, L34
- Zhang, B., & Yan, H. 2011, *ApJ*, 726, 90